Photophysical properties of π-conjugated molecular ions in the gas phase

Maj-Britt Suhr Kirketerp

Department of Physics and Astronomy
Aarhus University

PhD thesis
August 2011

This thesis has been submitted to the Faculty of Science at Aarhus University in order to fulfill the requirements for obtaining a PhD degree in physics. The work has been carried out under the supervision of associate professor Steen Brøndsted Nielsen at the Department of Physics and Astronomy.

Contents

Acknowledgements

First and foremost, I would like to thank my supervisor, Steen Brøndsted Nielsen. His positivity, passion and enthusiasm has made it a pleasure to be a member of his group. On top of fruitful discussions on physics and chemistry, I appreciate his contribution to my oral and written communication skills - despite the struggle it involved.

I would also like to thank Kristian Støchkel and Umesh Kadhane who trained me in the lab. If I only bring with me a percentage of your technical knowledge on instrumentation and electronics I am pleased. In this respect, the electronics department and the mechanical workshop are invaluable for the laboratory and I appreciate their support during the years.

My project was accomplished in close collaboration with Mogens Brøndsted Nielsen, Copenhagen University, who carried out the synthesis and solution phase experiments. Furthermore, theoretical calculations by the group of Angel Rubio, San Sebastian, Spain, added an important extra dimension to the project. Their contributions complete my project.

For one month, I had the pleasure to visit the group of Jacqueline Fayeton, University Paris sud, France. On top of the important lesson to value a well working lab and technical staff, I gained valuable insight into the research in another group and practiced to present and defend my own research. I would like to thank the whole group for a very interesting and rewarding stay. When it comes to international experiences, I recognize the unique opportunities given to me by the European program ITS LEIF.

All former and present members of the group are gratefully acknowledged for an always cozy atmosphere, and many enjoyable hours in the lab, at lunch, after work, and at conferences. Especially, I would like to thank Morten (for *the early years*), Anne (for *always being one steep ahead*), Lisbeth (for *fridays*), Camilla, and Kristian - I will miss our daily coffee breaks discussing this and that. Finally,

I would like to thank Anne, Dennis, Christian, and Lisbeth for proofreading this manuscript at different stages in the process. And also I would like to thank my family and friends for their support during the years.

Last but not least, I recognize and express my gratitude to the financial assistance of the Carlsberg foundation and *Lundbechfonden*.

Maj-Britt Suhr Kirketerp
Aarhus, 2011

Abstract

During my Ph.D. I have investigated the photophysical properties of π-conjugated chromophore ions isolated in the gas phase. The investigation is based on action spectroscopy and mass spectroscopy, and was carried out at two instrumental setups at the Department of Physics and Astronomy, Aarhus University, Denmark.

The present thesis reviews gas phase absorption spectroscopy on even-electron intermediate sized molecular ions. Hence, on top of my own research I have included the work of others to provide a broader perspective and to summarize the present status of this research field.

The aim is to obtain a thorough understanding of the basic optical properties of molecular ions. The understanding is important both from a fundamental point of view but also to comprehend the many light-driven or light-involving processes in nature. In this regard, absorption spectroscopy turns out to be a useful tool and moreover, it also serves as a general characterization tool for molecular ions.

A good starting point for this task is to understand the optical properties of a chromophore as this is the light absorbing part of a molecule. Delocalization of the electron in the chromophore is the primary parameter in determining the absorption properties, and the concept of resonance structures is a helpful tool to visualize the delocalization. As the electron delocalization depends on the whole geometrical (two and three dimensional) structure of the chromophore, this is indirectly revealed in the absorption spectrum. For many molecular ions, charge density is transferred in the transition, and the electronic coupling between parts of the chromophore becomes important for the absorption properties. The effect of charge transfer may in some cases dominate the effect of electron delocalization.

When a thorough understanding of the photophysical properties of the chromophore is obtained one can move on to investigate the more realistic situation where the chromophore is a part of a larger molecule or embedded in a complex or an environment. The perturbations to the optical properties of the chromophore

caused by the surroundings are considered. Here I discuss three types of perturbations; inductive effects caused by substituents, the effect of nearby charges, and of metal-ion complexation. Substituents to the conjugated network may induce a small charge on the chromophore and hence affect the electron delocalization. As this inductive effect is rather vague, the impact on the absorption spectrum is small, and it may be hard to disentangle this effect from other perturbations. Nearby charges, on the other hand, may drastically alter the absorption properties as the charge interacts with the delocalized electron cloud. For metal-ion complexes both the metal atom, the ligand, and their interplay are crucial for the absorption properties.

Ion spectroscopy, in general, is a diverse research field and UV-VIS spectroscopy on molecular ions is just a single piece in the overall puzzle. As all the pieces are gathered a colorful picture with a diversity of information is depicted. One corner will illustrate which chemistry occurs in the interstellar media, and how the molecules that surround us are formed. Another how the atmosphere protects us against radiation from the sun, and how this radiation at once can cause skin cancer and be a catalyst for important processes in our body. We will see how the conformers of a single molecular ion is responsible for how we perceive light, and another molecule responsible for the vital transport and storage of di-oxygen in our blood. We will learn to understand and mimic processes in nature, such as harvest the energy from the sun by artificial photosynthesis.

Dansk resumé

I løbet af min ph.d. har jeg undersøgt de fotofysiske egenskaber af π-konjugerede molekylære ioner, isoleret i gasfasen. Undersøgelserne er baseret på absorptionsspektroskopi, nærmere bestemt *action spectroscopy*, og massespektroskopi udført ved to instrumentelle opstillinger ved Institut for Fysik og Astronomi, Aarhus Universitet, Danmark.

Denne afhandling er en opsummering af gasfasespektroskopi på lige-elektron molekylære ioner i det ultraviolette og synlige område. Udover mine egne forskningsresultater har jeg således inddraget andres arbejde for at opnå et bredere perspektiv og sammenfatte forskningsfeltets nuværende status.

Målet er at opbygge en grundig viden om molekylære ioners basale optiske egenskaber; det er vigtigt fra et fundamentalt synspunkt, men også for at forstå de mange processer i naturen der drives af eller involverer lys. Absorptionsspektroskopi viser sig nyttig i denne henseende, men finder også anvendelse ved en generel karakterisering af molekylære ioner.

Et godt udgangspunkt for denne opgave er at opnå en forståelse af en kromofors optiske egenskaber, da kromoforen er den lysabsorberende del af et molekyle. Den primære parameter for at bestemme absorptionsegenskaberne er elektrondelokalisering, og resonansstrukturer viser sig at være et nyttigt redskab til at visualisere delokaliseringen. Da delokaliseringen afhænger af kromoforens geometriske (to og tredimensionelle) struktur, afsløres denne indirekte i absorptionsspektret. I mange kromoforer sker der ladningsoverførsel ved overgangen, og derved bliver den elektroniske kobling mellem dele af kromoforen vigtig for absorptionsegenskaberne. I nogle tilfælde kan effekten ved ladningsoverførsel endda dominere effekten af elektrondelokalisering.

Når en god forståelse af kromoforens optiske egenskaber er opnået, forsættes til den mere realistiske situation, hvor kromoforen er en del af et større molekyle eller er placeret i et kompleks eller omgivende miljø. Det diskuteres, hvordan kromo-

forens optiske egenskaber påvirkes af disse omgivelser. I afhandlingen diskuterer jeg tre forskellige påvirkninger; den induktive effekt skabt af substituenter, effekten af nærliggende ladninger og påvirkninger i metal-ion-komplekser. Substituenter på det konjugerede netværk inducerer en ladning på kromoforen, hvorved elektrondelokaliseringen påvirkes. Da denne induktive effekt er svag, er indflydelsen på absorptionsspektret lille, og effekten kan være svær at adskille fra andre effekter. Nærtliggende ladninger derimod kan i høj grad ændre absorptionsegenskaberne, idet ladningen vekselvirker med den delokaliserede elektronsky. For metal-ion-komplekser er både metalatomet, liganderne og samspillet mellem disse vigtige for de optiske egenskaber af komplekset.

Generelt er ionspektroskopi et bredt og mangeartet forskningsfelt, og absorptionsspektroskopi i det ultraviolette og synlige område er kun en enkelt brik i det store puslespil. Når alle brikkerne er samlet fremstår et farverigt billede med en mangfoldighed af informationer. Ét hjørne vil vise, hvilken kemi der foregår i det interstellare medie, og hvordan de molekyler, der omgiver os i dag, er formet. Et andet hvordan atmosfæren beskytter os mod stråling fra solen, og hvordan denne stråling på én gang kan forårsage kræft og samtidig være en katalysator for vigtige processer i vores krop. Vi vil se, hvordan et enkelt molekyles konformerer redegører for, hvordan vi opfatter lys, og at et andet molekyle er ansvarlig for den livsvigtige transport og lagring af di-oxygen i vores krop. Vi vil lære at forstå og efterligne processer i i naturen, såsom at høste solens energi ved kunstig fotosyntese.

CHAPTER 1

Introduction

That gas phase molecular ion spectroscopy is an ongoing and important research field is evident from a quick glance at the scientific journals from 2010. In addition to a large number of articles and a number of reviews, one also finds two special issues on the topic; a special issue in International Journal for Mass Spectrometry, vol. 297, edited by E. Williams from November 2010 and a special focus in The Journal of American Society of Mass Spectrometry, vol. 21, from May 2010. Even though it is not a new research field, it is still a field of rapid growth with plenty of exciting physics waiting to be unveiled.

The development of the research field is, as often, tied to technological progress. In the early days, the invention of ion traps facilitated spatial confinement of molecular ions and increased the timescale for investigation of and interaction with the ions. Later, the development of monochromatic tunable light sources led to further advancement. A major step forward was taken with the invention of soft ionization methods, such as matrix-assisted laser desorption ionization (MALDI) [1, 2], fast atom bombardment (FAB) [3], and electrospray ionization (ESI) [4], as it extended the field to larger and more complex systems such as biomolecules. More recently, employment of intense laser fields from free electron lasers (FEL) together with highly resolved spectra from cold ion traps opens up new possibilities in the field and ensures continuing progress.

The motivation to study molecular ions is partly fundamental as interesting physics comes about. Also, it is founded in reality as molecular ions are abundant

in nature and are responsible for important processes both in the atmosphere and in our body. Thereby, the research field is strongly driven by the desire to understand the nature that surrounds us.

Gas phase experiments are essential to probe the intrinsic properties of molecular ions without disturbances from a solvent. Obviously, this is desirable from a fundamental physics point of view, but it also holds relevance in reality. First, isolated molecular ions exist in nature for instance in vacuum-like pockets within proteins and in the interstellar medium. Second, a profound understanding of solvent effects is achieved from gas phase experiments, both from a gradual build-up of the solvent environment and from comparison between gas phase and solution phase experiments. Consequently, gas phase experiments are important as they provide a fundamental understanding of the intrinsic properties of the molecular ions and thereby serve as a solid foundation for further investigations.

In the aim to investigate molecular ions, spectroscopy turns out to be a strong characterization tool. Knowledge of the molecular structure is obtained as the optical properties depend on the geometrical two and three dimensional structure of the ion. Moreover, the electronic structure of the molecular ion can be identified by spectroscopic methods. In all, the optical spectrum is a clear fingerprint of a molecular ion and contains information on the molecular structure and electronic structure. In a broader perspective, light driven processes in nature are common, and hence a fundamental understanding of the interaction between light and molecular ions is desirable.

The light absorbing part of a molecule is called a chromophore. For large systems mainly the chromophore properties are probed by spectroscopy, however, these properties are affected by the surroundings, *e.g.*, the remaining part of the molecule. An investigation of the chromophore by spectroscopic methods, thereby indirectly reveals information on the whole molecular ion. This encourages firm knowledge on the optical properties of the chromophore and how spectral tuning is triggered by small modifications of the chromophore or by external perturbations. Besides a fundamental understanding of the underlying physics, it also enables the design of molecules with desired optical properties. Wide application of this design approach is found within materials science where one example is light-harvesting antennas applicable in artificial photosynthesis [5, 6]. In a long term perspective, the approach is also useful in molecular electronics where the electronic components are made from single (supra)-molecules [7].

In a biological framework, gas phase spectroscopy is an important tool to investigate the environment that surrounds the chromophore in, for instance, a protein. The gas phase experiment on the bare chromophore serves as a starting point,

upon which the surroundings subsequently can be build. Thus, the individual interactions with the surroundings, such as nearby charge sites, hydrogen bonds and folding, can be studied in a controlled manner [8, 9]. Gas phase spectroscopy on biological important species ranges from studies of the simple building blocks as nucleotides [10, 11], small DNA strands [12], single amino acids, and small peptides [13, 14] to studies on whole proteins [15].

A final motivating factor to be mentioned here is the need for gas phase experiments to benchmark theoretical calculations. Results from solution phase experiments are not suitable for verification of theoretical results as solvent effects are not easily accounted for in the calculations. Unfortunately, excited state calculations on medium sized molecules is a cumbersome and difficult task. Despite this, great advances have been achieved within the last decade concurrently with the increased number of gas phase results [16].

Unfortunately, gas phase spectroscopy on ions is not trivial due to a low number of absorbers in non-dense ion clouds. Consequently, conventional absorption spectroscopy based on Lambert-Beers law is not possible. This challenge is, to a certain extent, circumvented by action spectroscopy. In action spectroscopy one measures the result of absorption, for instance photodissociation or electron photodetachment, as a function of excitation energy to obtain absorption cross sections. One disadvantages of the method is that only relative, not absolute, cross sections are obtained, another that absorption which does not result in the chosen *action* is not sampled. Despite its shortcomings, action spectroscopy has proven to be a powerful technique.

Action spectroscopy is employed at different mass spectrometry instrumental setups such as quadrupole ion traps [17, 18, 19], tandem mass spectrometers [20, 21], time-of-flight (TOF) [22, 10, 23] instruments and fourier transform ion cyclotron resonance instruments (FT-ICR) [24, 25]. The setups differ in photofragment detection method (separation in time, space or cyclotron frequency), dissociation time (timescales from μs in TOF to seconds in FT-ICR) and sampling time (discrimination against slow/fast decay *i.e.* kinetic shifts and delayed experiments). Each setup possesses disadvantages such as collisions among the ions, consecutive dissociation, photodissociation of photofragments and radiative cooling. Hence, the perfect experiment for gas phase spectroscopy does not yet exist, and the experimental method needs to be keep in mind as results are examined and compared [26].

Overall, gas phase spectroscopy is a broad field that consists of various different methods such as infrared multiple-photon dissociation (IRMPD) spectroscopy [27, 28], IR-UV double resonance spectroscopy [14], femtosecond pump probe ex-

periments [29, 30, 31] and fluorescence spectroscopy [32, 33, 34, 35], to mention some. Each method has its advantages and provides distinct information. However, in this thesis I will focus only on UV-VIS spectroscopy. Also, I will only consider intermediate-sized molecular ions and restrict myself to even-electron ions; the only exceptions being C_{60}, the radical cation tetrathiafulvalene (TTF) and its derivatives. Extensive work exists on gas phase spectroscopy of radical cations and anions, see for instance work by R. Dunbar [36, 37].

The majority of the results presented in this thesis is from action spectroscopy experiments carried out at a storage ring facility in Aarhus. The action probed with this experimental setup is photodissociation and I will not specify this at each spectrum. In addition to my own results, results from the group of L. H. Andersen are also obtained from experiments carried out at this facility. The main advantages of this state-of-the-art setup is the long (on the timescale of molecular dissociation) sampling time, the possibility to cover a large region of dissociation times and a simultaneous measurement of all neutral photofragments. A thorough description of the setup and the different experiments is found in Appendix A.

To summarize, this thesis will review UV-VIS spectroscopy on intermediate sized even-electron gas phase molecular ions. In addition to presenting my own results, results from other groups will be included to put the findings into a broader perspective. Focus will be on spectral tuning, that is, how does small modifications and perturbations alter the optical properties of the chromophore. To produce and maintain a flow throughout the thesis, the motivation for the different experimental projects and the context and general description of each molecular ions I have studied, is found in the respective publications at the end of this document. For the same reason, the instrumental and experimental descriptions are also found in Appendix A. The outline of the thesis is as follows:

Chapters two, three and four consider small modification of bare chromophores.

Chapter 2 treats electron delocalization of the electrons.

Chapter 3 introduces the concept of resonance forms as a powerful tool to visualize electron delocalization.

Chapter 4 deals with charge transfer transitions.

Then I move on to how external perturbations, defined as parts not included in the π-conjugated network, affect the optical properties of the chromophore. This is the topic of chapters five, six and seven.

Chapter 5 discusses the rather vague effect caused by substituents.

Chapter 6 is devoted to nearby charges and how they affect the chromophore.

Chapter 7 regards metal-ion complexes and their photophysics.

Chapter 8 concludes the thesis with a short summary and outlook.

Appendix A is a thorough description of the two instrumental setups I have used. The different types of experiments are treated with focus on the action spectroscopy experiments.

After the bibliography I have attached the papers I have co-authored listed by order of appearance in this thesis. For easy reference, a roman number is given to each article, and this number is referred to throughout the thesis.

CHAPTER 2

Extent of the π-conjugated network

In the aim to understand the optical properties of bare chromophores, the key parameter to consider is the extent of the π-conjugated network. The electron cloud is delocalized over this region, and, in general, the higher degree of delocalization, the lower excitation energy. As a simplified picture one can consider a particle in a well and the decrease in energy level-spacing with increasing length of the well. However, the treatment is too simple and caution should be taken.

To a first approximation the extent of conjugation is a matter of counting the number of alternating single and double bonds. The first examples illustrate how such an extension of the conjugation shifts the absorption of the chromophore to lower energies.

As the full geometric structure of the chromophore is considered, the overlap of the p-orbitals and hence the conjugation may be broken. If so, the absorption is affected, and thereby the absorption spectrum is a fingerprint of the three dimensional structure of the chromophore. Absorption spectra of different conformers and isomer of a chromophore will demonstrate this.

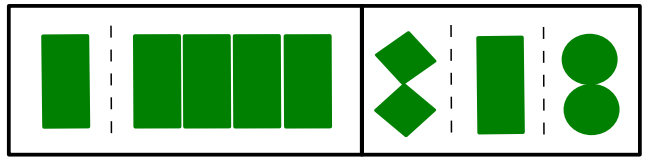

Early work by J. P. Honovich and R. C. Dunbar [24] nicely illustrates the redshift in the absorption caused by extended conjugation and more delocalized electrons. They measured the gas phase photodissociation mass spectra of several protonated acrolein derivatives, for which a summary of the absorption maxima is found in Figure 2.1 The conjugation is increased going from 3-penten-2-one (**1**) to 2,4-hexadienal (**4**) and to cinnamaldehyde (**6**) with phenyl (C_6H_5 ring) in conjugation, and a clear redshift from 262 nm to 340 nm to 410 nm was found in the absorption.

Also, B. S. Freiser and J. L. Beauchamp [38] measured the gas phase absorption of several benzene derivatives and found the absorption for the chromophores to be redshifted in the cases where the conjugation extended beyond the benzene ring.

TABLE I

no.	compd	λ_{max}, nm ion	λ_{max}, nm neutral	ΔPA,[b] eV
1	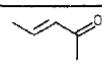	262 (2.4)	210	1.17
2	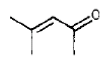	280	224	1.11
3	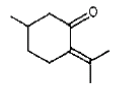	308	237	1.20
4	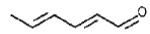	340 (4.6)[a]	246	1.39
5	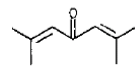	339 (5.0)[a]	248	1.34
6	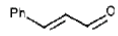	378 410	262	1.45 1.68
7	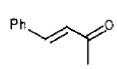	392 410	265	1.52 1.66

[a] λ_{max} photodissociation cross sections (σ) in units of 10^{-17} cm^2. [b] Uncertainty ±0.03 eV.

Figure 2.1. *Gas phase absorption maxima of different acrolein derivatives. A redshift is found in the absorption as the conjugation is increased. From reference [24].*

A more recent example of extended electron delocalization is found in work by L. H. Andersen *et al.* [39]. They recorded the gas phase action spectra of two anionic red fluorescent protein model chromophores, RFP(1) and RFP(2). They are extended forms of the green fluorescent protein (GFP) model chromophore obtained by insertion of one and two ethylenic groups (C_2H_2) to get RFP(1) and RFP(2), respectively, see Figure 2.2. Extension of the conjugation by one ethylenic group redshifts the absorption by 42 nm, and the second ethylenic group causes an

additional 28 nm redshift. Hence, the delocalization of the electrons is increased in the order from GFP to RFP(1) to RFP(2) result in a decrease of the transition energy. As we shall see later, a similar trend is found for the cationic species [40]. As a passing remark it is worth to mention that the GFP model chromophore was the first biomolecule for action spectroscopy at ELISA. From comparison with the protein absorption it was possible to identify an anionic form of the chromophore in the protein [41].

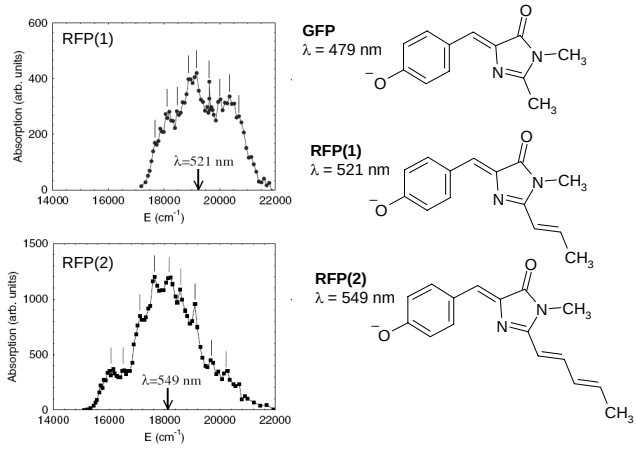

Figure 2.2. *Action spectra of two red fluorescent protein (RFP) model chromophores. Increasing the extend of conjugation from the chromophore of the green fluorescent protein model chromophore (GFP) to RFP(1) to RFP(2) results in 42-nm and additional 28-nm redshift in the absorption, respectively. Adapted from reference [39].*

The lesson so far is that an extension of the conjugation results in a lower transition energy. A final illustration of this important point is found with the C_{60} chromophore, known for its buckyball structure. C_{60} is highly conjugated with all 60 carbon atoms in conjugation, hence, it is expected to absorb at low energies. Figure 2.3 displays the action spectra of the C_{60} mono- (lower panel) and dianion (upper panel), and indeed the absorption is found at 1066 nm and 933 nm in the near-IR region, see also Article **I** ([42]) [43]. The congested spectrum, most pronounced for the monoanion, is due to a geometric distortion and coupling to so-called Jahn-Teller states, which will not be treated here.

Demonstrations on how absorption spectroscopy and the the above mentioned principle can be used to distinguish between different isomers and even conformers of a chromophore finalizes this chapter. The first study is on tetrathiafulvalene (TTF) and the isomer tetrathianaphthalene (TTN). For TTF the lowest energy iso-

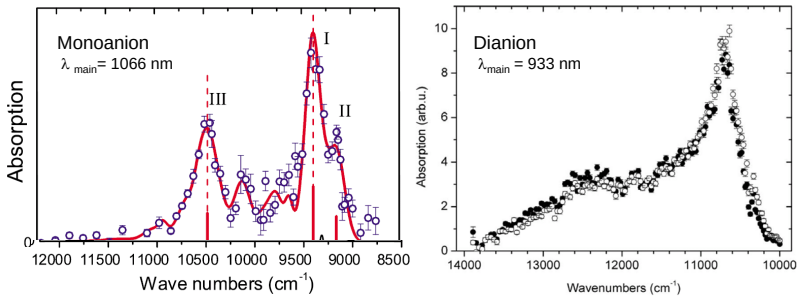

Figure 2.3. *Action spectra of the highly conjugated chromophore C_{60} as mono- (left) and dianion (right) with absorption found in the near-infrared region. The spectral features are due to vibrational excitation and Jahn Teller distorsion. Further details in Article* ***I*** *([42]) and in reference [43].*

mer consists of an exocyclic, fulvalene structure, but the isomer TTN with a fused ring structure is found only 0.78 eV higher in energy, see Figure 2.4, Article **II** ([44]). The figure displays the action spectra of the two isomers, and a massive difference (215 nm) in the absorption is found. TDDFT calculations, shown as the vertical lines in the spectra, correctly reproduce the relative shift, though not the actual values. Also solution phase experiments show a similar shift (714 - 900 nm) together with an expected small solvatochromic redshift of the $\pi\pi^*$ transition. Molecular structure calculations display a folded structure for TTN while a complete explanation for the large redshift is not clear. That is, even though the two isomers have the same number of atoms in conjugation, the electronic structure differ and causes the measured huge difference in the absorption. Notice, that for un-even electron species (radicals) the upper occupied orbital is the SOMO (single occupied molecular orbital). Transitions can then occur from this partly occupied orbital or from the fully occupied orbital (SOMO-1).

As regards conformers, the three dimensional structure of the chromophore may alter the conjugation if the overlap of the p-electron is broken. In this way the absorption spectrum provides information on the full geometric structure of the chromophore. A nice illustration of this is found in the work by the group of L. H. Andersen [45] on retinal protein model chromophore and model chromophores of its different conformers, cf. Figure 2.5. Conformers are different spatial arrangements of atoms due to rotations about a single bond in the molecule. In the retinal chromophore (**A**) the β-ionone ring is somewhat free to rotate, see Figure 2.5, and two almost isoenergetic conformers exist; one planar structure and one with a twisted ring. Model chromophore **B** and **C** resemble the planar conformer.

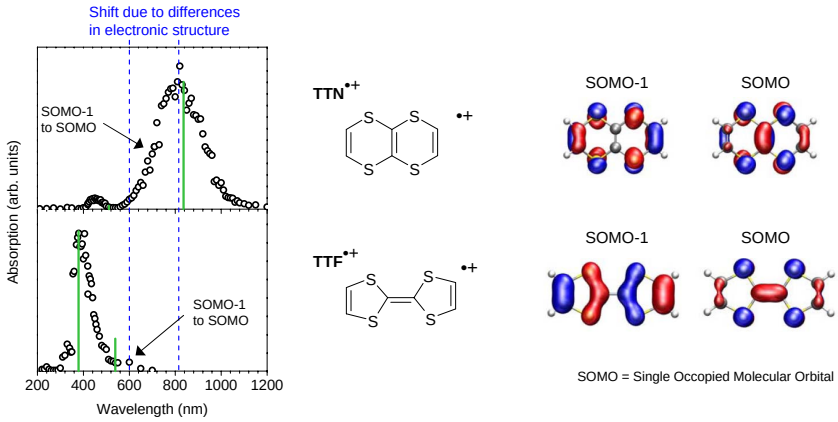

Figure 2.4. *Action spectra of two isomers; tetrathiafulvalene (TTF) and tetrathianaphtalene (TTN) radical cations. The difference in electronic structure results in a 215-nm shift of the lowest energy transition. TDDFT calculations (vertical lines) correctly reproduce the shift though not the actual values. Kohn-Sham molecular orbitals obtained from DFT/B3LYP calculations illustrate the similarity of the transition. Further details in Article* ***II*** *([44]).*

The position of the ring is locked in **C** but unlocked in **B**; hence, rotations may occur in the latter. For the non-planar structure the conjugation does not extend to the ring which is represented by model **D**. The gas phase action spectra revealed that broken conjugation (**D**) results in a blueshift in the absorption ($\lambda = 525$ nm) compared to the locked planar structure (**C**) ($\lambda = 630$ nm). The unlocked planar structure (**B**) was found in the intermediate ($\lambda = 618$ nm). The broad absorption band found for retinal chromophore (**A**) is a result of the different extent of conjugation for the two almost isoenergetic conformers present in the gas phase. On the contrary, for conformers emerged from rotations in the backbone [46, 47], similar absorption is found in agreement with the unaltered conjugation.

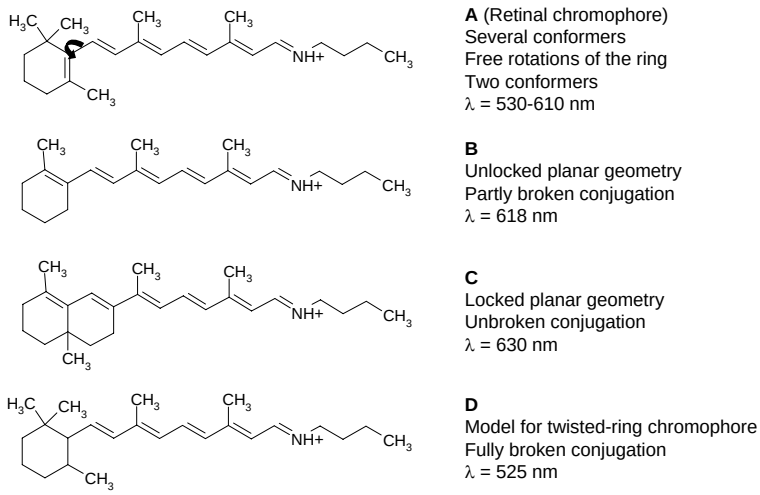

Figure 2.5. *Model chromophores for the conformers of retinal protein model chromophore (**A**). The conjugation in the planar structure **C** is partly or completely broken in **B** and **D**, respectively, and as a result the absorption is blueshifted. The presence of several conformers for **A** result in a broad absorption band. Adapted from reference [45].*

CHAPTER 3

Resonance structures

Resonance structures is a helpful tool to visualize the electron delocalization of the chromophore. Separated resonance structures exist only in theory as the overall wavefunction of the chromophore is a linear combination of all resonance structures. Only electrons are moved between different resonance structures, and for ions this corresponds to a change in the position of the charge. In this way the resonance structures visualize the electron delocalization. Several resonance structures indicate a delocalized electron cloud and hence a lower transition energy is expected.

How the concept of resonance structures add to the simple principle, that the extent of conjugation network determines the delocalization of the electron and thereby the absorption properties of the chromophore, is demonstrated. Here applied to a chromophore in different charge states and different tautomeric forms.

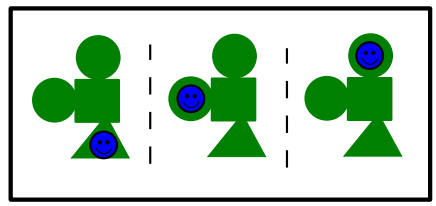

An illustration of how resonance forms shed light on the electronic structure of different chromophores is found in the work by L. H. Andersen *et al.* [40, 48, 49]. They have studied three different biological relevant chromophores as cations and anions, and the differences in absorption properties can be understood on the basis of resonance structures. The chromophores are model chromophores for the green fluorescent protein (GFP), red fluorescent protein (RFP) and the W7 protein, respectively. Structures of the neutral chromophores are shown in Figure 3.1. RFP(1) and RFP(2) are the previously treated extended forms of the GFP model chromophore. In W7, the phenol ring in GFP is replaced by an indole ring, and two tautomers exist for this chromophore. Tautomerism is a special case of isomerism where a hydrogen migrates between a carbon or nitrogen atom and an oxygen atom of an adjacent carbon. Throughout this thesis tautomers in equilibrium are indicated by two half-headed arrows.

A summary of the absorption maxima for the chromophores, protonated and deprotonated, is found in Figure 3.1. Two points attract attention. First, the GFP and RFP anions absorb to the red of the cations but for W7 the order is reversed. Second, the redshift in the absorption of W7 compared to that of GFP, expected from the extended structure of W7, is only found for the cation, not for the anion. To address these points we need to consider the important resonance structures (indicated by a single double headed arrow) of the protonated and deprotonated forms of the chromophores as presented in Figure 3.2.

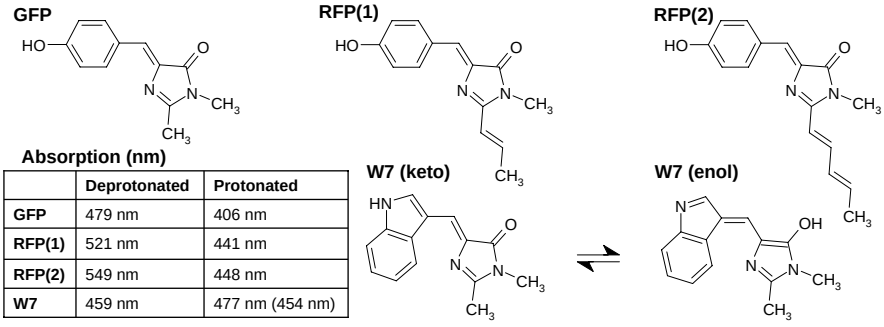

Absorption (nm)

	Deprotonated	Protonated
GFP	479 nm	406 nm
RFP(1)	521 nm	441 nm
RFP(2)	549 nm	448 nm
W7	459 nm	477 nm (454 nm)

Figure 3.1. *Structure of green fluorescent protein (GFP), red fluorescent protein (RFP(1) and RFP(2)) and W7 model chromophores. For W7 two tautomers exist. The table summarizes the gas phase absorption maxima for the deprotonated and protonated forms. Adapted from references [40, 48, 49].*

For deprotonated GFP and RFP, electron density is located at the carbonyl oxygen (**2b**) or at the hydroxyl group (**2a**), and for deprotonated W7 at the carbonyl

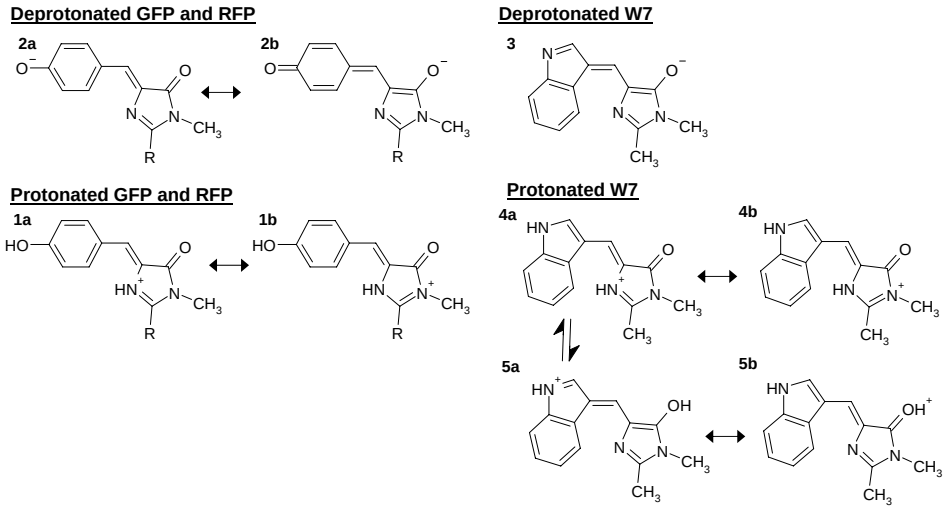

Figure 3.2. *The important resonance structures for GFP, RFP and W7 model chromophores. R represents CH_3, $(CH)_2CH_3$, and $(CH)_4CH_3$ for GFP, RFP(1), and RFP(2), respectively (see structures in Figure 3.1). The differences in absorption can be understood in the light of these resonance structures. Adapted from references [40, 48, 49].*

oxygen (**3**). The existence of more important resonance structures for GFP and RFP than for W7 illustrates the more delocalized electron cloud and explains the absorption found to the red of the W7 anion.

For the protonated forms, the positive charge is delocalized over the two imidazolinone ring nitrogens (**1a** and **1b**, **4a** and **4b**). Yet, for the second tautomer of W7 the electron is delocalized between the indole nitrogen (**5a**) and the carbonyl oxygen (**5b**). In accordance with the extended delocalization for this tautomer, the absorption of W7 cation is found to the red compared to that for the GFP and RFP cations, but also compared to the W7 anion. Two absorption bands are found in the spectrum of cationic W7 as a result of the two tautomers with different absorption.

Similar argumentation can be applied to the work by the group of R. A. Jockusch [50] on the fluorescein chromophore. The obtained gas phase action spectra of the cation, monoanion and dianion are presented in Figure 3.3 together with the important resonance structures for the mono- and dianion. The absorption maximum is found at 430 nm, 520 nm and 500 nm for the cation, monoanion and dication, respectively. For the monoanion two tautomers exist, but from comparison with tautomer-specific solution phase experiments and with experiments on fluorescein derivatives they conclude that mainly tautomer **B** is present in the gas phase. Two resonance structures exist for this tautomer, and hence the electron is more delocalized for the anion than for the cation and dianion. Although similar resonance

structures exist for the dianion, the contribution from the structure to the right is less due to the Coulomb repulsion between the two close charges, *i.e.* it is energetically unfavorable.

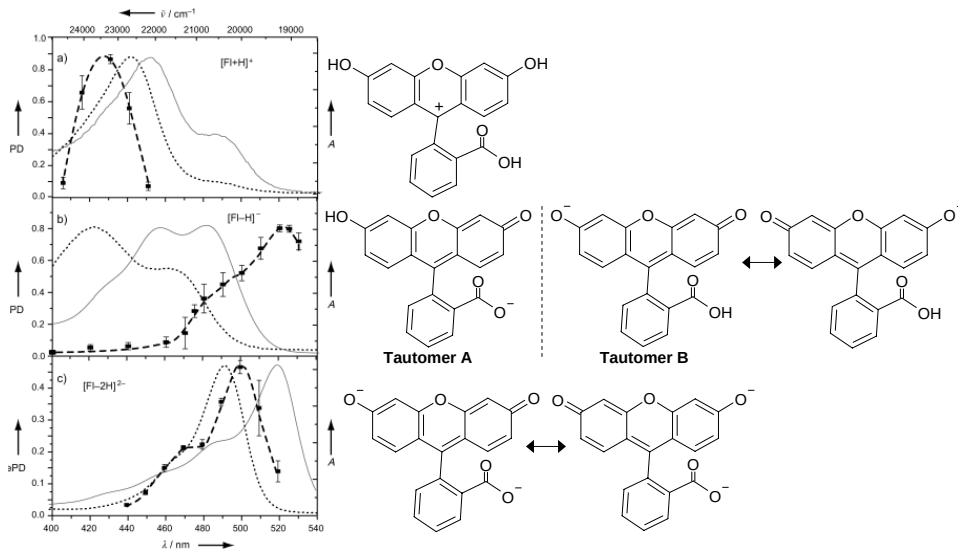

Figure 3.3. *Action spectra (symbols) of the cationic (upper panel), monoanionic (middle panel), and dianionic (lower panel) fluorescein chromophore. The important resonance structures are displayed to the right. Two tautomers exist for the monoanion where mainly structure* ***B*** *is believed to be present in the gas phase. The two important resonance structures for this tautomer explains the absorption to the red of the dianion and cation. The right resonance structure for the dianion is less important due to the Coulomb repulsion between the two nearby negative charges. Solid and dotted lines represent solution phase data (water and dimethyl sulfoxide solutions). Adapted from reference [50].*

That the absorption properties are tautomer specific is comprehensible as the charge distributions for different tautomers differ. A recent example of this is a direct comparison of the absorption found for different tautomers of protonated adenine. The gas phase photofragment spectrum of protonated adenine with an absorption at 4.53 eV ($\lambda = 274$ nm) was presented in 2005 by R. Weinkauf *et al.* [51]. Electrospray ionization was used to produce the ions, and from theoretical calculations they were able to determine the most abundant tautomer created from the source. Theory furthermore showed that the excitation energy is tautomer-specific. In a recent experiment by C. Jouvet and co-workers [52] protonated adenine is formed from cold adenine dimers, and a 0.3 eV redshift in the absorption ($\lambda = 293$ nm) was found compared to Weinkaufs results. According to theory,

they ascribed the shift to production of another tautomer from the fragmentation of dimers compared to electrospray ionization, see Figure 3.4.

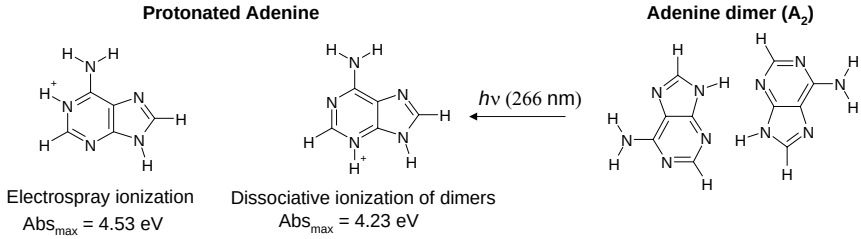

Figure 3.4. *Two tautomers of protonated adenine formed by electrospray ionization and from dissociative ionization of adenine dimers, respectively. A difference of 0.3 eV is found between the absorption maximum of the two tautomers. Adapted from references [52, 51].*

The clear fingerprint on tautomerism provided by absorption spectroscopy was utilized by L. H. Andersen and co-workers [53]. They measured the action spectrum of the photoactive yellow protein (PYP) model chromophore and model chromophores for its two different tautomers, see Figure 3.5. The charge density is localized at one end of the chromophore in one tautomer (**A1**) and in the other tautomer (**A2**) delocalized between the two ends. Hence, one expect the absorption properties of the two tautomers to be different. To ascertain which one of the two tautomers that is produced by electrospray ionization, they compared the gas phase action spectrum of the deprotonated chromophore with the action spectra of two methyl-substituted derivatives, see right part of the figure. Methyl (-CH_3) substitution at the phenol end (**B**) localizes the charge at the carboxyl oxygen, similar to tautomer **A1**. The derivative with the methyl at the carboxyl end (**C**) has two important resonance structures, hence the electron is delocalized as for tautomer **A2**. The obtained gas phase action spectra are shown in the left part of the figure. Surprisingly, similar absorption was found for all three chromophores, that is, charge localization does not seem to affect the absorption of the chromophore. Consequently, determination of the present tautomeric form of **A** was not possible from these experiments. Remarkably, they also measured the gas phase action spectrum of chromophore **A** with two water molecules attached to the phenol end and found a huge 85-nm blueshift upon charge-localization by the water molecules [54]. Clearly, more experiments are needed to fully understand the photophysics of this chromophore.

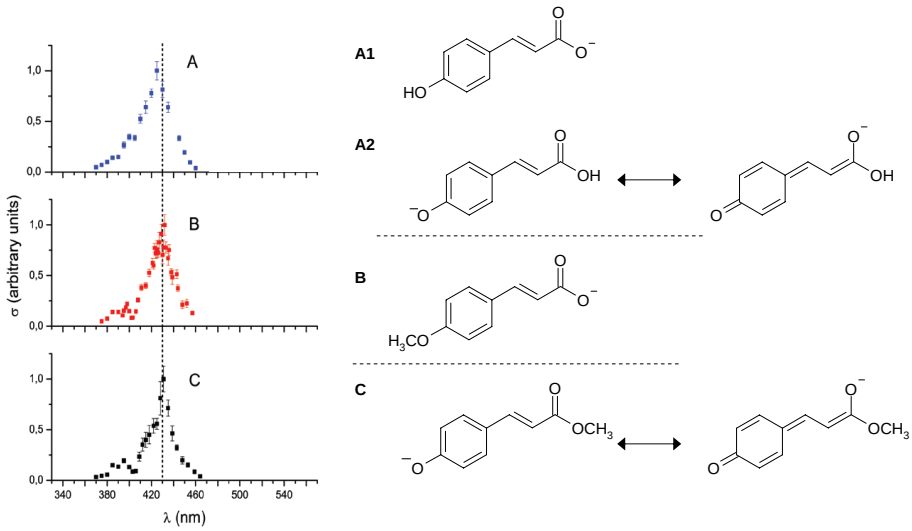

Figure 3.5. *Action spectra of the photoactive yellow protein (PYP) model chromophore (**A**) and two derivatives that model each of the two tautomers **A1** and **A2**. The important resonance structures illustrate how the charge is localized in **A1** and **B** but delocalized in **A2** and **C**. Surprisingly, similar absorption is found for the three chromophores, that is, charge delocalization does not seem to affect the optical properties of the chromophore. Adapted from references [53].*

CHAPTER 4

Charge transfer transitions

The type of transition that occurs upon excitation is obviously crucial for the absorption properties of the chromophore. For many chromophore ions charge density is transferred from one part of the chromophore to another upon excitation. Such charge transfer transitions are found at lower energies compared to the localized transitions due to the separated and non-coupled states involved. Hence, for charge transfer transitions the simple picture of electron delocalization discussed previously is not the full story. In addition to this, one also needs to consider how pronounced the charge transfer character of the transition is.

If the charge transfer is between two distinct groups of the chromophore, a so-called donor-acceptor chromophore, the spacer connecting the two groups becomes important. The spacer conveys the electronic coupling between the groups and hence determines the degree of charge transfer in the transition. The absorption spectrum provides a clear fingerprint of this, and thereby serves to characterize the spacer.

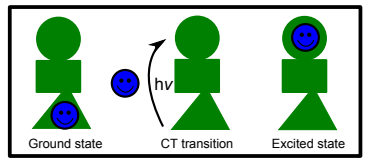

A lower excitation energy is found for charge transfer transitions, as displayed in Figure 4.1. If the two states among which the transition occurs are completely separated (zero overlap of the orbitals), the transition energy will be determined by the difference in energy of the individual states. As the states approach each other, they start to couple and form new states, as illustrated in the middle. This gives an increase in the transition energy. A further enhancement of the coupling between the states additionally increases the transition energy. For charge transfer transitions the situation approaches the first situation with non-coupled states, that is, the higher degree of charge transfer in the transition the lower transition energy.

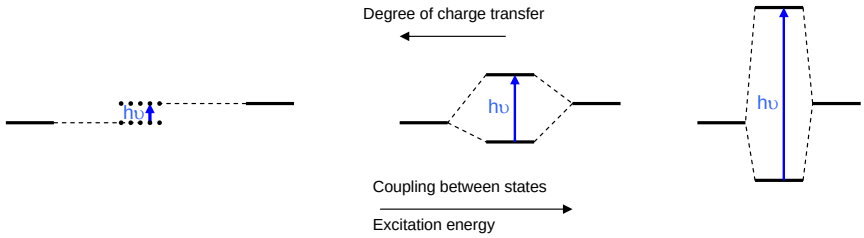

Figure 4.1. *Illustration of the lower transition energy found for charge transfer transitions (left) and how coupling between the states (right) increases the excitation energy.*

A simple example of charge transfer transition is found in protonated benzene dimers studied by the group of C. Jouvet [23]. For the dimer, charge is transferred from one ring to the other upon excitation, and this charge transfer transition is found at 440 nm. This is a severe redshift compared to the localized transition found in protonated benzene at 330 nm [55].

The group of C. Jouvet [56] extended the work to include three small protonated linear polycyclic aromatic hydrocarbons (PAHs) - naphthalene (two rings), anthracene (three rings), and tetracene (four rings) - where charge density in a similar manner as in benzene dimers can be transferred from one ring to another. The obtained photodissociation spectra are presented in Figure 4.2 together with the molecular orbitals. Naphthalene ($\lambda = 503$ nm) and anthracene ($\lambda = 491$ nm) are found to absorb in the same spectral region, whereas tetracene ($\lambda = 680$ nm) absorbs further to the red. From the molecular orbitals it is evident that the charge transfer character of the transition is more pronounced for the chromophores with an even number of rings, due to the asymmetry of the molecules. Moreover, the distance over which the charge density is transferred is larger for the larger chromophores which explaines the absorpion of tetracene compared to that of naphthalene. Hence, despite the larger molecular size of anthracene compared to that

of naphthalene, similar absorption is found for the two as a result of more charge transfer character of the transition in naphthalene.

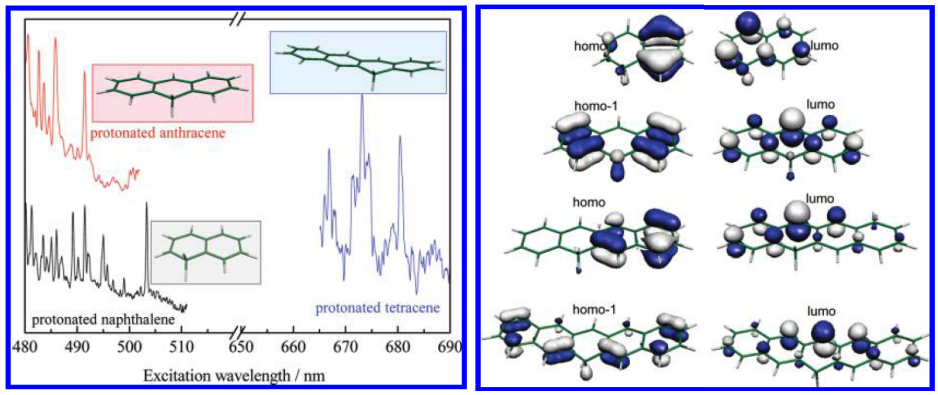

Figure 4.2. *Gas phase photofragment spectra of three cold protonated linear polycyclic aromatic hydrocarbons (PAHs). Due to a more pronounced charge transfer character of the transition in naphthalene, nearly similar absorption by naphthalene and anthracene is found despite the greater extent of conjugation in anthracene. Molecular orbitals reveal the charge transfer character for even-numbered rings. From reference [56].*

Charge transfer transitions are pronounced in donor-acceptor chromophores, where charge is transfered between two distinguished parts of the chromophores, separated by a spacer. The degree of charge transfer is determined by the spacer as it couples the two groups and convey the electronic communication. One example of such donor-acceptor chromophores is nitrophenolates. We have studied four different nitrophenolate anions characterized by different π-conjugated spacers between the donor and acceptor groups, see Figure 4.3, Article **III** ([57]). The lowest energy absorption maximum is found to redshift through the whole visible spectrum with increasing spacer-length, going from 392 nm for a single phenylene (C_6H_4) spacer (**A**) to 775 nm for three phenylene spacers (**D**). Hence, the coupling between the donor and acceptor groups decreases with increasing distance between the groups, *i.e.* the charge-transfer character of the transition is more pronounced for the larger chromophore, evident from the molecular orbitals shown in the figure. In solution a much smaller spectral region is covered and also the order is different ($\lambda = 387, 406, 435, 377$ nm in MeOH for **A**, **B**, **C**, **D**, respectively), *i.e.* counter ions and solvent dipoles play a huge role. Theoretical coupled cluster calculations, shown as the vertical lines in the spectra, provide good predictions of the relative shift of the absorption maxima.

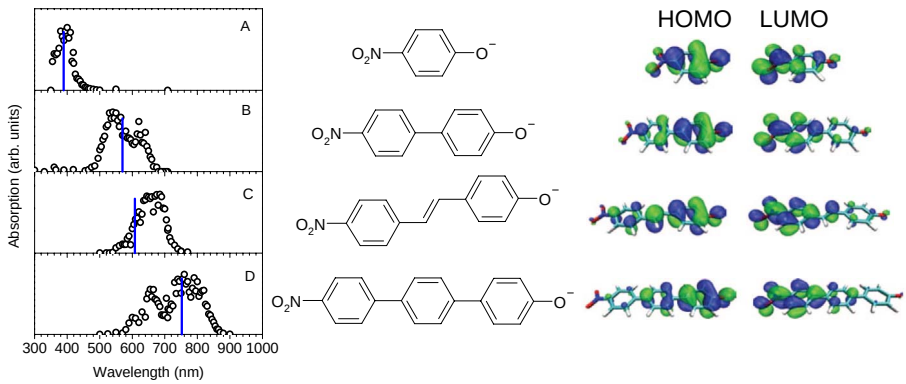

Figure 4.3. *Action spectra of four nitrophenolates anions with different spacers between the donor and acceptor groups. An increased distance, and hence lower coupling between the states, redshift the absorption through the whole visible spectrum. Molecular orbitals (right) illustrate the charge transfer character of the transition. Theoretical coupled cluster calculations (vertical lines) correctly reproduce the shift. Further details in Article* ***III*** *([57]).*

The coupling between the donor and acceptor end is not only determined by the length of the spacer connecting the ends, also the actual structure of the spacer is found to be important, Article **IV** ([58]). Figure 4.4 displays the action spectra of two nitrophenolate anions where one has an alkene unit (**A**) and the other an alkyne unit (**B**) as part of the conjugated entity connecting the donor and acceptor groups. For the alkene unit (double bond) the hybridization of the carbon atoms in the alkene bond is sp^2 whereas the carbon atoms in the alkyne unit (triple-bond) are *sp* hybridized. The absorption maximum is found at 685 nm for the alkene species and at 695 nm for the alkyne species, that is, the coupling is better conveyed by the alkene unit. Theoretical calculations with the coupled cluster method, shown as the vertical lines in the spectra, correctly reproduce the redshift from the alkyne species compared to the alkene species. Solution phase measurements (acetonitrile ($\lambda_A = 542$ nm and $\lambda_B = 497$ nm) and methanol ($\lambda_A = 435$ nm and $\lambda_B = 408$ nm)) on the contrary result in a shift in the opposite direction.

The coupling between the donor and acceptor ends is conveyed through the conjugated network. Hence, if the conjugation is broken (*i.e.* low coupling) the charge transfer degree is high and the absorption redshifts. An illustration of this is found by comparing the absorption of the different isomers of the nitrophenolate anion ([59]). Figure 4.5 displays the action spectra of the three isomers; *ortho* (upper panel), *meta* (middle panel) and *para* (lower panel). Similar absorption is

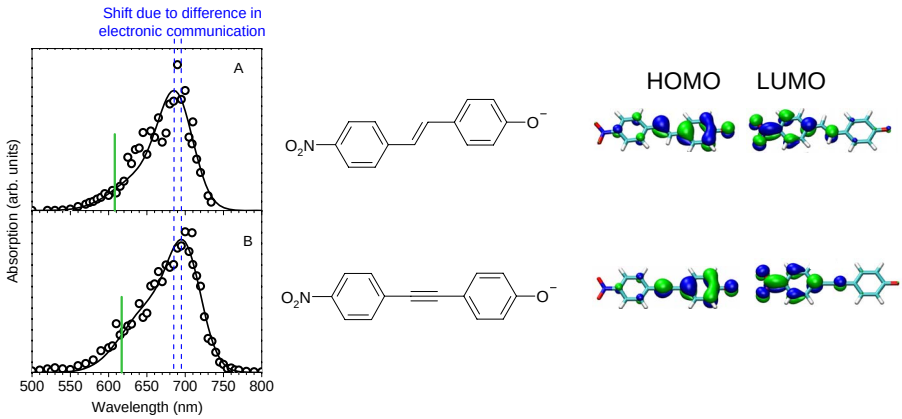

Figure 4.4. *Action spectra of two nitrophenolate anions; One with an alkene unit (**A**) and one with an alkyne unit (**B**) as part of the spacer between the donor and acceptor group. A difference of 10 nm is found in the absorption which reveals that the electronic coupling is better conveyed by the alkene unit. Theory (vertical lines) correctly reproduce the shift, and molecular orbitals show the charge transfer character of the transition. Further details in Article **IV** ([58]).*

found for *ortho* and *para* whereas the absorption by *meta* is blueshifted. The important resonance structures of the isomers are drawn to the left in the figure and visualizes that the donor and acceptor group are in conjugation in *ortho* and *para* as the charge may be moved between the two groups. For *meta* the two groups are not in conjugation, *i.e.*, the coupling is broken. Hence, according to the previous arguments on the degree of charge transfer we expect to find the absorption by *meta* to the red. In contrast to this we expect a redshift in the absorption of *ortho* and *para* due to the presence of two important resonance structures and hence a more delocalized electron cloud. This example illustrates how the two effects - electron delocalization and charge transfer character of the transition - may counteract each other, and a determination of which effect dominates is not always easy. As opposed to the gas phase results, and in agreement with the expectations for charge transfer transitions, both theory and solution phase report that the absorption of *meta* should be found to the red but with a low oscillator strength. Thus, this all suggest that the lowest energy absorption band is absent in the gas phase spectrum of *meta* as a result of a too low oscillator strength for this transition to be measured with our technique. The band measured to the blue for *meta* is most likely from a higher energy transition.

Support to the above conclusion is found in a similar study by the group of L. H. Andersen [60]. They measured the action spectra of the three different isomers

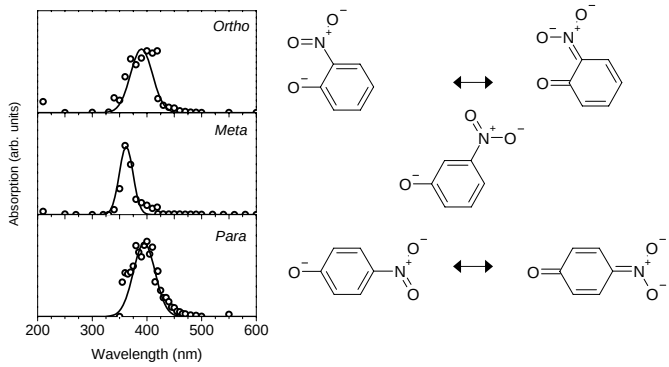

Figure 4.5. *Action spectra of three isomers of the nitrophenolate anion. Similar absorption is found for para and ortho whereas the absorption for meta is shifted to the blue. Most likely, the band measured for meta is from a higher energy transition, and the lowest energy absorption should be found to the red with a low oscillator strength, see text for details. Further details on the molecular ions in Article* ***III*** *and* ***IV****, data not published ([59]).*

of a donor acceptor chromophore that models the photoactive yellow protein (PYP) chromophore, see Figure 4.6. The lowest energy absorption is found to be similar for *ortho* and *para* whereas for *meta* a band with low oscillator strength is found to the red. Again, for *ortho* and *para* the donor and acceptor ends are in conjugation and the coupling (*i.e.* the electronic communication) is larger than in the case of *meta*. The lowest energy absorption of the latter is found to the red as the charge transfer character of the transition is more pronounced for this isomer. These results are in full agreement with our expectations and hence support the conclusion for the nitrophenolates above.

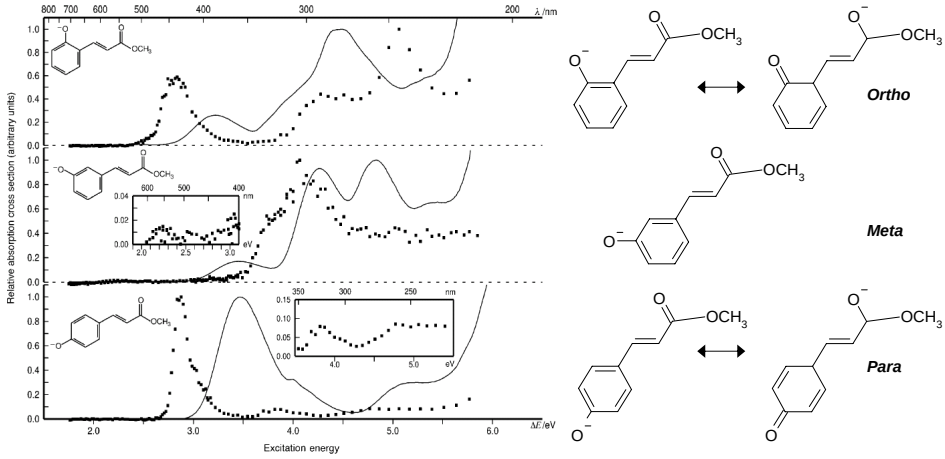

Figure 4.6. *Action spectra (symbols) of the three isomers, ortho (upper), meta (middle), and para (lower), for a photoactive yellow protein (PYP) model chromohore. Similar lowest energy absorption is found for the ortho and para whereas for meta the absorption is found to the red with low oscillator strength. The situation is similar to that of the nitrophenolate where the donor and acceptor ends of meta are not in conjugation, evident from the resonance structures, hence the more pronounced charge transfer character of the transition and the redshift in absorption. Solution phase results are shown as the solid lines. Adapted from reference [60].*

CHAPTER 5

Inductive effects

By now we understand the absorption properties of the bare chromophore on the basis of electron delocalization and the type of transition involved. We know that the absorption spectrum provides information on the three dimensional structure of the chromophore, the type of transition involved, the electronic coupling between different parts of the chromophore and on tautomerism. As the chromophore is a part of a larger molecule or embedded in a complex, the π-conjugated network is perturbed. The rest of this thesis is devoted to such external perturbations and how they manifest themselves in the absorption spectrum.

In this chapter we consider the inductive effect caused by substituents to the conjugated entity. The inductive effect is conveyed through the σ-bonds that connect the substituent to the chromophore, and the effect is to induce a small charge on the chromophore by pulling or pushing electrons towards or away from the substituent. This small induced charge density on the chromophore will obviously affect the π-electrons and hence cause a change in the absorption properties. As we shall see, the inductive effect is more subtle than the changes considered so far, and moreover the effect on the absorption is much smaller. Consequently, it may be hard to decouple the effect from other perturbations.

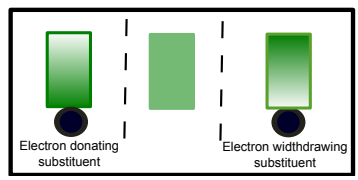

An illustration of the inductive effect caused by electron withdrawing and electron releasing substituents is presented in Figure 5.1. The negative charge induced by an electron releasing group (left side) interacts unfavorable with the π-electrons of the chromophore. Conversely, a favorable interaction is found when a positive charge is induced by an electron withdrawing group (right side). The stabilization and destabilization, respectively, is larger for the ground state than the excited state as the π-electron cloud is more diffuse in the excited state and therefore easier to polarize. Hence, the stabilization due to an electron widthdrawing group results in a blueshift and the destabilization found for an electron releasing group causes a redshift iof the absorption.

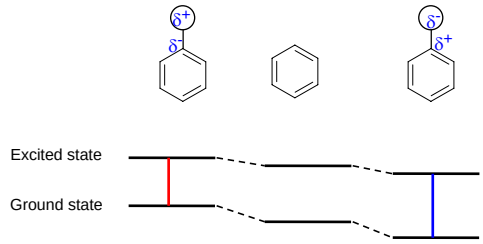

Figure 5.1. *Illustration of how the inductive effect caused by substituents to the conjugated entity affects the energy levels of the chromophore. An electron releasing and withdrawing substituent results in a blue- and redshifted absorption, respectively, as a result of the unfavorable or favorable interaction between the induced charge and the π-electron cloud.*

In the first example we consider an oligophenyleneethynylene (OPE) with and without two CH_2CH_3 groups attached, cf. Figure 5.2, Article **V** ([61]). The action spectra show that the substituents (**B**) cause a small 12-nm redshift of the absorption together with a broadening of the band. The lowest energy transition is still confined to the conjugated entity but the CH_2CH_3 groups induce a small negative charge on the chromophore. This induced charge interacts unfavorable with the π-electrons on the chromophore and hence causes the measured redshift in the absorption.

A similar situation is found for the TTF radical cation and the derivative TMT-TTF with four SCH_3 groups attached to the chromophore, cf. Figure 5.3, Article **II** ([44]). The action spectrum of the unsubstituted TTF has an absorption at 400 nm with a smaller band around 600 nm, being the SOMO to SOMO+2 and SOMO to SOMO+1, respectively. For the substituted chromophore two similar bands are found together with an extra band at lower energies. This extra band (SOMO-1

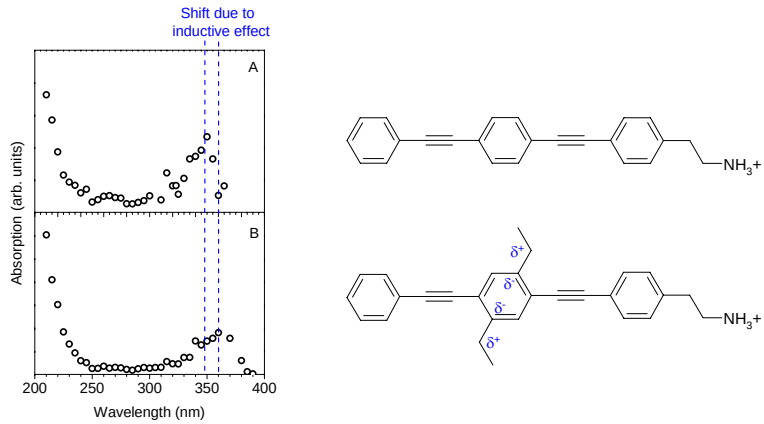

Figure 5.2. *Action spectra of two oligophenyleneethynylenes (OPE) cations, one with (**B**) and one without (**A**) substituents. The substituents induce a small negative charge on the chromophore and hence cause a small 12-nm redshift of the absorption. Further details on the molecules in Article **V** ([61]).*

to SOMO) is a charge transfer transition from the substituents to the chromophore entity. In the framework of inductive effect we disregard this charge transfer transition and focus instead on the 420 nm (SOMO to SOMO+4) transition, cf. molecular orbitals. This is a $\pi - \pi^*$ transition on the chromophore part, similar to the 400 nm (SOMO to SOMO+2) transition for TTF. Hence, the effect of the induced charge from the substituents is a 20 nm absorption redshift. The redshift indicates that the SCH_3 groups induce a small positive charge on the chromophore as for the OPE. However, the electronegativity of S compared to C is in contrast to this and a blueshifted absorption was expected. Hence, the simple principle described above comes to a short or other effects dominates. This example demonstrates how difficult it is to probe the inductive effect.

Also, L. H. Andersen *et al.* [9] have studied the inductive effect. An electron withdrawing bromo substituent was incorporated in the green fluorescent model chromophore treated earlier. From the simple principle the bromo substituent is electron widthdrawing and is expected to blueshift the absorption. Surprisingly, no effect of the substituent was found as similar action spectra were obtained for the chromophore with and without the substituent.

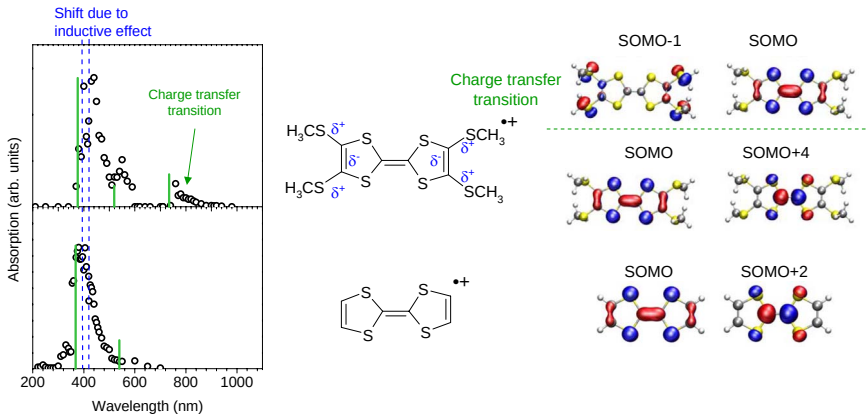

Figure 5.3. *Action spectra of tetrathiafulvalene radical cation, TTF, (lower) and the derivative, TMT-TTF (upper) with four SCH_3 substituents. The substituents cause a 20-nm redshift in the absorption. Theory correctly reproduces the shift caused by the inductive effect together with the position of the charge transfer transition at lower energies. Kohn-Sham molecular of the relevant transitions. Further information in Article* **II** *([44]).*

CHAPTER 6

Nearby charges

Charges in the near proximity of the chromophore is another highly important external perturbation. For many molecular ions the charge is placed outside the π-conjugated network of the chromophore and should be considered as an external nearby charge. Consequently, insight into the effect of nearby charges is essential to understand the optical properties of many molecular ions. The delocalized electron cloud will interact with the nearby charge, and this may alter the degree of delocalization. To investigate the effect of nearby charges complexation and folding is employed.

From a biological point of view, understanding the effect of nearby charges is important as charge sites are often present near the chromophore in a protein environment. Hence, nearby charges may contribute to the overall spectral tuning of the chromophore absorption by the surroundings.

A synthesis design approach to elucidate the effect of nearby charges is to attach a spectator charge to the chromophore. This enables a controlled investigation of the effect as the distance from the chromophore to the charge can be adjusted. By employment of nearby charges both the number of charges and the distance between the charge and the chromophore can be studied.

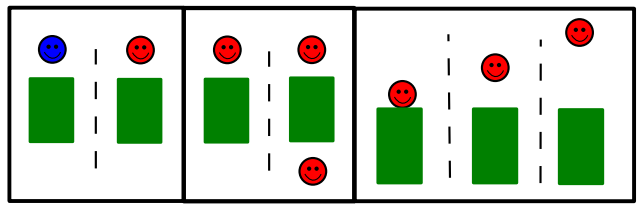

In the first couple of examples we consider the well studied amino acid tryptophan. In tryptophan the chromophore part is the indole ring over which the photoactive electron is delocalized, cf. Figure 6.1 left side, but the charge is found outside this part. For protonated tryptophan the charge is located on the ammonium group and thereby acts as a nearby charge. Consequently, tryptophan serves as a good system to examine how a chromophore is influenced by a nearby charge. Before proceeding to the experiments, a short introduction to the deexcitation pathways and the energy levels for protonated tryptophan is appropriate.

Figure 6.1 displays a simplified state level diagram of the energy levels in protonated tryptophan. For simplicity it only includes states on the chromophore and on the charge site. The state reached upon excitation of an electron in the indole aromatic ring is a $\pi\pi^*$(indole) state on the indole chromophore. This can couple to a lower lying repulsive $\pi\sigma^*(NH_3)$ state on the ammonium group that causes dissociation along the NH bond to give the tryptophan radical cation. The excited state lifetime of this state is short, hundreds of fs. Other deexcitation pathways exist with substantially longer lifetimes. Further details on the photophysics of protonated tryptophan will not be given here but are found in several papers [62, 63, 64, 65].

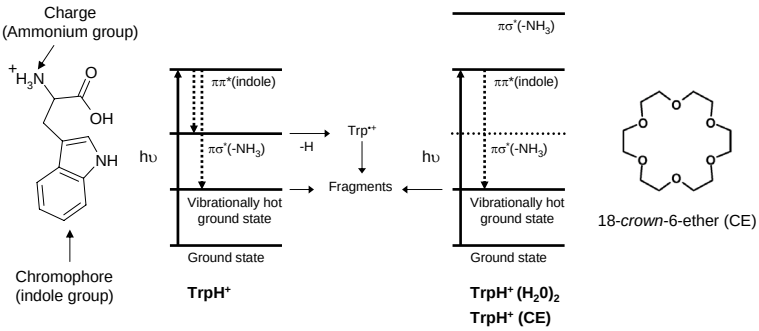

Figure 6.1. *Simplified state level diagram of protonated tryptophan and protonated tryptophan in complexation with water molecules or 18-crown-6-ether (CE). Complexation raises the $\pi\sigma^*(NH_3)$ state out of the spectral region, and disables coupling to this state and the concomitant hydrogen loss and formation of the radical cation.*

Experiments on protonated tryptophan by the group of T. Rizzo [66] illustrate how the interaction between the charge and the chromophore severely influences the optical properties of the chromophore. Alteration of the interaction is obtained by attachment of water molecules to the ammonium group. The left side of Figure 6.2 displays the gas phase photofragment action spectra of $\sim$10 K cold, protonated tryptophan with zero (upper panel), one (middle panel) and two (lower panel) water molecules attached. The broad spectra found for $TrpH^+$ and $TrpH^+(H_2O)$, despite

the low temperature, are due to a short excited state lifetime as internal conversion to the $\pi\sigma^*(NH_3)$ state occurs, *i.e.* lifetime broadening. Attachment of two water molecules results in a longer lifetime with a concomitant well resolved spectrum. Hydrogen bonds, formed between the ammonium group and the water molecules, raise the energy of the dissociative $\pi\sigma^*(NH_3)$ state by 1.3 eV and hence hinder coupling to this state, see right part of Figure 6.1. The fast hydrogen loss channel is thereby eliminated. That is, as the interaction between the nearby charge and the chromophore is weakened, the optical properties of the chromophore are greatly affected, in this case apparent from a longer excited state lifetime. Hence, the example illustrates the huge effect a nearby charge may cause on the photophysical properties of the chromophore. In the regard of the short lifetime found for some protonated aromatic molecules but not for others a recent discussion by C. Jouvet is found in reference [67].

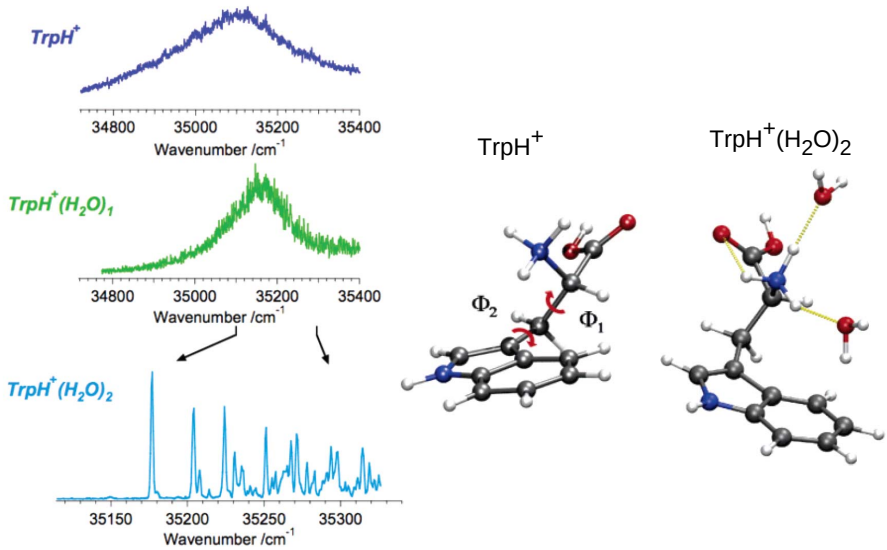

Figure 6.2. *Photofragment action spectra of protonated tryptophan with zero (upper panel), one (middle panel), and two (lower panel) water molecules attached. Addition of two water molecules results in a highly resolved spectrum in consequence of an increased lifetime. Water molecules weakens the coupling between the chromophore and the charge and eliminates the fast hydrogen loss channel. Adapted from reference [66].*

The group of K. Fuke [68] did a similar study on cold, microsolvated, protonated tryptophan. They measured the photodissociation spectrum of $TrpH^+(CH_3OH)_n$ (n = 0,1,2) and, as for the case of water solvation above, obtained a vibrationally resolved spectrum upon attached of two solvent molecules, see left panel of 6.3. They extended the study to include dipeptides of tryptophan with Alanine (Ala),

Valine (Val) and Glycine (Gly) [69], where only results for the latter are treated here. The spectrum of Trp-GlyH$^+$ (middle panel, lower spectrum) was similar to that of TrpH$^+$, whereas the absorption of bare Gly-TrpH$^+$ (right panel, upper spectrum) was found redshifted and substantially broadened. Hence, the sequence of the dipeptide matter for the optical properties. This is not surprising as the structure, and thereby the distance from the charge to the chromophore, will differ. Calculated structures show that for protonated Gly-Trp the structure is folded with a much shorter distance between the indole chromophore and the charge on the ammonium group compared to the distance in protonated tryptophan and Trp-Gly. Hence, the effect of the nearby charge is not only visible as a broadening of the spectrum due to a short lifetime but also as a shift in the absorption maxima. A verification of this interpretation is found as attachment of solvent molecules to Gly-TrpH$^+$ (right panel, middle and lower spectrum) increases the distance from the chromophore to the charge and shifts the absorption towards that of protonated tryptophan.

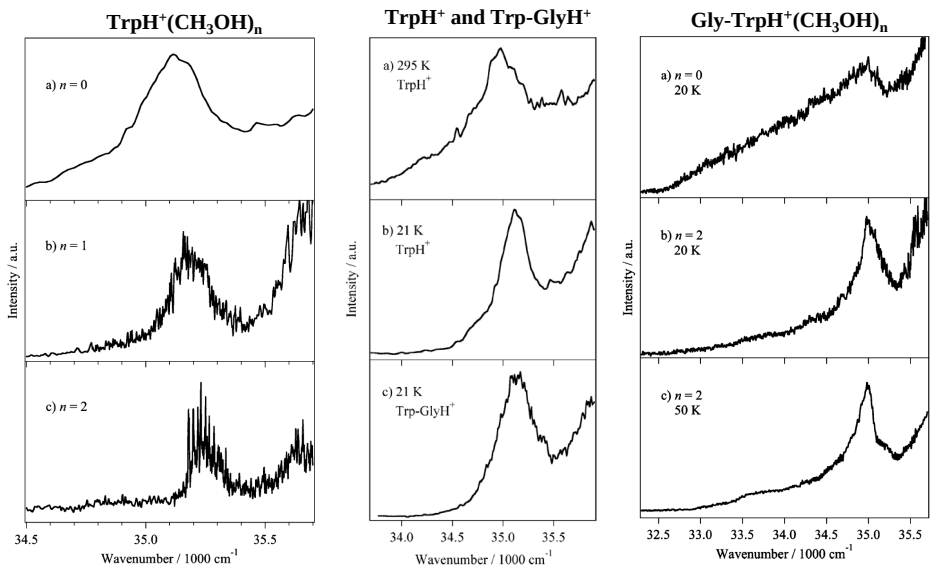

Figure 6.3. *UV photodissociation spectra of cold, microsolvated, protonated Tryptophan (left panel), bare protonated tryptophan, and Tryptophan-Glycine (middle panel) and of cold, microsolvated, protonated Glycine-Tryptophan, n=CH_3OH. The interaction between the π-electrons on the indole ring of tryptophan and the ammonium group redshifts the absorption of Gly-TrpH$^+$ and, as was seen for TrpH$^+(H_2O)_n$, this interaction is weakened by the solvent molecules. In result the spectrum of Gly-TrpH$^+(CH_3OH)_2$ approaches those of TrpH$^+$ and Trp-GlyH$^+$. Adapted from reference [69, 68].*

Identical reasoning and outcome was obtained for the protonated dipeptides GlyTrp and TrpGly in our laboratory, Article **VI** [70]. The action spectra of protonated GlyTrp and TrpGly is shown in Figure 6.4, left panel upper spectrum. The folded structure of protonated GlyTrp, see right part of the figure, with subsequent increased effect of the nearby charge results in a redshift of the 210-nm band compared to protonated TrpGly.[1] In this case attachment of 18-*crown*-6-ether is used to unfold the structure and verify that the redshift is a consequence of the closer nearby charge. Crown ether, cf. Figure 6.1 right part, binds like a collar to the ammonium group and thereby targets the three hydrogens. Just like solvent-molecule attachment above, crown ether attachment decouples the $\pi\sigma^*(NH_3)$ and $\pi\pi^*$(indole) states with a 2-3 eV energy raise of the $\pi\sigma^*(NH_3)$. Action spectra of the two crown-ether tagged dipeptides are displayed in the lower panel of Figure 6.4, and similar absorption is found. Hence, the redshift of the 210-nm absorption band for protonated GlyTrp is due to a stabilization of the excited state by the closer nearby charge in the folded structure. Theory (middle panel) are in nice agreement with the experimental results.

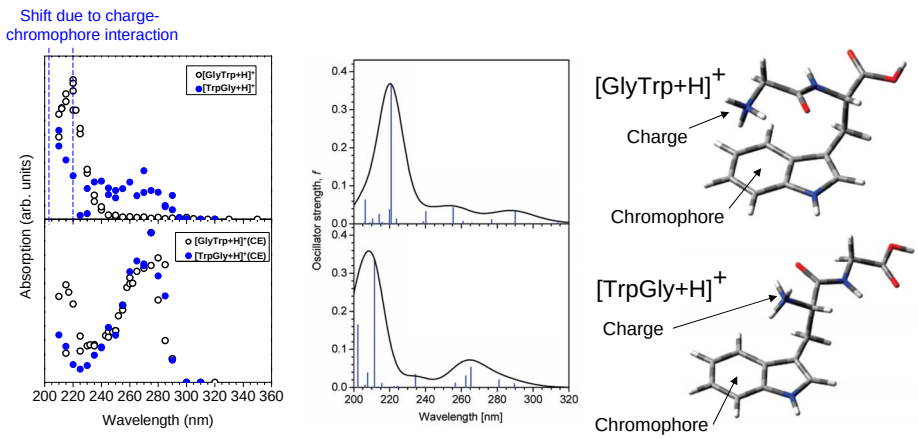

Figure 6.4. *Action spectra (left side) of the bare protonated dipeptides Gly-Trp and Trp-Gly (upper panel) and the protonated dipeptides in complexation with 18-crown-6-ether (lower panel). Increased interaction between the charge and chromophore in the folded structure of protonated Gly-Try (right side) redshifts the 210-nm absorption. Crow-ether complexation unfolds the structure and similar absorption is found for the two crown-ether tagged dipeptides. Calculated absorption spectra (middle panel) of protonated Gly-Trp (upper) and Trp-Gly (lower) are in agreement with the experimental results. Further details in Article* **VI** *([70]).*

[1] The discrepancy between the spectra at lower energy (270 nm) is a result of an artifact of the experiment, see discussion in reference [70]

Crown ether complexation of several amino acids and dipeptides clearly illustrate how the decoupling alters the lifetime, dissociation pathways and in some cases shifts the absorption, see Articles **VII**, **VIII** and **IX** ([71, 72, 73]).

From the above it is evident that the presence of a proton close to the indole ring in tryptophan affects the optical properties of the chromophore, but what about a nearby negative charge. Recently, the group of P. Dugourd [74] studied deprotonated tryptophan where a proton is removed from the carboxyl group (-COOH). Figure 6.5 shows the electron photodetachment spectrum of deprotonated tryptophan (open circles) together with the photodissociation spectrum of protonated tryptophan (dashed line). The anion spectrum is redshifted by 25 nm compared to the cation spectrum, and so the 210-nm band is shifted into the spectral window of the experiment. Based on theoretical calculations, they found that the nature of the lowest energy transition in deprotonated tryptophan is a $\pi\pi^*$ transition similar to the one found for neutral and protonated tryptophan, see right part of Figure 6.5. That is, the negative charge does not lead to a structural change or a different type of transition. Hence, the shift in the absorption is a direct effect of the remote negative charge, that destabilizes the ground state to a larger extend than the excited state. Furthermore, they showed from theory that the absorption of deprotonated tryptophan is tautomer-dependent (from 281 nm and 300 nm) in contrast to the tautomer-independent absorption of protonated tryptophan [17].

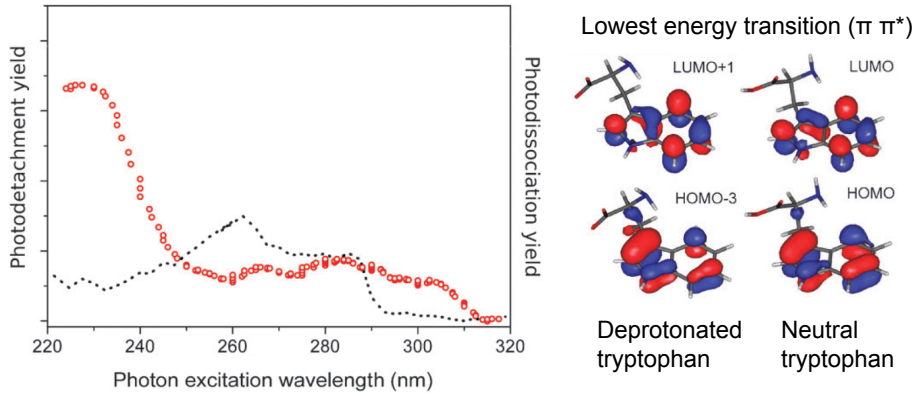

Figure 6.5. *Gas phase photodetachment spectrum of deprotonated tryptophan (open circles), and gas phase photodissociation spectrum of protonated tryptophan (dashed line). The nearby negative charge in deprotonated tryptophan results in a 25-nm redshift in the absorption compared to that for the protonated or neutral tryptophan. In both cases the main transition is a similar π π^* transition (right side). Adapted from reference [74].*

The succeeding examples demonstrate how attachment of spectator charges is another method to probe the effect of nearby charges on a chromophore. A spectator charge is a group that does not directly influence the chromophore, but it contains, for instance, a protonation site and thus provides a nearby positive charge. Insertion of different spacers between the charge and the chromophore probes the effect of a nearby charge in a controlled manner by variation of the distance from the chromophore to the charge. In the far-distance limit, the spectator charge does not affect the chromophore and properties of the neutral chromophore can be explored by conventional ion based instruments.

An example on neutral molecule investigations by employment of spectator charges is found in the work by L. H. Andersen and co-workers [75]. They attached a spectator charge to a retinal model chromophore with the aim to investigate the optical properties of the neutral retinal chromophore. The model chromophore is similar to the conformational sensitive chromophore presented earlier except for an extra CH_3 group at the ring. Absorption by the protonated model chromophore ($\mathbf{1}^+$) was compared to that by the model chromophore with $N(CH_3)_3^+$ ($\mathbf{3}^+$) and $(CH_2)_2N(CH_3)_3^+$ ($\mathbf{4}^+$) attached instead of the $(CH_2)_3CH_3$ tail, see Figure 6.6. A significant redshift is found in the absorption as the nearby charge approaches the chromophore, *i.e.* in the order from $\mathbf{4}^+$ to $\mathbf{3}^+$ to $\mathbf{1}^+$, and the explanation is straight forward: Upon excitation charge is transfered from the ring to the nitrogen, and the presence of a nearby positive charge at the base-end stabilizes the excited state and hence redshifts the absorption. The neutral retinal absorbs at 364 nm in solution, see **2** in lower panel, and as expected the gas phase absorption by the cations approaches this value as the charge is moved away from the chromophore.

In a similar manner, they attached spectator charges to the green fluorescent protein (GFP) model chromophore. They first used NH_3^+ as spectator-charge group but found that caution must be taken in the use of spectator charges as hydrogen bonds form between the ammonium group and the chromophore [76]. To further elucidate the effect of this hydrogen bond, they extended their study to include six different model chromophores, see Figure 6.7 [8]. Structure **A** and **B** have strong hydrogen bonds from the spectator charge to the carbonyl oxygen (indicated by red dotted lines), weaker hydrogen bonds are found for structure **C** and **D** whereas no hydrogen bonds are present in **E** and **F**. The distance from the charge to the chromophore is longest for structure **B**, **D** and **F**. Gas phase action spectroscopy revealed similar spectra for structure **C**-**F** whereas the absorption by structure **A** and **B** is shifted towards the red. Hence, hydrogen bonds do influence the chromophore as charge density is transferred from the spectator charge to the chromophore, *i.e.* different tautomers. As presented in Figure 6.8, important resonance structures of

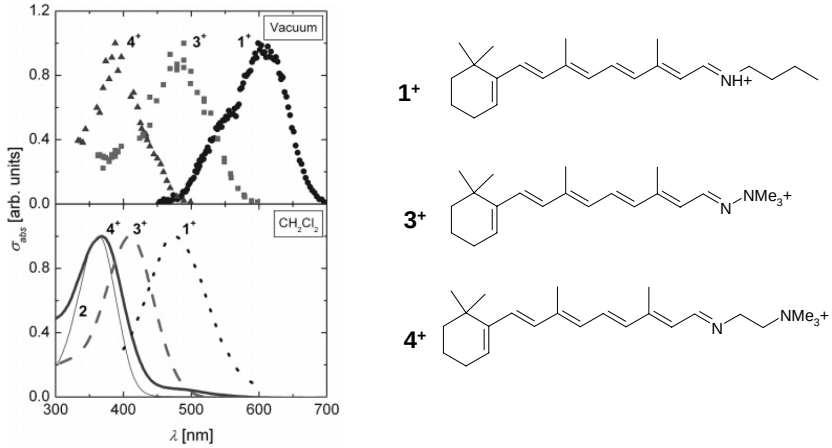

Figure 6.6. *Action spectra (upper panel) of the protonated retinal chromophore (**1**$^+$) and the neutral chromophore with nearby spectator charges, **3**$^+$ and **4**$^+$. Increased distance from the charge to the chromophore, from **3**$^+$ to **4**$^+$, blueshifts the absorption. At large distance the absorption approaches that of the neutral chromophore in solution (**2** in lower panel). Adapted from reference [75].*

the hydrogen bonding chromophores can be drawn, and the charge delocalization is in agreement with the redshift in the absorption. On the contrary, the distance from the chromophore to the charge, which was found to be important for the retinal chromophore above, does not influence the absorption, evident from the similar absorption of the four weak or non-hydrogen bonding structures.

A final example of the use of spectator charges is an investigation of oligophenoleneethynylenes (OPE), the molecule treated under the inductive effect, with one and two nearby charges, Article **X** ([77]). A $(CH_2)_2NH_3^+$ group was attached to one or both ends of the chromophore and the gas phase action spectra of the monocation (middle panel) and dication (lower panel) were measured, see Figure 6.9. The solution phase spectrum of the neutral bare chromophore is shown in the upper panel. While the spectrum of the dication resembles that of the neutral chromophore in solution, a clear redshift in the absorption is found for the monocation. A simple picture based on the potential of the photoactive electron in the two chromophores can be used to explain the shift, see sketch in the bottom of Figure 6.9. As for the retinal chromophore, a single nearby charge stabilizes the excited state as the electron moves closer to the positive charge upon excitation. But for the dication this stabilization is compensated for by a destabilization as the electron moves away from the other positive charge. Thus it seems as the important param-

eter here is the charge distribution - symmetric *versus* asymmetric - rather than the actual charge state.

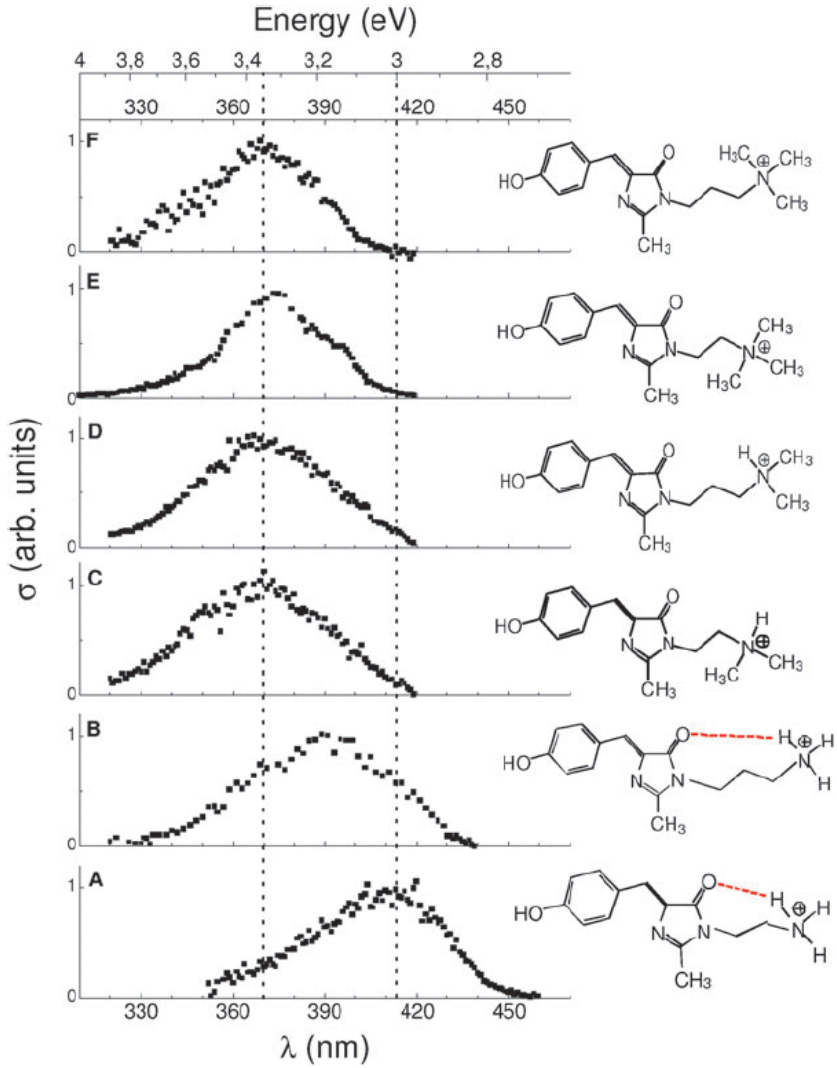

Figure 6.7. *Action spectra of six green fluorescent protein model chromophores to study the effect of hydrogen bonds (**A** and **B**) as well as the distance from the chromophore to the nearby charge **C**-**F**. A clear effect is found for the hydrogen bonds, cf. Figure 6.8, apparent from the redshift of the absorption for **A** and **B**, whereas the distance to the nearby charge does not affect the absorption of the chromophore. From reference [8].*

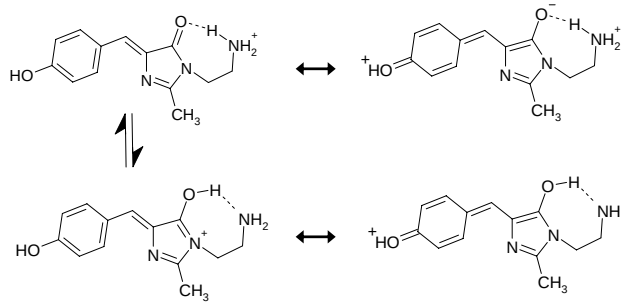

Figure 6.8. *Structure of the two tautomers of the green fluorescent protein model chromophore* **A**, *cf. Figure 6.7, with corresponding resonance structures. As the spectator group forms hydrogen bonds to the chromophore, charge is partly or completely transferred to the chromophore. Resonance structures for the charged chromophore cause a redshift in the absorption compared to the non-hydrogenbonded model chromophores, cf. Figure 6.7.*

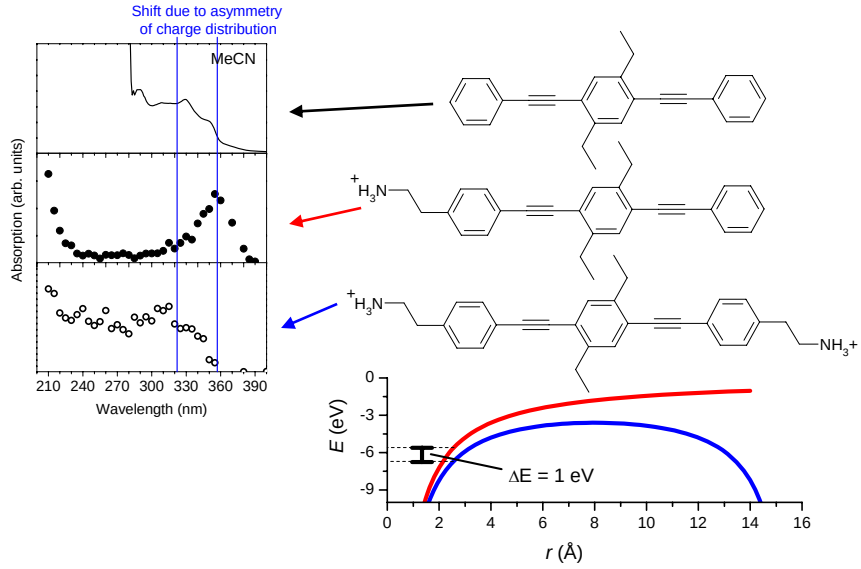

Figure 6.9. *Action spectra of oligophenyleneethynylene (OPE) with one (middle) and two (lower) nearby positive charges. The upper panel shows the absorption spectrum of the neutral bare chromophore in acetonitrile. Similar absorption is found for symmetric charge distribution (neutral and dication) and a redshifted absorption for the asymmetric charge distribution. Stabilization as the photo-active electron moves closer to the single positive charge causes the redshift. Potential of an electron for the mono- and dication is drawn in the lower right graph. The energy difference at the outer placed carbon is similar to the observed shift in absorption. Further details in Article* ***X*** *([77]).*

CHAPTER 7

Metal-ion Complexes

Turning towards larger molecular ions, metal-ion complexes is an important and interesting class, and these complexes are found widely in nature. One biological important example is Heme, responsible for dioxygen storage and transport in human blood and cells. Consequently, the photophysics of such complexes is interesting from a biological point of view, but the complexes are also interesting in their own right.

The absorption profile of such complexes contains bands assigned to different types of transitions being charge transfer between the metal and ligands, ligand centered transitions, and metal centered transitions. Hence, a replacement of the metal or ligands (the chromophore part of the complex) may affect the absorption of the complex. Furthermore, for symmetrical metal-ion complexes a comparison of the absorption in the gas phase and in solution enables a determination of the charge distribution in the excited state in solution.

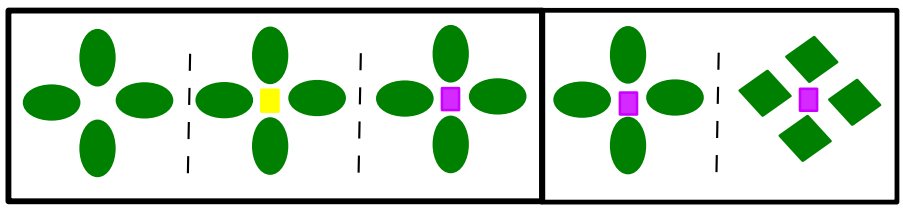

One metal-ion complex investigated in our laboratory is tris(2,2´-bipyridine)ruthenium(II) dication ($Ru(Bipy)_3^{2+}$), Article **XI** ([78]). The gas phase action spectrum is shown in Figure 7.1 (upper part). Each band in the spectrum is assigned to the involved type of transition, that is, metal-to-ligand (MLCT) ligand-to-metal (LMCT), metal centered (dd) and ligand centered ($\pi\pi^*$) transitions. The solution phase (acetonitrile) absorption spectrum is presented in the lower panel of Figure 7.1 and similar absorption is found apart from a 22-nm redshift of the 430-nm MLCT band in solution. In the MLCT transition charge is transferred from the metal to the ligand, and the measured shift reveals that in solution the charge is localized on a single ligand after excitation rather that delocalized over all three ligands, *i.e.* $(Ru(III)(Bipy)_2)^{3+}(Bipy)^-$ compared to $Ru(Bipy)_3^{2+}$. Polar solvent molecules will interact with a localized charge, stabilize the excited state and redshift the absorption in solution phase compared to gas phase (see sketch in right part of Figure 7.1). For a delocalized charge no or a very small shift is expected for the charge transfer transition upon solvation as the dipole moment (p) is zero for the symmetric charge distribution. Hence, in the case of $Ru(Bipy)_3^{2+}$ the comparison between gas phase and solution phase measurements indicates a non-zero dipole moment for the excited state of $Ru(Bipy)_3^{2+}$ in solution due to a localized charge transfer.

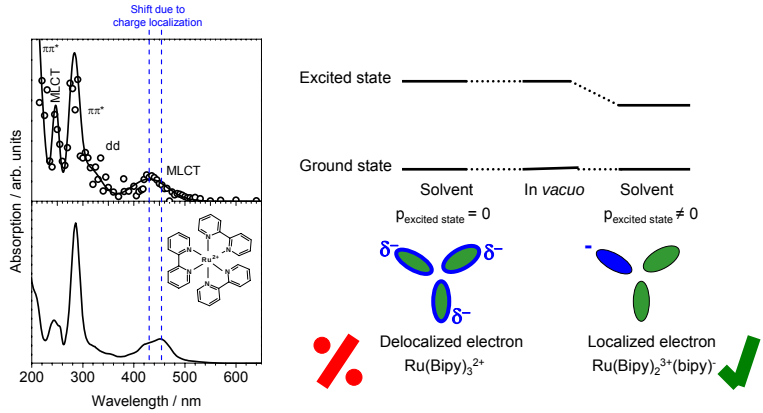

Figure 7.1. *Action spectrum (upper panel) and acetonitrile solution phase absorption spectrum (lower panel) of tris(2,2´-bipyridine)ruthenium(II) dication ($Ru(Bipy)_3^{2+}$). Each band is assigned to the type of transition involved. The redshift of the metal-to-ligand-charge-transfer (MLCT) 430-nm band in solution is a consequence of a localized charge in the excited state as illustrated by the sketch. Further details in Article* ***XI*** *([78]).*

The group of L. A. Posey [79, 80, 20] studied similar coordination complexes and how microsolvation affects the MLCT band. For instance, for

$[Fe(bpy)_3 \bullet (CH_3OH)_n]^{2+}$, n=2-6, each solvent molecule shifts the onset of the band to lower energies, gradually towards the solution phase spectrum (solid line), see Figure 7.2. A high dissociation energy for the bare complex necessitates loosely bound solvent molecules to measure the photodepletion spectrum. In a controlled manner, *i.e.* by sequential solvent molecule attachment, they measured the effect of solvation and obtained an upper limit for the absorption of the bare complex. In this sense, their study is in the intermediate of the above gas phase and solution phase experiments.

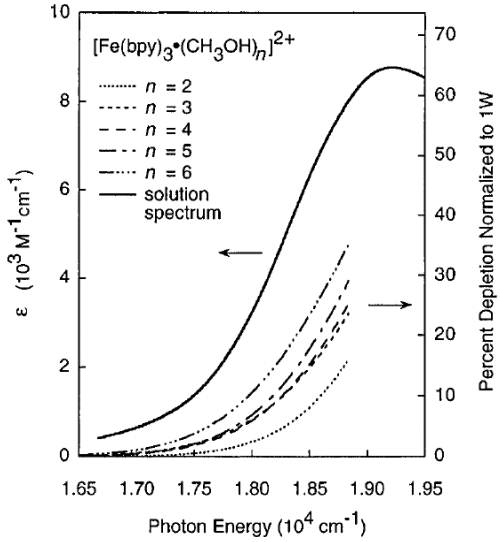

Figure 7.2. *Photodepletion spectra for $[Fe(bpy)_3 \bullet (CH_3OH)_n]^{2+}$, n=2-6. As more solvent molecules are added to the complex the onset of the MLCT band shifts to the red and thereby approaches the solution phase spectrum (solid line). The spectra indicate electron localization in the solution phase excited state. From reference [20].*

Another example of symmetric metal-ion complexes is the tetrathiocyanoplatinate(II) dianion ($Pt(SCN)_4^{2-}$), Article **XII** ([81]). Figure 7.3 shows the gas phase action spectrum of $Pt(SCN)_4^{2-}$ (symbols) and the solution phase spectrum measured in methanol (solid line). The main dissociation channel here is electron detachment. In contrast to $Ru(Bipy)_3^{2+}$, solvation has no effect on the onset of the absorption, and hence the photoactive electron is delocalized over all ligands in the excited state, *i.e.* zero dipole moment in the solution phase excited state.

Comparison of the above gas phase action spectrum of $Pt(SCN)_4^{2-}$ with the work by Weber and Kappes [82] on $Pt(Br)_4^{2-}$ brings insight into how ligands shield the metal center from solvent molecules. The solvent-insensitivity on the absorption for the Pt-SCN complex presented above is not found with Br as ligand. Not

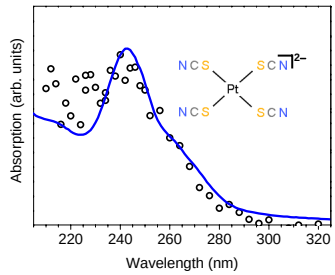

Figure 7.3. *Gas phase action spectrum (symbol) and solution phase absorption spectrum (solid line) of tetrathiocyanoplatinate(II) dianion ($Pt(SCN)_4^{2-}$). A delocalized charge in the solution phase excited state is evident from the similarity of the two spectra. Further details in Article* ***XII*** *([81]).*

surprisingly, the larger ligands (SCN^-) shield the metal center more effectively than the smaller ligands (Br^-).

To complete the picture, a similar solvent impact is found for $Ir(Br)_6^{2-}$ in work by Marcum and Weber [83]. But as the transitions are attributed to LMCT the solvent molecules stabilize the ground state instead of the excited state and hence blueshift the absorption.

Work by P. Dugourd *et al.* [84, 85] elucidates how different metals (M) affect the charge transfer transitions for $[TrpM]^+$ complexes. In these complexes the metal atom interacts with the carbon atoms of the indole ring, and the lowest energy excitation is a charge transfer from the indole chromophore to the metal atom found to the red of the $\pi\pi^*$ transition in bare Trp at 260 nm. Experimentally they have measured photodissociation mass spectra of the silver and gold complexes and find absorption at 332 nm and 400 nm, respectively. Theoretical calculations of the HOMO-LUMO gaps were performed for several metal complexes. The shift into the (near)-visible region facilitates the complexes as efficient protein labeling agents. They further show that complexation of peptides with small silver clusters ($[Ag]_n$,n=3-9) enhances the absorption and provides conformational control [86, 87].

The effect of replacing the metal in phthalocyanines was examined by Kappes *et al.* [25]. Photodepletion spectra of $XPc(SO_3)_4^{-4}$ with X = Cu, Ni or H_2 were measured in the spectral region from 570 nm - 695 nm. Similar spectra were found for the two metal coordinated complexes whereas the free base (X = H_2) stood out. Hence, in this case the metal orbitals do not influence the absorption as the transition are ligand centered. The primary difference for the free base is an extra absorption band in consequence of a splitting of the energy levels since the symmetry of the complex is broken.

Related compounds are porphyrin complexes, and for a large part of metalloporphyrins, so-called regular porphyrins, the metal orbitals are also known to have low impact on the absorption, which again is ligand centered [88]. This is also the case for zinc porphyrin examined in out laboratory [89]. Figure 7.4 shows the gas phase action spectra of the bare protoporphyrin-IX (PP) anion (upper panel) and the zinc complex $ZnPP^-$ (lower panel). Like for phthalocyanine, the asymmetry of PP splits the energy levels. On top of this, it seems as the metal complexation here leads to a small redshift of the spectrum. Interestingly, a MLCT transitions is apparent in the weak band at 660 nm.

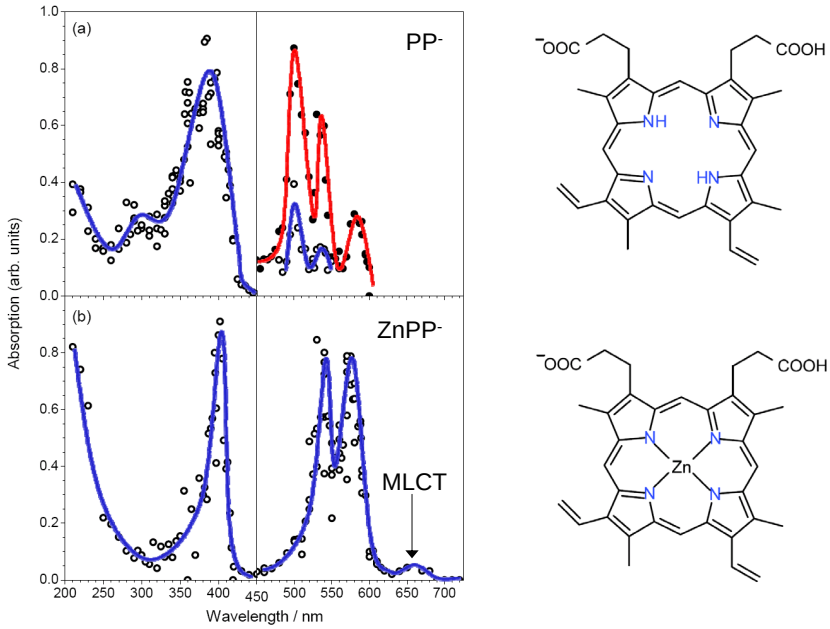

Figure 7.4. *Gas phase action spectra of anionic protoporphyrin-IX, PP^-, (upper panel) and the metallo-complex $ZnPP^-$ (lower panel). The asymmetry of the bare PP splits the energy levels with an extra band in the visible region in consequence. Upon complexation a weak MLCT transition arises at low energy. The vertical line is to distinguish two absorption regions with different absorption intensity. The two spectra presented at low energy for PP^- is from absorption of one (open circles, blue curve) and two (open circles, red line) photons, respectively. Adapted from reference [89].*

Experiments on another porphyrin, iron-protoporphyrin-IX complex (Heme), investigated the effect of the protein environment by complementary ligation. In the protein the complex binds to the amino acid Histidine, Article **XIII** ([90]) [91]. Histidine binds to the iron center and slightly pulls out the metal from the complex

plane, see Figure 7.5. The gas phase action spectra of Heme$^+$ and Heme-His$^+$ are presented in the left and middle part of the figure. The sharp peak at 350 nm in the Heme-His$^+$ spectrum is believed to be an artifact caused by the laser, and hence, no large effect of ligation is found. The broadening of the high energy band is ascribed to the aforementioned displacement of the metal caused by histidine. A metal-to-ligand charge transfer transition is found at low energy.

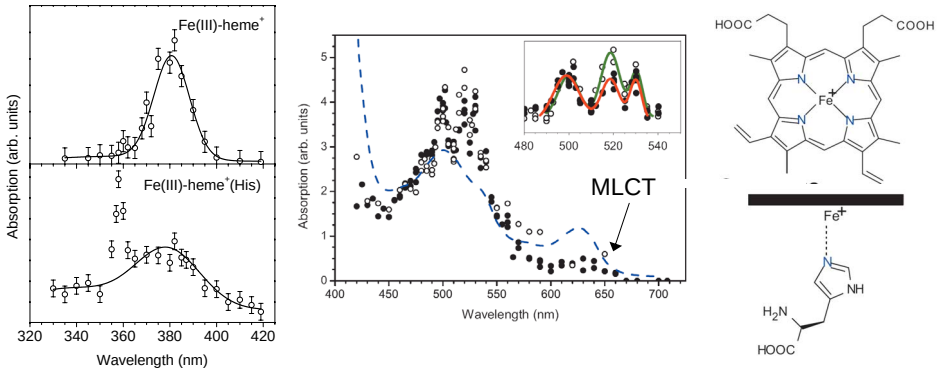

Figure 7.5. *Action spectra of Heme (upper panel and hollow circles) and Heme in complexation with Histidine (lower panel and filled circles). The main effect of complexation is a broadening of the high energy band due to a small displacement of the metal from the complex-plane (right lower side). Further details in Article* ***XIII*** *([90]). The low energy spectrum is adapted from reference [91]. More details on the molecular ion in Article* ***XIV*** *([92]).*

CHAPTER 8

Summary and outlook

By now, I have hopefully convinced you that gas phase spectroscopy is a strong characterization tool in the aim to understand molecular ions and their photophysics. In this thesis I have considered intermediate sized even electron ions studied by UV-VIS spectroscopy and investigated how the optical properties of the chromophores are affected by small modifications or perturbations. In the first part, I considered modifications of the isolated chromophore, that is, how the optical properties are determined by the structure, conformation, electronic structure, and type of transition. In the second part, external perturbations to the chromophore from the remaining molecule, such as nearby charges, complexation, and substituents, were considered.

The crucial parameter for the optical properties of the chromophore is electron delocalization - the more delocalized electrons the smaller excitation energy. The concept of resonance structures is a valuable tool to visualize the electron delocalization. From this foundation, it is possible to understand the different optical properties of, for instance, isomers, tautomers, and conformers. Also the type of transition is obviously necessary to consider, and generally one finds a lower transition energy if charge is transferred upon excitation (charge transfer transitions).

As the chromophore is a part of a larger molecule the spectral properties are tuned. First, substituents induce a small charge on the chromophore and thereby alter the electron delocalization. However, this inductive effect is vague. A more significant perturbation is from nearby charges where the charge interacts with

the photoactive electron on the chromophore and thereby alter the delocalization. Finally, metals (*i.e.* in metal-ion complexes) may or may not affect the optical properties of the chromophore.

The examples presented in this thesis cover a broad range of perspectives. Investigation of the green fluorescent protein chromophore results in an identification of an isolated anionic form of the chromophore in the protein. Furthermore, individual perturbations from an environment are studied. The chromophore is unaffected by a nearby positive charge whereas hydrogen bonds influence the chromophore. A gradual buildup of the protein environment is demonstrated in the case of Heme complex where ligation with the histidine amino acid only slightly modifies the action spectrum.

It is also illustrated how molecules with desired properties can be designed. One example is nitrophenolates, where the absorption shifts through the whole visible region as the distance between the donor and acceptor group is increased. Another example is the tryptophan-metal complexes, where charge transfer transitions from the metal to the chromophore are found in the (near)-visible region. Thus, these complexes may serve as efficient protein labeling agents.

Turning towards future perspectives they can be divided into two parts - instrumental and scientific. Scientific perspectives concerns new perturbations or type of molecular ions to investigate in the future. Regarding the perturbations treated here, the least understood is the inductive effect caused by substituents. Hence, a thorough understanding of this smaller effect necessitates further experiments. As for new types of molecular ions, one objective is to move towards supramolecular complexes. For complexes with several clearly separated chromophores interactions between the chromophores may occur. Preliminary studies of such complexes is done on DNA strands where the excited state is found to involve at least two chromophores, further details in Article **XV** ([93]).

As for the instrumental developments, only a few spectroscopy experiments has been carried out at the SEP1 facility so far. Thus, plenty of interesting experiments on molecular ions with a short dissociation time (few μs) are waiting. Furthermore, the configuration has recently been changed from a crossed beam to a merged beam configuration which increases the number of ions the laser interacts with. Hence, molecular ions with lower absorption cross section can be studied with this new configuration.

Another type of experiments, which would be interesting to continue, are the pump probe experiments at ELISA. Pump-probe experiments on the microsecond to millisecond timescale are possible at the storage ring facility. This was demon-

strated by a measure of the triplet-triplet absorption spectrum of protoporphyrin anions, further details in Article **XVI** ([94]).

In a long-term perspective, plans exist to build an FT-ICR instrument in the laboratory. One advantages is the possibility to cool the ions and thereby measure highly resolved spectra. Along this direction, it is interesting to follow the DESIREE project in Stockholm, Sweden, where a cryo-cooled double electrostatic ion storage ring is under construction [95]. Another aim with the FT-ICR is to do fluorescence experiments. Gas phase fluorescent experiments are so far only carried out in a few laboratories; Parks [33], Jouckusch [35] and Zenobi [34]. It is a nice characterization tool in complement to absorption spectroscopy. Also, in our action spectroscopy we assume that the fluorescent yield - if any - does not depend on the wavelength, and with a measure of fluorescence we would be able to test this for the different ions.

Personally, my fascination lies with the small molecular ions where the effect of small alterations can be studied in a controlled manner and the basic physic is more visible and less complex. It is impressive that much of the physics can be understood on the basis of simple electrostatics. One important lesson from my studies so far is that gas phase experiments go hand-in-hand with solution phase experiments and theory to unveil the full story. I believe that plenty of physics is to be learned from a structured study of small molecular ions.

APPENDIX A

Instrumental and experimental description

The experiments performed during my Ph.D. were carried out using two instrumental setups in Aarhus. SEP1 is a single pass tandem mass spectrometer, and ELISA is a storage ring facility, but similar ion source and laser system is used in both setups [96]. This appendix gives a general description of the two setups, the possible experiments and the concomitant analysis.

The two facilities complement each other with respect to the time scales of the processes studied, and both instruments provide action spectra and photodissociation mass spectra. On top of this, lifetime information is obtained from experiments at ELISA. Most of the results presented in this thesis are from action spectroscopy at ELISA, thus more details are given on this experimental method. It should also be mentioned that the instruments are used for other types of experiments, such as high energy collision experiments [97], electron capture experiments [98, 99] and cluster evaporation experiments [100], which are not presented here.

Electrospray ion source

Ions are produced by electrospray ionization, a soft ionization technique well suited to bring large fragile molecular ions intact into the gas phase [4, 101].[1] A sketch of the ion source setup is shown in Figure A.1. The electrospray produces highly charged droplets that contain analyte and solvent. The latter is boiled of as the droplets move to the capillary entrance and pass through the heated capillary, leaving the ions on the gas phase. Ion optics guide and focus the ions through chambers with differential pumping. Accumulation in a multi-pole ion trap [103, 104] followed by buffer gas cooling with He-gas for 0.1 ms, bunches the ions. Finally, the ion bunch enters the acceleration tube, where the pressure is 10^{-6} mbar, and the ions are accelerated to 22 keV and 50 keV kinetic energy per charge in ELISA and SEP1, respectively. After acceleration, the ions with the mass-to-charge ratio of interest are selected by a bending magnet and enter the ring and beam line, respectively. The ion current after the magnet is typically in the order of pA. The technique works for both cations, anions and multiple charged ions.

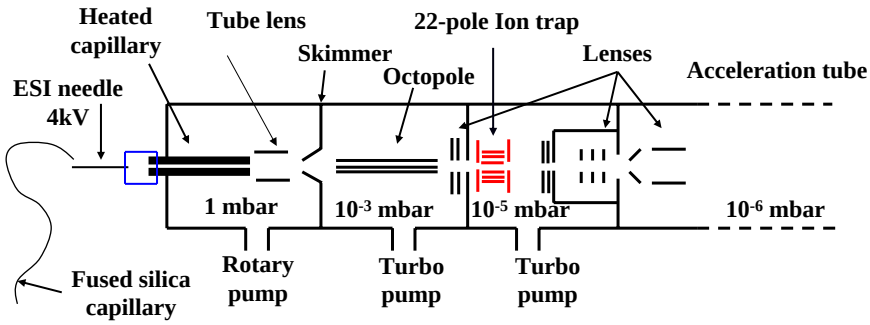

Figure A.1. *Electrospray ion source used in the two setups. A mulitipole ion trap is used to bunch the ions prior to acceleration.*

EKSPLA laser system

The laser used for photo excitation in both setups is a tunable laser from EKSPLA. It is a Nd:YAG laser where the third harmonic (355 nm) pumps an optical parametric oscillator (OPO). The visible output from this OPO is frequency doubled in a crystal providing UV light. Tuning between 210 nm and 2300 nm is possible, the pulse length is nanoseconds and the energy is in the order of 1 mJ per pulse

[1] Note that a Nielson plasma ion source was used for the C_{60} experiments included in this thesis but electrospray ionization is also possible [102].

depending on the wavelength. In the storage ring the laser beam is merged with the ion beam whereas the single pass setup at SEP1 is a crossed beam experiment.

Electrostatic Ion Storage Ring in Aarhus (ELISA)

The ring structure of ELISA consists of two cylindrical 160 degree deflectors, four 10 degree parallel-plate deflectors and electrostatic quadropole elements, see Figure A.2 [105]. One advantage of only using electrostatic components to store the ions is that the ions are stored due to their kinetic-energy-to-charge ratio, *i.e.* independent of mass. This makes operation easier as the ring parameters are kept fixed and only the ion source parameters and the mass-to-charge selection by the magnet is varied going from one ion to another. The circumference of the ring is 8.3 m which gives revolution times in the order of 50-100 μs. The ions are injected into the ring through a differentially pumped beam line leaving the pressure in the ring around 10^{-11} mbar which gives ion storage times of seconds.

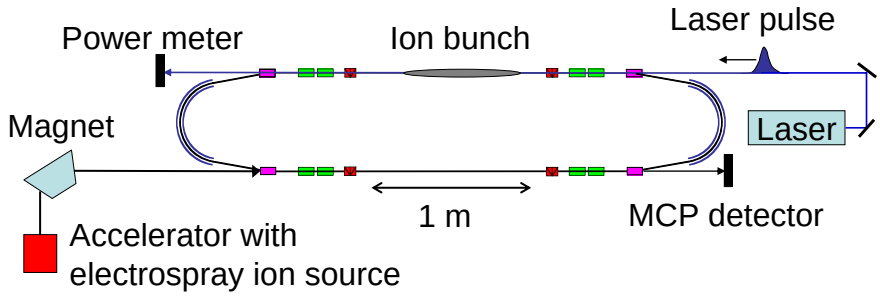

Figure A.2. *ELISA setup used for lifetime experiments, action spectroscopy, and photodissociation mass spectroscopy. The electrostatic storage ring is combined with an electrospray ion source and a tunable pulsed laser system.*

A micro-channel-plate (mcp) detector is located at one side of the ring and whenever neutrals are formed within that branch they are unaffected by the electric fields and hit the detector. We monitor the number of neutrals hitting the detector as a function of time to probe what happens to the ions as they circulate the ring. The photoexcitation occur on the opposite side of the ring compared to the mcp detector, hence, the experiments are delayed dissociation experiments where neutrals formed after half a revolution and onwards are sampled.[2] The repetition rate of the experiment is normally 10 Hz.

[2]Other detectors are positioned at the laser site of the ring used for detection of singly charged fragments from double charged ions and for detection of neutral fragments, but I have not used them for my experiments.

A typical spectrum with photoexcitation is shown in Figure A.3. The high yield of neutrals immediately after injection is due to metastable ions that have been excited during extraction from the ion trap or during injection into the ring. After a few milliseconds, the signal is dominated by collisional decay in the ring, seen as the approximately constant level reached. Photoexcitation takes place after 45.3 ms, and a clear increase in the neutral-formation due to photoinduced dissociation is seen. The inset shows a zoom around the time for photoexcitation and clearly illustrates the revolution time of the ions.

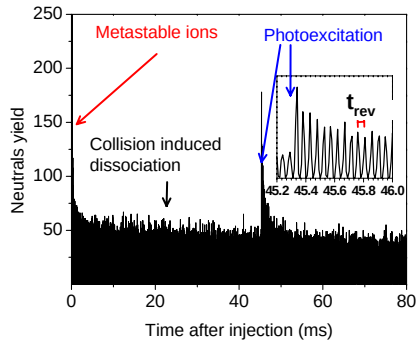

Figure A.3. *Typical spectrum obtained at ELISA. We monitor the number of neutrals hitting the detector as a function of time. In the first millisecond dissociation is dominated by metastable ions until a constant level due to collision induced dissociation is reached. Photoexcitation after 43.5 ms causes an increase in neutral formation due to photodissociation. The inset shows a zoom around photoexcitation and clearly illustrates the revolution time of the ion bunch.*

ELISA is a state-of-the-art instrument and an extremely strong tool for gas phase spectroscopy experiments. The timescales for the sampled dissociation span from tens of μs to hundreds of ms and three important informations are obtained from the experiments as described in the following. Similar electrostatic ion storage rings exist in Japan at KEK in Tsukuba [106] and the TMU ring in Tokyo [107, 108]. Recently, experiments are started at the Mini-Ring developed in Lyon, a transportable tabletop storage ring [109, 110]. Further rings are under construction; FLSR in Frankfurt [111], CSR in Heidelberg [112] and DESIREE in Stockholm [95]. The latter is a double ring construction for merged beam experiments. For the TMU, Mini-ring, CSR and DESIREE cooling of the ions to very cold temperatures is or will be possible.

Lifetime measurements

To obtain lifetime information the total number of neutrals that hits the detector per revolution is summed and plotted as a function of time after photoexcitation. A typical time spectrum and the corresponding lifetime is shown in Figure A.4. In an ideal picture the ions are excited to a well-defined internal energy upon photon absorption leading to a single exponential decay rate, but in reality the situation is more complex. One complication is the width of the internal energy distribution of the ion bunch from the room-temperature ion source which results in a tail to the exponential. This can be accounted for by an Arrhenius type analysis [113, 114, 115]. Another possibility is capture of the electron into a spin-forbidden state which results in a slower decay rate back to the ground state [114, 92]. Dissociation can also happen from the excited state, *i.e.* non-statistical dissociation, with time-constants much faster than statistical dissociation [116]. Finally, dissociation can happen after absorption of several photons which is tested for by a measure of the neutral yield as a function of laser energy [58, 91]. Several papers such as the above mentioned treat these topics and I will not go into further details here.

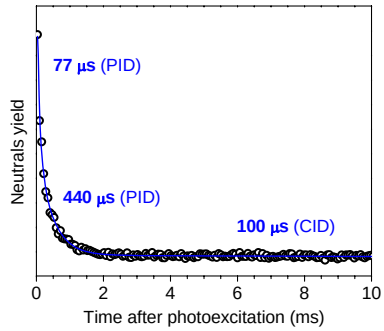

Figure A.4. *Total number of neutrals hitting the detector per revolution as a function of time after photoexcitation. Three exponentials is used to fit the data points; two exponentials describe the photoinduced dissociation (PID) whereas the long time component is due to collision induced dissociation (CID).*

Action spectroscopy

The ion beam density in ELISA is too low to cause a detectable decrease in the photon intensity from absorption, as is measured in conventional absorption spectroscopy. Instead we use action spectroscopy where we measure the photo induced dissociation as a function of wavelength - high absorption results in high production of neutrals. A drawback of this indirect technique is that we are blind to non-

dissociative absorption such as light emission. Absorption cross-sections (relative, not absolute numbers) are obtained from the time spectra as the number of neutrals formed after photoexcitation divided by the ion beam intensity and the number of photons. In a simple picture, see Figure A.5, we take the photoyield signal (counts in the blue region), substract the background signal (counts in the red region) and divide by the number of photons and the background signal. The latter is to correct for fluctuations in the ion beam intensity.

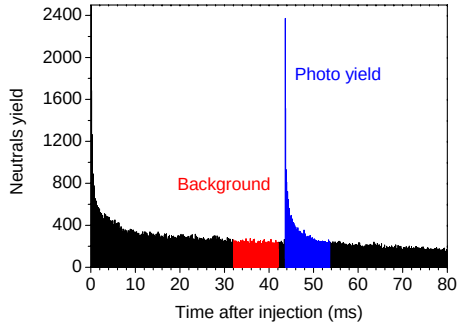

Figure A.5. *Simplified principle of calculating the absorption cross sections. Relative cross sections are obtained as the number of counts in Photo yield minus counts in Background, divided by the number of photons and the ion beam intensity, i.e. the Background level.*

In reality a more refined analysis based on exponential fitting to the data points is used, as illustrated in Figure A.6. Instead of summing the number of count in the photoyield region, we use the area under the fitted curve to give the (relative) number of photoexcited ions. The advantage lies in a correction for lifetime effects. Since the detector is located on the opposite side of the ring compared to excitation, the experiment is a delayed dissociation experiment, *i.e.*, we sample neutrals formed after half a revolution and after successive revolutions. By summing the number of neutrals hitting the detector we leave out the very fast decay, and if this time component is wavelength dependent we introduce a fault in the action spectrum. From the lifetime-fit we can extrapolate back to time zero, defined as the time where the laser is fired, and hence lifetime effects are accounted for. We are still blind to very fast processes but this time-region is covered by the other setup as described later. The strength of using a storage ring facility for action spectroscopy lies in the long sampling time, and thus we circumvent problems due to kinetic shifts.

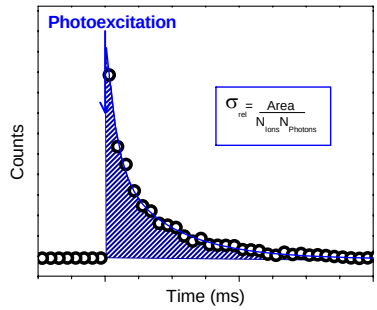

Figure A.6. *Principle of calculating the absorption cross-sections based on lifetime fit. The relative number of photoexcited ions is obtained as the area under the fitted curve. This method include dissociation within the first half revolution as it is possible to extrapolate back to times zero where the laser is fired.*

Daughter ion mass spectroscopy

Implementation of fast pulsed power supplies for all the ring elements provided the possibility to do time resolved daughter ion mass spectroscopy, Article **XVI** ([99]). The time scheme is shown in Figure A.7. After photoexcitation the voltage on the ring elements is switched from storage of parent ions to storage of daughter ions and after a couple of revolutions the ions are dumped onto the detector. The response time for the switches is microseconds, and the dumping is done by setting the 10 degree deflector in front of the detector to zero. A fragment mass spectrum is obtained by monitoring the daughter ion signal as a function of the ring voltages. In addition, it is possible to study the competition between dissociation channels as a function of time by changing the time (t_1) between excitation and switching. The timescales span from microseconds to milliseconds, a region not easily covered with other instruments. It should be noted, that the mass resolution of the spectra is rather poor due to the energy acceptance of the ring, hence some pre-knowledge of dissociation channels is needed.

Seperator1 (SEP1)

Seperator1 (SEP1) is a tandem mass spectrometer, *i.e.* a single pass experiment, where the ion identification is done by an electrostatic analyzer (ESA) that guides the ions with the kinetic-energy-to-charge ratio of interest to a channeltron detector. A sketch of the instrument is shown in Figure A.8. The pulsed tunable EKSPLA laser is combined with the setup in a crossed beam configuration and allows for photodissociation mass spectroscopy and action spectroscopy on the microsecond

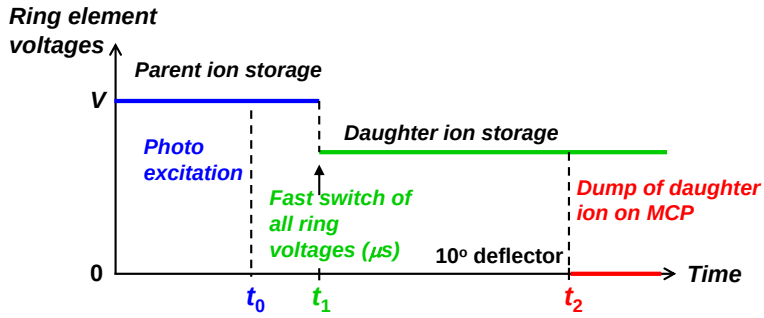

Figure A.7. *Time scheme for time resolved daughter ion mass spectroscopy. All ring element voltages are scaled to store some fragment ion which is subsequently dumped on the detector. A record of the detector signal through a continuous scan of the voltages provides the mass spectrum. Further details in Article* ***B-XVI*** *([99])*

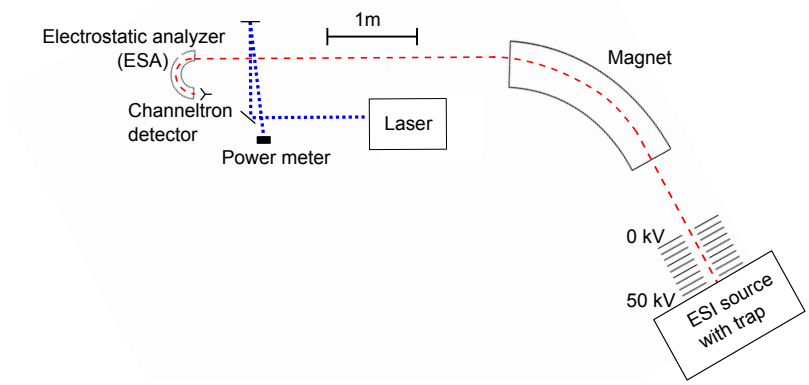

Figure A.8. *Sketch of the SEP1 setup. The tandem mass spectrometer is combined with an electrospray ion source. A multipole ion trap and a pulsed laser was implemented to enable photodissociation mass spectroscopy and action spectroscopy.*

timescale [77]. The distance from the interaction region to the entrance of the ESA is 60 cm which gives a flight time of a couple of μs. Hence, we sample photofragments formed within this time, nicely complementing the ELISA experiments.

A typical time spectrum of the number of ions, with a certain kinetic-energy-to-charge ratio, that hit the detector as a function of time is shown in Figure A.9. The width of the ion bunch is 25 μs, and a peak from photoinduced dissociation is clearly seen in the spectrum.

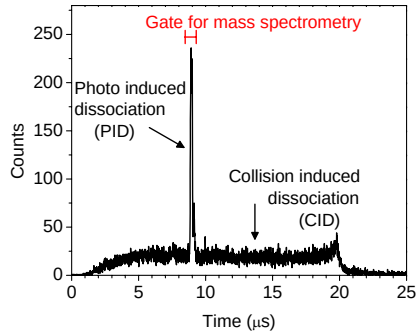

Figure A.9. *SEP1 Time spectrum where we monitor the number of ions, with a specific kinetic-energy-to-charge-ratio, hitting the detector as a function of time. An increase in the fragment ion formation due to photoexcitation is clearly seen. The background signal from collision induced dissociation serves as a measure of the ion beam intensity.*

Daughter ion mass spectroscopy

A photodissociation mass spectrum is obtained by scanning the ESA-voltage and monitor the number of ions that hits the detector as a function of the voltage, *i.e.* the kinetic-energy-to-charge ratio. To increase the signal-to-noise ratio we only sample the ions that arrive at the correct time, as indicated by the timing gate in Figure A.9. A spectrum without laser excitation is measured to take the contribution from collision-induced-dissociation into account. Compared to ELISA, a much higher mass-resolution is obtained by this setup.

Action spectroscopy

Absorption cross-sections (relative, not absolute numbers) are obtained from the time spectra as the number of fragment ions formed after photoexcitation divided by the ion beam intensity and the number of photons. One type of fragment-ion is guided to the detector, and time spectra are measured for different wavelength. The photo signal gives the number of photo induced fragment ions, and the background level gives the ion beam intensity. Such a spectrum is obtained for each photo-fragment channel in play in contrast to the ELISA experiment where all fragment channels are measured simultaneously.

Bibliography

[1] Karas, M. and Hillenkamp, F. *Anal. Chem.* **60**, 2299 (1988).

[2] Karas, M., Bachmann, D., Bahr, U., and Hillenkamp, F. *Int. J. Mass Spectrom. Ion Processes* **78**, 53 (1987).

[3] Barber, M., Bordoli, R. S., Sedgwick, R. D., and Tyler, A. N. *Nature* **293**, 270 (1981).

[4] Fenn, J. B., Mann, M., Meng, C. K., Wong, S. F., and Whitehouse, C. M. *Science* **246**, 64 (1989).

[5] Meyer, T. J. *Acc. Chem. Res.* **22**, 163 (1989).

[6] Alstrum-Acevedo, J. H., Brennaman, M. K., and Meyer, T. J. *Inorg. Chem.* **44**, 6802 (2005).

[7] Carroll, R. L. and Gorman, C. B. *Angew. Chem., Int. Ed.* **41**, 4379 (2002).

[8] Rajput, J., Rahbek, D. B., Andersen, L. H., Rocha-Rinza, T., Christiansen, O., Bravaya, K. B., Erokhin, A. V., Bochenkova, A. V., Solntsev, K. M., Dong, J., Kowalik, J., Tolbert, L. M., Petersen, M. Å., and Brøndsted Nielsen, M. *Phys. Chem. Chem. Phys.* **11**, 9996 (2009).

[9] Lincke, K., Sølling, T., Andersen, L. H., Klærke, B., Rahbek, D. B., Rajput, J., Oehlenschlæger, C. B., Petersen, M. Å., and Brøndsted Nielsen, M. *Chem. Commun.* **46**, 734 (2010).

[10] Marcum, J. C., Halevi, A., and Weber, J. M. *Phys. Chem. Chem. Phys.* **11**, 1740 (2009).

[11] Marcum, J. C., Kaufman, S. H., and Weber, J. M. *Int. J. Mass Spectrom.* **303** (2011).

[12] Rosu, F., Gabelica, V., Joly, L., Gregoireb, G., and De Pauw, E. *Phys. Chem. Chem. Phys* **12** (2010).

[13] Weinkauf, R., Schermann, J., de Vries, M., and Kleinermanns, K. *Eur. Phys. J. D* **20**, 309 (2002).

[14] Rizzo, T. R., Stearns, J. A., and Boyarkin, O. V. *Int. Rev. Phys. Chem.* **3**, 4810 (2009).

[15] Bellina, B., Compagnon, I., Joly, L., Albrieux, F., Allouche, A. R., Bertorelle, F., Lemoine, J., Antoine, R., and Dugourd, P. *Int. J. Mass Spectrom.* **297**, 36 (2010).

[16] Andersen, L. H. and Bochenkova, A. V. *Eur. Phys. J. D* **51**, 5 (2009).

[17] Nolting, D., Marian, C., and Weinkauf, R. *Phys. Chem. Chem. Phys.* **6**, 2633 (2004).

[18] Talbot, F. O., Tabarin, T., Antoine, R., Broyer, M., and Dugourd, P. *J. Chem. Phys.* **122**, 074310 (2005).

[19] Bian, Q., Forbes, M. W., Talbot, F. O., and Jockusch, R. A. *Phys. Chem. Chem. Phys.* **12**, 2590 (2010).

[20] Spence, T. G., Burns, T. D., Guckenberger, G. B., and Posey, L. A. *J. Phys. Chem. A* **101**, 1081 (1997).

[21] Stearns, J. A., Guidi, M., Boyarkin, O. V., and Rizzo, T. R. *J. Chem. Phys.* **127**, 154322 (2007).

[22] Schiedt, J. and Weinkauf, R. *J. Chem. Phys.* **110**, 304 (1999).

[23] Chakraborty, S., Omidyan, R., Alata, I., Nielsen, I. B., Dedonder, C., Broquier, M., and Jouvet, C. *J. Am. Chem. Soc.* **131**, 11091 (2009).

[24] Honovich, J. P. and Dunbar, R. C. *J. Phys. Chem.* **85**, 1558 (1981).

[25] Kordel, M., Schooss, D., Gilb, S., Blom, M. N., Hampe, O., and Kappes, M. M. *J. Phys. Chem. A* **108**, 4830 (2004).

[26] Støchkel, K., Milne, B. F., and Brøndsted Nielsen, S. *J. Phys. Chem. A* , In press (2001).

[27] Oomens, J., van Roij, A. J. A., Meijer, G., and von Helden, G. *Astrophys. J.* **542**, 404 (2000).

[28] Polfer, N. C., Oomens, J., Moore, D. T., von Helden, G., Meijer, G., and Dunbar, R. C. *J. Am. Chem. Soc.* **128**, 517 (2006).

[29] Kang, H., Dedonder-Lardeux, C., Jouvet, C., Gregoire, G., Desfrancois, C., Schermann, J. P., Barat, M., and Fayeton, J. A. *J. Phys. Chem. A* **109**, 2417 (2005).

[30] Ehrler, O. T., Yang, J. P., Hattig, C., Unterreiner, A.-N., Hippler, H., and Kappes, M. M. *J. Chem. Phys.* **125**, 074312 (2006).

[31] Guyon, L., Tabarin, T., Thuillier, B., Antoine, R., Broyer, M., Boutou, V., Wolf, J.-P., and Dugourd, P. *J. Chem. Phys.* **128**, 075103 (2008).

[32] Wang, Y., Hendrickson, C. L., and Marshall, A. G. *Chem. Phys. Lett.* **334**, 69 (2001).

[33] Iavarone, A. T., Duft, D., and Parks, J. H. *J. Phys. Chem. A* **110**, 12714 (2006).

[34] Dashtiev, M., Azov, V., Frankevich, V., Scharfenberg, L., and Zenobi, R. *J. Am. Soc. Mass Spectrom.* **16**, 1481 (2005).

[35] Bian, Q., Forbes, M., Talbot, F., and Jockusch, R. *Phys. Chem. Chem. Phys.* **12**, 2590 (2010).

[36] Baer, T. and Dunbar, R. C. *J. Am. Soc. Mass. Spectrom.* **21**, 681 (2010).

[37] Dunbar, R. C. *Int. J. Mass Spectrom.* **200**, 571 (2000).

[38] Freiser, B. S. and Beachamp, J. L. *J. Am. Chem. Soc.* **99**, 3214 (1977).

[39] Boye, S., Krogh, H., Nielsen, I. B., Brøndsted Nielsen, S., Pedersen, S. U., Pedersen, U. V., Andersen, L. H., Bell, A. F., He, X., and Tonge, P. J. *Phys. Rev. Lett.* **90**, 118103 (2003).

[40] Boye, S., Brøndsted Nielsen, S., Krogh, H., Nielsen, I., Pedersen, U. V., Bell, A. F., He, X., Tonge, P. J., and Andersen, L. H. *Phys. Chem. Chem. Phys.* **5**, 3021 (2003).

[41] Brøndsted Nielsen, S., Lapierre, A., Andersen, J. U., Pedersen, U. V., Tomita, S., and Andersen, L. H. *Phys. Rev. Lett.* **87** (2001).

[42] Kadhane, U., Andersen, J. U., Bonderup, E., Concina, B., Hvelplund, P., Kirketerp, M.-B. S., Liu, B., Brøndsted Nielsen, S., Panja, S., Rangama, J., Støchkel, K., Tomita, S., Zettergren, H., Hansen, K., Sunden, A. E. K., Canton, S. E., Echt, O., and Forster, J. S. *J. Chem. Phys.* **131**, 014301 (2009).

[43] Tomita, S., Andersen, J. U., Bonderup, E., Hvelplund, P., Liu, B., Brøndsted Nielsen, S., Pedersen, U. V., Rangama, J., Hansen, K., and Echt, O. *Phys. Rev. Lett.* **94**, 053002 (2005).

[44] Kirketerp, M.-B. S., Espinosa Leal, L. A., Varsano, D., Rubio, A., Jørgensen, T. J. D., Kilså, K., Brøndsted Nielsen, M., and Brøndsted Nielsen, S. *Chem. Commun.* **47**, 6900 (2011).

[45] Rajput, J., Rahbek, D. B., Andersen, L. H., Hirshfeld, A., Sheves, M., Altoe, P., Orlandi, G., and Garavelli, M. *Angew. Chem. Int. Ed.* **49**, 1790 (2010).

[46] Petersen, M. A., Nielsen, I. B., Kristensen, M. B., Kadziola, A., Lammich, L., Andersen, L. H., and Brøndsted Nielsen, M. *Org. Biomol. Chem.* **4**, 1546 (2006).

[47] Nielsen, I. B., Lammich, L., and Andersen, L. H. *Phys. Rev. Lett.* **96**, 018304 (2006).

[48] Andersen, L. H., Lapierre, A., Brøndsted Nielsen, S., Nielsen, I. B., Pedersen, S. U., Pedersen, U. V., and Tomita, S. *Eur. Phys. J. D* **20**, 597 (2002).

[49] Boye, S. V., Nielsen, I. B., Brøndsted Nielsen, S., Krogh, H., Lapierre, A., Pedersen, H. B., Pedersen, S. U., Pedersen, U. V., and Andersen, L. H. *J. Chem. Phys.* **119**, 338 (2003).

[50] McQueen, P. D., Sagoo, S., Yao, H., and Jockusch, R. A. *Angew. Chem. Int. Ed.* **49**, 9193 (2010).

[51] Marian, C., Nolting, D., and Weinkauf, R. *Phys. Chem. Chem. Phys.* **7**, 3306 (2005).

[52] Cheong, N. R., Nam, S. H., Park, H. S., Ryu, S., Song, J. K., Park, S. M., Perot, M., Lucas, B., Barat, M., Fayeton, J. A., and Jouvet, C. *Phys. Chem. Chem. Phys.* **13**, 291 (2011).

[53] Rocha-Rinza, T., Christiansen, O., Rajput, J., Gopalan, A., Rahbek, D. B., Andersen, L. H., Bochenkova, A. V., Granovsky, A. A., Bravaya, K. B., Nemukhin, A. V., Christiansen, K. L., and Brøndsted Nielsen, M. *J. Phys. Chem. A* **113**, 9442 (2009).

[54] Rajput, J., Rahbek, D. B., Aravind, G., and Andersen, L. H. *Biophys. J.* **98**, 488 (2010).

[55] Freiser, B. S. and Beachamp, J. L. *J. Am. Chem. Soc.* **98**, 3136 (1976).

[56] Alata, I., Dedonder, C., Broquier, M., Marceca, E., and Jouvet, C. *J. Am. Chem. Soc.* **132**, 17483 (2010).

[57] Kirketerp, M.-B. S., Petersen, M. Å., Wanko, M., Espinosa Leal, L. A., Zettergren, H., Raymo, F. M., Rubio, A., Brøndsted Nielsen, M., and Brøndsted Nielsen, S. *ChemPhysChem* **10**, 1207 (2009).

[58] Kirketerp, M.-B. S., Petersen, M. Å., Wanko, M., Zettergren, H., Rubio, A., Brøndsted Nielsen, M., and Brøndsted Nielsen, S. *ChemPhysChem* **11**, 2495 (2010).

[59] Kirketerp, M.-B. S., Petersen, M. Å., Wanko, M., Espinosa Leal, L. A., Zettergren, H., Raymo, F. M., Rubio, A., Brøndsted Nielsen, M., and Brøndsted Nielsen, S. *In preparation* .

[60] Rocha-Rinza, T., Christiansen, O., Rahbek, D. B., Klærke, B., Andersen, L. H., Lincke, K., and Brøndsted Nielsen, M. *Chem. Eur. J.* **16**, 11977 (2010).

[61] Ryhding, T., Kirketerp, M.-B. S., Kadhane, U., Lykkegaard, M. K., Panja, S., Brøndsted Nielsen, S., and Brøndsted Nielsen, M. *Tetrahedron* **64**, 11475 (2008).

[62] Kang, H., Dedonder-Lardeux, C., Jouvet, C., Martrenchard, S., Gregoire, G., Desfrancois, C., Schermann, J. P., Barat, M., and Fayeton, J. A. *Phys. Chem. Chem. Phys.* **6**, 2628 (2004).

[63] Lucas, B., Barat, M., Fayeton, J. A., Perot, M., Jouvet, C., Gregoire, G., and Brøndsted Nielsen, S. *J. Chem. Phys.* **128**, 164302 (2008).

[64] Gregoire, G., Lucas, B., Barat, M., Fayeton, J. A., Dedonder-Lardeux, C., and Jouvet, C. *Eur. Phys. J. D* **51**, 109 (2009).

[65] Lepere, V., Lucas, B., Barat, M., Fayeton, J. A., Picard, V. J., Jouvet, C., Carcabal, P., Nielsen, I., Dedonder-Lardeux, C., Gregoire, G., and Fujii, A. *J. Chem. Phys.* **127**, 134313 (2007).

[66] Mercier, S. R., Boyarkin, O. V., Kamariotis, A., Guglielmi, M., Tavernelli, I., Cascella, M., Rothlisberger, U., and Rizzo, T. R. *J. Am. Chem. Soc.* **128**, 16938 (2006).

[67] Alata, I., Omidyan, R., Dedonder-Lardeux, C., Broquier, M., and Jouvet, C. *Phys. Chem. Chem. Phys.* **11**, 11479 (2009).

[68] Fujihara, A., Noguchi, N., Yamada, Y., Ishikawa, H., and Fuke, K. *J. Phys. Chem. A* **113**, 8169–8175 (2009).

[69] Fujihara, A., Matsumoto, H., Shibata, Y., Ishikawa, H., and Fuke, K. *J. Phys. Chem. A* **112**, 1457–1463 (2008).

[70] Ehlerding, A., Wyer, J. A., Zettergren, H., Kirketerp, M.-B. S., and Brøndsted Nielsen, S. *J. Phys. Chem. A* **114**, 299 (2010).

[71] Kadhane, U., Andersen, J. U., Ehlerding, A., Hvelplund, P., Kirketerp, M.-B. S., Lykkegaard, M. K., Brøndsted Nielsen, S., Panja, S., Wyer, J. A., and Zettergren, H. *J. Chem. Phys.* **129**, 184304 (2008).

[72] Kadhane, U., Pérot, M., Lucas, B., Barat, M., Fayeton, J. A., Jouvet, C., Ehlerding, A., Kirketerp, M.-B. S., Brøndsted Nielsen, S., Wyer, J. A., and Zettergren, H. *Chem. Phys. Lett.* **480**, 57 (2009).

[73] Wyer, J. A., Ehlerding, A., Zettergren, H., Kirketerp, M.-B. S., and Brøndsted Nielsen, S. *J. Phys. Chem. A* **113**, 9277 (2009).

[74] Compagnon, I., Allouche, A.-R., Bertorelle, F., Antoine, R., and Dugourd, P. *Phys. Chem. Chem. Phys.* **12**, 3399 (2010).

[75] Nielsen, I. B., Petersen, M. Å., Lammich, L., Brøndsted Nielsen, M., and Andersen, L. H. *J. Phys. Chem. A* **110**, 12592 (2006).

[76] Lammich, L., Petersen, M. Å., Brøndsted Nielsen, M., and Andersen, L. H. *BioPhys J.* **92**, 201 (2007).

[77] Kirketerp, M.-B. S., Ryhding, T., Støchkel, K., Nielsen, M. B., and Nielsen, S. B. *J. Phys. Chem. A* **115**, 1222 (2011).

[78] Kirketerp, M.-B. and Brøndsted Nielsen, S. *Int. J. Mass Spectrom.* **297**, 63 (2010).

[79] Spence, T. G., Trotter, B. T., and Posey, L. A. *J. Phys. Chem. A* **102**, 7779 (1998).

[80] Spence, T. G., Trotter, B. T., Burns, T. D., and Posey, L. A. *J. Phys. Chem. A* **102**, 6101 (1998).

[81] Hansen, C. N., Kirketerp, M.-B. S., Kristensen, M. B., Nielsen, S. B., Støchkel, K., and Wyer, J. A. *Chem. Phys. Lett.* **502**, 53 (2011).

[82] Löffler, D., Weber, J. M., and Kappes, M. M. *J. Chem. Phys.* **123**, 224308 (2005).

[83] Marcum, J. C. and Weber, J. M. *J. Chem. Phys.* **131**, 194309 (2009).

[84] Antoine, R., Bertorelle, F., Broyer, M., Compagnon, I., Dugourd, P., Kulesza, A., Mitric, R., and Bonacic-Koutecky, V. *Angew. Chem., Int. Ed.* **48**, 7829 (2009).

[85] Antoine, R., Tabarin, T., Broyer, M., Dugourd, P., Mitric, R., and Bonacic-Koutecky, V. *ChemPhysChem* **7**, 524 (2006).

[86] Tabarin, T., Antoine, R., Broyer, M., and Dugourd, P. *Eur. Phys. J. D* **52**, 191 (2009).

[87] Tabarin, T., Kulesza, A., Antoine, R., Mitric, R., Broyer, M., Dugourd, P., and Bonacic-Koutecky, V. *Phys. Rev. Lett.* **101**, 213001 (2008).

[88] Gouterman, M. *The Porphyrins, Volume III, Physical Chemistry, Part A,* , ed. D. Dolphin, Academic Press (1978).

[89] Wyer, J. A., Jensen, C. S., and Brøndsted Nielsen, S. *Submitted* .

[90] Lykkegaard, M. K., Ehlerding, A., Hvelplund, P., Kadhane, U., Kirketerp, M.-B. S., Brøndsted Nielsen, S., Panja, S., Wyer, J. A., and Zettergren, H. *J. Am. Chem. Soc.* **130**, 11856 (2008).

[91] Wyer, J. A. and Brøndsted Nielsen, S. *J. Chem. Phys.* **133**, 084306 (2010).

[92] Lykkegaard, M. K., Zettergren, H., Kirketerp, M.-B. S., Ehlerding, A., Wyer, J. A., Kadhane, U., and Brøndsted Nielsen, S. *J. Phys. Chem. A* **113**, 1440 (2009).

[93] Nielsen, L. M., Pedersen, S. Ø., Kirketerp, M.-B. S., and Brøndsted Nielsen, S. *Submitted* .

[94] Støchkel, K., Wyer, J. A., Kirketerp, M.-B. S., and Brøndsted Nielsen, S. *J. Am. Soc. Mass Spectrom.* **21**, 1884 (2010).

[95] Schmidt, H. T., Johansson, H. A. B., Thomas, R. D., Geppert, W. D., Haag, N., Reinhed, P., Rosen, S., Larsson, M., Danared, H., Rensfelt, K. G., Liljeby, L., Bagge, L., Bjorkhage, M., Blom, M., Lofgren, P., Kallberg, A., Simonsson, A., Paal, A., Zettergren, H., and Cederquist, H. *Int. J. Astrobio.* **7**, 205 (2008).

[96] Brøndsted Nielsen, S., Andersen, J. U., Hvelplund, P., Liu, B., and Tomita, S. *J. Phys. B: At. Mol. Opt. Phys.* **37**, R25 (2004).

[97] Wyer, J. A., Feketeova, L., Brøndsted Nielsen, S., and O'Hair, R. A. J. *Phys. Chem. Chem. Phys.* **11**, 8752 (2009).

[98] Bernigaud, V., Drenck, K., Huber, B. A., Hvelplund, P., Jabot, T., Kadhane, U., Kirketerp, M.-B. S., Liu, B., Lykkegaard, M. K., Manil, B., and Brøndsted Nielsen, S. *J. Am. Soc. Mass Spectrom.* **19**, 809 (2008).

[99] Støchkel, K., Kadhane, U., Andersen, J. U., Holm, A. I. S., Hvelplund, P., Kirketerp, M.-B. S., Larsen, M. K., Lykkegaard, M. K., Brøndsted Nielsen, S., Panja, S., and Zettergren, H. *Rev. Sci. Instrum.* **79**, 023107 (2008).

[100] Sunden, A. E. K., Støchkel, K., Panja, S., Kadhane, U., Hvelplund, P., Brøndsted Nielsen, S., Zettergren, H., Dynefors, B., and Hansen, K. *J. Chem. Phys.* **130**, 224308 (2009).

[101] Andersen, J. U., Hvelplund, P., Brøndsted Nielsen, S., Tomita, S., Wahlgreen, H., Møller, S. P., Pedersen, U. V., Forster, J. S., and Jørgensen, T. J. D. *Rev. Sci. Instrum.* **73**, 1284 (2002).

[102] Nielsen, K. O. *Nucl. Instum. Methods* **1**, 289 (1957).

[103] Gerlich, D. *J. Chem. Soc., Faraday Trans.* **89**, 2199–2208 (1993).

[104] Gerlich, D. *Phys. Scripta* **T59**, 256–263 (1995).

[105] Møller, S. *Nucl. Instrum. Methods Phys. Res., Sect. A* **394**, 281 (1997).

[106] Tanabe, T., Chida, K., Noda, K., and Watanabe, I. *Nucl. Instrum. Methods A* **482**, 595 (2002).

[107] Jinno, S., Takao, T., Omata, Y., Satou, A., Tanuma, H., Azuma, T., Shiromaru, H., Okuno, K., Kobayashi, N., and Watanabe, I. *Nucl. Instrum. Methods A* **532**, 477 (2004).

[108] Jinno, S., Takao, T., Hanada, K., Goto, M., Okuno, K., Tanuma, H., Azuma, T., and Shiromaru, H. *Nucl. Instrum. Methods A* **572**, 568 (2007).

[109] Bernard, J., Montagne, G., Bredy, R., Terpend-Ordaciere, B., Bourgey, A., Kerleroux, M., Chen, L., Schmidt, H. T., Cederquist, H., and Martin, S. *Rev. Scient. Instum.* **79**, 075109 (2008).

[110] Bredy, R., Bernard, J., Chen, L., Montagne, G., Li, B., and Martin, S. *J. Phys. B* **42**, 154023 (2009).

[111] Stiebing, K. E., Alexandrov, V., Doerner, R., Enz, S., Kazarinov, N. Y., Kruppi, T., Schempp, A., Boecking, H. S., Voelp, M., Ziel, P., Dworak, M., and Dilfer, W. *Nucl. Instrum. Methods A.* **614**, 10 (2010).

[112] Zajfman, D., Wolf, A., Schwahn, D., Orlov, D. A., Grieser, M., von Hahn, R., Welsch, C. P., Lopez-Urrutia, J. R. C., Schroter, C. D., Urbain, X., and Ullrich, J. *J. Phys.: Conf. Ser.* **4**, 296 (2005).

[113] Andersen, J. U., Cederquist, H., Forster, J. S., Huber, B. A., Hvelplund, P., Jensen, J., Liu, B., Manil, B., Maunoury, L., Brøndsted Nielsen, S., Pedersen, U. V., Rangama, J., Schmidt, H. T., Tomita, S., and Zettergren, H. *Phys. Chem. Chem. Phys.* **6**, 2676 (2004).

[114] Calvo, M. R., Andersen, J. U., Hvelplund, P., Brøndsted Nielsen, S., Pedersen, U. V., Rangama, J., Tomita, S., and Forster, J. S. *J. Chem. Phys.* **120**, 5067 (2004).

[115] Andersen, J. U., Cederquist, H., Forster, J. S., Huber, B. A., Hvelplund, P., Jensen, J., Liu, B., Manil, B., Maunoury, L., Brøndsted Nielsen, S., Pedersen, U. V., Schmidt, H. T., Tomita, S., and Zettergren, H. *Eur. Phys. J. D* **25**, 139 (2003).

[116] Nielsen, S. B., Andersen, J. U., Forster, J. S., Hvelplund, P., Liu, B., Pedersen, U. V., and Tomita, S. *Phys. Rev. Lett.* **91**, 048302 (2003).

Publications

Publications listed in the order of appearance in this thesis. The articles are attached in the following.

(I) Near-infrared photoabsorption by C_{60} dianions in a storage ring, *J. Chem. Phys.* **131** 014301 (2009)

(II) On the Intrinsic Optical Absorption by Tetrathiafulvalene Radical Cations and Isomers, *Chem. Commun.* **47** 6900 (2011)

(III) Absorption Spectra of 4-Nitrophenolate Ions Measured *in Vacuo* and in Solution, *ChemPhysChem* **10** 1207 (2009)

(IV) Double-Bond versus Triple-Bond Bridges: Does it Matter for the Charge-Transfer Absorption by Donor-Acceptor Chromophores?, *ChemPhysChem* **11** 2495 (2010)

(V) Upon the intrinsic optical properties of oligo(*p*-phenyleneethynylene)s (OPEs). Synthesis of OPE3 for experimental gas-phase absorption studies, *Tetrahedron* **64** 11475 (2008)

(VI) UV Photodissociation of Protonated Gly-Trp and Trp-Gly Dipeptides and Their Complexes with Crown Ether in an Electrostatic Ion Storage Ring, *J. Phys. Chem. A* **114** 299 (2010)

(VII) Photodissociation of protonated tryptophan and alteration of dissociation pathways by complexation with crown ether, *J. Chem. Phys.* **129** 184304 (2008)

(VIII) Photodissociation of protonated tryptamine and its supramolecular complex with 18-crown-6-ether: Dissociation times and channels, absorption spectra, and excited state calculations, *Chem. Phys. Lett.* **480** 57 (2009)

(IX) Tagging of protonated Ala-Tyr and Tyr-Ala by Crown Ether Prevents Direct Hydrogen Loss and Proton Mobility after Photoexcitation: Importance for Gas-Phase Absorption Spectra, Dissociation Lifetimes, and Channels, *J. Phys. Chem. A* **113** 9277 (2009)

(X) Role of Nearby Charges on the Electronic Structure of π-Conjugated Molecules: Symmetric versus Asymmetric Charge Distributions in Oligo(p-phenyleneethynylene), *J. Phys. Chem. A* **115** 1222 (2011)

(XI) Absorption spectrum of isolated tris(2,2´-bipyridine)ruthenium(II) dications *in vacuo*, *Int. J. Mass Spectrom.* **297** 63 (2010)

(XII) On the stability of isolated $Pt(SCN)_4^{2-}$ dianions *in vacuo* and action spectroscopy experiments, *Chem. Phys. Lett.* **502** 53 (2011)

(XIII) A Soret Marker Band for Four-Coordinate Ferric Heme Proteins from Absorption Spectra of Isolated Fe(III)-Heme$^+$ and Fe(III)-Heme$^+$(His) Ions *in Vacuo J. Am. Chem. Soc.* **130** 11857 (2008)

(XIV) Photodissociation of Isolated Ferric Heme and Heme-His Cations in an Electrostatic Ion Storage Ring, *J. Phys. Chem. A* **113** 1440 (2009)

(XV) Absorption by DNA single strands of adenine isolated in vacuo: The role for multiple chromophores, *Submitted*

(XVI) Laser Pump-Probe Experiments on Microsecond to Millisecond Timescales at an Electrostatic Ion Storage Ring: Triplet-Triplet Absorption by Protoporphyrin-IX Anions, *J. Am. Soc. Mass Spectrom.* **21** 1884 (2010)

(XVII) A new technique for time-resolved daughter ion mass spectrometry on the microsecond to millisecond time scale using an electrostatic ion storage ring, *Rev. Sci. Instrum.* **79** 023107 (2008)

Articles not presented or referred to throughout this thesis:

(XVIII) Dianions of 7,7,8,8-tetracyano-p-quinodimethane and perfluorinated tetracyanoquinodimethane: Information on excited states from lifetime measurements in an electrostatic storage ring and optical absorption spectroscopy, *J. Chem. Phys.* **127** 124301 (2007)

(XIX) Electron-Capture-Induced Dissociation of Protoporphyrin IX Ions, *J. Am. Soc. Mass Spectrom.* **19** 809 (2008)

(XX) Unimolecular Dissociation of Anthracene and Acridine Cations - The C2H2 Loss and HCN Loss Channels, *Submitted*

Near-infrared photoabsorption by C_{60} dianions in a storage ring

U. Kadhane,[1,a] J. U. Andersen,[1,b] E. Bonderup,[1] B. Concina,[1] P. Hvelplund,[1] M.-B. Suhr Kirketerp,[1] B. Liu,[1] S. Brøndsted Nielsen,[1] S. Panja,[1] J. Rangama,[1] K. Støchkel,[1] S. Tomita,[1] H. Zettergren,[1] K. Hansen,[2] A. E. K. Sundén,[2] S. E. Canton,[3] O. Echt,[4] and J. S. Forster[5]

[1]*Department of Physics and Astronomy, Aarhus University, DK-8000 Aarhus C, Denmark*
[2]*Department of Physics, University of Gothenburg, SE-41296 Göteborg, Sweden*
[3]*Department of Chemical Physics, Lund University, SE-22100 Lund, Sweden*
[4]*Department of Physics, University of New Hampshire, Durham, New Hampshire 03824, USA*
[5]*Department of Physics, University of Montreal, H3C 3J7 Quebec, Canada*

(Received 23 February 2009; accepted 14 May 2009; published online 1 July 2009)

We present a detailed study of the electronic structure and the stability of C_{60} dianions in the gas phase. Monoanions were extracted from a plasma source and converted to dianions by electron transfer in a Na vapor cell. The dianions were then stored in an electrostatic ring, and their near-infrared absorption spectrum was measured by observation of laser induced electron detachment. From the time dependence of the detachment after photon absorption, we conclude that the reaction has contributions from both direct electron tunneling to the continuum and vibrationally assisted tunneling after internal conversion. This implies that the height of the Coulomb barrier confining the attached electrons is at least ~1.5 eV. For C_{60}^{2-} ions in solution electron spin resonance measurements have indicated a singlet ground state, and from the similarity of the absorption spectra we conclude that also the ground state of isolated C_{60}^{2-} ions is singlet. The observed spectrum corresponds to an electronic transition from a t_{1u} lowest unoccupied molecular orbital (LUMO) of C_{60} to the t_{1g} LUMO+1 level. The electronic levels of the dianion are split due to Jahn–Teller coupling to quadrupole deformations of the molecule, and a main absorption band at 10723 cm^{-1} corresponds to a transition between the Jahn–Teller ground states. Also transitions from pseudorotational states with 200 cm^{-1} and (probably) 420 cm^{-1} excitation are observed. We argue that a very broad absorption band from about 11 500 cm^{-1} to 13 500 cm^{-1} consists of transitions to so-called cone states, which are Jahn–Teller states on a higher potential-energy surface, stabilized by a pseudorotational angular momentum barrier. A previously observed, high-lying absorption band for C_{60}^{-} may also be a transition to a cone state. © *2009 American Institute of Physics*. [DOI: 10.1063/1.3149775]

I. INTRODUCTION

Fullerene anions are of broad interest, e.g., in high-T_c superconductivity[1,2] and molecular electronics.[3,4] In the dianions, the second electron is confined by a Coulomb barrier,[5] and fullerenes are ideal for studies of the dependence of the stability on the size of the dianion.[6] The dominant decay mode is electron tunneling through the Coulomb barrier, analogous to nuclear alpha decay, and the lifetime can be long even for negative binding.

Information on the level structure can be obtained from optical spectroscopy, and C_{60}^{2-} is of special interest because of the competition between Coulomb repulsion between the two electrons and Jahn–Teller (JT) coupling to quadrupole distortions of the highly symmetric C_{60} cage (icosahedral symmetry).[7–9] The interest in this problem has been stimulated by the discovery of superconductivity in alkali fullerides at relatively high temperatures.[1] The electron pairing leading to superconductivity is believed to originate in the JT coupling.[2,10,11]

In accordance with Hund's rules, the Coulomb energy is lowest in the triplet states, but the JT effect is strongest in the singlet state. Measurements on dianions in frozen solution indicate a singlet ground state with a close-lying triplet level,[12,13] but the delicate balance between Coulomb repulsion and JT coupling could be influenced by interactions with the matrix. Gas-phase measurements are needed as a benchmark for theory.

Owing to the weak binding of the second electron it is difficult to produce long lived dianions of C_{60}, but we have developed a method for production of intense beams of C_{60}^{-} ions and cold electron attachment to the monoanions in a Na vapor cell.[14] Subsequent storage in an electrostatic ring has allowed detailed studies of the stability of C_{60}^{2-} ions.[15] We concluded that the dianions are metastable in the ground state, with a lifetime of about 20 s (at $T=0$ K) and an energy of about 0.2 eV above that of the monoanion plus a free electron. Results of near-infrared laser spectroscopy on stored dianions are presented here.

[a]Present address: Department of Physics, Indian Institute of Technology, Madras, Chennai 600036, India.
[b]Electronic mail: jua@phys.au.dk.

II. EXPERIMENTAL DETAILS

The experiments were carried out at the electrostatic storage ring ELISA illustrated in Fig. 1.[16,17] Previously,[15] we used an electrospray source to produce a beam of C_{60}^- ions, but the electrospray is very unstable for fullerene anions. We have therefore constructed a new source based on a plasma source capable of delivering stable nanoampere currents of fullerene anions.[18,19] Hot C_{60}^- ions were extracted from the plasma source and focused by an Einzel lens into a 14-pole linear ion trap with a He trapping gas, which could be cooled to a temperature below 100 K by liquid nitrogen in a container around the trap. The ions were accumulated and stored for 0.1 s and then ejected as a 20–50 μs long bunch. After acceleration to 22 keV and mass selection with a magnet, the ions passed through a cell containing Na vapor, where dianions were formed by electron transfer. These ions were then stored in the ring with revolution time 108.15 μs.

For C_{60} anions in solution or in a solid matrix there are often several charge states present, and it can be difficult to separate their contributions to the absorption. Below we discuss a case where a feature of absorption in the dianion has been ascribed to the monoanion. In our experiment, the ring voltages select a single charge state but the beam could contain dianions of C_{60} isomers. Such a contamination was observed in Ref. 15 as a very small stable component. It is very likely that it consisted of ions with lower symmetry of the C_{60} cage structure (with pairs of adjacent pentagons). As shown in Ref. 20, such molecules have higher electron affinities and therefore should be more stable as dianions. Lifetime measurements with the new ion source have confirmed that the stable component is far too small to give a significant contribution to the absorption spectrum.

The laser used for spectroscopy was an optical parametric oscillator (OPO) pumped with third harmonic radiation from a Nd-doped yttrium-aluminum garnet laser with a pulse energy of about 1 mJ and a pulse length of 3 ns. The intensity profile of the laser is smooth, and the direction of the laser beam varies very little with wavelength, so the overlap with the ion beam could be kept constant in wavelength scans. Some lifetime measurements were made with a pulsed alexandrite laser with about 5 mJ pulse energy and a pulse length of 10 ns.

The near-infrared absorption spectrum was measured by detection of monoanions produced by electron autodetachment after absorption of a photon from a laser pulse. The monoanions were detected with a channeltron placed close to the beam after a 10° deflection (Fig. 1). The laser was fired when the bunch of stored ions was about 1.5 m in front of the detector after a variable number of ion revolutions in the ring.

III. LIFETIMES

The stored dianions are unstable, and their decay by electron detachment was monitored by detection of monoanions in the channeltron.[15] After photon absorption the yield is strongly enhanced, and the time dependence of the enhancement is shown in Fig. 2 for three wavelengths. The first point of the time spectra corresponds to detachment within the first

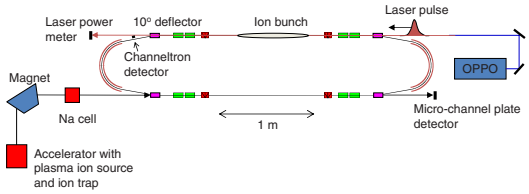

FIG. 1. Sketch of the electrostatic storage ring ELISA.

~20 μs, and the following points show the weaker enhancement after one or more revolutions of the ions in the ring. The points fall on straight lines in the semilog plot, consistent with exponential decay with the lifetimes indicated in the figure caption, except for the first point, which is too high by nearly an order of magnitude.

Internal conversion of electronic to vibrational excitation is known to take place on a subnanosecond time scale,[21,22] so the electron detachment observed after one or more revolutions of the beam must be due to a statistical process, i.e., vibrationally assisted electron tunneling. According to our modeling of the decay (see Fig. 7 in Ref. 15), the spectrum of microcanonical temperatures in the ensemble of ions ranges from below 100 to about 300 K, with an average temperature of about 200 K, for a trap temperature of 100 K and after storage for 10–16 ms in the ring. The spectrum after photon absorption and internal conversion is shifted to higher temperatures, with average values of about 490, 480, and 450 K for 735, 785, and 935 nm, and as demonstrated by the data in Fig. 2, the distributions in microcanonical temperature (or energy) are sufficiently narrow to give exponential decay. (When the variation in the rate constant over the energy distribution is large, the decay function is closer to a $1/t$ dependence, and the ions decaying at time t have a rate constant of $\sim 1/t$.)[23]

The high decay rate at very short times seen in Fig. 2 indicates that there is a competing process with very short lifetime, which we interpret as direct tunneling of the excited electron into the continuum (see also Ref. 24). With an estimated detection efficiency that is a factor of three higher for prompt decay than for delayed statistical decay, the probability for prompt decay is found to be about 0.4 with no significant dependence on photon energy. Note that the lifetime for direct tunneling is expected not to vary much with photon energy since the excited electronic state is the same at all photon energies.

Thus the lifetimes for direct tunneling from the excited state and for internal conversion of electronic to vibrational energy are found to be very similar. This is consistent with simple estimates of the lifetimes. For the monoanion C_{60}^-, the lifetime of an excited t_{1g} state has been measured to be 2.2 ps.[22] It may be expected to be somewhat shorter for the dianion partly because the excitation energy is about 10% higher and partly because the coupling to H_g vibrations is stronger than in the monoanion.[22] The excited state energy of about 1.5 eV is close to the maximum of the Coulomb barrier, about 1.7 eV,[15,25] so the decay rate is not much reduced by the barrier penetration. The attempt frequency used in the modeling was $\nu = 3 \times 10^{13}$ s^{-1}, and with an estimated

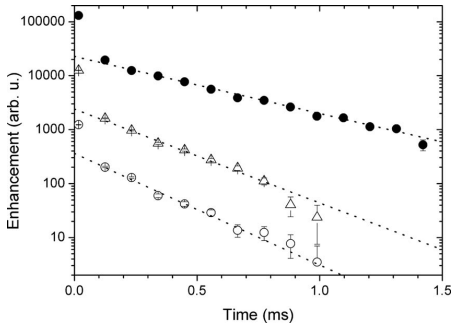

FIG. 2. Decay of stored C_{60}^{2-} ions after absorption of a photon. The lower two time spectra are for photons from the alexandrite laser with (○) 735 nm and (△) 785 nm wavelengths absorbed at 15.5 ms after ion injection, and the upper spectrum (●) is for 935 nm photons from the OPO laser absorbed at 10.8 ms after injection. For all spectra the trap was cooled to a temperature below 100 K. The separation of the points is the revolution time in the ring. The dotted lines are fitted exponential decays with lifetimes of 0.21 ms (735 nm), 0.25 ms (785 nm), and 0.41 ms (935 nm).

penetration probability of 0.2 one obtains a lifetime of order 0.2 ps. The uncertainty on this estimate is rather large, but the lifetimes for the two competing processes are clearly expected to be of the same order of magnitude.

In the modeling in Ref. 15 of the decay of the C_{60}^{2-} ions in the storage ring, the internal energy of the ions decaying at the shortest times was estimated on the basis of lifetime measurements in preliminary laser experiments. However, at the time we did not realize that there is a contribution from direct tunneling to the decay after photon absorption, and therefore the rate constant for statistical decay after internal conversion was overestimated by an order of magnitude. The implication is that the tail of the internal energy spectrum toward higher energies is even more pronounced than assumed in the modeling. The tail is produced partly by collisions with residual gas molecules just after extraction from the ion trap partly by electron transfer to excited states in the Na cell. This modification has no influence on the modeling of the decay of the ion ensemble at later times.

IV. ABSORPTION SPECTRA

From the variation with wavelength of the enhancement of the C_{60}^{-} signal normalized to the number of photons, the absorption spectrum was obtained. In Fig. 3 results are compared with absorption spectra for dianions in solution. All spectra have a main absorption band near 10 600 cm^{-1}, which is better resolved at the lower temperatures. The peak is at 10 723 cm^{-1} in the gas-phase spectra with 3 cm^{-1} subtracted for the Doppler shift. The general shape of our spectra is similar to the spectrum for C_{60}^{2-} in benzonitrile at room temperature apart from broadening and a small redshift in the solution. Very similar spectra were also observed in Refs. 28 and 13, where the singlet character of the ground state was established from measurements of electron spin resonance. As discussed below, the JT interaction is quite different in the triplet states, so the close similarity of the spectra indicates that the ground state is singlet also in the gas phase.

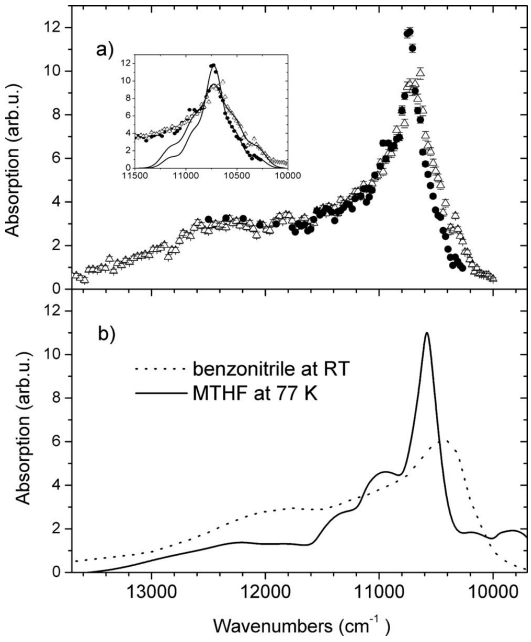

FIG. 3. (a) Absorption spectra for $T_{trap} \simeq 300$ K (△) and $T_{trap} \lesssim 100$ K (●) with delays between ion injection and laser pulse set to 10.8 and 32 ms, respectively. The inset shows the peak region with fits discussed in the text. (b) Absorption spectra for C_{60}^{2-} ions in MTHF at 77 K (Ref. 26) and in benzonitrile at room temperature (Ref. 27).

The simplest interpretation of the spectra is a transition from the t_{1u} lowest unoccupied molecular orbital (LUMO) level of C_{60} to the t_{1g} LUMO+1 level, both triply degenerate. The notation refers to subgroups of the icosahedral point group, but we may think of *p*-type orbitals with odd and even symmetries, respectively. For the interpretation it is very helpful to compare with the gas-phase absorption spectrum for the monoanion shown in Fig. 4. As for the dianion, there is a main absorption band, redshifted in solution. There are sidebands from vibrational excitation because the equilibrium deformation is different in the initial and final states, and similar bands should be contained in the broad tail toward higher energies in the spectrum for the dianion. Even stronger sidebands are observed in photodetachment from monoanions with a UV laser, where there is no distortion in the final (neutral) state of the molecule.[31,32]

A. JT coupling

To interpret the C_{60}^{2-} spectra in more detail we first consider the JT coupling in the initial $(t_{1u})^2$ electronic configuration.[7,8] The main JT interaction is with the eight H_g vibrations illustrated in Fig. 5. (We ignore the interaction with two A_g vibrations, which do not contribute to the JT splitting.) For triplet states, the JT problem is identical to the one for a single electron, but in the singlet ground state, with two electrons in the same orbital, the JT coupling is twice as strong as in the monoanion. As discussed above, we may assume that the electronic state is singlet. The orbital trans-

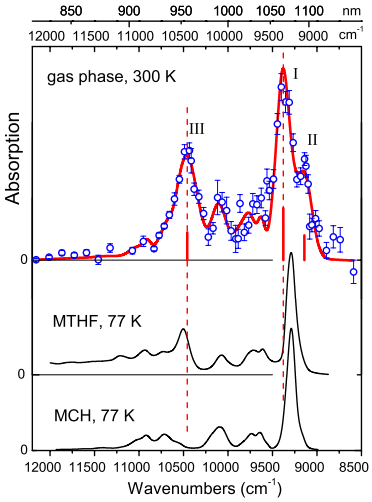

FIG. 4. Absorption spectra for C_{60}^- in the gas phase at ≃300 K (top) (Ref. 21), in a MTHF matrix at 77 K (middle) (Ref. 29), and in methylcyclohexane at 77 K (bottom) (Ref. 30).

forms as a vector under rotations in three dimensions; in the adiabatic approximation, the electron orbitals and the deformation are strongly coupled and rotate together, and the most important low-energy excitations correspond to such so-called pseudorotations of the molecule.

For linear JT coupling, the energy eigenstates have a well-defined pseudo-angular-momentum $L\hbar$ and symmetry requires L to be even. The pseudorotational energy is given by

$$E_{\mathrm{rot}}(L) = \frac{L(L+1)}{24k^2}, \tag{1}$$

in units of a weighted average of the energies of the H_g vibrations involved in the JT distortion. The effective moment of inertia is proportional to the square of the deformation, and since the equilibrium value of the deformation in the singlet ground state is twice as large as for the monoanion, the denominator in Eq. (1) is four times as large as in the corresponding formula for C_{60}^- [Eq. 2 in Ref. 21]. From an analysis of a photoelectron spectrum for C_{60}^-,[31] the average vibrational energy was estimated to be $\hbar\omega_0 \simeq 600$ cm^{-1}, and the value of $k^2 \simeq 2.4$ was obtained for the square of the JT-coupling parameter. As in Ref. 21 we shall use the value of $k^2 \sim 2$ in estimates of JT energies, and the two lowest excited levels are then at 75 cm^{-1} (L=2) and 250 cm^{-1} (L=4).

In the excited electronic state one electron is in a t_{1g} orbital, for which the JT coupling constant is similar in magnitude but has the opposite sign. The minimum of the total JT energy is therefore obtained for a so-called bimodal deformation, which is the same as that of the ground state of C_{60}^{3-} discussed in Refs. 7 and 8. The Hamiltonian is that of a symmetric top, and the energy depends on the total pseudo-angular-momentum $L\hbar$ and its projection $K\hbar$ on the symmetry axis,

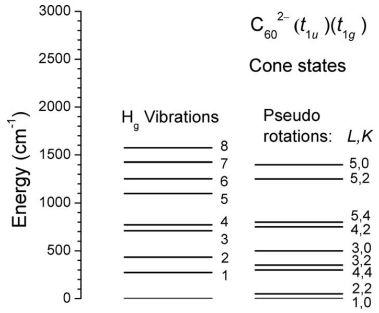

FIG. 5. To the left are indicated the energies of the eight H_g vibrations in C_{60} and to the right are energies from Eq. (2) of JT states of C_{60}^{2-} in the excited electronic state $(t_{1u})(t_{1g})$ relative to the energy of the lowest state, $(L,K)=(1,0)$.

$$E_{\mathrm{rot}}(L,K) = \frac{1}{6k^2}\left(L(L+1) - \frac{3}{4}K^2\right), \tag{2}$$

with the units in Eq. (1). Symmetry requires K to be even and K=0 is only allowed for odd L. Energy levels are shown in Fig. 5. We note that the rotational constant in Eq. (2) is the same as for pseudorotations of the monoanion.[21]

B. Interpretation of spectra

We now turn to the interpretation of the spectra in Fig. 3(a) and first consider the region close to the main peak, shown in detail in the inset. The region of the peak and the slope toward lower energies are fitted with three Gaussians, a main band at 10 723 cm^{-1} and weaker bands at 10 523 and 10 303 cm^{-1} with standard deviations of σ=80 cm^{-1} and σ=90 cm^{-1} for the two spectra. To aid the discussion, we have added symmetrically two Gaussians at higher energies. The two spectra in Fig. 3(a) are recorded for ions with different distributions in internal energy. From modeling as described in Ref. 15 the average microcanonical temperatures are estimated to be of the order of 200 and 300 K. The peak at 10 523 cm^{-1} cannot be a sideband with destruction of a vibrational excitation since there should then be a symmetrically placed sideband for vibrational excitation with much higher intensity. The natural interpretation is that this peak is a transition from an excited pseudorotational state to the same final state, $(L,K)=(1,0)$. Relative to the main peak, the heights of the peaks displaced by −200 cm^{-1} are 34% and 58% at 200 and 300 K, respectively, and the relative strength in the two spectra is consistent with this interpretation. Probably the peak at 10 303 cm^{-1} should be interpreted in a similar way.

According to Eq. (1) the excited state at 200 cm^{-1} could be L=4. A dipole transition to $(L,K)=(1,0)$ is not allowed from this level ($|\Delta L| \leq 1$), but there are significant nonlinear effects giving a warping of the JT-potential-energy surface and consequent mixing of states with different L.[7,8] The nonlinearity is not very strong for the monoanion,[8,31] but it must be more pronounced for the singlet ground state of the dianion because the JT coupling is twice as strong. The symmetries of the eigenstates should then be specified under the

icosahedral group, e.g., A_g, H_g, $G_g \oplus H_g$, and $A_g \oplus T_{1g} \oplus G_g \oplus H_g$ instead of $L=0$, $L=2$, $L=4$, and $L=6$, and the selection rules are modified.

As mentioned above, the continuum for photon energies just above the main peak should contain sidebands corresponding to excitations of H_g vibrations that appear because the JT deformation is different in the initial and final electronic states. There may also be transitions to excited pseudorotational states. Note that the two level spectra in Fig. 5 are of a very different nature. The energy levels of H_g vibrations to the left are the spacings in independent harmonic oscillators, while the spectrum to the right is the low-energy part of the complete spectrum of excitations of the three vibrational degrees of freedom converted to pseudorotations.

The vibrations are excited by shake up in the transition, and since the equilibrium deformation in the final electronic state is a compromise between the optimum deformations for the two electrons with opposite signs of JT interaction, the deformation change is not very different from that experienced by C_{60}^- in the corresponding transition. The sidebands seen in the well resolved spectrum at the bottom of Fig. 4 can all be accounted for as single excitations of the H_g vibrations illustrated in Fig. 5. As seen in Fig. 5, it is therefore very unlikely that such bands can account for the absorption at the highest energies. There may be multiple excitations corresponding to overtones of the vibrational frequencies, but they should be weaker.[32]

C. Transitions to cone states

A possible explanation of the strong absorption at high energies is transition to so-called cone states, which are JT states with the opposite sign of the deformation amplitude and positive JT energy.[33–35] In the JT ground state the magnitude of the deformation amplitude q is determined by a balance between the JT force driving the deformation and the harmonic restoring force, but for cone states with the opposite sign of q these forces act together to reduce the magnitude of q. The deformation is instead stabilized by the centrifugal force associated with pseudorotations.

Let us see whether the observation of transitions to final states 2000–3000 cm^{-1} above the lowest JT level for the excited electronic state is consistent with this explanation. The lowest JT energy is of the order of $-(3/2)k^2\hbar\omega_0 \simeq -1800$ cm^{-1}, and since the JT energy of cone states should be positive and there should also be a pseudorotational energy to stabilize the states, the total energies should be higher by at least ~ 3000 cm^{-1}. However, the energy could be somewhat lower if the reversed deformation is stable only for the lower-frequency H_g vibrations. According to the analysis in Ref. 34, the reversed deformation can be stabilized by pseudorotation only if the frequency of rotation is higher than the vibrational frequency.

To estimate the rotation frequency, we use the classical relation $L\hbar = I\omega_r$, where I is the moment of inertia and ω_r is the rotation frequency. The energy is $L(L+1)\hbar^2/2I$ and from a comparison with Eq. (2) with $K=0$, we obtain $I=3k^2\hbar/\omega_0$. Inserting this into the above relation between L and ω_r we obtain $\omega_r/\omega_0 = L/3k^2$. For a vibration with frequency ω the stability requirement $\omega < \omega_r$ then becomes $\omega < (L/3k^2)\omega_0$. With $k^2 \sim 2$, the factor on ω_0 is less than unity except for very large L, and the relation is only fulfilled for the lowest vibrational frequencies in Fig. 5.

However, when we consider the stability of cone states, we should think of the energy as a pseudo-angular-momentum barrier. The moment of inertia is proportional to the square of the deformation amplitude q, and the pseudorotational energy proportional to q^{-2} prevents collapse, $q \to 0$. It therefore seems appropriate to evaluate the stability criterion at a somewhat smaller deformation, say, about half of the equilibrium deformation corresponding to Eq. (2). We should then insert the value of $k^2 \simeq 1/2$ into the stability criterion above, and for $L=3$ we obtain $\omega < 2\omega_0$. This is well fulfilled for the lower-energy vibrations in Fig. 5 but excludes the upper three energies.

From these estimates it appears that transitions to final states with a reversed deformation for only some of the H_g vibrations might be an explanation for the broad high-energy band in the absorption spectra. Admittedly, this assignment is somewhat speculative, and we have not found any theoretical work on such states, except for a remark in Ref. 34. However, the assignment is supported by a strong qualitative argument: the absorption spectrum for the dianion is nearly twice as broad as for the monoanion, while vibrational sidebands and pseudorotational excitations in the final electronic state should be very similar for the two ions. The JT energy is three times larger in the final state for the dianion, but it seems that the only way this energy can come into play is through the Slonczewski mechanism of excitation to states on a higher JT-potential-energy surface.[34]

With the new information on absorption in C_{60}^{2-} we may take a fresh look at the interpretation of the absorption spectra for the monoanion in Fig. 4. The band III in the top spectrum was in Ref. 21, interpreted as a transition from an excited JT state (T_{2u} with a t_{1u} electronic orbital) to a pseudorotational final state with $L=4$ and with a t_{1g} electronic orbital, but the calculated transition energy was about 25% too low. An alternative explanation might be a transition to a cone state. Band III is 1315 cm^{-1} higher in energy than band II, and this separation is about right. Compared with the estimate above for cone states of C_{60}^{2-}, the JT potential energy is lower by a factor of three, while the pseudorotational energies are the same.

The special interpretation of the high-energy part of the absorption spectra for the dianion in Figs. 3(a) and 6 is supported by a comparison with the absorption spectrum in Fig. 3(b) for C_{60}^{2-} ions at 77 K in frozen 2-methyltetrahydrofuran (MTHF). It was obtained from the trace h in Fig. 1 in Ref. 26 after subtraction of a linear background. (At higher irradiation doses there are indications of a small contribution from absorption in trianions.)[36] Apart from the small redshift, the low-energy part of the spectrum is not very different from the gas-phase spectra. The signal below the peak at 10 600 cm^{-1} is due to absorption by monoanions, which extends up to about 11 000 cm^{-1} (Fig. 4, bottom) and explains the steep decrease just above 11 000 cm^{-1}. However, there is also a marked drop in absorption around 11 500 cm^{-1}, and the relative strength of the absorption between 11 600 and

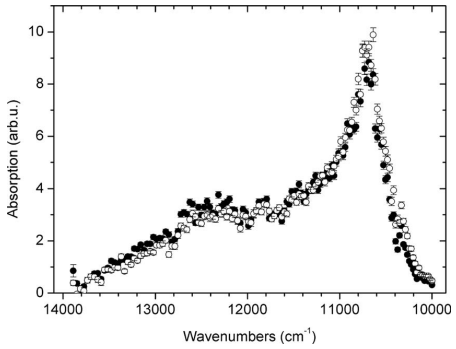

FIG. 6. Photoabsorption by stored C_{60}^{2-} ions at 10.8 ms after ion injection. The trap temperatures were $T_{trap} \simeq 300$ K (open circles) and $T_{trap} \lesssim 100$ K (full circles).

13 600 cm^{-1} is lower by about a factor of two than in benzonitrile at room temperature and in the gas-phase spectra.

The most likely explanation for this difference is the temperature difference. For free ions we see no decrease in the high-energy absorption with decreasing temperature, as indicated in Fig. 3(a) and illustrated in Fig. 6 by a comparison of two complete scans with the same laser delay time but different temperatures of the ion trap. However, if the energy of the lowest five-fold degenerate H_g level relative to the A_g ground state is close to the estimated 75 cm^{-1}, the populations of the two levels are about equal at 77 K. For the gas-phase spectra in Figs. 3 and 6, the average (microcanonical) temperature of the ions is much higher, $T \sim 200-300$ K, and the population of A_g is only $\simeq 17\%$. A very low strength of optical transitions from the JT ground state to cone states could therefore explain the observed reduction in the high-energy part of the MTHF spectrum in Fig. 3(b). This is not unreasonable since, as discussed above, the stabilization of cone states requires a significant pseudo-angular-momentum, and dipole transitions from the A_g ground state may be forbidden.

This explanation of the temperature dependence of the high-energy absorption band for C_{60}^{2-} is analogous to the interpretation in Ref. 21 of the temperature dependence of band III in the top spectrum for the monoanion in Fig. 4. The lowest pseudo-rotational excitation in the electronic ground state is for this case so high that the transition from this excited state to the lowest JT level for the final electronic state is resolved (band II). Neither band II nor band III are observed at 77 K, and it was concluded that band III also corresponds to transitions from the excited state.

Note that the small peak near the position of band III for absorption in an MTHF matrix at 77 K (middle spectrum in Fig. 4) is a contamination from absorption in dianions, and the discussion of this peak in Ref. 21 and in earlier work[8,29] was based on an incorrect assignment. The middle spectrum in Fig. 4 was obtained with the same technique as applied in Ref. 26, where absorbance spectra were recorded for a sequence of γ-irradiation levels with increasing concentration of free electrons. The series of traces in Fig. 1 in Ref. 26 reflects the initial formation of C_{60}^- ions and gradual conversion to dianions. Trace *d* in this series is very similar to the middle spectrum in Fig. 4, and it is clear that the peak near 10 600 cm^{-1} belongs to the dianion spectrum and not to that of the monoanion. At higher irradiation levels, this peak evolves into the main absorption peak in trace *h*, shown as the full-drawn spectrum in Fig. 3(b).

It appears that we have obtained a consistent picture of the near-infrared absorption spectra for the monoanions and dianions of C_{60}, but support from detailed theoretical calculations is needed. In this respect, a recent study of the electronic level density in a C_{60}^- molecule is very interesting.[37] The current through a single C_{60} molecule was measured by scanning-tunneling microscopy (STM) as a function of bias voltage, and for negative bias of the STM tip, the derivative of the current with respect to voltage is proportional to the density of unoccupied levels in the molecule. The main features of the measured spectrum are a sharp main peak and a broad sideband at about 1850 cm^{-1} higher energy.

The measurements are compared with density-functional calculations including JT coupling. The injection of an electron into the C_{60} molecule is the inverse of electron detachment, for example, photoemission.[32] As in the photoelectron spectrum analyzed in Ref. 32 there are sidebands from excitation of vibrations due to a change in the equilibrium deformation now in C_{60}^- and slightly shifted in energy due to the JT interaction. The calculations also reproduce the broad sideband at about 1850 cm^{-1}, and a comparison to calculations with JT coupling to the different vibrations separately shows that this sideband results from the combined interaction with all the vibrations. The origin of the band is not discussed in detail in Ref. 37, but it is tempting to assign it to a combination of two narrow sidebands corresponding to the highest vibrational frequencies and cone states with positive JT energy from the interaction with the lower-frequency vibrations.

Qualitatively, this interpretation is consistent with our new interpretation of band III in Fig. 4. The separation of 1315 cm^{-1} between bands II and III is smaller than the separation of 1850 cm^{-1} between the main level density peaks for the LUMO level, but this might be due to the JT interaction in the LUMO+1 level being weaker by $\sim 15\%$. It should also be noted that in earlier absorption measurements for C_{60}^- in solution, the high-energy band was observed at somewhat higher energy.[38] We plan to repeat the gas-phase experiment for C_{60}^- with the new, more stable ion source and with a more powerful laser to check the positions of the bands and determine the temperature dependence of their strength.

V. SUMMARY AND CONCLUSIONS

In summary, we have reported near-infrared absorption spectra of C_{60}^{2-} ions in the gas phase. The absorption leads to electron loss and both direct electron tunneling into the continuum and statistical autodetachment after internal conversion are observed. Since the excited electronic state is close to the maximum (~ 1.7 eV) of the Coulomb barrier calculated in Ref. 15, this is evidence against the suggestion in Ref. 6 of much lower Coulomb barriers for fullerene dianions and is consistent with a recent determination by photo-

emission of a 1.6 eV Coulomb barrier for C_{70}^{2-} (Ref. 39) and slightly lower values for C_{76}^{2-}, C_{78}^{2-}, and C_{84}^{2-}.[40]

The absorption spectra reveal the strong JT interaction in the dianions of C_{60}, and the electronic ground state is determined to be singlet. Transitions from both the JT ground state and excited pseudorotational states have been observed. There is evidence for interpretation of a broad high-energy band as transitions to states with positive JT energy stabilized by pseudorotations (cone states), and we suggest a similar assignment for a high-energy absorption band in the monoanion.

ACKNOWLEDGMENTS

We want to thank Lars H. Andersen for his kind assistance with the laser system and Robert N. Compton for discussions. This experiment has been performed at ELISA, part of the distributed LEIF infrastructure. The support received through the European Project ITS LEIF (Grant No. RII3/026015), from the Danish and Swedish National Research Councils, and from the Göteborg Nanoparticle Platform is gratefully acknowledged.

[1] S. E. Erwin and W. E. Pickett, Science **254**, 842 (1991).
[2] M. Capone, M. Fabrizio, C. Castellani, and E. Tosatti, Science **296**, 2364 (2002).
[3] A. V. Danilov, P. Hedegård, D. S. Golubev, T. Bjørnholm, and S. E. Kubatkin, Nano Lett. **8**, 2393 (2008).
[4] C. A. Martin, D. Ding, J. Kryger Sørensen, T. Bjørnholm, J. M. van Ruitenbeek, and H. S. J. van der Zant, J. Am. Chem. Soc. **130**, 13198 (2008).
[5] M. K. Scheller, R. N. Compton, and L. S. Cederbaum, Science **270**, 1160 (1995).
[6] O. T. Ehrler, F. Furche, J. M. Weber, and M. M. Kappes, J. Chem. Phys. **122**, 094321 (2005).
[7] M. C. M. O'Brien, Phys. Rev. B **53**, 3775 (1996).
[8] C. C. Chancey and M. C. M. O'Brien, *The Jahn–Teller Effect in* C_{60} *and Other Icosahedral Complexes* (Princeton University Press, Princeton, NJ, 1997).
[9] A. V. Nikolaev and K. H. Michel, J. Chem. Phys. **117**, 4761 (2002).
[10] J. E. Han, E. Koch, and O. Gunnarsson, Phys. Rev. Lett. **84**, 1276 (2000).
[11] O. Gunnarsson, J. E. Han, E. Koch, and V. H. Crespi, Struct. Bond. (Berlin) **114**, 71 (2005).
[12] C. A. Reed and R. D. Bolskar, Chem. Rev. (Washington, D.C.) **100**, 1075 (2000).
[13] P. R. Trulove, R. T. Carlin, G. R. Eaton, and S. S. Eaton, J. Am. Chem. Soc. **117**, 6265 (1995).
[14] B. Liu, P. Hvelplund, S. B. Nielsen, and S. Tomita, Phys. Rev. Lett. **92**, 168301 (2004).
[15] S. Tomita, J. U. Andersen, H. Cederquist, B. Concina, O. Echt, J. S. Forster, K. Hansen, B. A. Huber, P. Hvelplund, J. Jensen, B. Liu, B. Manil, L. Maunoury, S. B. Nielsen, J. Rangama, H. T. Schmidt, and H. Zettergren, J. Chem. Phys. **124**, 024310 (2006).
[16] S. P. Møller, Nucl. Instrum. Methods Phys. Res. A **394**, 281 (1997).
[17] J. U. Andersen, P. Hvelplund, S. B. Nielsen, S. Tomita, H. Wahlgreen, S. P. Møller, U. V. Pedersen, J. S. Forster, and T. J. D. Jørgensen, Rev. Sci. Instrum. **73**, 1284 (2002).
[18] K. O. Nielsen, Nucl. Instrum. Methods **1**, 289 (1957).
[19] D. H. Yu, L. H. Andersen, C. Brink, and P. Hvelplund, Mol. Mater. **4**, 237 (1994).
[20] H. Zettergren, M. Alcami, and F. Martin, Phys. Rev. A **76**, 043205 (2007).
[21] S. Tomita, J. U. Andersen, E. Bonderup, P. Hvelplund, B. Liu, S. B. Nielsen, U. V. Pedersen, J. Rangama, K. Hansen, and O. Echt, Phys. Rev. Lett. **94**, 053002 (2005).
[22] O. T. Ehrler, J. P. Yang, C. Hättig, A.-N. Unterreiner, H. Hippler, and M. M. Kappes, J. Chem. Phys. **125**, 074312 (2006).
[23] K. Hansen, J. U. Andersen, P. Hvelplund, S. P. Møller, U. V. Pedersen, and V. V. Petrunin, Phys. Rev. Lett. **87**, 123401 (2001).
[24] O. T. Ehrler, J.-P. Yang, A. B. Sugiharto, A. N. Unterreiner, and M. M. Kappes, J. Chem. Phys. **127**, 184301 (2007).
[25] There is an error in the plot of the barrier in Fig. 6 in Ref. 15. The division by two of the second term in Eq. (1) was omitted.
[26] H. Hase, Y. Kitajima, Y. Miyamoto, Y. Miyataki, Y. Tajima, and M. Hoshino, Chem. Phys. Lett. **326**, 186 (2000).
[27] D. V. Konarev, N. V. Drishko, V. N. Semkin, and A. Graja, Synth. Met. **103**, 2384 (1999).
[28] D. R. Lawson, D. L. Feldheim, C. A. Foss, P. K. Dorhout, C. M. Elliott, C. R. Martin, and B. Parkinson, J. Electrochem. Soc. **139**, L68 (1992).
[29] H. Kondo, T. Momose, and T. Shida, Chem. Phys. Lett. **237**, 111 (1995).
[30] J. Fulara, M. Jakobi, and J. P. Maier, Chem. Phys. Lett. **211**, 227 (1993).
[31] O. Gunnarsson, H. Handschuh, P. S. Bechthold, B. Kessler, G. Ganteför, and W. Eberhardt, Phys. Rev. Lett. **74**, 1875 (1995).
[32] X.-B. Wang, H.-K. Woo, and L.-S. Wang, J. Chem. Phys. **123**, 051106 (2005).
[33] H. C. Longuet–Higgins, O. Öpik, M. H. L. Pryce, and R. A. Sack, Proc. R. Soc. London **A244**, 1 (1958).
[34] J. C. Slonczewski, Phys. Rev. **131**, 1596 (1963).
[35] T. Sato, L. F. Chibotaru, and A. Ceulemans, J. Chem. Phys. **122**, 054104 (2005).
[36] G. A. Heath, J. E. McGrady, and R. L. Martin, J. Chem. Soc., Chem. Commun. **17**, 1272 (1992).
[37] T. Frederiksen, K. J. Franke, A. Arnau, G. Schulze, J. I. Pascual, and N. Lorente, Phys. Rev. B **78**, 233401 (2008).
[38] R. D. Bolskar, S. H. Gallagher, R. S. Armstrong, P. A. Lay, and C. A. Reed, Chem. Phys. Lett. **247**, 57 (1995).
[39] X.-B. Wang, H.-K. Woo, X. Huang, M. M. Kappes, and L.-S. Wang, Phys. Rev. Lett. **96**, 143002 (2006).
[40] X.-B. Wang, H.-K. Woo, J. Yang, M. M. Kappes, and L.-S. Wang, J. Phys. Chem. C **111**, 17684 (2007).

ChemComm

View Online
Dynamic Article Links

II

Cite this: *Chem. Commun.*, 2011, **47**, 6900–6902

www.rsc.org/chemcomm

COMMUNICATION

On the intrinsic optical absorptions by tetrathiafulvalene radical cations and isomers†

Maj-Britt Suhr Kirketerp,[a] Leonardo Andrés Espinosa Leal,[b] Daniele Varsano,[c] Angel Rubio,*[b] Thomas J. D. Jørgensen,[d] Kristine Kilså,[e] Mogens Brøndsted Nielsen*[e] and Steen Brøndsted Nielsen*[a]

Received 6th April 2011, Accepted 5th May 2011
DOI: 10.1039/c1cc11936b

Gas-phase action spectroscopy shows unambiguously that the low-energy absorptions by tetramethylthiotetrathiafulvalene and tetrathianaphthalene cations in solution phase are due to monomers and not π-dimers.

Tetrathiafulvalene (TTF, Chart 1) is a redox-active molecule that has been explored considerably in supramolecular chemistry, molecular electronics, and materials science.[1] The ability of TTF and alkylthio-substituted TTF radical cations to form π-dimers (TTF_2^{2+}) has been a subject of some controversy. $TTF^{\bullet+}$ exhibits an absorption maximum at a longest-wavelength absorption of 580 nm in CH_3CN,[2] which has been assigned to an intrinsic absorption by the cation. However, in EtOH at 225 K, absorption at 714 nm is observed, and it was interpreted as due to the formation of π-dimers.[3] This assignment was supported by Khodorkovsky and co-workers[4] from ESR studies and calculations. Recently, Sallé and co-workers[5] demonstrated that dimerisation can be enforced between two closely situated TTFs in a calixarene assembly, and along the same line Stoddart and co-workers[6] observed dimerisation in TTF-containing rotaxanes and catenanes. For the radical cation of tetramethylthio-TTF (TMT-TTF, Chart 1) and related derivatives, absorption around 840 nm was in several studies[7] ascribed to a π-dimer. Studies on a bis-TTF macrocycle showed a concentration dependent absorption (in comparison to a higher energy absorption), which was taken as evidence of the intermolecular character of the transition.[7c] Nevertheless, ESR and calculational studies pointed in the opposite direction, namely that $TMT\text{-}TTF^{\bullet+}$ cations do not dimerise.[4] Thus, while π-dimerisation is an intriguing design element for supramolecular chemistry, the substituents seem to play a major role for its occurrence.

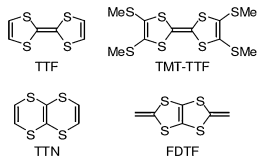

Chart 1 Sulfur-heterocycles.

Here we shed further light on the intrinsic absorptions by TTF cations from gas-phase experiments; these provide both the isolated molecule characteristics and, by comparison with solution phase absorptions, reveal any possible solvent influence. In addition to $TTF^{\bullet+}$ and $TMT\text{-}TTF^{\bullet+}$, we have studied the properties of tetrathianaphthalene (TTN, Chart 1), an isomer of TTF. Spectra were compared to calculated excitation energies. A third isomer of TTF was investigated theoretically, a fused dithiafulvene (FDTF, Chart 1).

First, absorption bands in solution for the radical cations under study are listed in Table 1; values for $TTF^{\bullet+}$ and $TMT\text{-}TTF^{\bullet+}$ were taken from the literature.[2,3,7c,8] It was previously

Table 1 Absorption maxima of TTF radical cations and isomers (in nm). For $TMT\text{-}TTF^{\bullet+}$ the first theory data row corresponds to maxima for the lowest energy conformer and the next row to another conformer. LDA and CASSCF methods give similar results (see ESI†)

		Gas phase	
Compound	Solution[a]	Experiment	Theory
$TTF^{\bullet+}$	430,[b] 580,[b] 714[c]	395, ~590	368, 539
$TMT\text{-}TTF^{\bullet+}$	470,[d] 843[d]	425, 540, 790	386, 424, 873
	454,[e] 480 (sh),[e] 560 (sh),[e] 850[e]		376, 519, 734
$TTN^{\bullet+}$	900[f]	450, 815	511, 836
$FDTF^{\bullet+}$	—	—	390, 773

[a] Only wavelengths >400 nm are listed. [b] In MeCN; ref. 2. [c] In EtOH at low temperature; ref. 3. [d] In CH_2Cl_2; ref. 7c. [e] In MeCN; sh = shoulder; ref. 8. [f] In MeCN; this work.

[a] *Department of Physics and Astronomy, Aarhus University, Ny Munkegade, DK-8000, Aarhus C, Denmark. E-mail: sbn@phys.au.dk*
[b] *Nano-Bio Spectroscopy Group and ETSF Scientific Development Centre, Dpto. Física de Materiales, Universidad del País Vasco, Centro de Física de Materiales CSIC-UPV/EHU-MPC and DIPC, Av. Tolosa 72, San Sebastián, Spain. E-mail: angel.rubio@ehu.es*
[c] *Department of Physics, University of Rome 'La Sapienza', Rome, Italy*
[d] *Department of Biochemistry and Molecular Biology, University of Southern Denmark, Campusvej 55, DK-5230 Odense, Denmark*
[e] *Department of Chemistry, University of Copenhagen, Universitetsparken 5, DK-2100 Copenhagen Ø, Denmark. E-mail: mbn@kiku.dk*

† Electronic supplementary information (ESI) available: Details on ESI mass spectrometry, calculated absorption spectra, Kohn–Sham orbitals, and molecular coordinates. See DOI: 10.1039/c1cc11936b

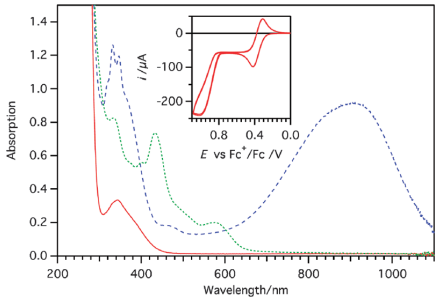

Fig. 1 Absorption spectra of TTN (red solid line) and $TTN^{\bullet+}$ (blue dashed line). Spectroelectrochemistry was done under a constant potential of 0.507 V *vs.* Fc^+/Fc. Upon returning to the neutral species (−0.113 V *vs.* Fc^+/Fc), some other absorption features emerge (green dotted line). The inset shows the CV of TTN in 0.1 M $TBAPF_6$ in CH_3CN.

shown that TTN undergoes one reversible oxidation and a subsequent irreversible oxidation,[9] but to our knowledge the absorption properties of the radical cation were never measured. For this reason we performed spectroelectrochemical studies on TTN. The cyclic voltammogram (CV) is shown in the inset of Fig. 1. A reversible oxidation was found at $E_0(TTN^+/TTN) = 0.36$ V (half-wave potential) *vs.* Fc^+/Fc and an irreversible oxidation at $E_p(TTN^{2+}/TTN^+) = 1.01$ V *vs.* Fc^+/Fc. Spectroelectrochemistry revealed a λ_{max} of $TTN^{\bullet+}$ at *ca.* 900 nm (Fig. 1). We note that bulk electrolysis was not completely reversible as upon returning to the neutral species some other absorption features emerge, in addition to the expected disappearance of the radical cation absorption band.

Our next objective was to measure the intrinsic absorptions by $TTF^{\bullet+}$, TMT-$TTF^{\bullet+}$, and $TTN^{\bullet+}$ *in vacuo*. Action spectroscopy was done at the electrostatic ion storage ring in Aarhus, ELISA.[10] Briefly, ions were formed by electrospray ionisation, accumulated in a 22-pole ion trap, accelerated as a bunch to 22 keV kinetic energies, mass-to-charge selected by a bending magnet and injected into the ring. In the absence of a stabilising solvent, the presence of dimer dications with the same m/z as the monomer cations in the ion beam is expected to be insignificant due to the Coulomb repulsion between two like charges. This was verified by a mass spectrum of TMT-TTF measured at another instrument providing higher mass resolution: the isotope pattern is completely accounted for by monomers (Fig. 2, see ESI†). After storage of the ions for 35 ms in the ring to allow for the decay of metastable ions, the ions were photoexcited using a pulsed tunable EKSPLA

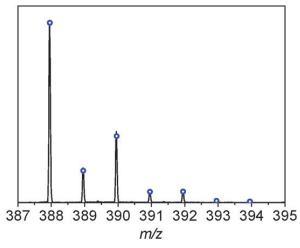

Fig. 2 Electrospray mass spectrum of TMT-TTF. The theoretical isotope pattern of TMT-$TTF^{\bullet+}$ is indicated by the blue circles.

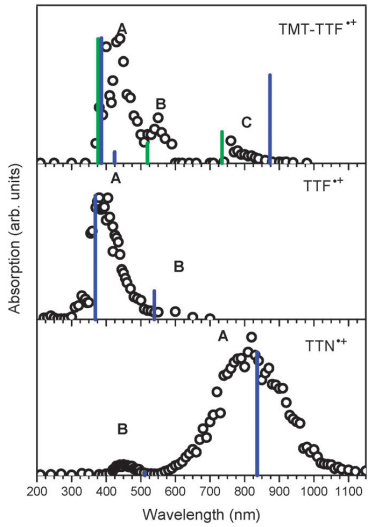

Fig. 3 Gas-phase action spectra and calculated values (vertical lines). The intensities are normalised to the maximum peak. For TMT-$TTF^{\bullet+}$ the results appear in blue for the lowest energy conformation and in green for the second one (see text).

laser (Nd:YAG in combination with an OPO). The number of neutrals formed on one side of the ring was measured as a function of time. Dissociation was a result of one-photon absorption for $TTF^{\bullet+}$ and $TTN^{\bullet+}$ and also for TMT-$TTF^{\bullet+}$ at low wavelengths (<500 nm). At higher wavelengths the dissociation of TMT-$TTF^{\bullet+}$ was due to two-photon absorption. Cross-sections (relative, not absolute, numbers) are obtained as the number of neutrals formed after photoexcitation divided by the ion beam intensity and the number of photons in the laser pulse (raised either to the power of one or two).

The resulting action spectra are shown in Fig. 3, and the band maxima are given in Table 1. In addition, we have calculated the absorption maxima for the compounds including also $FDTP^{\bullet+}$ by time-dependent density functional theory using B3LYP/6-311++G(d,p).[11] Other local and semi-local[11] functionals are able to describe properly the more intense bands but fail in first excitations of TMT-$TTF^{\bullet+}$ (see ESI†). Values are provided in Table 1 and presented in Fig. 3 by vertical lines (see also ESI†). Structures were optimised at the B3LYP/6-311++G(d,p) level, and a planar symmetry was found for both $TTF^{\bullet+}$ and $FDTF^{\bullet+}$ while $TTN^{\bullet+}$ adopts a folded geometry, *i.e.*, ionisation changes the conformation of the molecule. Good agreement between experimental and calculated absorption maxima was obtained, and from the calculations the lowest-energy absorptions for $TTF^{\bullet+}$ (B), $FDTF^{\bullet+}$, and $TTN^{\bullet+}$ (A) are assigned to π–π* transitions from the SOMO − 1 to the SOMO, *cf.* Fig. 4. The low-energy absorption at *ca.* 714 nm by $TTF^{\bullet+}$ in solution at low temperature (*vide supra*) is absent in the gas phase spectrum, which supports the interpretation of this band as a π-dimer absorption. In contrast, a low-energy absorption at 836 nm (A) of $TTN^{\bullet+}$ in the gas phase indicates that the strong absorption in solution around 900 nm is an intrinsic absorption and not originating from π-dimers. This lowest-energy

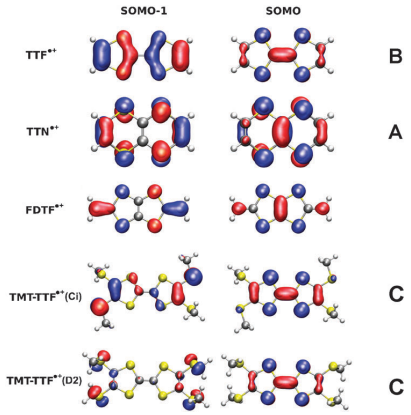

Fig. 4 Kohn–Sham orbitals obtained from DFT/B3LYP calculations. The positive (negative) part is depicted with blue (red), and the isosurfaces were plotted with the 20% of the highest value.

absorption of $TTN^{\bullet+}$ is significantly redshifted relatively to that of $TTF^{\bullet+}$ (by 225 nm *in vacuo*). As expected a solvatochromic redshift is found for the π–π* transitions in both $TTF^{\bullet+}$ and $TTN^{\bullet+}$. The lowest-energy absorption of the $FDTF^{\bullet+}$ isomer is calculated to be in between that of $TTF^{\bullet+}$ and $TTN^{\bullet+}$; no experimental data exist for this ion. The strong band at 395 nm for $TTF^{\bullet+}$ (A) corresponds mainly to a SOMO to SOMO + 2 transition which is of π–π* nature. The band at 450 nm for $TTN^{\bullet+}$ (B) is ascribed to a SOMO to SOMO + 1 transition (also π–π* transition).

The gas-phase action spectrum of $TMT\text{-}TTF^{\bullet+}$ displays three bands labeled A (425 nm), B (540 nm) and C (790 nm), respectively (Fig. 3). In the calculations, we took into account two stable symmetrical structures (due to a low energy barrier for rotation of the methyl groups). The energy difference between the two is around 54 meV, and the TTF core structure remains almost invariant. In the lowest-energy conformer of C_i symmetry, the two diagonally positioned methyl groups are in the same plane as the TTF unit while the other two are perpendicular to the plane and in the opposite direction. In the other one of D_2 symmetry, the methyl groups are slightly inclined, opposite to each other, and perpendicular to the TTF plane. Based on the calculations we assign the three bands to a π–π* transition (A, C_i)/n–π* transition (A, D_2), a π–π* transition (B, more intense for D_2 than for C_i), and a charge-transfer transition from the external sulfur-methylthio to the central C–C bridge (C, both conformers). Importantly, the presence of the low-energy band at 790 nm (C) is clear evidence that in solution the origin of this band is from an intramolecular transition and not the result of π-dimers, hence supporting the conclusion of Khodorkovsky *et al.*[4] We caution that the signal giving rise to the C band is the result of two consecutive absorption processes, and that it therefore can be difficult to compare the intensity to those of the A and B bands both of which are due to one-photon absorption. Also the laser beam exit changes at 710 nm, which may cause slightly different overlaps between the laser light and the ion bunch below and above 710 nm.

In conclusion this study provides the first intrinsic optical properties of $TTF^{\bullet+}$, $TMT\text{-}TTF^{\bullet+}$, and $TTN^{\bullet+}$, and the solution-phase spectrum of $TTN^{\bullet+}$. Based on these results we have firmly established that the low-energy absorption by TMT-TTF and TTN radical cations in solution can be assigned to the monomer. On the other hand, the absence of a low-energy absorption around 714 nm in the gas-phase spectrum of $TTF^{\bullet+}$ is in agreement with the assignment of this absorption to π-dimers in solution, but it cannot be taken as evidence hereof.

The Aarhus and Copenhagen groups acknowledge support from Lundbeckfonden and The Danish Council for Independent Research | Natural Sciences (#10-082088), DV the European Research Council project no. 240624, DV, LAE and AR e-I3 ETSF project (Contract #211956), and CINECA CPU time granted through ISCRA, LAE and AR MEC (FIS2010-21282-C02-01), European Research Council Advanced Grant DYNamo (ERC-2010-AdG-Proposal No. 267374), ACI-Promociona (ACI2009-1036), "Grupos Consolidados UPV/EHU del Gobierno Vasco" (IT-319-07) and computational time by the Barcelona Supercomputing Center, "Red Española de Supercomputacion" and *IZO-SGI*/ARINA cluster.

Notes and references

1 (*a*) M. R. Bryce, *Adv. Mater.*, 1999, **11**, 11; (*b*) M. B. Nielsen, C. Lomholt and J. Becher, *Chem. Soc. Rev.*, 2000, **29**, 153; (*c*) M. R. Bryce, *J. Mater. Chem.*, 2000, **10**, 589; (*d*) J. L. Segura and N. Martín, *Angew. Chem., Int. Ed.*, 2001, **40**, 1372; (*e*) J. F. Stoddart, *Chem. Soc. Rev.*, 2009, **38**, 1802; (*f*) D. Canevet, M. Sallé, G. X. Zhang, D. Zhang and D. Zhu, *Chem. Commun.*, 2009, 2245.
2 L. Huchet, S. Akoudad, E. Levillain, J. Roncali, A. Emge and P. Bäuerle, *J. Phys. Chem. B*, 1998, **102**, 7776.
3 J. B. Torrance, B. A. Scott, B. Welber, F. B. Kaufman and P. E. Seiden, *Phys. Rev. B*, 1979, **19**, 730.
4 V. Khodorkovsky, L. Shapiro, P. Krief, A. Shames, G. Mabon, A. Gorgues and M. Giffard, *Chem. Commun.*, 2001, 2736.
5 J. Lyskawa, M. Sallé, J.-Y. Balandier, F. Le Derf, E. Levillain, M. Alain, P. Viel and S. Palacin, *Chem. Commun.*, 2006, 2233.
6 (*a*) I. Aprahamian, J.-C. Olsen, A. Trabolsi and J. F. Stoddart, *J. Am. Chem. Soc.*, 2008, **14**, 3889; (*b*) J. M. Spruell, A. Coskun, D. C. Friedman, R. S. Forgan, A. A. Sarjeant, A. Trabolsi, A. C. Fahrenbach, G. Barin, W. F. Paxton, S. K. Dey, M. A. Olson, D. Benítez, E. Tkatchouk, M. T. Colvin, R. Carmielli, S. T. Caldwell, G. M. Rosair, S. G. Hewage, F. Duclairoir, J. L. Seymour, A. M. Z. Slawin, W. A. Goddard, M. R. Wasielewski, G. Cooke and J. F. Stoddart, *Nat. Chem.*, 2010, **2**, 870; (*c*) A. Coskun, J. M. Spruell, G. Barin, A. C. Fahrenbach, R. S. Forgan, M. T. Colvin, R. Carmieli, D. Benítez, E. Tkatchouk, D. C. Friedman, A. A. Sarjeant, M. R. Wasielewski, W. A. Goddard, III and J. F. Stoddart, *J. Am. Chem. Soc.*, 2011, **133**, 4538.
7 (*a*) M. R. Bryce, W. Devonport, L. M. Goldenberg and C. Wang, *Chem. Commun.*, 1998, 945; (*b*) C. A. Christensen, L. M. Goldenberg, M. R. Bryce and J. Becher, *Chem. Commun.*, 2000, 331; (*c*) H. Spanggaard, J. Prehn, M. B. Nielsen, E. Levillain, M. Allain and J. Becher, *J. Am. Chem. Soc.*, 2000, **122**, 9486.
8 J. Kreicberga and O. Neilands, *Zh. Org. Khim.*, 1985, **21**, 2009.
9 M. Mizuno, M. P. Cava and A. F. Garito, *J. Org. Chem.*, 1976, **41**, 1485.
10 (*a*) S. P. Møller, *Nucl. Instrum. Methods Phys. Res., Sect. A*, 1997, **394**, 281; (*b*) J. U. Andersen, P. Hvelplund, S. B. Nielsen, S. Tomita, H. Wahlgreen, S. P. Møller, U. V. Pedersen, J. S. Forster and T. J. D. Jørgensen, *Rev. Sci. Instrum.*, 2002, **73**, 1284; (*c*) S. B. Nielsen, J. U. Andersen, P. Hvelplund, B. Liu and S. Tomita, *J. Phys. B: At., Mol. Opt. Phys.*, 2004, **37**, R25.
11 A. Castro, H. Appel, M. Oliveira, C. A. Rozzi, X. Andrade, F. Lorenzen, M. A. L. Marques, E. K. U. Gross and A. Rubio, *Phys. Status Solidi B*, 2006, **243**, 2465.

DOI: 10.1002/cphc.200900174

Absorption Spectra of 4-Nitrophenolate Ions Measured *in Vacuo* and in Solution

Maj-Britt Suhr Kirketerp,[c] Michael Åxman Petersen,[b] Marius Wanko,[a] Leonardo Andres Espinosa Leal,[a] Henning Zettergren,[c] Françisco M. Raymo,[d] Angel Rubio,*[a] Mogens Brøndsted Nielsen,*[b] and Steen Brøndsted Nielsen*[c]

Hyperpolarizable organic molecules that display intramolecular charge transfer (ICT) transitions are important building blocks for advanced optical materials.[1] One such class of species is the *p*-nitrophenolates that serve as donor–acceptor molecules, or so-called push–pull chromophores, since an electron is transferred from the negatively charged phenolate to the nitro group upon photoexcitation, with a significant change in the charge distribution. The $\pi\pi^*$ transition is not purely CT in character due to the highly delocalized donor and acceptor orbitals. Both the phenolate and nitro group oxygen atoms are strong hydrogen-bond acceptors and the nitro group has an additional tendency to coordinate with metal centers—properties successfully employed for engineering of nonlinear optical (NLO) materials.[2] In this regard, it is advantageous to know the intrinsic absorption of the isolated molecule or ion to shed light on the electronic perturbation by a microenvironment and, not least, to provide a reference to benchmark theory. An approximate approach is to characterize molecules spectroscopically in solvents of varying polarity and thereafter to extrapolate to vacuum. Several scales have been developed based on the energy of inter- or intramolecular CT transitions, such as the Dimroth–Reichard $E_T(30)$,[3] the Z-scale,[4] the π^*-scale,[5] and taking into account H-bond interactions.[6] The situation is more complicated when one wants to correlate the ICT of anionic nitrophenolates with solvent polarity. Ionophores are not easily dissolved in nonpolar solvents and even then there are field effects from counter ions. In polar solvents, the ground and excited states are stabilized to different extents, which results in solvatochromic shifts.

To determine the intrinsic optical properties, it is necessary to carry out experiments on bare molecular ions in vacuo. Herein we report gas-phase absorption spectra of four *p*-nitrophenolates, $\mathbf{1}^-$, $\mathbf{2}^-$, $\mathbf{3}^-$, and $\mathbf{4}^-$ (Figure 1).[7] The ions are characterized by different π-conjugated spacers between the donor and acceptor groups and were chosen to elucidate the influence of the number of phenylene spacers and deviations from planarity. Results are compared to advanced quantum-chemical calculations and solution-phase measurements.

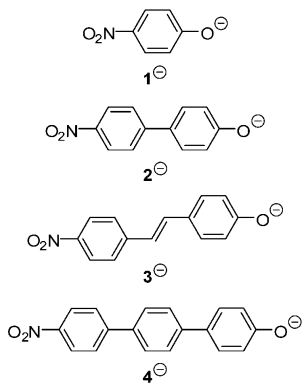

Figure 1. Phenylogous nitrate ions (**1**, **2**, **4**) and a combination of a phenylogous and a vinylogous nitrate ion (**3**) chosen for study.

Gas-phase spectroscopy on molecules that are easily evaporated is routinely done whereas experiments on ions require specialized instrumentation. An inherent problem in the latter case is the presence of too few chromophores to cause a measurable decrease in the incoming light intensity, implying that conventional spectroscopy does not work. Instead, gas-phase UV/Vis absorption spectra are derived from the photoinduced homolytic dissociation of the chromophore and by monitoring one or more of its photoproducts. We use the electrostatic ion storage ring in Aarhus, ELISA (Figure 2), which, when combined with lasers, work as a gas-phase optical cell.[8] Ions are produced by electrospray ionization, stored in a 22-pole pretrap, accelerated as a bunch to 22 keV energies and in-

[a] *Dr. M. Wanko, L. Andres Espinosa Leal, Prof. A. Rubio*
NanoBio Spectroscopy Group and ETSF Centre for Scientific Development
Centro Mixto CSIC-UPV/EHU "Fisica de Materiales"
University of the Basque Country
UPV/EHU Centro Joxe Mari Korta
Avenida de Tolosa, 72, E-20018 Donostia-San Sebastian (Spain)
Fax: (+34) 943018390
E-mail: Angel.Rubio@ehu.es

[b] *Dr. M. Åxman Petersen, Prof. M. Brøndsted Nielsen*
Department of Chemistry
University of Copenhagen, Universitetsparken 5
DK-2100 Copenhagen Ø (Denmark)
Fax: (+45) 35320212
E-mail: mbn@kiku.dk

[c] *M.-B. Suhr Kirketerp, Dr. H. Zettergren, Prof. S. Brøndsted Nielsen*
Department of Physics and Astronomy
Aarhus University, Ny Munkegade
DK-8000 Aarhus C (Denmark)
Fax: (+45) 86120740
E-mail: sbn@phys.au.dk

[d] *Prof. F. M. Raymo*
Department of Chemistry
University of Miami, 1301 Memorial Drive
Florida, 33146-0431 (USA)

Supporting information for this article is available on the WWW under http://dx.doi.org/10.1002/cphc.200900174.

III

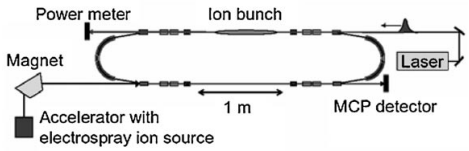

Figure 2. Instrumental setup for gas-phase spectroscopy.

jected into the ring. Here they circulate until they change their kinetic-energy-to-charge ratio by dissociation. After tens of milliseconds, the ions are irradiated by light at one side of the ring. If ionic dissociation occurs at the opposite side to the laser interaction region, the neutrals formed move undisturbed and hit the MCP detector at the end of the track, which gives rise to counts. A spectrum of the neutrals yield is obtained as a function of excitation wavelength.[9,10]

The dominant reaction after photoexcitation of nitrophenolates is loss of NO, occurring on a μs to ms time scale, and identified by operating ELISA as a mass spectrometer.[11] The number of photoexcited ions as a function of λ was obtained from exponential fits to time decay spectra and normalized by the photon flux and ion beam intensity (Figure 3). The lowest-energy absorption maxima are at 392, 541, 660, and 775 nm for $\mathbf{1}^-$, $\mathbf{2}^-$, $\mathbf{3}^-$, and $\mathbf{4}^-$, respectively. Thus, our data show that λ_{max} red-shifts along the progression $\mathbf{1}^-$, $\mathbf{2}^-$, $\mathbf{4}^-$. The absorption of the stilbene derivative $\mathbf{3}^-$ is found intermediate that of $\mathbf{2}^-$ and $\mathbf{4}^-$.

Theoretical results were obtained with time-dependent density functional theory (TDDFT) and the CC2 coupled-cluster linear response methods.[12] The dipole-allowed ππ* transition is to the 2^1A_1 excited state, which is lowest in energy. The frontier orbitals are of B_1 symmetry (C_{2v}), and the transition dipole moment is along the long axis of the molecule. CC2 transition energies (Figure 3 and Table 1) are in excellent agreement with the experiments. TDDFT performs as well for $\mathbf{1}^-$, $\mathbf{2}^-$, $\mathbf{3}^-$ but less so for $\mathbf{4}^-$ (Table 1).

Table 1. Longest-wavelength absorption maxima (λ_{max}) of *p*-nitrophenolates[a] in different solvents and in the gas phase. The values of λ_{max} are in nm.

Compound	Solution				Gas phase		
	H_2O	MeOH	Toluene (+18C6)	MeCN	Exp	Theory	
						CC2	TDDFT
$\mathbf{1}^-$	402[7d]	387	408	430	392	389	379
$\mathbf{2}^-$	400[7c]	406	472	507	541	570	593
$\mathbf{3}^-$		435	504	543	660	608	626
$\mathbf{4}^-$		377	445	466	775	752	918

[a] As sodium phenolate in solution (obtained by deprotonation of corresponding phenol by NaOMe).

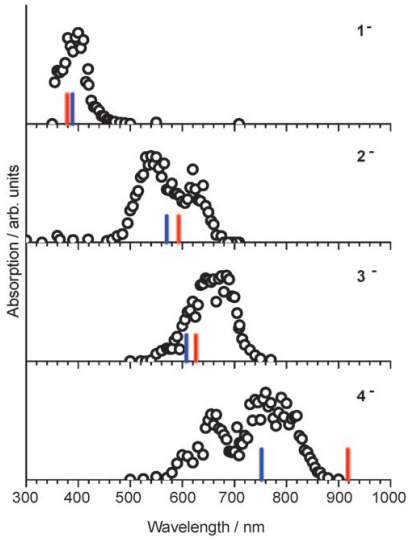

Figure 3. Gas phase absorption spectra. The vertical lines are calculated λ_{max} values, in blue CC2 and in red TDDFT.

Both DFT and MP2 predict non-planar geometries for $\mathbf{2}^-$ and $\mathbf{4}^-$ but a nearly flat potential energy surface. The planar transition state for $\mathbf{2}^-$ is 0.02 eV above the minimum (MP2/TZVPP). The dihedral angle between the phenyl rings depends on the method. Hybrid DFT (PBE0/TZVP) predicts rotations of 15–22° and MP2/TZVPP 20.1–28.7°. According to MP2, the angle decreases with the completeness of the basis set. Hence the planar and non-planar geometries represent limiting cases to estimate the fluctuation in the vertical excitation energy at 0.05–0.07 eV and 0.06–0.17 eV for $\mathbf{2}^-$ and $\mathbf{4}^-$, respectively, (Table S2); an angle of 0° results in a blue-shift. This may explain the sidebands in the spectra as there are no other dipole-allowed transitions in the region. The bands may, however, also be due to vibrational progressions.

The λ_{max} of the anions in three solvents are given in Table 1. Phenolates were obtained by deprotonation of phenols using NaOMe as base. In MeCN, the λ_{max} of $\mathbf{1}^-$ is red-shifted by 38 nm compared to vacuum, characteristic for ππ* transitions. A significant blue-shift is seen for the other three anions, most pronounced for $\mathbf{4}^-$ (309 nm), in agreement with HOMO and LUMO orbitals (Figure 4). Thus, SORCI[13] and CC2 calculations predict a considerable CT from phenolate to nitrophenyl, and that the difference in dipole moment between the ground and the first excited state increases with the length of the molecule, 27 D for $\mathbf{4}^-$! (See the Supporting Information, which contains experimental and computational details; calculated vertical excitation energies, oscillator strengths, difference dipole moments, and solvent shifts.) Counter ions and solvent dipoles therefore stabilize the ground state more than the excited state, an effect that increases in the order $\mathbf{2}^- < \mathbf{3}^- < \mathbf{4}^-$. The CT is slightly enhanced by out-of-plane torsion of the phenyl

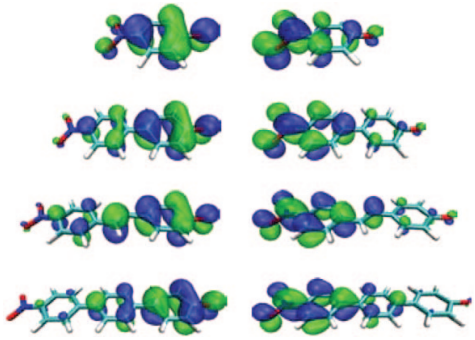

Figure 4. State-averaged natural orbitals from 2-root DDCI2 calculations. Left: HOMO, right: LUMO.

rings, which again increases in the presence of a counter ion. Nonetheless, the shift is almost the same for the planar and the nonplanar geometries. In water and methanol, the blue-shift is even larger for $\mathbf{2}^-$, $\mathbf{3}^-$, and $\mathbf{4}^-$ owing to H-bonds.

Sodium phenolates are not soluble in toluene, but are brought into solution using the crown ether 18-crown-6 (18C6) that encapsulates Na^+ in its cavity. While the maxima in this medium are red-shifted relative to those in MeOH, they are in fact all at higher energy than those in the more polar solvent MeCN. Clearly, interactions with the metal ion play an important role in toluene. According to ion-pair calculations and a continuum electrostatic model, H-bonding, structural effects and the shielding of the counter ion by the crown ether in toluene are essential.

In conclusion, we have recorded gas phase absorption spectra of four nitrophenolate anions and found that the CC2 model provides excellent predictions of the maxima. While only a relatively narrow spectral region is covered by the four chromophores in solution, they cover the entire visible region when isolated in vacuo. The large shifts can be explained by the CT character of the electronic transition. Calculations reveal that the solvent shift is mainly a result of counter ion and H-bond interactions. Therefore, it does not seem viable to correlate the data with one of the solvent polarity scales. For setting the reference point for the intrinsic absorptions of the chromophore anions, gas phase results are indeed required.

Acknowledgements

The AU and KU groups acknowledge support from Lundbeckfonden, Dir. Ib Henriksens Fond, Carlsbergfondet, FNU, and VKR, the San Sebastian group the Spanish MEC (FIS2007-65702-C02-01), "Grupos Consolidados UPV/EHU del Gobierno Vasco" (IT-319-07), CSIC, the European Community through e-I3 ETSF project (Contract Number 211956), DNA-NANODEVICES (IST-2006-029192) and NANO-ERA CHEMISTRY, and the Barcelona Supercomputing Center, "Red Espanola de Supercomputacion" and SGIker ARINA (UPV/EHU). F.M.R. thanks the National Science Foundation (CAREER Award CHE-0237578 and CHE-0749840) and UM for financial support.

Keywords: charge-transfer · density functional calculations · gas-phase spectroscopy · nitrophenolates · solvent effects

[1] M. J. Cho, D. H. Choi, P. A. Sullivan, A. J. P. Akelaitis, L. R. Dalton, *Prog. Polym. Sci.* **2008**, *33*, 1013.
[2] a) L.-T. Cheng, W. Tam, S. R. Marder, A. E. Stiegman, G. Rikken, C. W. Spangler, *J. Phys. Chem.* **1991**, *95*, 10643; b) M. Muthuraman, M. Bagieu-Beucher, R. Masse, J.-F. Nicoud, G. R. Desiraju, *J. Mater. Chem.* **1999**, *9*, 1471; c) M. Muthuraman, J.-F. Nicoud, R. Masse, G. R. Desiraju, *Mol. Cryst. Liq. Cryst.* **2001**, *356*, 1; d) B. M. Boaz, S. J. Das, *J. Cryst. Growth* **2005**, *279*, 383.
[3] a) K. Dimroth, A. Schweig, C. Reichard, *Justus Liebigs Ann. Chem.* **1963**, *669*, 95; b) C. Reichardt, *Chem. Rev.* **1994**, *94*, 2319; c) C. Reichardt, *Pure Appl. Chem.* **2008**, *80*, 1415.
[4] E. M. Kosower, *J. Am. Chem. Soc.* **1958**, *80*, 3253.
[5] M. J. Kamlet, J. L. Abboud, R. W. Taft, *J. Am. Chem. Soc.* **1977**, *99*, 6027.
[6] a) M. J. Kamlet, R. W. Taft, *J. Am. Chem. Soc.* **1976**, *98*, 377; b) R. W. Taft, M. J. Kamlet, *J. Am. Chem. Soc.* **1976**, *98*, 2886.
[7] Phenolates were prepared from known phenols: a) B. Jones, F. Chapman, *J. Chem. Soc.* **1952**, 1829; b) V. P. Kreiter, W. A. Bonner, R. H. Eastman, *J. Am. Chem. Soc.* **1954**, *76*, 5770; c) P. Culling, G. W. Gray, D. Lewis, *J. Chem. Soc.* **1960**, 2699; d) T. Abe, *Bull. Chem. Soc. Jpn.* **1962**, *35*, 318; e) H. Chaumeil, V. Diemer, A. Defoin, C. Carré, *Synthesis* **2007**, 3333; f) Y. Kitamura, A. Sakurai, T. Udzu, T. Maegawa, Y. Monguchi, H. Sajiki, *Tetrahedron* **2007**, *63*, 10596.
[8] a) S. P. Møller, *Nucl. Instrum. Methods Phys. Res. Sect. A* **1997**, *394*, 281; b) J. U. Andersen, P. Hvelplund, S. Brøndsted Nielsen, S. Tomita, H. Wahlgreen, S. P. Møller, U. V. Pedersen, J. S. Forster, T. J. D. Jørgensen, *Rev. Sci. Instrum.* **2002**, *73*, 1284; c) S. Brøndsted Nielsen, J. U. Andersen, P. Hvelplund, B. Liu, S. Tomita, *J. Phys. B* **2004**, *37*, R25; d) S. Brøndsted Nielsen, L. H. Andersen, *Biophys. Chem.* **2006**, *124*, 229.
[9] a) S. Brøndsted Nielsen, A. Lapierre, J. U. Andersen, U. V. Pedersen, S. Tomita, L. H. Andersen, *Phys. Rev. Lett.* **2001**, *87*, 228102; b) L. H. Andersen, I. B. Nielsen, M. B. Kristensen, M. O. A. El Ghazaly, S. Haacke, M. B. Nielsen, M. Å. Petersen, *J. Am. Chem. Soc.* **2005**, *127*, 12347.
[10] a) S. Tomita, J. U. Andersen, O. Echt, K. Hansen, P. Hvelplund, B. Liu, S. Brøndsted Nielsen, U. V. Pedersen, J. Rangama, *Phys. Rev. Lett.* **2005**, *94*, 053002; b) S. Panja, U. Kadhane, J. U. Andersen, A. I. S. Holm, P. Hvelplund, M.-B. S. Kirketerp, S. Brøndsted Nielsen, K. Støckhel, R. N. Compton, J. S. Forster, K. Kilså, M. B. Nielsen, *J. Chem. Phys.* **2007**, *127*, 124301; c) T. Ryhding, M.-B. S. Kirketerp, U. Kadhane, M. K. Lykkegaard, S. Panja, S. Brøndsted Nielsen, M. B. Nielsen, *Tetrahedron* **2008**, *64*, 11475.
[11] K. Støchkel, U. Kadhane, J. U. Andersen, A. I. S. Holm, P. Hvelplund, M.-B. S. Kirketerp, M. K. Larsen, M. K. Lykkegaard, S. Brøndsted Nielsen, S. Panja, H. Zettergren, *Rev. Sci. Instrum.* **2008**, *79*, 023 107.
[12] a) TURBOMOLE V5–10, 14 Jan 2008, Copyright (C) 2008 University of Karlsruhe; b) O. Christiansen, H. Koch, P. Jørgensen, *Chem. Phys. Lett.* **1995**, *243*, 409.
[13] F. Neese, *J. Chem. Phys.* **2003**, *119*, 9428.

Received: March 8, 2009
Published online on April 2, 2009

DOI: 10.1002/cphc.201000464

Double-Bond versus Triple-Bond Bridges: Does it Matter for the Charge-Transfer Absorption by Donor–Acceptor Chromophores?

IV

Maj-Britt Suhr Kirketerp,*[a] Michael Åxman Petersen,[c] Marius Wanko,[d] Henning Zettergren,[b] Angel Rubio,[d] Mogens Brøndsted Nielsen,[c] and Steen Brøndsted Nielsen[a]

Much work has focused on elucidating the different abilities of alkene and alkyne units to transmit donor–acceptor conjugation. One approach is to compare the characteristic charge-transfer (CT) absorption band maxima.[1] The CT band relies on both donor and acceptor strengths, that is, the energy of the separate HOMO of the donor and the separate LUMO of the acceptor, as well as on the electronic coupling between the two orbitals conveyed by the spacer. In the strong coupling regime, the resulting HOMO and LUMO orbitals are more separated in energy (blue-shifted absorption). In the weak coupling regime, each end of the molecule is unperturbed and the smallest HOMO–LUMO gap is obtained.

Figure 1 shows a variety of alkene and alkyne extended donor–acceptor chromophores and their CT absorptions in solution. Comparison of stilbene and tolane derivatives **1a** and **1b** as well as **2a** and **2b**[2] shows that exchange of a double bond for a triple bond results in a blue-shifted CT absorption. In contrast, the absorption maxima of tetrathiafulvalene (TTF) compounds **3a**[3] and **3b**[4] indicate that the electronic coupling between the donor (TTF) and acceptor ends is lowest when the spacer is an alkyne.[5] Yet, it is imperative to take solvent effects into account when comparing CT absorptions,[6] and particularly so for charged donor–acceptor chromophores (vide infra). In addition, conformational flexibility of the chromophore in question plays an important role for the overlap of π orbitals.

We have recently studied the intrinsic optical properties and solvatochromism of a series of *p*-nitrophenolates by state-of-the-art gas-phase experiments and quantum chemical calculations.[7] In the electronic transition, electron density is transferred from the phenolate oxygen to the nitro group. Compared to solution spectra, the isolated chromophores exhibited not only significantly red-shifted CT absorptions in the gas phase, but the relative positions in the series were also not identical to the sequence obtained in different solvents. Herein, we shed light on the difference between alkene and alkyne bridges by comparing two simple *p*-nitrophenolates **4a** and **4b** (Figure 1). We establish from gas-phase action spectroscopy that the coupling is strongest for the alkene spacer (**4a**).

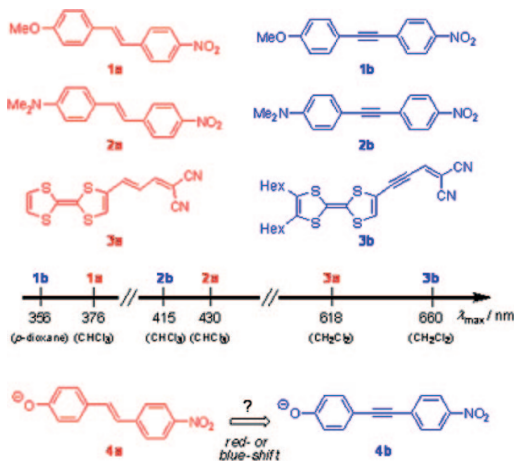

Figure 1. Selection of donor–acceptor chromophores with alkene or alkyne spacers. The absorption maxima of the CT absorptions measured in solution are given.[2–4]

The experimental setup consists of an electrostatic ion storage ring in combination with an electrospray ion source and a laser system (Figure 2).[8] The number of neutrals formed at one side of the ring is measured as a function of time, and from the increased number of neutrals formed after photoexcitation, we obtain a relative number for the absorption cross section, known as action spectroscopy. The detector is positioned on the opposite side of the ring as to where the photoexcitation takes place. Hence we measure neutrals formed by delayed dissociation, 30 μs after photoexcitation in the first instance and then after successive circulations in the ring. In a separate experiment in which the ring was used as a mass spectrometer,[9] the dissociation channels were found to be loss of NO and to a minor extent loss of NO_2 (Supporting Information). For comparison, loss of NO from nitrobenzene is also a low-energy dissociation channel.[10]

[a] *M.-B. S. Kirketerp, Prof. S. B. Nielsen*
Department of Physics and Astronomy
Aarhus University, Ny Munkegade, DK-8000 Aarhus C (Denmark)
Fax: (+45) 86120740
E-mail: msk@phys.au.dk

[b] *Dr. H. Zettergren*
Department of Physics, Stockholm University
AlbaNova University Center, 10691 Stockholm (Sweden)

[c] *Dr. M. Å. Petersen, Prof. M. B. Nielsen*
Department of Chemistry, University of Copenhagen
Universitetsparken 5, DK-2100 Copenhagen (Denmark)

[d] *Dr. M. Wanko, Prof. A. Rubio*
CIC nanoGUNE, European Theoretical Spectroscopy Facility (ETSF)
Centro Mixto CSIC-UPV/EHU and Departamento de Fisica de Materiales
Universidad del Pais Vasco
Avenida de Tolosa 72, 20018 San Sebastian (Spain)

Supporting information for this article is available on the WWW under http://dx.doi.org/10.1002/cphc.201000464.

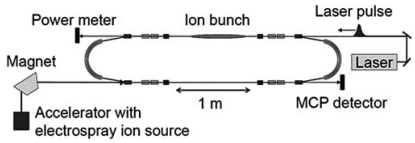

Figure 2. Instrumental setup for gas-phase action spectroscopy. An electrostatic ion storage ring in combination with an electrospray ion source and a laser system.

Time spectra of **4a** and **4b** after photoexcitation at 690 and 710 nm, respectively, are shown in Figure 3. The spectra are similar for the two ions. The data can be accounted for by

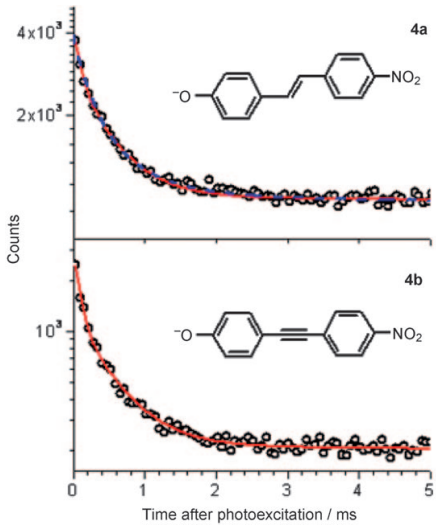

Figure 3. Time spectra at 690 nm and 710 nm for **4a** and **4b**, respectively. The exponential fit (solid red curve) includes a time constant for collision-induced dissociation (100 ms) and two sub-millisecond time constants for photodissociation (90 μs and 500 μs). The dashed blue curve in the upper panel is the result from the statistical model. The two curves overlap completely.

three exponentials. The slowest decay with a time constant of 100 ms is due to collision-induced dissociation as the ions collide with residual gas in the ring, where the pressure is about 10^{-10} mbar. This lifetime was also obtained from a separate measurement without laser excitation. The need for two sub-ms lifetimes is due to the width of the internal energy distribution of the ions, which causes a tail to the exponential; ions with lower internal energy dissociate with longer time constants. This was verified from a calculation of decay rates as a function of time based on the internal energy distribution and statistical rate constants (Arrhenius model, single dissociation pathway), see Figure 3 and the Supporting Information.[11] Hence the use of two exponentials in our analysis is merely an analytical tool to properly obtain the number of photoexcited ions (vide infra).

The dissociation results from stepwise absorption of two photons as the yield of neutrals increases to the second order with the number of photons in the laser pulse (see Figure 4). We emphasize that it is not a coherent two-photon absorption process where two photons are absorbed at the same time, as the laser pulses are several nanoseconds long. Instead, one

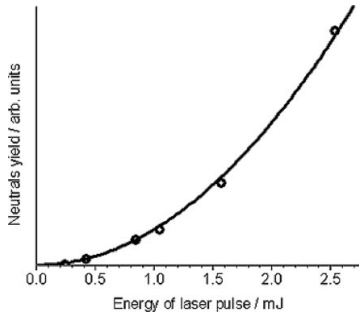

Figure 4. Yield of neutrals formed after photoexcitation as a function of the laser pulse energy for **4b** taken at 710 nm. From a fit to a parabola it is evident that the dissociation is due to two-photon absorption.

photon is absorbed followed by internal conversion to the electronic ground state, absorption of a second photon, internal conversion and finally ionic dissociation on the microseconds to millisecond timescale (Figure 3). The energy of one 690 nm photon is 1.8 eV, which is less than the transition state for NO loss of 2.8 eV as predicted by B3LYP/TZVPP calculations (Experimental Section and Supporting Information). This supports the finding that the decay is due to the absorption of two photons. The photoyield therefore depends on the absorption cross section of the room-temperature ions (first absorption) and that of these vibrationally excited ions (second absorption). The absorption cross section may depend on the internal energy of the ions in which case the two absorption cross sections are not identical.

From fits to the time spectra it was possible to extrapolate back to time zero, defined as the time when the laser was fired. This allowed us to obtain the total number of photoexcited ions for each wavelength used (relative, not absolute, numbers) and subsequently deduce the absorption from this information.[12] The number of photoexcited ions is proportional to the area under the fitted curve, not including the collision-induced dissociation seen as the base level reached after a couple of milliseconds. This area (time constant multiplied by the pre-exponential factor) was divided by the neutrals yield directly before photoexcitation to correct for changes in the ion-beam intensity and by the square of the number of photons in the laser pulse.[1]

[1] *The spectrum of **4a** reported in ref. [7] arises from an erroneous one-photon analysis and as a result the shape is different. The band maximum is red-shifted from 660 nm to 685 nm with the use of two-photon analysis and a narrower band is obtained.*

The gas-phase absorption spectra are shown in Figure 5. One point represents the absorption cross section of room-temperature ions multiplied by that of ions that have absorbed one photon. Two Gaussian functions are fitted to the data. The

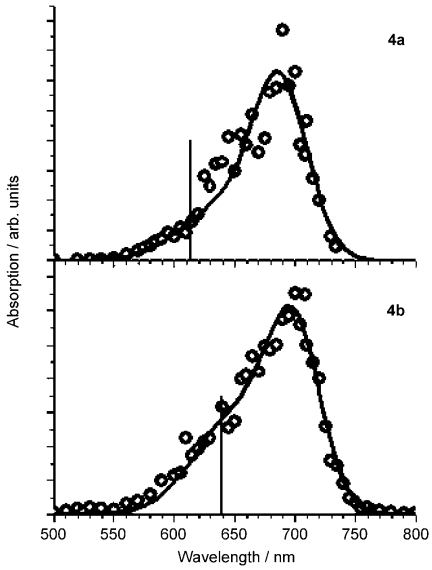

Figure 5. Gas-phase absorption spectra of **4a** and **4b**, including Gaussian fits to the data points. The lowest energy absorption maximum is at 685 nm and 695 nm for **4a** and **4b**, respectively. The solid vertical lines are the theoretical results.

lowest energy absorption maximum is at 685 and 695 nm for **4a** and **4b**, respectively, and the band width is around 80 nm. Hence the alkyne bridge results in a red-shift in the CT absorption as compared to the alkene bridge. In other words the coupling between the donor and acceptor groups is decreased for the alkyne bridge relative to the alkene one.

Theoretical results obtained with the CC2 coupled-cluster method for the planar structure are presented in Figure 5 by bars. The calculated vertical excitation energies (613 and 639 nm for **4a** and **4b**, respectively) are 0.16–0.22 eV higher than the experimental band maxima, but the red-shift from **4a** to **4b** is correctly predicted. Again a difference between theory and experiment could be due to a change in absorption cross section after absorption of the first photon since the experimental absorption spectrum depends on two cross sections while the calculation only accounts for the absorption of the first photon.

In acetonitrile (MeCN) solution, both absorption maxima are blue-shifted to 542 and 497 nm for the sodium salts of **4a** and **4b**, respectively (see Figure 6). In methanol (MeOH), the sodium salt of **4a** exhibits an absorption maximum at 435 nm,[7] while the sodium salt of **4b** absorbs at 408 nm. Thus, in both solvents the absorption maximum of **4a** lies lower in energy than that of **4b** in contrast to the situation in

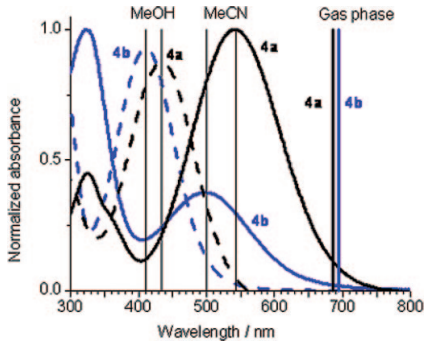

Figure 6. Solution-phase, MeCN (solid curve) and MeOH (dashed curve), absorption spectra of the sodium phenolates of **4a** (black curve) and **4b** (blue curve). In both solvents, the blue-shift from **4a** to **4b** is 0.2 eV. The gas-phase absorption maxima are illustrated by the two solid vertical lines on the right. The other four lines represent the band maxima of the solution absorption spectra. The normalization of the spectra in methanol was performed based on a higher energy absorption maximum that is not shown.

vacuo. The larger solvent blue-shift of **4b** is most likely due to the larger change in dipole moment (18.3 D) compared to that of **4a** (12.6 D), as predicted by the CC2 calculations (see Figure 7 for the molecular orbitals). The hypsochromic solvent shift is the result of an excitation-induced CT that works against the electric field of the solvent dipoles.

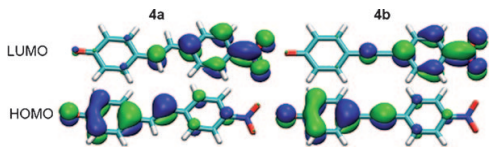

Figure 7. State-averaged (S_0, S_1) natural orbitals of **4a** (left) and **4b** (right). The S_1 excited state is strongly dominated by a transition from the HOMO (bottom) to the LUMO (top).

The solubility of the compounds limits solution studies to polar solvents. Anyhow, ion pairing effects would complicate the interpretation of absorption data obtained in nonpolar solvents. Such effects are totally eliminated when studying the isolated, anionic chromophores in the gas phase.

In conclusion, gas-phase absorption spectra of two *p*-nitrophenolate ions were measured to reveal the importance of the bridge between the donor and acceptor group being an alkene or alkyne unit. We find that the coupling between the donor and the acceptor group is lowest for the tolane compound as it absorbs further to the red (λ_{max} = 695 nm) than the stilbene compound (λ_{max} = 685 nm). Coupled-cluster calculations also reveal a clear red-shift (26 nm) of the vertical excitation energy from **4a** to **4b**. From solution studies, one would have drawn the opposite and wrong conclusion regarding the ability of the two spacers to convey the electronic communication in nitrophenolates. Our findings can likely be generalized to neutral solutes in the case where the dipole moment is re-

duced or reverted upon excitation. Finally, the central stilbene and tolane units belong to the series of oligo(phenylenevinylene)s (OPVs) and oligo(phenyleneethynylene)s (OPEs), respectively, which are conjugated oligomers that have been exploited widely as wires for molecular electronics.[13] The stronger electronic coupling observed for **4a** relative to **4b** is in line with the higher conductance of OPVs relative to OPEs.[14]

Experimental and Computational Methods

Experiments were performed at the electrostatic ion storage ring in Aarhus, ELISA. The setup is described in detail elsewhere.[8] Ions were produced by electrospray ionisation, stored in a 22-pole pretrap and accelerated as a bunch to 22 keV energies. Ions with the mass-over-charge of interest were selected by a magnet and injected into the ring where they circulated until they changed their kinetic-energy-to-charge ratio by dissociation. After 35 ms, the ions were irradiated by a nanosecond light pulse from a tunable EKSPLA laser. This is an Nd:YAG laser where the third harmonic (355 nm) pumps an optical parametric oscillator (OPO). The repetition rate of the experiment was 10 Hz. Lifetimes were obtained from measurements of the yield of neutrals hitting the microchannel plate (MCP) detector located at the end of the straight section opposite to the side where photoexcitation takes place.

The compounds corresponding to **4a** and **4b** were prepared according to ref. [15].

Computational Methods: CC2/aug-cc-pVTZ calculations were performed on MP2/TZVPP optimized geometries using TURBOMOLE (tm61).[16] The first-order transition state for the NO cleavage reaction for **4a** has been optimized with B3LYP/TZVPP, checked for triplet singularities and its energy corrected by the zero-point vibrational energy from the full Hessian. For the Arrhenius analysis, unscaled vibrational frequencies from B3LYP/TZVPP were used.

Acknowledgements

The Aarhus and Copenhagen groups gratefully acknowledge support from Lundbeckfonden; the San Sebastian group acknowledges funding by the Spanish MEC (FIS2007–65702-C02–01), "Grupos Consolidados UPV/EHU del Gobierno Vasco" (IT-319–07), the European Community through the e-I3 ETSF project (Contract Number 211956), Ikerbasque and by the Barcelona Supercomputing Center, "Red Espanola de Supercomputacion", SGIker ARINA (UPV/EHU), ACI-Promociona (ACI2009–1036), and ETORTEK (inanoGUNE).

Keywords: action spectroscopy · charge transfer · donor–acceptor systems · nitrophenolates · π-delocalized orbitals

[1] a) M. Brøndsted Nielsen, F. Diederich, *Chem. Rev.* **2005**, *105*, 1837; M. Gholami, R. R. Tykwinski, *Chem. Rev.* **2006**, *106*, 4997; b) M. Kivala, F. Diederich, *Pure Appl. Chem.* **2008**, *80*, 411; c) M. Kivala, F. Diederich, *Acc. Chem. Res.* **2009**, *42*, 235.

[2] L. T. Cheng, W. Tam, S. R. Marder, A. E. Stiegman, G. Rikken, C. W. Spangler, *J. Phys. Chem.* **1991**, *95*, 10643.

[3] R. Andreu, A. I. deLucas, J. Garin, N. Martin, J. Orduna, L. Sanchez, C. Seoane, *Synth. Met.* **1997**, *86*, 1817.

[4] A. S. Andersson, F. Diederich, M. Brøndsted Nielsen, *Org. Biomol. Chem.* **2009**, *7*, 3474.

[5] Proceeding from a triene to a diethynylethene bridge in $(alkyl)_2NC_6H_4$-bridge-$C_6H_4NO_2$ chromophores results in a blue-shifted CT absorption in solution, while proceeding from the diethynylethene to a triyne bridge instead results in a red-shifted CT absorption; see: a) L. T. Cheng, W. Tam, S. R. Marder, A. E. Stiegman, G. Rikken, C. W. Sprangler, *J. Phys. Chem.* **1991**, *95*, 10643; b) R. R. Tykwinski, F. Diederich, B. Gramlich, P. Seiler, *Helv. Chim. Acta* **1996**, *79*, 634; c) B. Traber, J. J. Wolff, F. Rominger, T. Oeser, R. Gleiter, M. Goebel, R. Wortmann, *Chem. Eur. J.* **2004**, *10*, 1227.

[6] a) E. M. Kosower, *J. Am. Chem. Soc.* **1958**, *80*, 3267; b) K. Dimroth, A. Schweig, C. Reichard, *Justus Liebigs Ann. Chem.* **1963**, *669*, 95; c) M. J. Kamlet, R. W. Taft, *J. Am. Chem. Soc.* **1976**, *98*, 377; R. W. Taft, M. J. Kamlet, *J. Am. Chem. Soc.* **1976**, *98*, 2886; d) M. J. Kamlet, J. L. Abboud, R. W. Taft, *J. Am. Chem. Soc.* **1977**, *99*, 6027; e) R. R. Pappalardo, E. S. Marcos, M. F. Ruiz-López, D. Rinaldi, J. L. Rivali, *J. Am. Chem. Soc.* **1993**, *115*, 3722; f) D. Laage, W. H. Thompson, M. Blanchard-Desce, J. T. Hynes, *J. Phys. Chem. A* **2003**, *107*, 6032; g) C. Reichardt, *Pure Appl. Chem.* **2008**, *80*, 1415; h) F. Bureš, O. Pytela, F. Diederich, *J. Phys. Org. Chem.* **2009**, *22*, 155.

[7] M. B. S. Kirketerp, M. Å. Petersen, M. Wanko, L. A. E. Leal, H. Zettergren, F. M. Raymo, A. Rubio, M. Brøndsted Nielsen, S. Brøndsted Nielsen, *ChemPhysChem* **2009**, *10*, 1207.

[8] a) S. P. Møller, *Nucl. Instrum. Meth. A* **1997**, *394*, 281; b) J. U. Andersen, P. Hvelplund, S. Brøndsted Nielsen, S. Tomita, H. Wahlgreen, S. P. Møller, U. V. Pedersen, J. S. Forster, T. J. D. Jørgensen, *Rev. Sci. Instrum.* **2002**, *73*, 1284.

[9] K. Støchkel, U. Kadhane, J. U. Andersen, A. I. S. Holm, P. Hvelplund, M. B. S. Kirketerp, M. K. Larsen, M. K. Lykkegaard, S. Brøndsted Nielsen, S. Panja, H. Zettergren, *Rev. Sci. Instrum.* **2008**, *79*, 023107.

[10] a) S. C. Xu, M. C. Lin, *J. Phys. Chem. B* **2005**, *109*, 8367; b) G. Fayet, L. Joubert, P. Rotureau, C. Adamo, *J. Phys. Chem. A* **2008**, *112*, 4054.

[11] J. U. Andersen, H. Cederquist, J. S. Forster, B. A. Huber, P. Hvelplund, J. Jensen, B. Liu, B. Manil, L. Maunoury, S. Brøndsted Nielsen, U. V. Pedersen, J. Rangama, H. T. Schmidt, S. Tomita, H. Zettergren, *Phys. Chem. Chem. Phys.* **2004**, *6*, 2676.

[12] J. A. Wyer, A. Ehlerding, H. Zettergren, M. B. S. Kirketerp, S. Brøndsted Nielsen, *J. Phys. Chem. A* **2009**, *113*, 9277.

[13] a) J. M. Tour, *Acc. Chem. Res.* **2000**, *33*, 791; b) N. Robertson, C. A. McGowan, *Chem. Soc. Rev.* **2003**, *32*, 96; c) K. Nørgaard, M. Brøndsted Nielsen, T. Bjørnholm, *Functional Organic Materials*, Wiley-VCH, Weinheim, **2007**, 353–392; d) K. Moth-Poulsen, T. Bjørnholm, *Nat. Nanotechnol.* **2009**, *4*, 551.

[14] a) J. G. Kushmerick, D. B. Holt, S. K. Pollack, M. A. Ratner, J. C. Yang, T. L. Schull, J. Naciri, M. H. Moore, R. Shashidhar, *J. Am. Chem. Soc.* **2002**, *124*, 10654; b) L. T. Cai, H. Skulason, J. G. Kushmerick, S. K. Pollack, J. Naciri, R. Shashidhar, D. L. Allara, T. E. Mallouk, T. S. Mayer, *J. Phys. Chem. B* **2004**, *108*, 2827; c) R. Huber, M. T. González, S. Wu, M. Langer, S. Grunder, V. Horhoiu, M. Mayor, M. R. Bryce, C. S. Wang, R. Jitchati, C. Schönenberger, M. Calame, *J. Am. Chem. Soc.* **2008**, *130*, 1080.

[15] M. Å. Petersen, E. Deniz, M. Brøndsted Nielsen, S. Sortino, F. M. Raymo, *Eur. J. Org. Chem.* **2009**, 4333.

[16] TURBOMOLE V6.1 **2009**, a development of University of Karlsruhe and Forschungszentrum Karlsruhe GmbH, 1989–2007, TURBOMOLE GmbH. since 2007; available from http://www.turbomole.com.

Received: June 8, 2010
Published online on August 2, 2010

Tetrahedron 64 (2008) 11475–11479

Contents lists available at ScienceDirect

Tetrahedron

journal homepage: www.elsevier.com/locate/tet

V

Upon the intrinsic optical properties of oligo(*p*-phenyleneethynylene)s (OPEs). Synthesis of OPE3 for experimental gas-phase absorption studies

Torben Ryhding [a], Maj-Britt Suhr Kirketerp [b], Umesh Kadhane [b], Morten Køcks Lykkegaard [b], Subhasis Panja [b], Steen Brøndsted Nielsen [b,*], Mogens Brøndsted Nielsen [a,*]

[a] Department of Chemistry, University of Copenhagen, Universitetsparken 5, DK-2100 Copenhagen Ø, Denmark
[b] Department of Physics and Astronomy, University of Aarhus, Ny Munkegade, DK-8000 Aarhus C, Denmark

ARTICLE INFO

Article history:
Received 5 June 2008
Accepted 20 August 2008
Available online 27 August 2008

Keywords:
Cross-coupling
Electrostatic interactions
Ionization energy
OPE
Spectroscopy

ABSTRACT

A new oligo(*p*-phenyleneethynylene) (OPE3) was synthesized by step-wise Pd-catalyzed cross-coupling reactions. The molecule incorporates an amine functionality, which allows for transfer of the protonated molecule to the gas phase by electrospray ionization leaving the OPE entity neutral. This method has allowed for the first experimental gas-phase absorption spectrum of an OPE3 by action spectroscopy, employing an electrostatic ion storage ring in combination with a laser system. The studies reveal the effect of having a positive charge in proximity to the conjugated backbone of OPE3 in the absence of any interfering solvent molecules. In addition, ionization energies and electron affinities of OPE2–OPE17 were calculated at the density functional theory (DFT) level.

1. Introduction

Conjugated polymers have found wide applications in materials chemistry as laser dyes, light-emitting diodes, organic conductors, photoconductors and nonlinear optical (NLO) materials.[1] Their materials' properties are to a large extent determined by the optical band gap. The poly(*p*-phenyleneethynylene)s (PPEs) represent one type of conjugated polymers that by suitable functionalization can be employed, for example, for explosive detection or polarizers for LC displays.[2] In the conjugated oligomer approach,[3] the optical properties of a series of monodisperse oligomers are investigated and then extrapolated to ideal infinite polymers. These conjugated oligomers are interesting in their own right, for example, as molecular wires for molecular electronics.[4]

One challenge is to make meaningful comparisons between experimental excitation energies obtained in solution or in the solid state and those calculated by quantum chemical means on isolated molecules. Intermolecular or molecule–solvent interactions as well as solid-state packing effects may perturb the electronic structure and cause a shift in the transition energy. This problem calls for studies on isolated molecules in the gas phase, free of a disturbing environment. However, often the macromolecules are too fragile to be evaporated for gas-phase absorption spectroscopy. Instead charged chromophores can often be brought in the gas phase by electrospray ionization (ESI) and their absorption can then be measured by sophisticated action spectroscopy techniques, that is, absorption is monitored by a detection of ionic fragmentation. In Aarhus, we use the electrostatic ion storage ring, ELISA,[5] as a gas-phase optical cell for such measurements. As an example, several biochromophores have been investigated using this approach, shedding light on absorption tuning by protein interactions.[6]

For investigating neutral chromophores by this method, we need to attach a charged group, a so-called spectator charge, to allow for electrospray ionization. Otherwise the chromophore itself would become charged under the conditions. This spectator charge should be placed at a remote position if the goal is to reveal the intrinsic properties of the neutral chromophore; i.e., the spectator charge should for this purpose be placed at a position at which it does not interfere with the chromophore. On the other hand, the method also allows us to investigate systematically the influence of approaching a positive or negative charge to the chromophore. We became interested to explore the properties of oligo(*p*-phenyleneethynylene)s (OPEs, Fig. 1) and present here the synthesis of an OPE3 incorporating an amino group as protonation site. The first experimental gas-phase absorption spectrum was recorded of this OPE under the influence of a positive ammonium group as spectator charge. The result of this nontrivial experiment can be compared directly with quantum chemical calculations. In addition, the

* Corresponding authors.
E-mail addresses: sbn@phys.au.dk (S.B. Nielsen), mbn@kiku.dk (M.B. Nielsen).

0040-4020/$ – see front matter © 2008 Elsevier Ltd. All rights reserved.
doi:10.1016/j.tet.2008.08.068

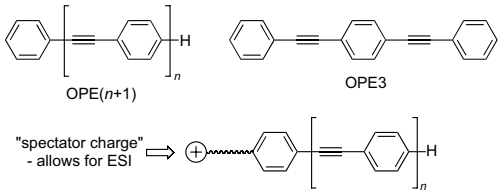

Figure 1. Oligo(*p*-phenyleneethynylene)s (OPEs). To allow for electrospray ionization (ESI), a charged group is attached, a so-called spectator charge.

intrinsic properties of OPEs were investigated in a computational study of ionization energies and electron affinities.

2. Results and discussion

2.1. Synthesis

The synthesis of the OPE3 model compound is shown in Scheme 1. We chose to attach an amine functionality, being precursor for an ammonium spectator ion, by an ethyl linker to the chromophore. First, a Sonogashira cross-coupling reaction[7] between phenylacetylene **1** and aryl iodide **2**[8] gave compound **3**. This compound was desilylated using K_2CO_3 in MeOH/THF, and the resulting terminal alkyne was then subjected to a cross-coupling reaction with the aryl bromide **4** to furnish the OPE3 **5**. Here the catalyst conditions for coupling of aryl bromides developed by Hundertmark et al.[9] were employed. These conditions allowed coupling of the aryl bromide **4** at 40 °C. The product **5** exhibited limited solubility, but it was soluble enough to allow for the gas-phase spectroscopic studies aimed at.

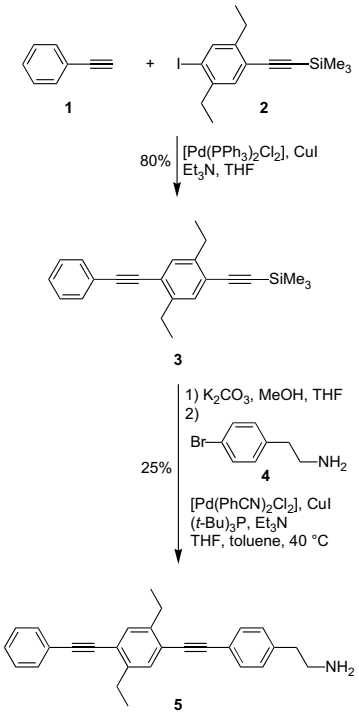

Scheme 1.

2.2. Gas-phase action spectroscopy

Gas-phase experiments on the OPE3 **5** were carried out at the ELectrostatic Ion Storage ring in Aarhus (ELISA). The experimental setup is shown in Figure 2 and has been described in detail elsewhere.[5,6] Electrospray ionization of **5** dissolved in water and methanol (1:1) with 5% acetic acid added produced the bare $\mathbf{5}\cdot H^+$ ions in the gas phase. Ions were accumulated for 0.1 s in a 22-pole ion trap in which they were thermalized from collisions with helium buffer gas. The ion bunch was accelerated to 22-keV kinetic energies, and selection of ions of interest according to their mass-to-charge ratio was then done by a bending magnet ($\mathbf{5}\cdot H^+$: m/z=378). These ions were injected into the ring and stored. The storage time in the ring was about a second, limited by collisions with residual gas at a pressure of a few times 10^{-11} mbar. Ionic dissociation in the same side as the injection side was monitored from counting the neutral particles that hit the microchannel plate detector at the end of the section. After about 35.1 ms, ions were irradiated with a 4-ns pulse of light from an EKSPLA laser that produced tunable light between 210 and 390 nm. Light absorption was monitored by an increased yield of neutrals from delayed dissociation of the photoexcited ions. A measurement of the neutrals yield divided by the number of photons in the pulse and normalized to the yield from collision induced dissociation as a function of wavelength provided the absorption spectrum.

The decay spectrum of isolated $\mathbf{5}\cdot H^+$ ions in the ring is shown in Figure 3. The revolution time of the ions in the ring is

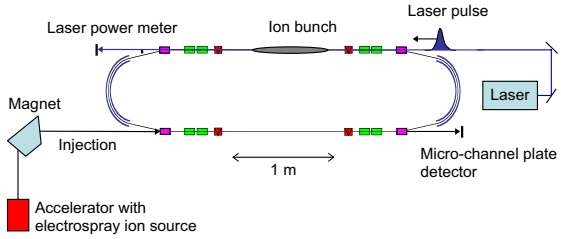

Figure 2. The electrostatic ion storage ring in Aarhus, ELISA, in combination with a laser system. The photofragment yield was measured as a function of wavelength from the signal of neutrals hitting the detector. See text for details.

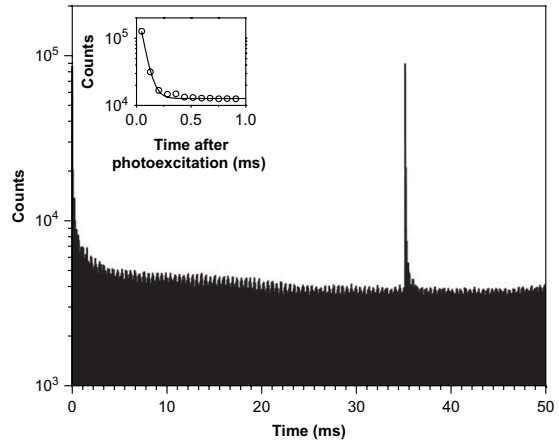

Figure 3. Decay spectrum of $\mathbf{5}\cdot H^+$ ions. After 35.1 ms of storage, the ions were photoexcited with 320-nm light. The inset shows the signal as a function of time after photoexcitation.

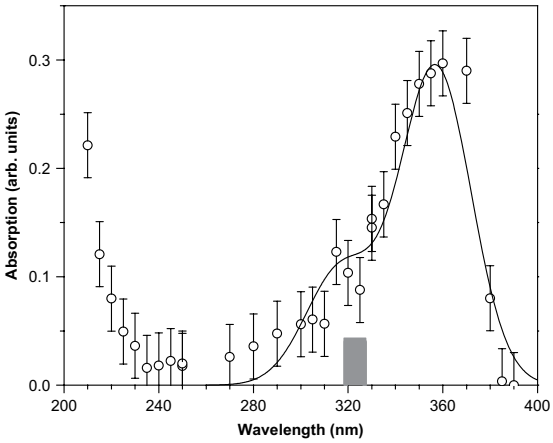

Figure 4. Absorption spectrum of $\mathbf{5}\cdot H^+$ ions isolated in vacuo. The grey box indicates the region in which λ_{max} is usually found in solution for OPE3s (see text for details).

78 μs. The high number of neutrals detected immediately after injection is due to metastable ions that have been excited during extraction from the ion trap. After a few milliseconds, the signal is dominated by collisional decay in the ring. After 35.1 ms, the ions were photoexcited with 320-nm light, which resulted in a large number of neutrals from delayed ionic dissociation. The decay is due to one-photon absorption according to a power dependence study (data not shown) and is well-described by an exponential with a time constant of 46 μs. From a separate experiment in which ring voltages were switched to store daughter ions,[10] the dominant reaction channel was found to be loss of ammonia.

In Figure 4 we present the absorption spectrum of bare $\mathbf{5}\cdot H^+$ ions. The gas-phase spectrum reveals maximum absorption at λ_{max}=357 nm, a shoulder at ca. 317 nm and an absorption band with maximum below 210 nm, the lower limit of the laser. Previous solution studies (in hexane) on the parent unsubstituted OPE3 revealed an absorption maximum at 319 nm and a shoulder at 338 nm.[11] In chloroform, absorption at 322 nm was reported and in dioxane at 320 nm.[12] For compound **6** incorporating two ethyl substituents at the central ring, a slightly redshifted absorption maximum at 327 nm in dichloromethane was reported.[13] It is noticed that the absorption band of the neutral chromophore in solution phase is in between the two bands observed for the cation in gas phase. Since a small redshift of the absorption is expected if the cation is dissolved in an apolar solvent, the difference between the absorption of the cation and neutral chromophore must be ascribed to the presence of the charged ammonium group. In other words, the ammonium group is not an innocent spectator when placed at the current position. A simple explanation of the two bands of the cation is an asymmetric charge distribution in the excited state: either the active electron is closer to the positive charge in the excited state than in the ground state or it has moved in the opposite direction, away from the charge. In the first case, we have an excited state that is stabilized more than the ground state and in the second a ground state that is stabilized more than the excited state by the presence of the charge. This model would result in one band to the blue and one to the red relative to the neutral chromophore. To test this idea, we plan in the future to place an ammonium group symmetrically at both sides of the chromophore, in which case only a single band is expected. In another approach, the spectator charge is to be placed at a more remote position in order not to interfere with the absorption properties.

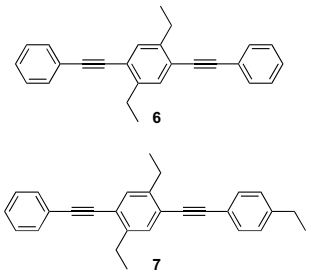

James et al.[14] have calculated the excitation energy of the parent OPE3 and obtained a value of 360 nm using time-dependent density functional theory (TD-DFT) and a value of 365 nm at the ZINDO/S level. We also performed TD-DFT calculations (B3LYP/6-311++G*) on B3LYP/6-31G(d) geometry-optimized structures using the Gaussian 03 program package.[15] The calculated value for the neutral, parent OPE3 is 367 nm, while the ethyl-substituted OPE3s **6** and **7** exhibit slightly redshifted values of 370 and 374 nm, respectively. Despite the fact that the calculated values are close to the experimental one, they still seem to overestimate the intrinsic absorption maximum as the experimental value is influenced by the positive charge in proximity to the conjugated system.

2.3. Computational study: ionization energies and electron affinities

A selection of OPE(n)s (n=2–17) was geometry-optimized at the semi-empirical PM3 level. The structure of fully planar OPE17 is shown in Figure 5. Then, single-point energies were calculated at the B3LYP/6-311++G(2d,p) level on the neutral, radical cation and radical anion structures (using the geometries of the neutral molecules). From these data, the vertical ionization energies (IE) and vertical electron affinities (EA) were calculated and collected in Table 1. These energies are plotted as a function of the inverse total number (N) of π-electrons in Figure 6. Linear extrapolation to an infinite PPE provides an IE of 5.80 eV. Hovewer, it should be noted that the points do not follow a straight line perfectly, and this IE of an infinite polymer seems to be slightly overestimated. For comparison, an experimental IE of PPE was determined to be 6.3 eV with ultraviolet photoelectron spectroscopy and 5.8 eV with cyclic voltammetry.[16] By extrapolation of the calculated data, an EA of 2.34 eV for PPE is obtained. Deviation from a perfect straight line is

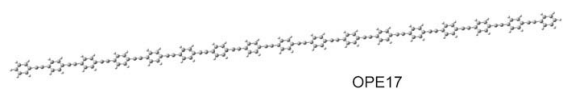

Figure 5. PM3-optimized structure of planar OPE17.

Table 1
Vertical ionization energies (IE) and electron affinities (EA) calculated at the B3LYP/6-311++G(2d,p) level on PM3 geometry-optimized neutral structures

	OPE2	OPE3	OPE4	OPE5	OPE6	OPE7	OPE8	OPE9
IE/eV	7.60	7.02	6.72	6.54	6.41	6.31	6.27	6.19
EA/eV	0.17	0.84	1.19	1.40	1.57	1.70	1.79	1.88
	OPE10	OPE11	OPE12	OPE13	OPE14	OPE15	OPE16	OPE17
IE/eV	6.15	6.14	6.05	6.03	6.01	5.94	5.93	6.01
EA/eV	1.94	1.97	2.02	2.06	2.09	2.12	2.15	2.16

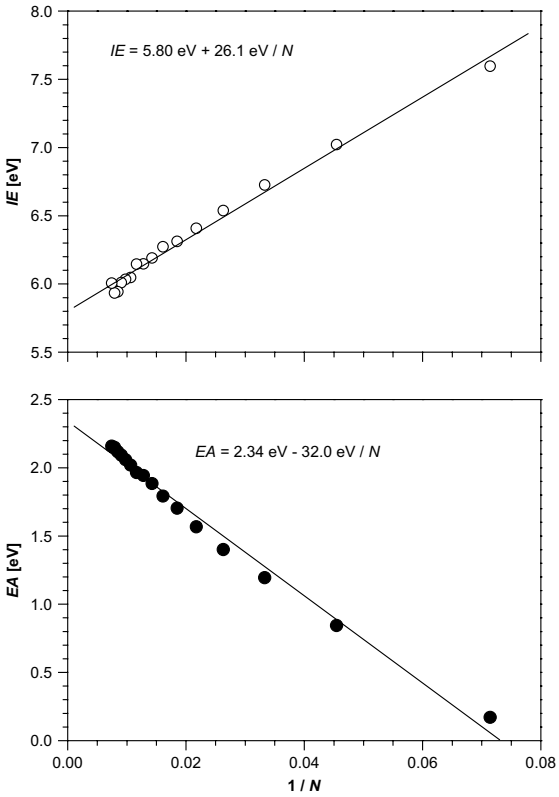

Figure 6. Ionization energies (IE) and electron affinities (EA) for OPEs as a function of the inverse number of π-electrons (*N*).

more significant here and may underestimate the EA of PPE by ca. 0.1 eV. Subtracting the linearly extrapolated IE and EA values gives a band gap of 3.46 eV for PPE. This value is the estimated band gap of an isolated, completely planar PPE. For comparison, alkyl-substituted PPEs typically exhibit a broad unresolved absorption in solution at 384/388 nm (ca. 3.2 eV), and an absorption in films at 435 nm (2.9 eV).[2,17]

3. Conclusions

An OPE3 incorporating an amino functionality was prepared by step-wise cross-coupling reactions. The amino group allows for transfer of the chromophore as the protonated species to the gas phase by electrospray ionization. Electrospray ionization in combination with the storage ring technique prevents the necessity for evaporating the molecules in order to perform gas-phase spectroscopy and we have measured the first experimental gas-phase absorption spectrum of an OPE3 ammonium cation. The major absorption maximum is found to be significantly redshifted in the gas phase as compared to solution phase, which is ascribed to the stabilizing effect of the excess charge on the diffuse $\pi\pi^*$ state. The method is by no way trivial and the optical properties of other OPE model compounds await to be investigated in future work. In addition, we have calculated vertical ionization energies and electron affinities for a large selection of OPEs and predict by extrapolation values of 5.80 and 2.34 eV, respectively, for an isolated, completely planar PPE.

4. Experimental

4.1. General experimental procedures

Dry solvents were provided by an Innovative Technology Puresolv apparatus, or dried over 4 Å molecular sieves. Merck silica gel (0.040–0.063 mm) was used for flash column chromatography. TLC was performed on silica gel coated aluminium foils (Merck alumina foil 60 F_{254}). NMR spectra were obtained using a Varian 300 MHz NMR spectrometer at room temperature. Fast Atom Bombardment (FAB) mass spectra were obtained on a Jeol JMS-HX 110 Tandem Mass Spectrometer in the positive ion mode. Electrospray ionization spectra were recorded on a ZAB-EQ (VG-Analytical) instrument. Melting points were measured on a Reichert melting point apparatus equipped with a microscope and are uncorrected. Elemental analyses were performed at Department of Chemistry, University of Copenhagen.

4.2. 1,4-Diethyl-2-(phenylethynyl)-5-(trimethylsilylethynyl)-benzene (3)

To a solution of the iodide **2** (0.51 g, 1.43 mmol), $Pd(PPh_3)_2Cl_2$ (50 mg, 0.07 mmol) and CuI (24 mg, 0.13 mmol) in THF (10 mL) were added phenylacetylene **1** (0.20 mL, 1.7 mmol) and Et_3N (2 mL). The reaction mixture was stirred for 24 h under Ar. Then, it was diluted with CH_2Cl_2 (20 mL) and washed with saturated aqueous NH_4Cl (20 mL). The organic phase was dried with $MgSO_4$, filtered and concentrated in vacuo. Purification by flash chromatography (SiO_2, *c*-hexane) gave the product as a colourless oil (0.38 g, 80%). ^{1}H NMR ($CDCl_3$, 300 MHz) δ=0.28 (s, 9H, CH_3), 1.27 (t, J=7.5 Hz, 3H, CH_3), 1.30 (t, J=7.4 Hz, 3H, CH_3), 2.79 (q, J=7.5 Hz, 2H, CH_2), 2.84 (q, J=7.4 Hz, 2H, CH_2), 7.36 (m, 5H, Ar), 7.54 (m, 2H, Ar). ^{13}C NMR ($CDCl_3$, 75 MHz) δ=0.23, 14.77, 14.95, 27.37, 27.40, 88.38, 94.30, 99.36, 104.07, 122.54, 122.87, 123.66, 128.53, 128.63, 131.72, 131.74, 132.07, 143.56, 144.19. MS (FAB): m/z=330 (M^+). Anal. Calcd for $C_{23}H_{26}Si$: C, 83.57; H, 7.93. Found: C, 83.51; H, 8.17.

4.3. 1-[4-(2-Aminoethyl)phenylethynyl]-2,5-diethyl-4-(phenylethynyl)benzene (5)

Compound **3** (0.121 g, 0.367 mmol) was treated with K_2CO_3 (0.20 g, 1.4 mmol) in a MeOH/CH_2Cl_2 mixture (1:1, 10 mL). After complete desilylation (judged by TLC, approx. 45 min), the mixture was diluted with Et_2O (20 mL) and washed with water (2×20 mL). The organic phase was dried with $MgSO_4$, filtered and concentrated in vacuo to furnish the deprotected alkyne. $Pd(PhCN)_2Cl_2$ (25 mg, 0.065 mmol) and CuI (6 mg, 0.03 mmol) were dissolved in THF (1 mL) and toluene (1 mL). Then, *i*-Pr_2NH (0.34 mL) and *t*-Bu_3P (0.25 mL, 10% in hexanes) were added to this catalyst mixture. The catalyst solution was then added to the deprotected alkyne and aryl bromide **4** (0.109 g, 0.55 mmol) under argon, and the reaction mixture was left overnight at 40 °C. The mixture was concentrated in vacuo, whereupon the residue was dissolved in warm toluene. Pentane was added to precipitate the product as a slightly yellow solid (37 mg, 25%) of limited solubility. Mp 180 °C (decomp.). ^{1}H NMR (DMSO-d_6, 300 MHz): δ=1.21 (m, 6H, CH_3), 2.75–3.03 (m, 8H, 4×CH_2), 7.21 (d, J=7.2 Hz, 2H, Ar), 7.34 (d, J=7.3 Hz, 2H, Ar), 7.44 (m, 2H, Ar), 7.50 (m, 3H, Ar). HRMS (ESI): m/z=378.2211 (MH^+); calcd for $C_{28}H_{28}N$: 378.2216.

Acknowledgements

This work was supported by Lundbeckfonden and Direktør Ib Henriksens Fond.

V

V

References and notes

1. (a) Meier, H. *Angew. Chem., Int. Ed. Engl.* **1992**, *31*, 1399; (b) *Nonlinear Optics of Organic Molecules and Polymers*; Nalwa, H. S., Miyata, S., Eds.; CRC: New York, NY, 1997.
2. Bunz, U. H. F. *Chem. Rev.* **2000**, *100*, 1605.
3. (a) *Electronic Materials: The Oligomer Approach*; Müllen, K., Wegner, G., Eds.; Wiley-VCH: Weinheim, Germany, 1998; (b) Martin, R. E.; Diederich, F. *Angew. Chem., Int. Ed.* **1999**, *38*, 1350; (c) Nielsen, M. B.; Diederich, F. *Chem. Rev.* **2005**, *105*, 1837; (d) Gierschner, J.; Cornil, J.; Egelhaaf, H.-J. *Adv. Mater.* **2007**, *19*, 173.
4. (a) Donhauser, Z. J.; Mantooth, B. A.; Kelly, K. F.; Bumm, L. A.; Monnell, J. D.; Stapleton, J. J.; Price, D. W., Jr.; Rawlett, A. M.; Allara, D. L.; Tour, J. M.; Weiss, P. S. *Science* **2001**, *292*, 2303; (b) Kubatkin, S.; Danilov, A.; Hjort, M.; Cornil, J.; Brédas, J.-L.; Stuhr-Hansen, N.; Hedegård, P.; Bjørnholm, T. *Nature* **2003**, *425*, 698; (c) Stuhr-Hansen, N.; Sørensen, J. K.; Moth-Poulsen, K.; Christensen, J. B.; Bjørnholm, T.; Nielsen, M. B. *Tetrahedron* **2005**, *61*, 12288; (d) Sørensen, J. K.; Vestergaard, M.; Kadziola, A.; Kilså, K.; Nielsen, M. B. *Org. Lett.* **2006**, *8*, 1173.
5. (a) Møller, S. P. *Nucl. Instrum. Methods Phys. Res., Sect. A* **1997**, *394*, 281; (b) Andersen, J. U.; Hvelplund, P.; Brøndsted Nielsen, S.; Tomita, S.; Wahlgreen, H.; Møller, S. P.; Pedersen, U. V.; Forster, J. S.; Jørgensen, T. J. D. *Rev. Sci. Instrum.* **2002**, *73*, 1284; (c) Andersen, L. H.; Heber, O.; Zajfman, D. *J. Phys. B: At. Mol. Opt. Phys.* **2004**, *37*, R57; (d) Brøndsted Nielsen, S.; Andersen, J. U.; Hvelplund, P.; Liu, B.; Tomita, S. *J. Phys. B: At. Mol. Opt. Phys.* **2004**, *37*, R25.
6. (a) Brøndsted Nielsen, S.; Lapierre, A.; Andersen, J. U.; Pedersen, U. V.; Tomita, S.; Andersen, L. H. *Phys. Rev. Lett.* **2001**, *87*, 228102; (b) Andersen, L. H.; Nielsen, I. B.; Kristensen, M. B.; El Ghazaly, M. O. A.; Haacke, S.; Nielsen, M. B.; Petersen, M. Å. *J. Am. Chem. Soc.* **2005**, *127*, 12347; (c) Petersen, M. Å.; Nielsen, I. B.; Kristensen, M. B.; Kadziola, A.; Lammich, L.; Andersen, L. H.; Nielsen, M. B. *Org. Biomol. Chem.* **2006**, *4*, 1546; (d) Nielsen, I. B.; Petersen, M. Å.; Lammich, L.; Nielsen, M. B.; Andersen, L. H. *J. Phys. Chem. A* **2006**, *110*, 12592; (e) Lammich, L.; Andersen, L. H.; Petersen, M. Å.; Nielsen, M. B. *Biophys. J.* **2007**, *92*, 201.
7. Sonogashira, K.; Tohda, Y.; Hagihara, N. *Tetrahedron Lett.* **1975**, *16*, 4467.
8. Flatt, A. K.; Yao, Y.; Maya, F.; Tour, J. M. *J. Org. Chem.* **2004**, *69*, 1752.
9. Hundertmark, T.; Littke, A. F.; Buchwald, S. L.; Fu, G. C. *Org. Lett.* **2000**, *2*, 1729.
10. Støchkel, K.; Kadhane, U.; Andersen, J. U.; Holm, A. I. S.; Hvelplund, P.; Kirketerp, M.-B. S.; Larsen, M. K.; Lykkegaard, M. K.; Brøndsted Nielsen, S.; Panja, S.; Zettergren, H. *Rev. Sci. Instrum.* **2008**, *79*, 023107.
11. Drefahl, G.; Plötner, G. *Chem. Ber.* **1958**, 1280.
12. Nakatsuji, S.; Matsuda, K.; Uesugi, Y.; Nakashima, K.; Akiyama, S.; Fabian, W. *J. Chem. Soc., Perkin Trans. 1* **1992**, 755.
13. Ding, C.; Babu, G.; Orita, A.; Hirate, T.; Otera, J. *Synlett* **2007**, 2559.
14. James, P. V.; Sudeep, P. K.; Suresh, C. H.; Thomas, K. G. *J. Phys. Chem. A* **2006**, *110*, 4329.
15. Frisch, M. J.; Trucks, G. W.; Schlegel, H. B.; Scuseria, G. E.; Robb, M. A.; Cheeseman, J. R.; Montgomery, J. A., Jr.; Vreven, T.; Kudin, K. N.; Burant, J. C.; Millam, J. M.; Iyengar, S. S.; Tomasi, J.; Barone, V.; Mennucci, B.; Cossi, M.; Scalmani, G.; Rega, N.; Petersson, G. A.; Nakatsuji, H.; Hada, M.; Ehara, M.; Toyota, K.; Fukuda, R.; Hasegawa, J.; Ishida, M.; Nakajima, T.; Honda, Y.; Kitao, O.; Nakai, H.; Klene, M.; Li, X.; Knox, J. E.; Hratchian, H. P.; Cross, J. B.; Adamo, C.; Jaramillo, J.; Gomperts, R.; Stratmann, R. E.; Yazyev, O.; Austin, A. J.; Cammi, R.; Pomelli, C.; Ochterski, J. W.; Ayala, P. Y.; Morokuma, K.; Voth, G. A.; Salvador, P.; Dannenberg, J. J.; Zakrzewski, V. G.; Dapprich, S.; Daniels, A. D.; Strain, M. C.; Farkas, O.; Malick, D. K.; Rabuck, A. D.; Raghavachari, K.; Foresman, J. B.; Ortiz, J. V.; Cui, Q.; Baboul, A. G.; Clifford, S.; Cioslowski, J.; Stefanov, B. B.; Liu, G.; Liashenko, A.; Piskorz, P.; Komaromi, I.; Martin, R. L.; Fox, D. J.; Keith, T.; Al-Laham, M. A.; Peng, C. Y.; Nanayakkara, A.; Challacombe, M.; Gill, P. M. W.; Johnson, B.; Chen, W.; Wong, M. W.; Gonzalez, C.; Pople, J. A. *Gaussian 03, Revision B.03*; Gaussian: Pittsburgh, PA, 2003.
16. Montali, A.; Smith, P.; Weder, C. *Synth. Met.* **1998**, *97*, 123.
17. (a) Mangel, T.; Eberhardt, A.; Scherf, U.; Bunz, U. H. F.; Müllen, K. *Macromol. Rapid Commun.* **1995**, *16*, 571; (b) Halkyard, C. E.; Rampey, M. E.; Kloppenburg, L.; Studer-Martinez, S. L.; Bunz, U. H. F. *Macromolecules* **1998**, *31*, 8655.

UV Photodissociation of Protonated Gly-Trp and Trp-Gly Dipeptides and Their Complexes with Crown Ether in an Electrostatic Ion Storage Ring

Anneli Ehlerding, Jean Ann Wyer, Henning Zettergren, Maj-Britt Suhr Kirketerp, and Steen Brøndsted Nielsen*

Department of Physics and Astronomy, Aarhus University, Ny Munkegade, DK-8000 Aarhus C, Denmark

Received: September 7, 2009; Revised Manuscript Received: November 17, 2009

Photodissociation of protonated GW, WG (G = glycine, W = tryptophan), and their complexes with 18-*crown*-6-ether (CE) was performed in an electrostatic ion storage ring using a tunable laser system. On the basis of lifetime measurements, action spectra were obtained from 210 to 360 nm. These reveal that whereas $[GW + H]^+$ absorbs maximally at ~220 nm, the absorption maximum is <210 nm for $[WG + H]^+$, which is in good accordance with density functional theory calculations that predict band maxima at 221 and 212 nm, respectively. This difference in absorption is ascribed to the ammonium group interacting with the indole ring in the case of GW, thereby lowering the energy of the excited state more than that of the ground state. A broad band at higher wavelengths is observed for WG but not for GW, which again may be linked to differences in conformational structures between the two ions. Absorption spectra for the two CE tagged ions are very similar to each other: The high-energy band is now <210 nm for both peptide ions, and they display an absorption band with a maximum at 270 nm. The crown ether targets the ammonium protons, preventing an interaction between ammonium and indole, and the photophysics of the two complexes is therefore similar. The complexes have significantly longer lifetimes with respect to dissociation than the bare ions. Finally, we report product ion mass spectra at two different excitation wavelengths, 210 and 270 nm. There are significant differences between the two peptides, and the crown ether enhances certain channels, such as the loss of CO + H_2O and the tryptophan side chain.

VI

Introduction

In photobiology, the aromatic amino acids phenylalanine, tyrosine, and tryptophan are highly important spectroscopic probes for protein conformations and dynamics.[1,2] They act as markers because of the fact that their photophysics (i.e., absorption, fluorescence, and vibrational signatures) are highly dependent on the chemical environment. To have a proper reference for the intrinsic properties, it is necessary to establish the electronic properties of amino acids without any perturbations from solvent molecules, counterions, or other amino acids. This requires gas-phase experiments on individual molecules. Developments in mass spectrometry have allowed for studies of fragile ions isolated in gas phase, and in recent years, a significant amount of spectroscopy work has been done for protonated amino acids and small protonated peptides.[3−31]

In the present work, we have subjected protonated GW and WG dipeptides (Figure 1) to photodissociation experiments using an electrostatic ion storage ring. The photoactive unit is the indole chromophore of the tryptophan residue. For a thorough discussion of the photophysics of indole and the coupling of the initially reached $\pi\pi^*$ state with other states, such as the $\pi\sigma^*$ state on ammonium and the $\pi\pi^*$ state on CO, we refer to references 3, 7, and 31.

Similar experiments were carried out on complexes between the peptide cations and 18-*crown*-6-ether (CE). Tagging the ammonium group with CE causes at least two changes: (1) The charge-transfer state located on ammonium, $\pi\sigma^*(NH_3)$, is raised in energy so that it is out of the spectral region for high wavelengths, which implies that the hydrogen loss channel is switched off.[22,23] (2) The ammonium protons are no longer mobile but stay sequestered at the nitrogen. Both of these changes affect the dissociation lifetimes and channels.

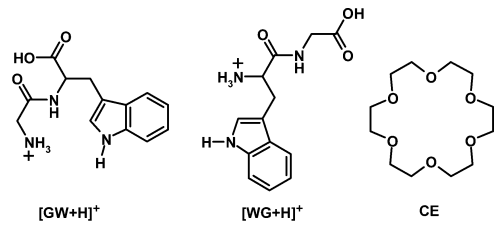

Figure 1. Structures of $[GW + H]^+$ and $[WG + H]^+$ dipeptides and 18-*crown*-6-ether.

Lifetime measurements, absorption spectra from 210 to 360 nm, and photodissociation mass spectra are presented. The results are compared with density functional theory calculations of excited states. This work is a continuation of recent studies on protonated AY and YA dipeptides (A = alanine, Y = tyrosine) that were done by our group.[23]

Experimental Section

All compounds were purchased from Sigma-Aldrich.

Experiments were carried out at the electrostatic ion storage ring in Aarhus (ELISA).[32,33] Electrospray ionization was used to produce the ions that were subsequently accumulated in a 22-pole ion trap and thermally equilibrated by collisions with a helium buffer gas therein. The ions were accelerated as an ion bunch to kinetic energies of 22 keV, and a bending magnet was used to select the appropriate ions according to their mass-to-

* Corresponding author. E-mail: sbn@phys.au.dk.

10.1021/jp9086317
Published on Web 12/03/2009

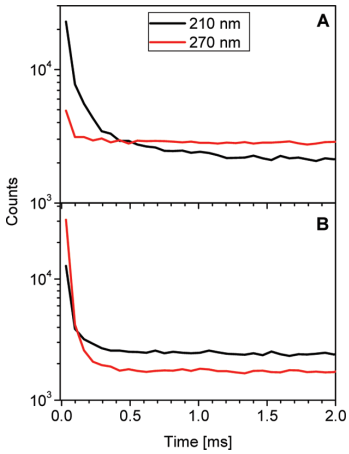

Figure 2. Time spectra of (A) $[GW + H]^+$ and (B) $[WG + H]^+$ after 210 and 270 nm photoexcitation. The time resolution is 72 μs.

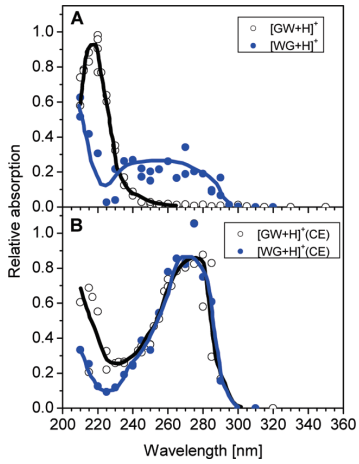

Figure 3. Absorption spectra of (A) $[GW + H]^+$ and $[WG + H]^+$ and (B) $[GW + H]^+$(CE) and $[WG + H]^+$(CE) in vacuo. Solid lines are drawn to guide the eye.

charge ratio. Following injection into the ring, the ions were stored for ~40 ms before being irradiated by a nanosecond light pulse from a tunable EKSPLA laser. This is an Nd/YAG laser where the third harmonic (355 nm) pumps an optical parametric oscillator (OPO). The visible output from this OPO is frequency doubled in a crystal providing UV light. The repetition rate of the experiment was 10 Hz. Dissociation was a result of one photon absorption according to a power-dependence study. Lifetimes were obtained from measurements of the yield of neutrals hitting the microchannel plate (MCP) detector located at the end of the straight section opposite to the side where photoexcitation was performed. It should be mentioned that because daughter ions have lower kinetic energies than those of the parent ions, they are not stored in the ring. An exception to this is dehydrogenated ions because their kinetic energies are too close to those of the parent ions to be differentiated.

In separate experiments, the ring voltages were changed at a particular time after photoexcitation to store product ions with the appropriate kinetic energy. This product ion mass spectroscopy was possible because ELISA has been equipped with pulsed power supplies of microsecond response times.[34] After a specific number of revolutions, the product ions were dumped into the MCP detector. To increase the resolution, a beam scraper was put in on one side of the ring. The signal from the detector as a function of the scaling of the ring voltages provided the product ion mass spectrum.

The pressure in the ring was a few times 10^{-11} mbar, which set an upper limit of seconds on the storage time.

Results and Discussion

Protonated GW and WG. Time spectra of $[GW + H]^+$ and $[WG + H]^+$ after photoexcitation at either 210 or 270 nm, measured by detecting the neutral fragments on one side of the ring, are shown in Figure 2. This experiment is a delayed dissociation experiment meaning that the dissociation of ions in the laser interaction region is not being sampled. Therefore, the neutrals were produced ~36 μs after photoexcitation in the first instance and then after successive rotations in the ring. Three exponentials are required to fit the data. The two fastest decays had time constants of submilliseconds, whereas the slowest decay, with a time constant of 0.5 s, is associated with collision-induced dissociation (CID) of nonirradiated ions.

The lifetime due to collisions is calculated to be 3 s on the basis of an ion speed of 10^5 m/s and an estimate of the mean free path in the ring of 3×10^5 m.[35] Please note that there is an uncertainty in the value for the collision cross section, which introduces an uncertainty in the calculated lifetime value. In addition to collisional losses, nonideal storage ring conditions could also contribute to ion losses. Nevertheless, the calculated value is close to the measured one (0.5 s). Ultimately, however, the time constant for ion losses is incidental as long as it is significantly longer than the lifetimes of the photoexcited ions (submilliseconds).

The short time constant is associated with ions that after photoexcitation return to the electronic ground state and then dissociate statistically. It is possible that the second decay is due to excitation into a triplet state, but it is more likely a tail associated with the first decay due to the width of the energy distribution, as has been described in detail previously.[21,36] From fits to the experimental data, it was possible to extrapolate back to time zero, defined as the time when the laser was fired, to obtain the total number of photoexcited ions for each wavelength used (relative, not absolute, number) and subsequently deduce the absorption from this information.

Figure 3A shows the absorption spectra for the two peptide ions. It can be seen that GW displays an absorption band with a maximum at 220 nm, whereas the usual band seen for W at higher wavelengths is absent. In our experiment, we rely on the dissociation that occurs on a time scale that is longer than 10 μs but still shorter than the time scale for CID to identify absorption. Ions that have lost hydrogen because of a crossing from the initially reached $\pi\pi^*$ state to the $\pi\sigma^*(NH_3)$ state are stored in the ring along with the parent ions, but most of the radical cations likely have too little internal energy for further dissociation at the high wavelengths because the hydrogen carries away some kinetic energy, as has been explained in detail for AY and YA.[23] In the case of WG, the high-energy absorption band is below 210 nm (the lowest accessible wavelength in our experiment), but a broad absorption band is now seen between 220 and 290 nm.

Because the lifetimes are short and comparable to ion revolution times (72 μs), it is possible that we, at low wavelengths, obtain too small an absorption, which will skew the absorption band to the red. This problem is largest for WG

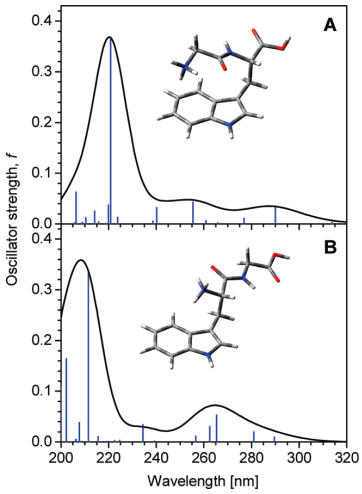

Figure 4. Calculated absorption spectra of (A) $[GW + H]^+$ and (B) $[WG + H]^+$.

because its lifetime is shorter than that of GW at low wavelengths. (See Figure 2.) However, any appropriate correction along this line will still result in the absorption band of GW being to the red of that of WG and WG absorbing maximally below 210 nm.

An explanation for the difference in absorption in the low wavelength region may be linked to the conformation of the ions: Fujihara et al.[28,29] have shown that the structure of $[WG + H]^+$ is different from that of $[GW + H]^+$ or $[AW + H]^+$. In the latter two, the ammonium group interacts directly with the indole π-electron cloud, which has the effect of red-shifting the L_a band. The conformation also determines the electronic coupling between the $\pi\pi^*$(indole) and $\pi\sigma^*(NH_3)$ states. Because the ammonium group is close to the indole for GW, there is most likely more H loss for GW than for WG, resulting in $[GW]^{+\bullet}$ radical cations that are too cold for further dissociation. The absence of a peak in the high wavelength region for GW is therefore the result of an instrumental limitation in this kind of action spectroscopy.

Time-dependent density functional theory calculations[37] (TDB3LYP/6-311++g(2d,p)//B3LYP/6-31G(d) level of theory) of the most stable $[WG + H]^+$ structure found by Fujihara et al.[28] predict the absorption band maximum to be at 212 nm, whereas a $[GW + H]^+$ structure similar to the most stable $[AW + H]^+$ structure (isomer IIIa in ref 28) has the maximum at 221 nm (Figure 4). These results are in full agreement with our experimental findings, which suggests that these species correspond to the most abundant isomers under the present experimental conditions. It should be noted that, in general, predictions made by TDDFT calculations can be off by a few tenths of an electronvolt, and the agreement should thus be taken with some caution. However, the 10 nm shift of the absorption band maximum is well-reproduced at a lower level of theory (TDB3LYP/6-31G(d)), although the predicted values are slightly shifted toward shorter wavelengths (211 and 201 nm for $[GW + H]^+$ and $[WG + H]^+$, respectively).

Next, we recorded photodissociation mass spectra. Representative examples at 210 and 270 nm are shown in Figures 5 and 6. In this experiment, we sample fragment ions formed up to ~24 μs after photoexcitation. Note that the lifetime experiment first sampled ionic dissociation after 36 μs. The spectra

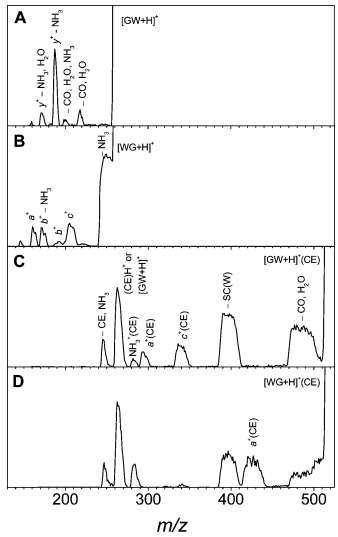

Figure 5. Photodissociation mass spectra of (A) $[GW + H]^+$ (m/z 262), (B) $[WG + H]^+$, (C) $[GW + H]^+$(CE) (m/z 526), and (D) $[WG + H]^+$(CE) after 210 nm photoexcitation. The −SC(W) label refers to the loss of the tryptophan side chain. An assignment labeled, for example, −CO, H_2O, means the loss of both CO and H_2O.

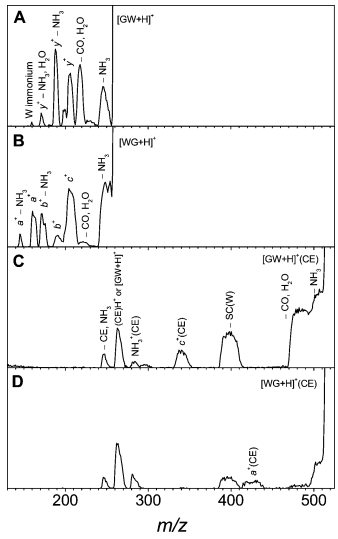

Figure 6. Photodissociation mass spectra of (A) $[GW + H]^+$ (m/z 262), (B) $[WG + H]^+$, (C) $[GW + H]^+$(CE) (m/z 526), and (D) $[WG + H]^+$(CE) after 270 nm photoexcitation. The −SC(W) label refers to the loss of the tryptophan side chain. An assignment labeled, for example, −CO, H_2O, means the loss of both CO and H_2O.

were calibrated on the basis of a comparison with previously published mass spectra by Fujihara et al.[28] More lower-mass ions are formed at 210 nm than at 270 nm, which is indicative of consecutive dissociations. Significantly, the 270 nm spectrum for $[GW + H]^+$ clearly shows that the ions do indeed absorb light at this wavelength even though a band appears to be absent in the action spectrum. Note that the relative fragment ion intensities change in time because the dissociation of ions with lower and lower internal energies are being sampled. Therefore, in the lifetime experiments where fragmentation was measured on a longer time scale, ions formed after two consecutive

VI

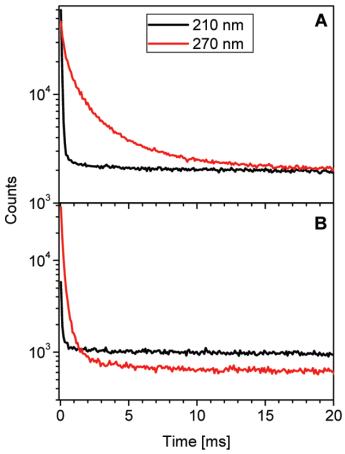

Figure 7. Time spectra of (A) $[GW + H]^+$(CE) and (B) $[WG + H]^+$(CE) after 210 and 270 nm photoexcitation. The time resolution is 92 μs.

dissociations, such as the y^+-NH_3 ions, are less dominant (data not shown). Much more ammonia loss is observed at 210 nm than at 270 nm for $[WG + H]^+$. This is likely to be accounted for by the more favored population of the $\pi\sigma^*(NH_3)$ state at 210 nm, followed by prompt dissociation along the repulsive C−N coordinate. The fragmentation patterns of the two peptide ions are similar to those previously reported for $[AW + H]^+$, $[LW + H]^+$, $[WL + H]^+$, and $[GWG + H]^+$ after UV photoexcitation[24−28] and will not be further commented on here.

Crown Ether Complexes. Sample time spectra for $[GW + H]^+$(CE) and $[WG + H]^+$(CE) after 210 and 270 nm photoexcitation are shown in Figure 7. Clearly, the time constants for dissociation are now longer than those for the bare ions by an order of magnitude or so. It should also be noticed that the excited GW complex lives longer than the WG one, which implies that the barrier for dissociation is higher for $[GW + H]^+$(CE) than for $[WG + H]^+$(CE), the prefactor is lower, or both. The crown ether tag prohibits hydrogen loss, and as a result, we sample the decay of vibrationally hot intact ions.

The lifetime spectra were used to obtain the absorption spectra in Figure 3B. The high-energy band now has its maximum below 210 nm for both ions, which is in accordance with open structures where there is no interaction between the ammonium group and the indole ring. This is in agreement with previous measurements on protonated tryptophan and tryptamine that both absorb maximally below 210 nm, either with or without crown ether attached.[22,38] For comparison, tryptophan displays an absorption band at 216 nm (^1B_b transition) in solution,[39] and hence hydration causes a red shift of >6 nm (0.2 eV). The lower-energy band is more or less identical for the two ions with a band maximum at ~270 nm, which is again in accordance with similar open structures.

Photodissociation mass spectra taken at 210 and 270 nm of $[GW + H]^+$(CE) and $[WG + H]^+$(CE) are shown in Figures 5 and 6 (fragments formed up to ~31 μs). Except for changes in relative intensities, the spectra are quite similar at the two wavelengths. One important peak could be from either formation of $(CE)H^+$ (*m/z* 265) or $[peptide + H]^+$ (*m/z* 262); we cannot tell which one is formed because the difference in mass is three and our mass resolution and calibration are too poor. The peaks at *m/z* 281 and *m/z* 245 can be assigned to $CE(NH_3)^+$ and $[peptide + H]^+ - NH_3$, respectively. In the latter case, the ion is formed after the loss of both CE and NH_3. Another dominant channel is the loss of both H_2O and CO (*m/z* 480). This is a much more important pathway for these ions than for the bare peptide ions. The $\pi\sigma^*(NH_3)$ state has moved out of the spectral region because of CE attachment, and it is therefore now more likely for the electron to jump to the $\pi\pi^*$(COOH) state. Earlier explanations for the prompt loss of H_2O and CO involve proton transfer subsequent or concomitant to the population of an antibonding orbital on the carboxylic acid group.[7] The channel leading to the loss of these two molecules is observed to be more important for $[GW + H]^+$(CE) than for $[WG + H]^+$(CE), which is due to the indole being closer to the carboxylic acid group in the former. A further channel of significance, which also arises from the population of the $\pi\pi^*$(COOH) state, is the loss of the W side chain. As discussed earlier for protonated tryptophan, the resultant radical character of both the indole ring and the carboxylic carbon drives the $C_\alpha - C_\beta$ bond breakage.[7] A similar finding was obtained for $[AY + H]^+$(CE) and $[YA + H]^+$(CE), where photoexcitation led to the loss of the tyrosine side chain.[23] Finally, an intriguing peak at *m/z* 338 in the GW spectrum appears to suggest the formation of c^+(CE) ions. This may be a result of the electron jumping to the amide group, followed by $N - C_\alpha$ bond breakage; the photoactive electron essentially does the same job as the electrons involved in the electron capture dissociation of peptide ions.[40,41] Interestingly, such charge transfer from the $\pi\pi^*$ state of indole to the amide group of the peptide backbone has been shown by Callis et al.[42] to quench fluorescence of proteins. It is unclear why $N - C_\alpha$ bond cleavage is not observed for WG.

Conclusions

To summarize, we have found that the high-energy absorption band close to 210 nm of protonated GW and WG dipeptides strongly depends on the ion conformation. An interaction between the ammonium group and the indole ring causes a red shift of the band, but this interaction can be canceled by the attachment of crown ether to ammonium. The low-energy absorption band at 270 nm is the same for the two peptides when tagged by crown ether because both peptides are in open structures with no internal ionic hydrogen bonding. Finally, the crown ether increases the importance of crossing from the initially reached $\pi\pi^*$ state to electronically excited states other than the $\pi\sigma^*$ state on ammonium, for example, the $\pi\pi^*$ states located on either the carboxylic acid or the amide.

Acknowledgment. S.B.N. gratefully acknowledges support from Lundbeckfonden (Junior Group Leader Fellowship).

References and Notes

(1) Lakowicz, J. R. *Principles of Fluorescence Spectroscopy*; Kluwer Academic/Plenum Publishers: New York, 1999.
(2) Harada, I.; Takeuchi, H. Raman and Ultraviolet Resonance Raman Spectra of Proteins and Related Compounds. In *Spectroscopy of Biological Systems*; Clark, R. J. H., Hester, R. E., Eds.; Advances in Spectroscopy *13*; Wiley: New York, 1986.
(3) Gregoire, G.; Lucas, B.; Barat, M.; Fayeton, J. A.; Dedonder-Lardeux, C.; Jouvet, C. *Eur. Phys. J. D* **2009**, *51*, 109.
(4) Kang, H.; Jouvet, C.; Dedonder-Lardeux, C.; Martrenchard, S.; Gregoire, G.; Desfrancois, C.; Schermann, J. P.; Barat, M.; Fayeton, J. A. *Phys. Chem. Chem. Phys.* **2005**, *7*, 394.
(5) Tabarin, T.; Kulesza, A.; Antoine, R.; Mitric, R.; Broyer, M.; Dugourd, P.; Bonacic-Koutecky, V. *Phys. Rev. Lett.* **2008**, *101*, 213001.
(6) Talbot, F. O.; Tabarin, T.; Antoine, R.; Broyer, M.; Dugourd, P. *J. Chem. Phys.* **2005**, *122*, 074310.
(7) Lucas, B.; Barat, M.; Fayeton, J. A.; Perot, M.; Jouvet, C.; Gregoire, G.; Brøndsted Nielsen, S. *J. Chem. Phys.* **2008**, *128*, 164302.
(8) Weinkauf, R.; Schanen, P.; Metsala, A.; Schlag, E. W.; Burgle, M.; Kessler, H. *J. Phys. Chem.* **1996**, *100*, 18567.

(9) Weinkauf, R.; Schlag, E. W.; Martinez, T. J.; Levine, R. D. *J. Phys. Chem. A* **1997**, *101*, 7702.
(10) Nolting, D.; Marian, C.; Weinkauf, R. *Phys. Chem. Chem. Phys.* **2004**, *6*, 2633.
(11) Hu, Y. J.; Hadas, B.; Davidovitz, M.; Balta, B.; Lifshitz, C. *J. Phys. Chem. A* **2003**, *107*, 6507.
(12) Cui, W.; Hu, Y.; Lifshitz, C. *Eur. Phys. J. D* **2002**, *20*, 565.
(13) Boyarkin, O. V.; Mercier, S. R.; Kamariotis, A.; Rizzo, T. R. *J. Am. Chem. Soc.* **2006**, *128*, 2816.
(14) Yoon, S. H.; Kim, M. S. *J. Am. Soc. Mass Spectrom.* **2007**, *18*, 1729.
(15) Oh, J. Y.; Moon, J. H.; Kim, M. S. *J. Mass Spectrom.* **2005**, *40*, 899.
(16) Weinkauf, R.; Schanen, P.; Yang, D.; Sonkara, S.; Schlag, E. W. *J. Phys. Chem.* **1995**, *99*, 11255.
(17) Sobolewski, A. L.; Shemesh, D.; Domcke, W. *J. Phys. Chem. A* **2009**, *113*, 542.
(18) Cohen, R.; Brauer, B.; Nir, E.; Grace, L.; de Vries, M. S. *J. Phys. Chem. A* **2000**, *104*, 6351.
(19) Joly, L.; Antoine, R.; Allouche, A. R.; Broyer, M.; Lemoine, J.; Dugourd, P. *J. Am. Chem. Soc.* **2007**, *129*, 8428.
(20) Joly, L.; Antoine, R.; Broyer, M.; Lemoine, J.; Dugourd, P. *J. Phys. Chem. A* **2008**, *112*, 898.
(21) Andersen, J. U.; Cederquist, H.; Forster, J. S.; Huber, B. A.; Hvelplund, P.; Jensen, J.; Liu, B.; Manil, B.; Maunoury, L.; Brøndsted; Nielsen, S.; Pedersen, U. V.; Rangama, J.; Schmidt, H. T.; Tomita, S.; Zettergren, H. *Phys. Chem. Chem. Phys.* **2004**, *6*, 2676.
(22) Kadhane, U.; Andersen, J. U.; Ehlerding, A.; Hvelplund, P.; Kirketerp, M. B. S.; Lykkegaard, M. K.; Brøndsted Nielsen, S.; Panja, S.; Wyer, J. A.; Zettergren, H. *J. Chem. Phys.* **2008**, *129*, 184304.
(23) Wyer, J. A.; Ehlerding, A.; Zettergren, H.; Kirketerp, M.-B. S.; Brøndsted Nielsen, S. *J. Phys. Chem. A* **2009**, *113*, 9277.
(24) Nolting, D.; Schultz, T.; Hertel, I. V.; Weinkauf, R. *Phys. Chem. Chem. Phys.* **2006**, *8*, 5247.
(25) Lucas, B.; Barat, M.; Fayeton, J. A.; Jouvet, C.; Carcabal, P.; Gregoire, G. *Chem. Phys.* **2008**, *347*, 324.
(26) Gregoire, G.; Dedonder-Lardeux, C.; Jouvet, C.; Desfrancois, C.; Fayeton, J. A. *Phys. Chem. Chem. Phys.* **2007**, *9*, 78.
(27) Gregoire, G.; Hang, H.; Dedonder-Lardeux, C.; Jouvet, C.; Desfrancois, C.; Onidas, D.; Lepere, V.; Fayeton, J. A. *Phys. Chem. Chem. Phys.* **2006**, *8*, 122.
(28) Fujihara, A.; Matsumoto, H.; Shibata, Y.; Ishikawa, H.; Fuke, K. *J. Phys. Chem. A* **2008**, *112*, 1457.
(29) Fujihara, A.; Noguchi, N.; Yamada, Y.; Ishikawa, H.; Fuke, K. *J. Phys. Chem. A* **2009**, *113*, 8169.
(30) Lepere, V.; Lucas, B.; Barat, M.; Fayeton, J. A.; Picard, V. J.; Jouvet, C.; Carcabal, P.; Nielsen, I.; Dedonder-Lardeux, C.; Gregoire, G.; Fujii, A. *J. Chem. Phys.* **2007**, *127*, 134313.
(31) Kang, H.; Dedonder-Lardeux, C.; Jouvet, C.; Martrenchard, S.; Gregoire, G.; Desfrancois, C.; Schermann, J. P.; Barat, M.; Fayeton, J. A. *Phys. Chem. Chem. Phys.* **2004**, *6*, 2628.
(32) Møller, S. P. *Nucl. Instrum. Methods Phys. Res., Sect. A* **1997**, *394*, 281.
(33) Andersen, J. U.; Hvelplund, P.; Brøndsted Nielsen, S.; Tomita, S.; Wahlgreen, H.; Møller, S. P.; Pedersen, U. V.; Forster, J. S.; Jørgensen, T. J. D. *Rev. Sci. Instrum.* **2002**, *73*, 1284.
(34) Støchkel, K.; Kadhane, U.; Andersen, J. U.; Holm, A. I. S.; Hvelplund, P.; Kirketerp, M. B. S.; Larsen, M. K.; Lykkegaard, M. K.; Brøndsted Nielsen, S.; Panja, S.; Zettergren, H. *Rev. Sci. Instrum.* **2008**, *79*, 023107.
(35) The mean free path is calculated from $k_BT/(2^{1/2}\sigma p)$, where k_B is the Boltzmann constant, T is the temperature of the residual gas in the ring (298 K), σ is the collision cross section (taken to be 10^{-18} m^2), and p is the pressure (about 10^{-10} mbar $= 10^{-8}$ Pa). See Atkins, P. W. *Physical Chemistry*, 4th ed.; Oxford University Press: Oxford, U.K., 1990; p 732.
(36) Andersen, J. U.; Cederquist, H.; Forster, J. S.; Huber, B. A.; Hvelplund, P.; Jensen, J.; Liu, B.; Manil, B.; Maunoury, L.; Brøndsted Nielsen, S.; Pedersen, U. V.; Schmidt, H. T.; Tomita, S.; Zettergren, H. *Eur. Phys. J. D* **2003**, *25*, 139.
(37) (a) Geometry optimizations were performed using density functional theory at B3LYP/6-31G(d) level with the aid of the Gaussian 03 package.[37b] The excited-state energies were calculated at a higher theoretical level using time-dependent density functional theory (TDB3LYP/6-311++G(2d,p)). (b) Frisch, M. J.; Trucks, G. W.; Schlegel, H. B.; Scuseria, G. E.; Robb, M. A.; Cheeseman, J. R.; Montgomery, J. A., Jr.; Vreven, T.; Kudin, K. N.; Burant, J. C.; Millam, J. M.; Iyengar, S. S.; Tomasi, J.; Barone, V.; Mennucci, B.; Cossi, M.; Scalmani, G.; Rega, N.; Petersson, G. A.; Nakatsuji, H.; Hada, M.; Ehara, M.; Toyota, K.; Fukuda, R.; Hasegawa, J.; Ishida, M.; Nakajima, T.; Honda, Y.; Kitao, O.; Nakai, H.; Klene, M.; Li, X.; Knox, J. E.; Hratchian, H. P.; Cross, J. B.; Adamo, C.; Jaramillo, J.; Gomperts, R.; Stratmann, R. E.; Yazyev, O.; Austn, A. J.; Cammi, R.; Pomelli, C.; Ochterski, J. W.; Ayala, P. Y.; Morokuma, K.; Voth, G. A.; Salvador, P.; Dannenberg, J. J.; Zakrzewski, V. G.; Dapprich, S.; Daniels, A. D.; Strain, M. C.; Farkas, O.; Malick, D. K.; Rabuck, A. D.; Raghavachari, K.; Foresman, J. B.; Ortiz, J. V.; Cui, Q.; Baboul, A. G.; Clifford, S.; Cioslowski, J.; Stefanov, B. B.; Liu, G.; Liashenko, A.; Piskorz, P.; Komaromi, I.; Martin, R. L.; Fox, D. J.; Keith, T.; Al-Laham, M. A.; Peng, C. Y.; Nanayakkara, A.; Challacombe, M.; Gill, P. M. W.; Johnson, B.; Chen, W.; Wong, M. W.; Gonzalez, C.; Pople, J. A. *Gaussian 03*, revision D.01; Gaussian: Wallingford, CT, 2004.
(38) Kadhane, U.; Perot, M.; Lucas, B.; Barat, M.; Fayeton, J. A.; Jouvet, C.; Ehlerding, A.; Kirketerp, M.-B. S.; Brøndsted Nielsen, S.; Wyer, J. A.; Zettergren, H. *Chem. Phys. Lett.* **2009**, *480*, 57.
(39) Auer, H. E. *J. Am. Chem. Soc.* **1973**, *95*, 3003.
(40) Zubarev, R. A.; Kelleher, N. L.; McLafferty, F. W. *J. Am. Chem. Soc.* **1998**, *120*, 3265.
(41) Zubarev, R. A. *Mass Spectrom. Rev.* **2003**, *22*, 57.
(42) (a) Callis, P. R.; Vivian, J. T. *Chem. Phys. Lett.* **2003**, *369*, 409. (b) Callis, P. R.; Liu, T. *J. Phys. Chem. B* **2004**, *108*, 4248. (c) Vivian, J. T.; Callis, P. R. *Biophys. J.* **2001**, *80*, 2093.

JP9086317

Photodissociation of protonated tryptophan and alteration of dissociation pathways by complexation with crown ether

Umesh Kadhane,[a] Jens Ulrik Andersen, Anneli Ehlerding, Preben Hvelplund, Maj-Britt S. Kirketerp, Morten Køcks Lykkegaard, Steen Brøndsted Nielsen, Subhasis Panja, Jean Ann Wyer, and Henning Zettergren
Department of Physics and Astronomy, University of Aarhus, Ny Munkegade, DK-8000 Aarhus C, Denmark

(Received 1 July 2008; accepted 6 October 2008; published online 11 November 2008)

The behavior of protonated tryptophan ($TrpH^+$) and its complex with 18-crown-6-ether (CE) after photoexcitation has been explored based on measurements of dissociation lifetimes, fragmentation channels, and absorption spectra using an electrostatic ion storage ring. A recent implementation of pulsed power supplies for the ring elements with microsecond response times allows us to identify the daughter ion fragment masses and to disentangle fragmentation that occurs from excited states immediately after photoexcitation from that occurring on a longer time scale of several microseconds to milliseconds. We find that attachment of crown ether significantly alters the dissociation channels since it renders the $\pi\sigma^*(NH_3)$ state inaccessible and hence prevents the N–H bond breakage which is an important fragmentation channel of $TrpH^+$. As a result, on a long time scale ($>10\ \mu s$), photoexcited $TrpH^+(CE)$ decays exponentially whereas $TrpH^+$ displays a power-law decay. The only ions remaining in the latter case are $Trp^{+\cdot}$ radical cations with a broad internal energy distribution caused by the departing hydrogen. Large changes in the fragment branching ratios as functions of excitation wavelength between 210 and 290 nm were found for both $TrpH^+$ and $TrpH^+(CE)$. © *2008 American Institute of Physics*. [DOI: 10.1063/1.3009222]

VII

I. INTRODUCTION

The photophysics and dissociation dynamics of isolated protonated tryptophan (Fig. 1) in the gas phase have been studied in great detail in recent years[1–12] because this amino acid plays a dominant role in protein photobiology. After UV excitation of an electron in the indole aromatic ring to a $\pi\pi^*$ state, there are several deexcitation pathways available in addition to fluorescence. Internal conversion to the electronic ground state followed by intramolecular vibrational redistribution of the energy leads to vibrationally excited ions that dissociate statistically within a few nanoseconds by loss of, e.g., ammonia. The $\pi\pi^*$ state can also couple with a lower lying repulsive $\pi\sigma^*(NH_3)$ state, located on the ammonium group [charge transfer (CT) state], that dissociates along the NH bond to give the tryptophan radical cation, $Trp^{+\cdot}$. Since the hydrogen atom can depart with a kinetic energy within a broad range, the internal energy distribution of $Trp^{+\cdot}$ is broad. According to lifetime measurements, subsequent dissociation (C_α–C_β bond rupture) occurs on a microsecond to millisecond time scale.[2,5] This is different from the case of protonated tyrosine, where the $\pi\sigma^*(NH_3)$ state is situated at a higher energy, making the NH fragmentation pathway less accessible.[13] Another recently suggested pathway is internal conversion from the indole $\pi\pi^*$ state to a state where the photoexcited electron is located on the oxygen of the carbonyl group, a $\pi\pi^*(CO)$ CT state. This also results in breakage of the C_α–C_β bond due to the radical character of the indole cation or in loss of H_2O and CO after internal proton transfer from the ammonium group to the carboxylic acid group.[1] A more complete description of the fragmentation channels including their time scales can be found in Refs. 1–3.

In this work, we have explored the photophysics of $TrpH^+$ and of the complex between $TrpH^+$ and 18-crown-6-ether (Fig. 1). The recombination energy of CH_3–NH_3^+, for example, is calculated to be about 2.5 eV higher than that of CH_3–$NH_3^+(CE)$.[14] Hence, the energy cost of transferring an electron from indole to the ammonium group of protonated tryptophan is about 2–3 eV higher when crown ether is bound. The $\pi\sigma^*$ state is therefore raised with this amount of energy for $TrpH^+(CE)$ compared to $TrpH^+$. This is under the assumption that the stabilizing effect of the indole positive charge on the ammonium radical is similar for the bare ion and for the complex. The increase in energy of the $\pi\sigma^*$ state renders it inaccessible after 260 nm excitation. In other words, the state is switched off, and it does not contribute to the dissociation dynamics of the cation anymore. The impact on the $\pi\pi^*(CO)$ state, on the other hand, is expected to be much smaller. We find that the dissociation kinetics and fragmentation patterns are indeed changed upon crown ether complexation. In addition, we report the absorption spectra of $TrpH^+$ and $TrpH^+(CE)$ as well as the branching ratios between the fragmentation channels as functions of wavelength between 210 and 290 nm.

II. EXPERIMENTAL

The experiments were performed at the electrostatic ion storage ring in Aarhus (ELISA), which has been equipped with pulsed power supplies of microsecond response times to allow for daughter ion mass spectrometry.[15–17] Ions were produced by electrospray ionization and accumulated in a

[a]Electronic mail: kumesh@phys.au.dk

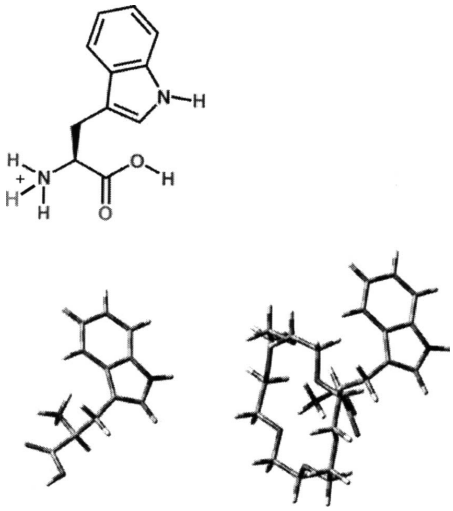

FIG. 1. Structures of $TrpH^+$ and $TrpH^+$(CE) optimized at the B3LYP/6-31G level of theory.

22-pole ion trap where they were thermally equilibrated by collisions with a helium buffer gas. The ions were accelerated as an ion bunch to kinetic energies of 22 keV, and those of interest were selected by a bending magnet. After injection into the ring, the ions were stored for about 35 ms before being irradiated by a nanosecond light pulse from an EKSPLA laser. The repetition rate of the experiment was 10 Hz. Lifetimes were obtained from measurements of the yield of neutrals hitting the microchannel plate (MCP) detector located at the end of the straight section opposite to the side where photoexcitation was performed. The dependence of the fragmentation yield on laser power was checked in the case of $TrpH^+$ and found to be linear in the range of intensities used. In separate experiments, ring voltages were changed at a particular time after photoexcitation to store daughter ions with the appropriate kinetic energy. After 12 revolutions (in the case of $TrpH^+$), the daughter ions were dumped into the MCP detector. The signal from the detector as a function of the scaling of the ring voltages provided the daughter ion mass spectrum. The pressure in the ring was of the order of 10^{-11} mbar, which set an upper limit of seconds on the storage time.

III. RESULTS AND DISCUSSION

First, we consider the fragmentation channels of $TrpH^+$ after 266 nm photoexcitation. A daughter ion mass spectrum recorded right after photoexcitation is shown in Fig. 2(a). In this experiment, dissociation was sampled between 0 and 15 μs after photon absorption. The fragmentation spectrum is in good agreement with previously published spectra[1,2,6,11] except for differences in the relative ratios of the peaks. For example, the m/z-170 peak, corresponding to the ion formed after consecutive loss of NH_3 and H_2O, is higher in our experiment. This may be due to different fragmentation sampling times: <5 μs in Refs. 1 and 2, 1 s in Ref. 6, and

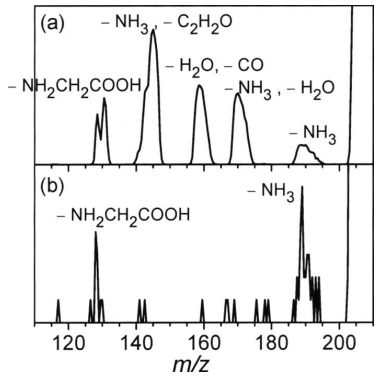

FIG. 2. Photodissociation mass spectra of $TrpH^+$. (a) Fragment ions formed up to 15 μs after photoexcitation. (b) Fragment ions formed between 57 and 72 μs after photoexcitation. Wavelength=266 nm.

VII

<15 μs in our experiment. The other channels are loss of NH_3 (m/z 188), CO and H_2O (m/z 159), NH_3 and CO_2 (m/z 146), NH_3 and C_2H_2O (m/z 144), $C_2H_3NO_2$ (m/z 132), and glycine (m/z 130) with the accompanying fragment ion masses given in brackets. Since the resolution was quite poor, we cannot distinguish between m/z 130 and m/z 132 and between m/z 144 and m/z 146 and rely on assignments from previous works.[1,2,6,11] As the yields of fragment ions in our experiment increase linearly with the laser power, we can conclude that they are all formed after absorption of a single photon.

In a separate experiment, the photoexcited ions were stored for 57 μs before the ring voltages were switched to store fragment ions and produce the daughter ion mass spectrum shown in Fig. 2(b). Two dominant fragmentation channels were observed, one loss of ammonia and the other loss of glycine. For the former case, we presently have no explanation why NH_3 loss should be such a dominant channel. One possibility is fluorescence to the ground state (electronic) in a higher vibrational state leading to slow loss of NH_3. The latter is associated with the breakage of the C_α–C_β bond, which gives a fragment ion with m/z 130. The m/z-130 fragment ion dominates the dissociation of $Trp^{+\cdot}$ radical cations formed either by electron impact or photoionization of Trp.[3,18,19] The daughter ion mass spectra support the fact that a fraction of $TrpH^+$ lose hydrogen immediately upon photoexcitation, and that dissociation at long times is due to the fragmentation of the resulting $Trp^{+\cdot}$ ions with a kinetic energy of 21.9 keV ($204/205\times22$ keV). Storage of these ions in the ring is possible within the energy acceptance of the electrostatic elements.[1]

To suppress or eliminate the hydrogen-loss channel, experiments on the complex between protonated tryptophan and crown ether were done. The fragmentation after photoexcitation of $TrpH^+$(CE) (m/z 469) is different from that of bare $TrpH^+$ (Fig. 3), and the dissociation is well described by a single exponential with a time constant of 0.219 ms (Fig. 4). The deviation at late times is due to the fact that all $TrpH^+$ ions do not have exactly the same internal energy, and ions belonging to the lower energy part of the distribution

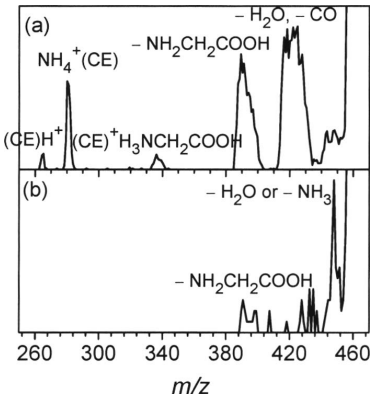

FIG. 3. Photodissociation mass spectra of TrpH$^+$(CE). (a) Fragment ions formed up to 20 μs after photoexcitation. (b) Fragment ions formed between 87 and 107 μs after photoexcitation. Wavelength=266 nm.

VII

have longer lifetimes. As mentioned earlier, the crown ether forms three hydrogen bonds to each of the ammonium protons (Fig. 1), which prevents direct hydrogen loss and at the same time renders it energetically impossible to reach the $\pi\sigma^*(NH_3)$ state required for N–H dissociation with a 266 nm photon. Instead, we sample the statistical dissociation of vibrationally hot TrpH$^+$(CE) ions. According to the daughter ion mass spectrum recorded at late times (>87 μs), the statistical dissociation channels are glycine loss (m/z 394) and possibly H_2O loss (m/z 451) [Fig. 3(b)]. At shorter times ($0<t<20$ μs), the fragmentation spectrum reveals several dissociation channels [Fig. 3(a)]: formation of protonated crown ether (m/z 265), NH_4^+(CE) (m/z 282), and [glycine+H]$^+$(CE) (m/z 340), and loss of glycine (m/z 394), H_2O and CO (m/z 423), and of H_2O or NH_3 (m/z 451/450). A scan over lower masses gave no signal from TrpH$^+$ (m/z 205) formed by loss of crown ether, which is in accordance with the higher proton affinity of CE relative to Trp (967.0 kJ/mol versus 948.9 kJ/mol).[20]

The loss of glycine is intriguing since a structure where the indole ring is protonated and bound to the crown ether lies higher in energy by 1.43 eV according to density functional calculations (performed using GAUSSIAN, B3LYP/6-31G level). Under the conditions of the current experiment,

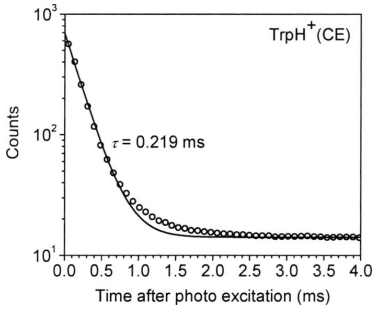

FIG. 4. Decay spectrum of TrpH$^+$(CE) photoexcited by 266 nm light. The solid curve is an exponential fit to the data points.

where ions are equilibrated at room temperature in an ion trap, such a structure can be assumed not to be present in the ion beam. It implies that directly after photoexcitation, the crown ether is mobile and can rearrange to the indole cation.

Interestingly, the largest fragment peak is associated with the loss of H_2O and CO. This channel was in the case of TrpH$^+$ explained by location of the photoexcited electron on the CO group and the abstraction of a proton from the ammonium group to give $-C(OH)_2$ followed by the successive loss of H_2O and CO. Attachment of crown ether to the ammonium group slows down the proton transfer from this end since it requires the movement of CE to the indole group as discussed above. It is possible that the anion instead abstracts a proton from the indole cation. In any case, our data indicate that while the crown ether attachment switches off the $\pi\sigma^*(NH_3)$ state, the $\pi\pi^*$(CO) state still plays an important role.

Large variations in the fragmentation channels of TrpH$^+$ as a function of excitation wavelength from 215 to 320 nm were reported by Talbot *et al.*[6] Their experiment was conducted in an ion trap, and the ions were irradiated by light for about 1 s (20 laser pulses). As the authors point out, photofragments may reabsorb light and dissociate further so that the observed products may result from multiple photodissociation, and it was therefore difficult to draw a firm conclusion on the change in pathways with the photon energy. In addition, it is important to note that even under single photon absorption conditions, various fragments would undergo subsequent statistical dissociation because of the long time scale of the experiment (1 s). In contrast to the trap experiment, the ions were in the present ring experiment only photoexcited once with a nanosecond light pulse, and photodissociation of fragment ions was highly unlikely. Hence, in order to examine the fragmentation channels as functions of wavelength, we repeated our experiment at different wavelengths (210–300 nm).

As an example, fragmentation spectra of TrpH$^+$ and TrpH$^+$(CE) obtained after 220 nm photexcitation are shown in Fig. 5. The fragmentation channels are the same as after 266 nm excitation but there are changes in the relative intensities, especially in the case of TrpH$^+$ where the ammonia-loss peak has almost disappeared at 220 nm. The branching ratios as functions of excitation wavelength are shown in Fig. 6. For TrpH$^+$, these ratios are different from those reported by Talbot *et al.* which, as described before, may be explained by the different measurement time scales as well as photodissociation of fragment ions. It can be clearly seen in Fig. 6(a) that loss of NH_3 is the lowest energy channel, consistent with the previously known results.[21] Loss of NH_3 is followed by successive dissociation and, as a result, the NH_3-loss peak at m/z 188 decreases with lower excitation wavelengths compared to the other peaks in the spectrum. The yield of the m/z-130/132 ions decreases relative to that of the m/z-159 ion with increasing wavelength. In the case of TrpH$^+$(CE), all the channels which involve loss of NH_3 are suppressed, as expected. It appears that the loss of glycine is in competition with the loss of CO and H_2O, and that the relative importance of these two channels depends strongly on wavelength: loss of CO and H_2O dominates at

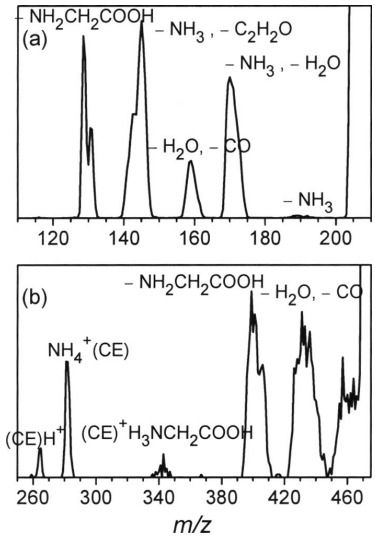

FIG. 5. Photodissociation mass spectra of (a) $TrpH^+$ and (b) $TrpH^+(CE)$. Fragment ions formed up to 15 and 20 μs after photoexcitation, respectively. Wavelength=220 nm.

wavelengths longer than ~260 nm and shorter than ~230 nm whereas glycine loss takes over in the region between 230 and 260 nm.

Absorption spectra of $TrpH^+$ have earlier been reported by Nolting *et al.*,[11] Talbot *et al.*,[6] and for very cold ions (10 K) by Rizzo and co-workers.[10,12] We obtained absorption spectra of both $TrpH^+$ and $TrpH^+(CE)$ from our photofragment yields (Fig. 7). $TrpH^+$ has a broad absorption band at about 260 nm and an even stronger band with maximum below 210 nm. The spectrum compares reasonably well with those published previously by Nolting *et al.*[11] and Talbot *et al.*[6] except that in the present spectrum no sharp features are observed. This may be due to differences in ion temperature. In the case of $TrpH^+(CE)$, the 260 nm band redshifts to 270 nm and the band is narrower than that of $TrpH^+$. A proper understanding of this change in absorption requires calculations of high-level excited states that are beyond the scope of this paper.

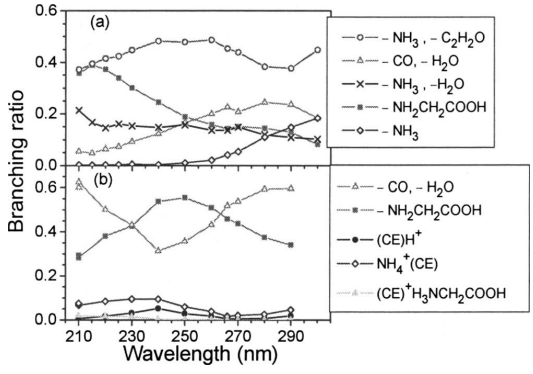

FIG. 6. Branching ratios for fragmentation channels of (a) $TrpH^+$ and (b) $TrpH^+(CE)$ as functions of excitation wavelength.

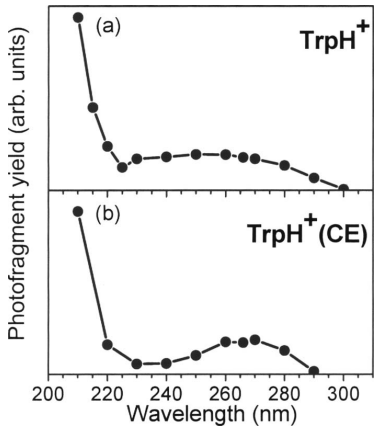

FIG. 7. Absorption spectra of (a) $TrpH^+$ and (b) $TrpH^+(CE)$.

IV. CONCLUSIONS

In summary, we have found that crown ether attachment to protonated tryptophan significantly changes the fragmentation channels as well as the lifetimes for dissociation. This may be explained by the fact that the $\pi\sigma^*(NH_3)$ state is no longer accessible. The dissociation channels are therefore no longer determined by the reactions of a hypervalent nitrogen species. The crown ether also affects the UV absorption band, resulting in a narrower band and a redshift of the maximum. This work demonstrates the strength of an electrostatic ion storage ring in providing three important pieces of information from a single experiment: absorption spectra, lifetimes, and fragmentation channels on a microsecond to millisecond time scale.

ACKNOWLEDGMENTS

This work was supported by the Danish Natural Science Research Council (Grant Nos. 21-04-0514 and 272-06-0427), Carlsbergfondet (Grant No. 2006-01-0229), Lundbeckfonden, Villum Kann Rassmussen Fonden, and dir. Ib Henriksens Fond.

[1] B. Lucas, M. Barat, J. A. Fayeton, M. Perot, C. Jouvet, G. Grégoire, and S. Brøndsted Nielsen, J. Chem. Phys. **128**, 164302 (2008).
[2] V. Lepère, B. Lucas, M. Barat, J. A. Fayeton, V. J. Picard, C. Jouvet, P. Çarçabal, I. Nielsen, C. Dedonder-Lardeux, G. Grégoire, and A. Fujii, J. Chem. Phys. **127**, 134313 (2007).
[3] H. Kang, C. Dedonder-Lardeux, C. Jouvet, S. Martrenchard, G. Gregoire, C. Desfrancois, J. P. Schermann, M. Barat, and J. A. Fayeton, Phys. Chem. Chem. Phys. **6**, 2628 (2004).
[4] H. Kang, C. Dedonder-Lardeux, C. Jouvet, G. Gregoire, C. Desfrancois, J. P. Schermann, M. Barat, and J. A. Fayeton, J. Phys. Chem. A **109**, 2417 (2005).
[5] J. U. Andersen, H. Cederquist, J. S. Forster, B. A. Huber, P. Hvelplund, J. Jensen, B. Liu, B. Manil, L. Maunoury, S. Brøndsted Nielsen, U. V. Pedersen, J. Rangama, H. T. Schmidt, S. Tomita, and H. Zettergren, Phys. Chem. Chem. Phys. **6**, 2676 (2004).
[6] F. O. Talbot, T. Tabarin, R. Antoine, M. Broyer, and P. Dugourd, J. Chem. Phys. **122**, 074310 (2005).
[7] G. Gregoire, H. Kang, C. Dedonder-Lardeux, C. Jouvet, C. Desfrancois, D. Onidas, V. Lepere, and J. A. Fayeton, Phys. Chem. Chem. Phys. **8**, 122 (2006).
[8] G. Gregoire, C. Jouvet, C. Dedonder, and A. L. Sobolewski, Chem. Phys.

324, 398 (2006).
[9] H. Kang, C. Jouvet, C. Dedonder-Lardeux, S. Martrenchard, C. Charriere, G. Gregoire, C. Desfrancois, J. P. Schermann, M. Barat, and J. A. Fayeton, J. Chem. Phys. **122**, 084307 (2005).
[10] O. V. Boyarkin, S. R. Mercier, A. Kamariotis, and T. R. Rizzo, J. Am. Chem. Soc. **128**, 2816 (2006).
[11] D. Nolting, C. Marian, and R. Weinkauf, Phys. Chem. Chem. Phys. **6**, 2633 (2004).
[12] S. R. Mercier, O. V. Boyarkin, A. Kamariotis, M. Guglielmi, I. Tavernelli, M. Cascella, U. Rothlisberger, and T. R. Rizzo, J. Am. Chem. Soc. **128**, 16943 (2006).
[13] H. Kang, C. Jouvet, C. Dedonder-Lardeux, S. Martrenchard, G. Gregoire, C. Desfrancois, J. P. Schermann, M. Barat, and J. A. Fayeton, Phys. Chem. Chem. Phys. **7**, 394 (2005).
[14] A. I. S. Holm, M. K. Larsen, S. Panja, P. Hvelplund, S. Brøndsted Nielsen, R. D. Leib, W. A. Donald, E. R. Williams, C. Hao, and F. Tureček, Int. J. Mass. Spectrom. **276**, 116 (2008).
[15] S. P. Møller, Nucl. Instrum. Methods Phys. Res. A **394**, 281 (1997).
[16] J. U. Andersen, P. Hvelplund, S. Brøndsted Nielsen, S. Tomita, H. Wahlgreen, S. P. Møller, U. V. Pedersen, J. S. Forster, and T. J. D. Jørgensen, Rev. Sci. Instrum. **73**, 1284 (2002).
[17] K. Støchkel, U. Kadhane, J. U. Andersen, A. I. S. Holm, P. Hvelplund, M. S. Kirketerp, M. K. Larsen, M. K. Lykkegaard, S. Brøndsted Nielsen, S. Panja, and H. Zettergren, Rev. Sci. Instrum. **79**, 023107 (2008).
[18] T. R. Rizzo, Y. D. Park, L. A. Peteanu, and D. H. Levy, J. Chem. Phys. **84**, 2534 (1986).
[19] *NIST Chemistry WebBook*, NIST Standard Reference Database Number 69, edited by P. J. Linstrom and W. G. Mallard (National Institute of Standards and Technology, Gaithersburg, MD, 2005), http://webbooK.nist.gov.
[20] *NIST Chemistry WebBook*, NIST Standard Reference Database Number 69, edited by P. J. Linstrom and W. G. Mallard (National Institute of Standards and Technology, Gaithersburg, MD, 2005).
[21] H. El Aribi, G. Orlova, A. C. Hopkinson, and K. W. M. Siu, J. Phys. Chem. A **108**, 3844 (2004).

Chemical Physics Letters 480 (2009) 57–61

Contents lists available at ScienceDirect

Chemical Physics Letters

journal homepage: www.elsevier.com/locate/cplett

Photodissociation of protonated tryptamine and its supramolecular complex with 18-crown-6 ether: Dissociation times and channels, absorption spectra, and excited states calculations

U. Kadhane [a,b,1], M. Pérot [a,c], B. Lucas [a,b], M. Barat [a,b], J.A. Fayeton [a,b,*], C. Jouvet [c,d], A. Ehlerding [e], M.-B.S. Kirketerp [e], S. Brøndsted Nielsen [e,*], J.A. Wyer [e], H. Zettergren [e]

[a] Univ. Paris-Sud, Laboratoire des Collisions Atomiques et Moléculaires, UMR 8625, Bât. 351, Orsay F-91405, France
[b] CNRS, UMR 8625, Orsay F-91405, France
[c] Univ. Paris-Sud, Laboratoire de Photophysique Moléculaire, UPR 3361, Bât. 210, Orsay F-91405, France
[d] CNRS, UPR 3361, Orsay F-91405, France
[e] Department of Physics and Astronomy, Aarhus University, Ny Munkegade, DK-8000 Aarhus C, Denmark

VIII

ARTICLE INFO

Article history:
Received 9 July 2009
In final form 27 August 2009
Available online 31 August 2009

ABSTRACT

Photodissociation of the complex between protonated tryptamine, $TryH^+$, and 18-crown-6 ether (CE) was investigated. Absorption maxima of $TryH^+$ and $TryH^+$(CE) are at 249 and 273 nm, respectively. Ions decay exponentially on a microsecond timescale, and mass spectra reveal that NH_3 loss is an important channel even though CE targets this group. TD-DFT calculations identified an electronically excited state, where the photoactive electron is located in an antibonding orbital between C and NH_3. Dissociation along this coordinate and CE rearrangement to the new charge site accounts for ammonia loss. Photodissociation in an electric field and time-of-flight measurements corroborate such a non-statistical bond-breakage.

1. Introduction

The photophysics of protonated tryptophan, $TrpH^+$, isolated in the gas phase has been explored in detail because of the great importance this amino acid has in photobiology. UV irradiation leads to excitation of the indole chromophore (a $\pi\pi^*$ transition) followed by several competing deactivation pathways [1–14]. Internal conversion back to the ground state and intramolecular vibrational redistribution of the energy results in a vibrationally hot ion that dissociates on the nanosecond time scale. The photoactive electron may also jump to the ammonium group populating a σ^* orbital that is antibonding between N and H. Prompt hydrogen loss occurs while the ion is in this $\pi\sigma^*$ state, and the formed $Trp^{+\cdot}$ radical cation then undergoes C_α–C_β cleavage on a much longer time scale (microseconds to milliseconds). Another scenario is internal conversion from the $\pi\pi^*$(indole) state to a $\pi\pi^*$(CO) state where the photoactive electron is located on the carboxylic acid. This electron jump is associated with concomitant proton transfer from the ammonium group to the negatively charged oxygen. The so-formed ion quickly undergoes C_α–C_β cleavage (nanoseconds time scale). To simplify the deexcitation pathways, the carboxylic acid group in Trp is replaced by hydrogen to eliminate the latter channel [1,10]. This molecule is called tryptamine (Try). It has been shown that the $\pi\sigma^*$(N–H) state is removed from the spectral region by the attachment of 18-crown-6 ether (CE) to protonated Trp or Try [14]. The size of the chosen crown ether is optimum for the formation of three hydrogen bonds with ammonium [15–17], which raises the $\pi\sigma^*$(N–H) state up in energy by about 1–2 eV [14,18].

In the present work, we have subjected protonated tryptamine and its complex with CE (Fig. 1) to photodissociation studies. Experiments were done in two different laboratories, Orsay (O) and Aarhus (A), to reveal different pieces of information: dissociation on the nanosecond time scale (O), absorption spectra (A), binary vs. ternary dissociation (O), dissociation on a longer time scale (A), and dissociation channels as a function of excitation wavelength (A).

2. Experimental

Aarhus (A) experiments: ions were produced by electrospray ionization of dissolved tryptamine in water and methanol (1:1) with acetic acid added (5% in volume). 18-Crown-6 ether was added to the solution to form complexes. All compounds were purchased from Sigma–Aldrich. Ions were accumulated in a 22-pole

* Corresponding authors.
E-mail addresses: jacqueline.fayeton@u-psud.fr (J.A. Fayeton), sbn@phys.au.dk (S. Brøndsted Nielsen).
[1] Present address: Department of Physics, Indian Institute of Technology Madras, Chennai 600 036, India.

0009-2614/$ - see front matter © 2009 Elsevier B.V. All rights reserved.
doi:10.1016/j.cplett.2009.08.064

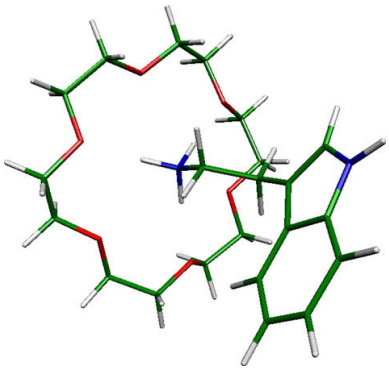

Fig. 1. The structure of $TryH^+(CE)$ calculated at the TD-DFT and SV(P) level of theory.

ion trap, filled with helium buffer gas, for 0.1 s, which allowed the ions to acquire room temperature, before they were accelerated as an ion bunch to 22-keV kinetic energies. An electromagnet selected ions of interest according to their mass-to-charge ratio. These ions were injected into the electrostatic ion storage ring in Aarhus (ELISA) and stored [19–21]. After about 40 ms, they were irradiated by laser light at one side of the ring. The light source was a tunable EKSPLA laser. This is an Nd:YAG laser where the third harmonic (355 nm) pumps an optical parametric oscillator (OPO). The visible output from this OPO is frequency doubled in a crystal providing UV light. The repetition rate of the experiment was 10 Hz.

In one experiment, lifetimes of photoexcited ions were measured from the yield of neutrals hitting a multi-channel plate (MCP) detector placed at the end of the side opposite to the laser interaction region (i.e., delayed dissociation). Measurements were done at different excitation wavelengths to obtain absorption spectra.

In another experiment, all ring voltages were changed right after photoexcitation to store particular daughter ions [22]. These ions undertook 20.5 and 13.5 revolutions, for $TryH^+$ and $TryH^+(CE)$, respectively, before they were dumped in the MCP detector. A scan of the ring voltages provided the daughter ion mass spectrum. Delayed dissociation was measured by postponing the change of ring voltages until the parent ions had taken half a revolution in the ring.

Orsay (O) experiments: Ions were produced by electrospray ionization as described in the (A) experiment and investigated through the use of a home-built beam instrument. Ions were trapped inside a hexapole for one millisecond and then accelerated to kinetic energies of 2.5 keV as described previously [2]. Ion bunches of 100 ns time width produced at a 1 kHz repetition rate were selected by an electrical chopper. The ions then entered a Zajfmann ion trap [23] in which they can be stored for a few hundred milliseconds. At the exit of the trap the ions were post-accelerated to 5-keV kinetic energies in order to increase the detection efficiency for neutral fragments. The ions were irradiated by a 263-nm light pulse (fourth harmonic of a Nd:YLF kHz laser of 160 μJ and 200 ns time width) either in the ion trap or downstream inside a polarized region. The latter allowed for the study of fast fragmentation (10 ns to 5 μs). The neutral fragments reached a position sensitive detector (PSD) located one meter from the laser interaction region. The ionic fragments were deflected in a 45° electrostatic analyzer and detected by a second PSD. An ionic fragment of a given mass was selected with the electrostatic analyzer and detected in coincidence with neutral fragment(s) that arose from the same fragmentation event. Long fragmentation times, typically larger than 5 μs, were obtained from the time spectra of neutral fragments escaping the trap when ions were stored. Neutrals were produced in the half-period during which the projectiles travelled towards the detector. The identification of the ionic fragments associated with these neutrals produced after a long storage time was obtained by emptying the trap and measuring the ion kinetic energies.

3. Theoretical details

The excited state fragmentation pathway along the C–NH_3 coordinate was obtained at the TD-DFT/B3LYP level with the SV(P) basis set using the TURBOMOLE package [24]. The minimum energy path (MEP) is obtained by fixing the CN coordinate and relaxing all the other degrees of freedom in the excited state. The TD-DFT method is questionable when the excited state is a charge transfer state. However, in the tryptamine case where the charge transfer state consists of an electron localized around the positive charge, it has been shown in previous work that DFT calculations are in good agreement with more costly methods such as MRCI [12] and the ri-CC2 method [8–10].

4. Results and discussion

4.1. Time spectra

Decay spectra obtained after photoexcitation of $TryH^+$ and $TryH^+(CE)$ at 266 nm in ELISA (A) are shown in Fig. 2. The revolution times in the ring are 51 μs and 83 μs, respectively. In the case of $TryH^+$, we sample the dissociation of $Try^{+\cdot}$ radical cations since all photoexcited $TryH^+$ ions decay within 100 ns according to previous (O) measurements [1]. The ions that have lost hydrogen have kinetic energies of 22 keV × 160/161 and are stored in the ring due to the large energy acceptance of all electrostatic deflectors [5,14].

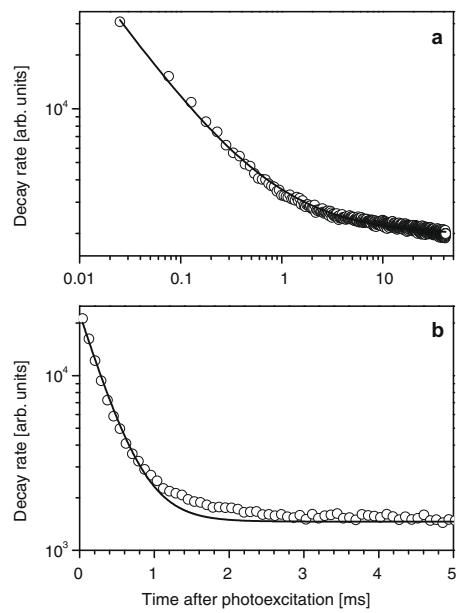

Fig. 2. Time spectra obtained after photoexcitation of $TryH^+$ (a) and $TryH^+(CE)$ (b) by 266-nm light in ELISA (A). The ions were stored for about 40 ms in the ring before excitation. Fits to the data points with a power-law function and an exponential function are shown for $TryH^+$ and $TryH^+(CE)$, respectively.

The hydrogen atom can depart with a broad range of kinetic energies, leaving the $Try^{+\cdot}$ radical cations with a broad energy distribution. The decay is well described by a power law, $N\,t^{-0.79}$ + constant [25], where the constant accounts for dissociation after collisions with residual gas in the ring (time constant of a few hundred milliseconds). There are at least two explanations for a power numerically less than one [5,25,26]. The internal energy distribution is not flat, and if we happen to sample the decay of ions from the high-energy side of the maximum, the number of ions in the distribution increases with decreasing energy. Thus, the decay curve appears less steep than that for t^{-1} decay. Another possibility is competing reaction channels that also reduce the power numerically. As the energy distribution depletes from the high-energy side, other dissociation channels may take over, and the decay is therefore less steep than the case where one channel dominates over the whole energy range. In agreement with these findings, when photoexcitation was done inside the Zajfman trap, two ions were clearly separated in time after four oscillations corresponding to $Try^{+\cdot}$ and non-irradiated $TryH^+$ ions (the same has been observed for $TrpH^+$ [2]).

In the case of the $TryH^+$(CE) complex, the decay is ascribed to excited ions in high vibrational levels, and it occurs with a time constant of 310 μs from a fit of an exponential to the data (Fig. 2b). The tail at longer times is a result of the width of the internal energy distribution since ions with lower internal energy will dissociate on a longer time scale. The hydrogen loss channel is most likely not open after photoexcitation since the $\pi\sigma^*$(N–H) state cannot be accessed. A similar experiment carried out with the Zajfman trap provided a shorter lifetime of 15 μs, which indicates that the ions are more vibrationally excited in the (O) experiment than in the (A) experiment. No H loss was observed in the (O) experiment, in accordance with the exponential decays. From RRKM calculations, it appears that the temperatures of the parent ions are about 300 K and 800 K in the (A) and (O) experiments, respectively.

4.2. Absorption spectra

Gas-phase absorption spectra of $TryH^+$ and $TryH^+$(CE) recorded at the ring setup are shown in Fig. 3. The first ten peaks in the time spectrum (neutrals counts) after laser excitation were summed and corrected for the background signal due to collisions. This number was then scaled by the background signal and the number of photons to obtain a value for the absorption at a certain wavelength. There is an absorption band with maximum at approximately 249 nm (5.0 eV) for $TryH^+$, which is about 10 nm blueshifted compared to that of protonated Trp. The attachment of CE to $TryH^+$ causes a broadening of the band, and a significant redshift of the maximum to 273 nm (4.5 eV), which is similar to that for the $TrpH^+$ case [14]. It indicates that the absorption depends on the nearby electric field, determined largely by the ion conformation. TD-DFT calculations predict the energies of the L_a and L_b states to be at 4.80 eV and 4.92 eV for $TryH^+$ and 4.71 eV and 4.88 eV for $TryH^+$(CE) in reasonable agreement with the experimental values though the calculated redshift is less than that observed experimentally. The charge transfer state increases in energy from 4.22 eV for $TryH^+$ to 5.34 eV for $TryH^+$(CE). In the latter case it is not within the spectral region for $\lambda > \sim 230$ nm in accordance with the earlier discussion. Both ions display absorption with maxima below 210 nm (Fig. 3).

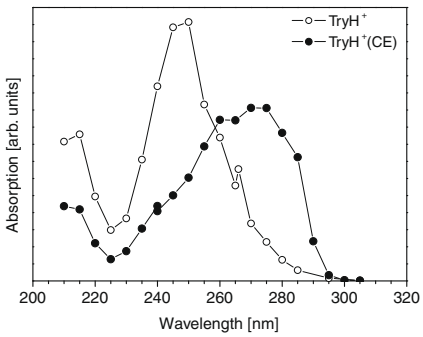

Fig. 3. Absorption spectra of $TryH^+$ and $TryH^+$(CE) recorded in Aarhus at ELISA.

4.3. Photodissociation mass spectra

A daughter ion mass spectrum of $TryH^+$ (*m/z* 161) recorded right after photoexcitation with 266 nm in ELISA showed that loss of NH_3 (*m/z* 144), CH_3NH_2 (*m/z* 130), and $CH_3CH_2NH_2$ (or $CH_2CH_2 + NH_3$) (*m/z* 116) occurred in accordance with previous results from the Orsay group [4]. Fragmentation was sampled between 0 μs and 17 μs after photon absorption. The NH_3 loss channel occurs with a time constant of 20 ns and is therefore fully complete at the end of the sampling interval. We carried out experiments at different wavelengths from 210 nm to 290 nm and measured the branching ratios between the three channels (Fig. 4). It is evident that loss of NH_3 is in competition with loss of CH_3NH_2, favoring the former at low excitation energies. The formation of the *m/z*-116 ion is more or less independent of the photon energy. In a separate experiment, the photoexcited ions were stored for half a revolution before the ring voltages were switched. Here we measure the decay of $Try^{+\cdot}$ radical cations, and the dominant channel is now C_α–C_β cleavage giving the *m/z*-130 ion as expected [1]. Interestingly, another channel for $Try^{+\cdot}$ is ammonia loss, which was also seen for $Trp^{+\cdot}$ formed after photoexcitation of $TrpH^+$ [14].

Next we consider the dissociation of $TryH^+$(CE) (*m/z* 425) after photoexcitation with 266-nm light in the ring (A) (Fig. 5b). In the time interval from 0 to about 28 μs (Fig. 5b), the dissociation channels are loss of NH_3 (*m/z* 408) and CH_3NH_2 (*m/z* 394), as seen for $TryH^+$, but there are also peaks corresponding to H^+(CE) (*m/z* 265), NH_3^+(CE) (*m/z* 281), and $CH_3NH_2^+$(CE) (*m/z* 295) present in the spectrum. We cannot exclude the formation of $TryH^+$ since there is large discrimination against storage of lower mass ions in this experiment. The loss of NH_3 and CH_3NH_2 is intriguing since the CE is initially bound to the ammonium group; the isomer where CE is bound to protonated indole is higher in energy by 1 eV according to theoretical modeling [27,28]. This implies that

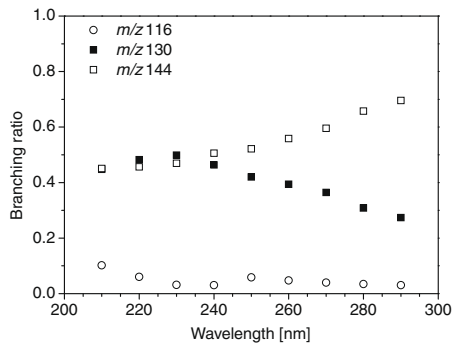

Fig. 4. Branching ratios between the three fragmentation channels of $TryH^+$ after photoexcitation (A). The values are calculated from peak areas in the photodissociation mass spectra.

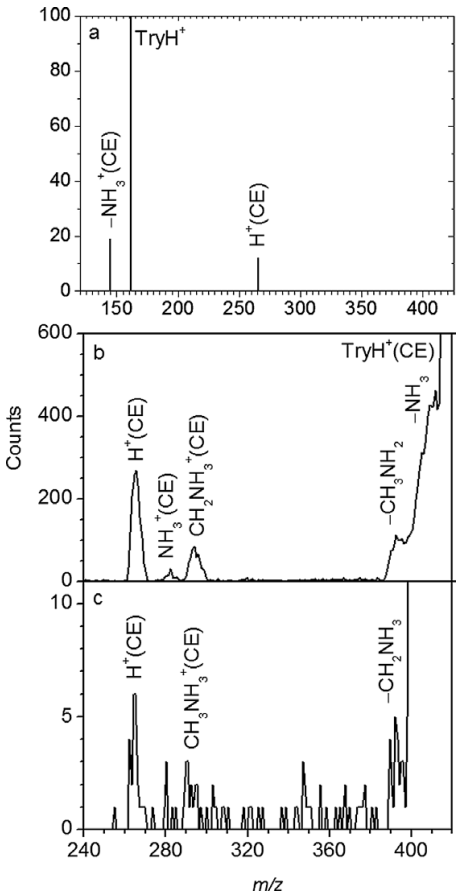

Fig. 5. Photodissociation mass spectra of $TryH^+(CE)$. (a) (O) spectrum: fragment ions were produced in a 0–250 ns time window after photoexcitation at 263 nm. (b) (A) spectrum: fragment ions formed up to 28 μs after photoexcitation at 266 nm. (c) (A) spectrum: fragment ions formed between 42 μs and 69 μs after photoexcitation at 266 nm.

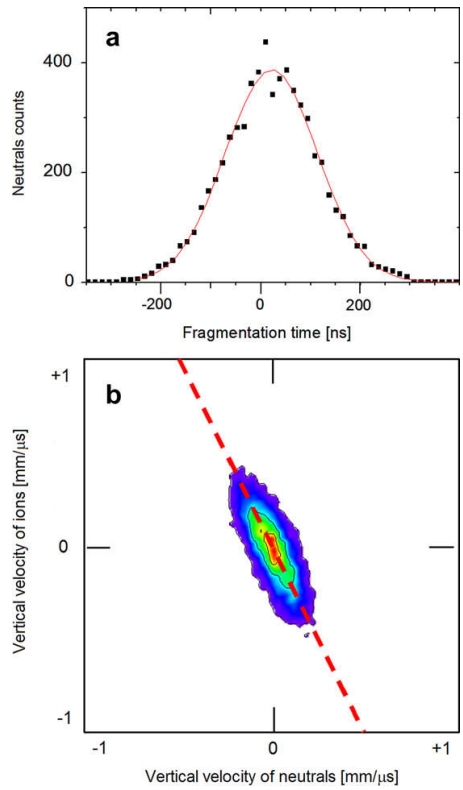

Fig. 6. (a) Photodissociation of $TryH^+(CE)$ in an electric field of 10 V/mm and sampling the loss of $NH_3(CE)$ to give m/z 144, (O) experiment. The fragmentation time spectrum displays a peak with a symmetric shape, and the time scale is nanoseconds. The peak width is due to the kinetic energy released in the fragmentation process. The curve is a Monte Carlo simulation to a 30-ns fragmentation time. (b) 'Vz Vz' correlation diagram for m/z = 144 (Vz = vertical velocity). Horizontal and vertical axes are the horizontal and vertical components of the velocities for neutral and ionic fragments. For a binary fragmentation, the data must be situated along a line the slope of which is given by the mass ratio between the two fragments. The dotted line corresponds to the mass ratio given by a binary mechanism.

during dissociation along the C–NH_3 coordinate, the CE has time to rearrange. Likely an ion–molecule complex is formed from which either NH_3 or CH_3NH_2 escapes. Delayed dissociation occurring in the time interval of 42–69 μs reveals the same dissociation channels but the signal-to-noise ratio is low because there were too few ions (Fig. 5c).

The (O) photodissociation mass spectrum is shown in Fig. 5a. In the m/z-region from 250 to 425, only $H^+(CE)$ ions from $TryH^+(CE)$ are measured, in clear contrast to the (A) experiment. At lower m/z, peaks can be assigned to correspond to $TryH^+$ (m/z 161) and the loss of $NH_3(CE)$ to give $[TryH–NH_3]^+$ (m/z 144). The fact that crown ether was found to stay bound to the ion in the (A) experiment is again in accordance with a lower internal energy distribution in the (A) experiment compared to that in the (O) experiment, cf., the discussion of time constants above.

Photodissociation of $TryH^+(CE)$ in an electric field in combination with a time-of-flight analysis reveals that the losses of $NH_3(CE)$ and Try are complete within 30 ns (Fig. 6a), and a Vz Vz correlation plot indicates that both fragmentations are binary (see Fig. 6b in the case of $NH_3(CE)$ loss). The channel is more expensive than just losing ammonia due to the favorable binding of CE to $[TryH–NH_3]^+$. A time scale of nanoseconds compared to the microsecond time constants obtained from the trap experiments may suggest that the breakage of the C–NH_3 bond is non-statistical occurring in an electronic excited state.

4.4. Theoretical modeling of the C–NH_3 dissociative channel

We have done TD-DFT calculations to better understand the apparently non-statistical process in which both ammonia and CE are lost and have identified an electronically excited state denoted as $\pi\sigma^*$(C–NH_3) that is located within the spectral region used for excitation (Fig. 7). This state is not the lowest as in the case of bare protonated Try. The minimum energy path along the C–NH_3 coordinate exhibits a small barrier to the excited state dissociation. This barrier is due to the fact that the lowest excited state of $\pi\pi^*$ character is attractive along this coordinate, whereas the $\pi\sigma^*$(C–NH_3) is dissociative. Owing to the energy content of the excited molecule (photon energy and internal energy prior to photoexcitation) and the uncertainties of the calculations, one can consider that this excited state fragmentation channel is open. It should be noticed that this dissociation is the result of a transfer

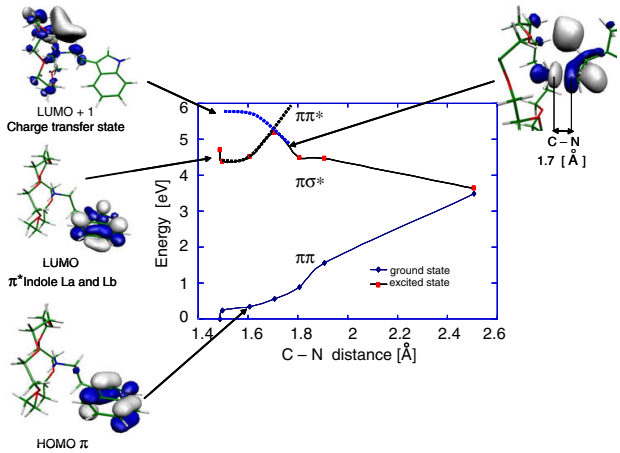

Fig. 7. Minimum energy paths (MEP) along the C–N stretch. HOMO, LUMO and LUMO+1 potential energy curves of $TryH^+$(CE) calculated at the TD-DFT level with the SV(P) level of theory showing the charge transfer near 1.7 Å.

VIII

of the photoactive electron from the indole chromophore to an antibonding orbital located between carbon and NH_3. We expect that this state plays a role also upon photoexcitation of bare $TryH^+$ ions but cannot in this case disentangle it from statistical loss of ammonia that also occurs on a nanosecond time scale. For $TryH^+$ the fragmentation is barrierless in contrast to $TryH^+$(CE), which suggests a longer excited state lifetime for $TryH^+$(CE); this will be tested in the near future.

Acknowledgements

S.B.N. gratefully acknowledges support from Lundbeckfonden (Junior Group Leader Fellowship) and Dir. Ib Henriksens Fond. U.K. thanks the relations Internationales of the Université Paris Sud for financial support.

References

[1] B. Lucas, M. Barat, J.A. Fayeton, M. Perot, C. Jouvet, G. Grégoire, S. Brøndsted Nielsen, J. Chem. Phys. 128 (2008) 164302.
[2] V. Lepère et al., J. Chem. Phys. 127 (2007) 134313.
[3] H. Kang et al., Phys. Chem. Chem. Phys. 6 (2004) 2628.
[4] H. Kang et al., J. Phys. Chem. A 109 (2005) 2417.
[5] J.U. Andersen et al., Phys. Chem. Chem. Phys. 6 (2004) 2676.
[6] F.O. Talbot, T. Tabarin, R. Antoine, M. Broyer, P. Dugourd, J. Chem. Phys. 122 (2005) 074310.
[7] G. Gregoire et al., Phys. Chem. Chem. Phys. 8 (2006) 122.
[8] G. Gregoire, C. Jouvet, C. Dedonder, A.L. Sobolewski, Chem. Phys. 324 (2006) 398.
[9] G. Gregoire, C. Jouvet, C. Dedonder, A.L. Sobolewski, J. Am. Chem. Soc. 129 (2007) 6223.
[10] H. Kang et al., J. Chem. Phys. 122 (2005) 084307.
[11] O.V. Boyarkin, S.R. Mercier, A. Kamariotis, T.R. Rizzo, J. Am. Chem. Soc. 128 (2006) 2816.
[12] D. Nolting, C. Marian, R. Weinkauf, Phys. Chem. Chem. Phys. 6 (2004) 2633.
[13] S.R. Mercier et al., J. Am. Chem. Soc. 128 (2006) 16943.
[14] U. Kadhane et al., J. Chem. Phys. 129 (2008) 184304.
[15] O.A. Raevsky, V.P. Solovev, A.F. Solotnov, H.J. Schneider, V. Rudiger, J. Org. Chem. 61 (1996) 8113.
[16] R.R. Julian, J.L. Beauchamp, Int. J. Mass Spectrom. 210 (2001) 613.
[17] J.J. Wilson, G.J. Kirkovits, J.L. Sessler, J.S. Brodbelt, J. Am. Soc. Mass Spectrom. 19 (2008) 257.
[18] A.I.S. Holm et al., Int. J. Mass Spectrom. 276 (2008) 116.
[19] S.P. Møller, Instrum. Methods Phys. Res. Sect. A 394 (1997) 281.
[20] J.U. Andersen et al., Rev. Sci. Instrum. 73 (2002) 1284.
[21] S. Brøndsted Nielsen, L.H. Andersen, Biophys. Chem. 124 (2006) 229.
[22] K. Støchkel et al., Rev. Sci. Instrum. 79 (2008) 023107.
[23] H.B. Pedersen et al., Phys. Rev. Lett. 87 (2001) 055001.
[24] TURBOMOLE V5.9 2008, A Development of University of Karlsruhe and Forschungszentrum Karlsruhe GmbH, 1989–2007, TURBOMOLE GmbH, Since 2007. <http://www.turbomole.com>.
[25] J.U. Andersen et al., Eur. Phys. J. D 25 (2003) 139.
[26] M. Brøndsted Nielsen, T.J.D. Jørgensen, J.S. Forster, G. Bojesen, S. Brøndsted Nielsen, Int. J. Mass Spectrom. 248 (2006) 47.
[27] Z.B. Maksic, B. Kovacevic, Chem. Phys. Lett. 309 (1999) 497.
[28] H. Lioe, R.A.J. O'Hair, G.E. Reid, J. Am. Soc. Mass Spectrom. 15 (2004) 65.

Tagging of Protonated Ala-Tyr and Tyr-Ala by Crown Ether Prevents Direct Hydrogen Loss and Proton Mobility after Photoexcitation: Importance for Gas-Phase Absorption Spectra, Dissociation Lifetimes, and Channels

Jean Ann Wyer,* Anneli Ehlerding, Henning Zettergren, Maj-Britt S. Kirketerp, and Steen Brøndsted Nielsen

Department of Physics and Astronomy, Aarhus University, Ny Munkegade, DK-8000 Aarhus C, Denmark

Received: May 1, 2009; Revised Manuscript Received: July 9, 2009

Photodissociation of protonated Tyr, Ala-Tyr, Tyr-Ala (Ala = alanine, Tyr = tyrosine), and their complexes with 18-crown-6-ether (CE) was performed in an electrostatic ion storage ring using a tunable laser system. While the three bare ions all absorb strongly at 222 nm, absorption at higher wavelengths was barely visible from sampling the neutrals formed in delayed dissociation. A band at 270 nm was introduced, however, as a consequence of CE attachment to the bare ions. To understand the difference between bare ions and complexes, electronically excited states are considered: The initially reached $\pi\pi^*$ state on phenol couples with the dissociative $\pi\sigma^*$ state on ammonium, which leads to direct hydrogen loss. Cold radical cations are formed that at high wavelengths do not have enough energy for further dissociation. Excitation within the 222-nm band on the other hand leads to delayed dissociation of stored radical cations that is monitored in the present setup. The $\pi\sigma^*$ state moves out of the spectral region upon CE attachment, and instead statistical dissociation is sampled on the microsecond to millisecond time scale at all wavelengths. Our data demonstrate the strength of using supramolecular complexes for action spectroscopy experiments to prevent erroneous spectra as a result of undesired dissociation (H loss) from electronically excited states. The gas-phase absorption spectra firmly establish the perturbations of the phenol electronic structure by a water solvent: The 270-nm band red shifts by ~5 nm, whereas the 222-nm band changes by ~3 nm. Both transitions occur in the phenol group. These results may be useful for protein dynamics experiments that rely on electronic excitations. Product ion mass spectra of $[Tyr + H]^+$, $[Ala\text{-}Tyr + H]^+$, $[Tyr\text{-}Ala + H]^+$, $[Ala\text{-}Tyr + H]^+$(CE), and $[Tyr\text{-}Ala + H]^+$(CE) significantly depend on the excitation wavelength from 210 to 310 nm and on whether the ionizing proton is mobile or not.

IX

Introduction

Electronic absorption by biochromophore ions in vacuo has become a topic of high current interest since the first gas-phase absorption spectrum of the isolated green fluorescent protein (GFP) chromophore anion was published in 2001.[1] A comparison with the protein absorption spectrum revealed that the best way to approximate the environment of the buried chromophore was to take it as being a vacuum. On the other hand, the absorption was completely different in bulk water solution due to charge localization by the polar water molecules. Other work has concentrated on protonated Schiff-base retinal,[2,3] which is the chromophore responsible for vision. Here, the amino acid residues in the neighborhood of the chromophore play a significant role in color tuning, which allows us to perceive light from red to blue. Metalloporphyrins are another class of highly important biochromophores. Recently, the Soret marker band of isolated Fe(III)-heme cations was reported by Lykkegaard et al.[4] along with the spectral changes upon histidine ligation. If four-center ferric heme exists inside a hydrophobic pocket or crevice of a heme protein, its absorption should resemble that of the isolated species. The gas-phase absorption spectra serve a dual purpose as they are also used extensively to benchmark theoretical models.[5−13]

Gas-phase absorption spectroscopy on macromolecular ions has been made possible in our laboratory from the combination of an electrospray ion source, an electrostatic ion storage ring, and pulsed lasers.[14,15] In the ring, the ions are photoexcited, and their lifetimes are measured with respect to dissociation. The problem with finite sampling intervals encountered in finite length time-of-flight instruments (kinetic shifts) is circumvented, and the actual number of photoexcited ions at all wavelengths may be obtained from fits to exponential decays of the ions. A new implementation of pulsed power supplies for all ring elements has allowed for time-dependent photodissociation mass spectroscopy on the microsecond to millisecond time scale,[14−16] which is not routinely done with other instruments. While the mass resolution is poor (about 100), it is in most cases high enough to determine the dissociation channels and their time dependence.

In the present work, the focus is on the photophysics and photodissociation of isolated peptide cations. Knowledge on how the absorption of amino acids and peptides changes as the environment varies is useful for optical probing and labeling and for the choice of wavelength for UV resonance Raman experiments on proteins.[17] Interestingly, recent work on silver trimer−dipeptide bioconjugates showed that peptide absorption was enhanced and extended to a larger range of wavelengths due to Ag_3^+ complexation.[18]

Peptides containing the aromatic amino acid tyrosine absorb in the UV and are photodissociated in mass spectroscopy

* To whom correspondence should be addressed. E-mail: jeanwyer@phys.au.dk.

10.1021/jp904053d CCC: $40.75
Published on Web 07/29/2009

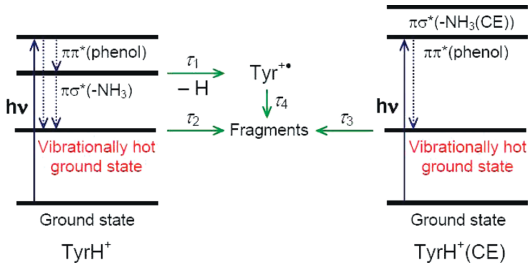

Figure 1. Simplified state level diagrams including some important states. After photoexcitation of protonated tyrosine ($\pi\pi^*$ transition in the phenol group), internal conversion (IC) occurs either back to the electronic ground state (GS) or to a charge-transfer (CT) state located on ammonium, cf. dashed arrows. In the former case a vibrationally excited ion that decays statistically is formed. In the latter case, hydrogen loss is in competition with IC to the GS. The CT state is not accessible in the supramolecular complex between protonated tyrosine and 18-crown-6 ether, and the pathway is IC back to the GS followed by statistical dissociation. The relationship between the time constants is as follows: $\tau_1 \ll \tau_2 \ll \tau_3 < \tau_4$. τ_4 represents a broad range of time constants.

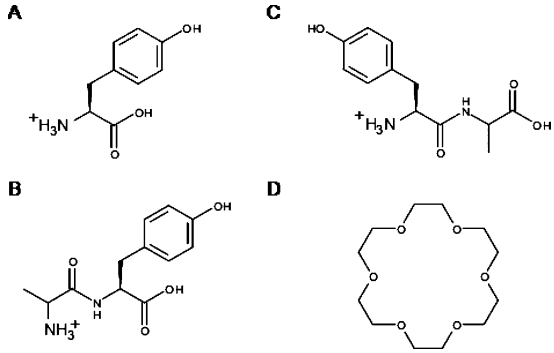

Figure 2. Structures of (A) $[Tyr + H]^+$, (B) $[Ala\text{-}Tyr + H]^+$, (C) $[Tyr\text{-}Ala + H]^+$, and (D) 18-crown-6 ether.

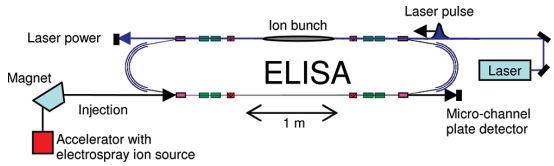

Figure 3. Schematic of the ELISA electrostatic storage ring in combination with a laser system. The photofragment yield was obtained as a function of wavelength from the signal of neutrals hitting the detector.

experiments with conventional lasers.[19−22] If the initial energy is known, the excitation energy after photon absorption is well-defined. This offers an advantage over methods using collisional excitation.[23] Many previous experiments on tyrosine and tyrosine-containing peptides have been completed in conjunction with another biologically significant amino acid, tryptophan (Trp).[18−22,24−35] Subsequent to UV excitation of the indole aromatic ring in tryptophan to a $\pi\pi^*$ state, several dissociation pathways are available.[36] In one such dissociation channel, the $\pi\pi^*$ state couples with a lower lying repulsive $\pi\sigma^*(NH_3)$ state, located on the ammonium group leading to dissociation along the NH coordinate. The energy distribution of the remaining radical cation $Trp^{+\bullet}$ is broad as the kinetic energy range of the ejected hydrogen atom is large. Consecutive dissociation occurs on a microsecond to millisecond time scale.[25,37,38] For protonated tyrosine, however, the NH fragmentation pathway is less accessible after 266-nm photoexcitation as the $\pi\sigma^*(NH_3)$ state is situated at a higher energy (3.4 eV for Trp vs 4.0 eV for Tyr).[25] Previous work has shown that the energy of the $\pi\sigma^*(NH_3)$ state is higher when 18-crown-6 ether (CE) is attached to the ammonium group, rendering the state inaccessible after 260-nm excitation (see Figure 1).[39,40] The size of the chosen crown ether is optimum for the formation of three hydrogen bonds with ammonium.[41−43] Tagging of peptide ammonium groups by crown ether impacts not only the photophysics but, as we will show, also the dissociation channels.

Here we have explored the photophysics of protonated Ala-Tyr, Tyr-Ala (Ala = alanine and Tyr = tyrosine), and their complexes with CE isolated in vacuo (Figure 2), and whether or not water has an influence on the electronic transition energies. Lifetime measurements, absorption spectra, and photodissociation mass spectra are presented, and the results compared to those for protonated Tyr. $[Tyr + H]^+$ has earlier been studied in detail by Kang et al.[25] for 266-nm photoexcitation, but we have extended the excitation region down to 210 nm, accessing a different electronic transition.

Experimental Section

All compounds were purchased from Sigma-Aldrich.

Gas-Phase Experiments. Experiments were carried out at the electrostatic ion storage ring in Aarhus (ELISA) (see Figure 3).[14,15] Electrospray ionization was used to produce the ions which were subsequently accumulated in a 22-pole ion trap and thermally equilibrated by collisions with a helium buffer gas therein. The ions were accelerated as an ion bunch to kinetic energies of 22 keV, and a bending magnet was used to select the appropriate ions. Following injection into the ring, the ions were stored for about 40 ms before being irradiated by a nanosecond light pulse from a tunable EKSPLA laser. This is an Nd:YAG laser where the third harmonic (355 nm) pumps an optical parametric oscillator (OPO). The visible output from this OPO is frequency doubled in a crystal providing UV light. The repetition rate of the experiment was 10 Hz. Dissociation was a result of one photon absorption. Lifetimes were obtained from measurements of the yield of neutrals hitting the micro-channel plate (MCP) detector located at the end of the straight section opposite to the side where photoexcitation was performed.

In separate experiments, the ring voltages were changed at a particular time after photoexcitation to store product ions with the appropriate kinetic energy. This product ion mass spectrometry was possible as ELISA has been equipped with pulsed power supplies of microsecond response times.[14−16] After a specific number of revolutions, the product ions were dumped into the MCP detector. Ions with a lower kinetic energy were evident when a low number of revolutions was used, while ions with a higher kinetic energy were indistinguishable in such a case as ELISA preferentially stores ions with a larger kinetic energy. Ions with a higher kinetic energy were resolved when a higher number of revolutions were undertaken prior to dumping on the detector. Ions with a lower kinetic energy were, however, not evident on such spectra. To increase the resolution, a beam scraper was put in on one side of the ring. The signal from the detector as a function of the scaling of the ring voltages provided the product ion mass spectrum. The pressure in the ring was of the order of 10^{-11} mbar, which set an upper limit of seconds on the storage time.

Solution-Phase Experiments. Solution-phase absorption spectroscopy experiments were carried out using a Thermo

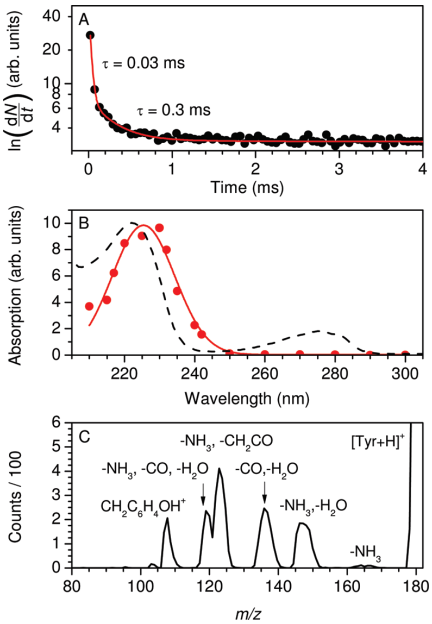

Figure 4. (A) Time spectrum of $[Tyr + H]^+$ (*m/z* 182) after 220-nm photoexcitation. The solid curve is a fit of three exponentials to the data. It was found that the lifetimes associated with the first two exponentials were 0.03 and 0.3 ms, and the lifetime associated with the exponential corresponding to the background decay was 0.4 s. (B) Absorption spectrum of $[Tyr + H]^+$ in vacuo. A Gaussian fit to the data (red points) is shown as a solid line. The solution-phase absorption spectrum is shown as a dashed line. (C) Photodissociation mass spectrum of $[Tyr + H]^+$ after 220-nm photoexcitation.

Spectronic heλios α instrument. Compounds were dissolved in water and spectra recorded from 190 to 325 nm.

Results and Discussion

Protonated Tyrosine. Our initial experiments focused on the decay of $[Tyr + H]^+$ after photoexcitation. A sample time spectrum of $[Tyr + H]^+$ after photoexcitation, measured by detecting the neutral fragments on one side of the ring, is shown in Figure 4A. These were produced between 27 and 45 μs after photoexcitation in the first instance and then after successive rotations in the ring. In order to fit the data, it was found that three separate exponentials were required. The fastest decay had time constants of the order of 10^{-2} ms. The next decay had time constants of the order of 10^{-1} ms, and while it is possible that this decay is due to excitation into a triplet state, it is more likely a tail associated with the first decay due to a broad energy distribution.[38] The more exponentials that are required, the broader the internal energy distribution; in the extreme, the decay follows a power-law decay.[44] The time constants for the slowest decay were set to that found after fitting the decay of $[Tyr + H]^+$ when no photoexcitation occurred (CID decay). From a fit to the experimental data, it was possible to extrapolate back to time zero, defined as the time when the laser was fired, and sum the decay due to both decay channels for each wavelength used. Summing over the entire time of decay is important as changes in lifetimes with λ could significantly affect the calculated values of absorption if not calculated over the entire decay time from time zero. The resulting absorption spectrum for $[Tyr + H]^+$ in vacuo is shown in Figure 4B where it can be seen that there is one band which ranges from 210 nm, the lowest end of our scale, to ~255 nm, peaking at about 225 nm. The solution-phase spectrum is also included in the figure. In water, the first band maximum is at 222 nm, but the second band at 275 nm is absent from the gas-phase spectrum. Explanations for this are discussed below.

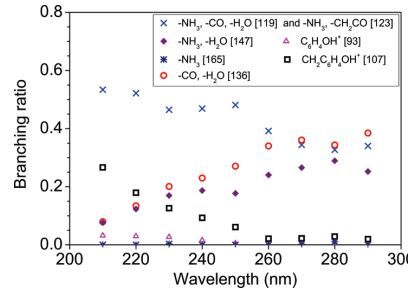

Figure 5. Branching ratios for fragmentation channels of $[Tyr + H]^+$ (*m/z* 182) as a function of excitation wavelength. The resolution is too low to separate *m/z* 119 and 123 so they are summed. The signal for each peak was divided by the mass to correct for sampling efficiency. Fragment ion masses are in brackets.

Photodissociation mass spectra of $[Tyr + H]^+$ (*m/z* 182) after excitation in the range 210−300 nm were also measured (for 220-nm absorption, see Figure 4C). Fragment ions formed in the time from 0 to 18 μs after photoexcitation were sampled. Peaks can be assigned to ions that have lost NH_3 (*m/z* 165), NH_3 and H_2O (*m/z* 147), CO and H_2O (*m/z* 136), NH_3 and CH_2CO (*m/z* 123), and NH_3, CO, and H_2O (*m/z* 119), and a peak which corresponds to the side chain ion (*m/z* 107). The observation of these peaks is in accordance with a previously reported spectrum by Kang et al.[25] recorded at 266 nm. In our spectrum there are two additional peaks at *m/z* 93 corresponding to $C_6H_4OH^+$ and at *m/z* 103, currently unassigned.

The branching ratios for the different fragment ions as a function of excitation wavelength are shown in Figure 5. It is evident that the *m/z*-107 peak decreases in importance with λ. This peak is a fingerprint for the formation of the tyrosine radical cation by hydrogen loss from photoexcited $[Tyr + H]^+$. As shown by Kang et al.,[25] a crossing from the initially reached $\pi\pi^*$ state on the phenol to the $\pi\sigma^*$ state on the ammonium occurs with about 25% probability after 266-nm photoexcitation. H loss requires 4.0 eV, and taking into account the fact that the hydrogen leaves with a significant amount of energy, the $Tyr^{+\bullet}$ radical cations have limited energy but a broad internal energy distribution as shown earlier in the case of tryptophan.[40] The side chain cation (*m/z* 107) is then formed from the $Tyr^{+\bullet}$ radical after $C_\alpha - C_\beta$ bond cleavage. Competing internal conversion from the $\pi\pi^*$ state back to the electronic ground state leads instead to hot $[Tyr + H]^+$ ions that dissociate with a time constant of less than 10 μs (see Figure 1).[45] In the present measurements, it is impossible to distinguish between $[Tyr + H]^+$ and $Tyr^{+\bullet}$ due to the poor mass resolution of the ring elements.

It is now possible to explain the absence of the 270-nm band in the action spectrum: Dissociation occurs over longer time periods when the ion has less energy; hence, further dissociation after hydrogen loss subsequent to 270-nm photoexcitation may not occur on the time scales investigated in the current experiments. In contrast, further dissociation after hydrogen loss following 220-nm photoexcitation is more probable due to the larger amounts of energy deposited. The photon energy at 270 nm is 4.6 eV, while it is more than 1 eV higher at 220 nm (5.7 eV), which would clearly have a noticeable effect on the lifetime of $Tyr^{+\bullet}$ ions. Consequently, absorption at 220 nm has been

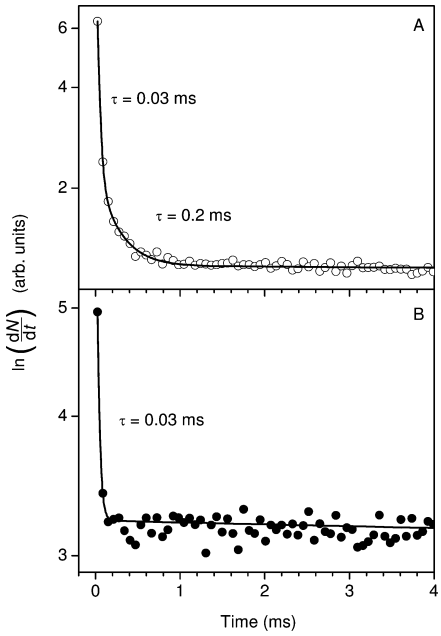

Figure 6. Time spectra of (A) $[Ala\text{-}Tyr + H]^+$ (m/z 253) and (B) $[Tyr\text{-}Ala + H]^+$ (m/z 253) after 220-nm photoexcitation. The solid curve in (A) is the fit of three exponentials to the data with one of the exponentials corresponding to the background decay (τ = 0.3 s). Lifetimes associated with the other decays are indicated on the graph. The solid curve in (B) is the fit of two exponentials to the data with one of the exponentials corresponding to the background decay (τ = 0.3 s). The lifetime associated with the other decay is indicated on the graph.

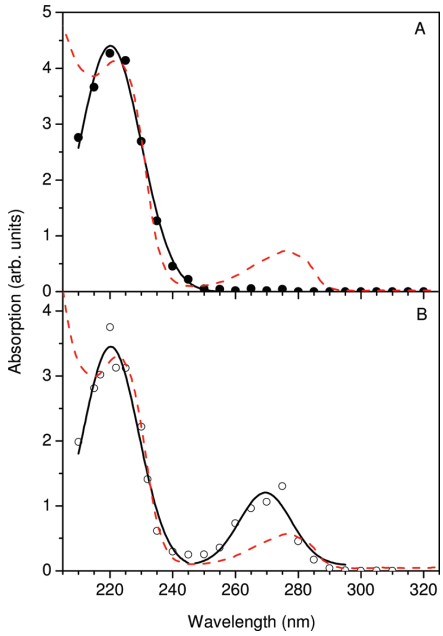

Figure 7. Absorption spectra of (A) $[Ala\text{-}Tyr + H]^+$ (m/z 253) and (B) $[Ala\text{-}Tyr + H]^+$(CE) (m/z 517) in vacuo. Gaussian fits to the data are shown as solid lines. Absorption spectra of solution-phase Ala-Tyr and Ala-Tyr(CE) are shown as red dashed lines. Addition of crown ether to the solution does not change the absorption.

IX

measured, whereas absorption at 270 nm appears to be absent when the first neutrals sampled are formed after 27 μs. It should be mentioned that delayed dissociation has earlier been observed where photodissociation was achieved using the fourth harmonic light of a Nd:YAG laser (266 nm).[38] The light intensity was an order of magnitude higher than that in the present experiment, resulting in more photoexcited ions and consequently a higher yield of neutrals. We assume that it is only ions at the upper end of the internal energy distribution that have enough energy for dissociation. Another complication besides too few $Tyr^{+\bullet}$ ions dissociating at high wavelengths arises from the fact that the crossing to the $\pi\sigma^*(NH_3)$ state may depend strongly on excitation wavelength; hence, an action spectrum based on integration of the yield of all product ions, formed from 0 to 18 μs, not including $Tyr^{+\bullet}$ could also be incorrect.

Protonated Ala-Tyr and Tyr-Ala. Time spectra of $[Ala\text{-}Tyr + H]^+$ and $[Tyr\text{-}Ala + H]^+$ are shown in Figure 6 after 220-nm photoexcitation (initially sampling neutrals produced between 31 and 52 μs after photoexcitation, and then after successive rotations in the ring). Both ions dissociate with a time constant of 0.03 ms, which indicates that the dissociation channels are similar or that the activation energies and preexponential factors are. The better statistics in the spectrum for $[Ala\text{-}Tyr + H]^+$ reveals a tail to longer times that can be fit with an exponential associated with a time constant of 0.2 ms. The tail is a result of the width of the internal energy distribution; not all ions have exactly the same energy after photoexcitation. The experiment was repeated at higher wavelengths, 250−280 nm, but no photoinduced signal could be discerned from the background collision induced dissociation signal. Based on the lifetimes, we obtain the gas-phase absorption spectra shown in Figures 7A and 8A. For both peptides the band is at ∼220 nm, which is close to that obtained in water solution (Figures 7A and 8A). The band shapes are very similar for the solution- and gas-phase experiments. In addition, they are comparable to that measured for protonated tyrosine, which indicates that for the dipeptides the electronic transition is also due to excitation of the phenol ring.

We now describe the fragmentation channels for the two dipeptides. Photodissociation mass spectra of $[Ala\text{-}Tyr + H]^+$ recorded at excitation wavelengths of 210 and 270 nm are shown in Figure 9. Fragment ions formed from 0 to 21 μs after photoexcitation were sampled. At the highest wavelength, the largest peak corresponds to y^+ ions (m/z 180), whereas x^+ (m/z 208) or ions that have lost $CO + H_2O$ (m/z 207) ions are formed dominantly at the low wavelength. Side chain cleavages also occur, with most at 220 nm. In accordance with this, the specific fragmentation of the $C_\alpha - C_\beta$ bond of the tyrosyl residue was observed to occur after 262-nm excitation of larger tyrosyl-containing peptides.[46,47] In our work, there is also a small signal due to loss of ammonia. The wavelength dependence of the different channels is presented in Figure 10A, where it is evident that the transition from y^+ to m/z 207/208 occurs gradually with decreasing λ.

The y^+ ions are expectedly formed after internal conversion to the electronic ground state since rupture of the peptide bond is a dominant channel in low-energy CID experiments. The fact that no delayed dissociation is observed at 270 nm then implies that the time constant for statistical dissociation is too short for the photoexcited parent ions to survive half a revolution in the ring (32 μs); the same is true for $[Tyr\text{-}Ala + H]^+$.

IR-UV double resonance spectroscopy of cold $[Ala\text{-}Tyr + H]^+$ ions by Stearns et al.[48,49] revealed a strong interaction

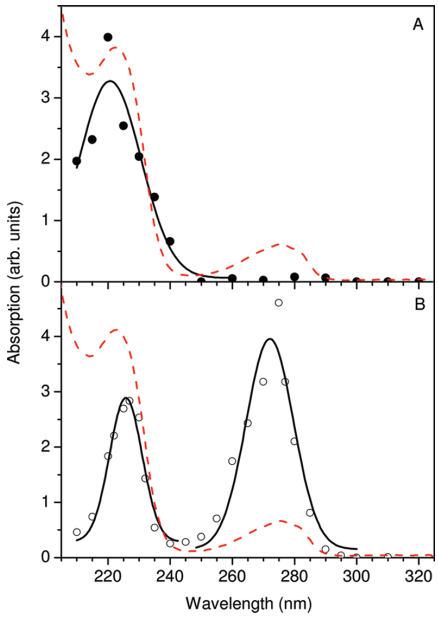

Figure 8. Absorption spectra of (A) $[Tyr\text{-}Ala + H]^+$ (m/z 253) and (B) $[Tyr\text{-}Ala + H]^+(CE)$ (m/z 517) in vacuo. Gaussian fits to the data are shown as solid lines. Absorption spectra of solution-phase Tyr-Ala and Tyr-Ala(CE) are shown as red dashed lines. Addition of crown ether to the solution does not change the absorption.

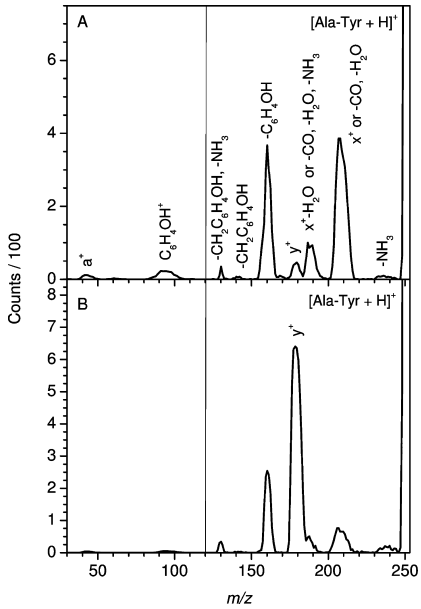

Figure 9. Photodissociation mass spectra of $[Ala\text{-}Tyr + H]^+$ (m/z 253) after (A) 210-nm and (B) 270-nm photoexcitation. The ions with m/z < 120 were dumped on the detector after 1.5 revolutions, while the ions with m/z > 120 were dumped on the detector after 7.5 revolutions.

between the ammonium group and the π cloud of the phenol; it is likely that some ions in such a structure are present in our ion beam (room temperature internal energy distribution). The high crossing probability to the $\pi\sigma^*(NH_3)$ state is then most likely due to the short distance the photoactive electron has to jump. The $\pi\sigma^*(NH_3)$ state may, however, efficiently couple with the ground state preventing hydrogen loss. For comparison, Gregoire et al.[24] found that while the $\pi\sigma^*$ state is populated in $[Gly\text{-}Tyr\text{-}Gly + H]^+$ after 266-nm photoexcitation, hydrogen loss did not occur. It was suggested that H loss would be suppressed by a kind of cage effect. In agreement with this, we have earlier shown that $[Lys\text{-}Tyr\text{-}Lys + H]^+$ after 266-nm photon absorption decays exponentially.[38] Finally, the suppression of H loss was observed in related experiments involving electron transfer from sodium atoms to peptide dications. In this work, all dipeptides studied lost hydrogen, whereas the intact charge-reduced cation was observed in high yield for tripeptides and larger peptides.[50] Solvation had a similar effect, namely, preventing hydrogen loss. Tabarin et al.,[46] however, found that the protonated leucine-enkephalin lost hydrogen at 220-nm excitation but not at 260 nm. In any case, ions that lose hydrogen at 277 nm will be too cold for subsequent dissociation, while the larger local energy depositions at 220 nm may lead to more hydrogen loss and radical cations that now dissociate on a time scale which is within the window of the experiment.

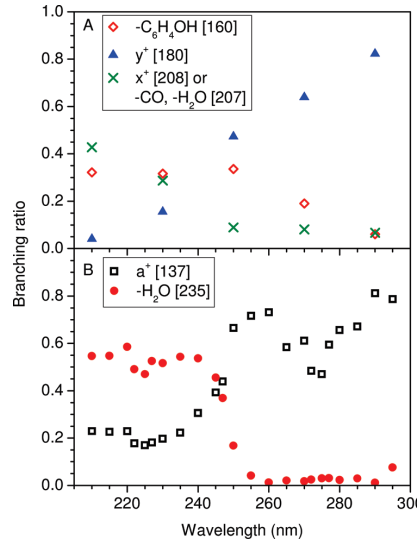

Figure 10. Branching ratios for the main fragmentation channels of (A) $[Ala\text{-}Tyr + H]^+$ and (B) $[Tyr\text{-}Ala + H]^+$ as a function of excitation wavelength. Fragmentation channels with branching ratios <10% are not included on the graphs for clarity but were included in the branching ratio calculations. The signal for each peak was divided by the mass to correct for sampling efficiency. Fragment ion masses are in brackets.

The corresponding photodissociation mass spectra of $[Tyr\text{-}Ala + H]^+$ are shown in Figure 11. Fragment ions were formed from 0 to 21 μs after photoexcitation. At both 210 and 270 nm, a^+ ions (Y immonium) (m/z 136) are formed with a high yield and $a^+\text{-}NH_3$ (m/z 120) with a minor yield. The a^+ fragment ion was also found to be dominant after 266-nm, 277-nm, and 284-nm photon excitation in ion traps reported by Gabryelski et al.,[51] Yoon et al.,[52] and Stearns et al.,[49] respectively. At the low wavelength, H_2O loss occurs to a large extent (m/z 235). This loss may be linked to the photoactive electron jumping to the carboxylic acid group and concomitant proton transfer to the negatively charged COOH group from ammonium, as described in the case of protonated tryptophan.[53] A wavelength dependent study (Figure 10B) reveals that water loss is dominant after

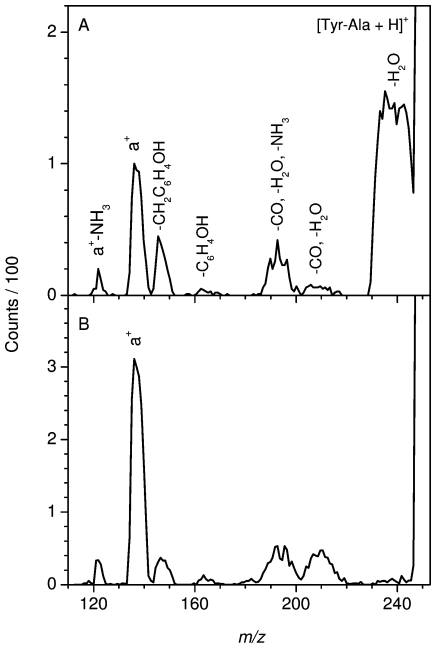

Figure 11. Photodissociation mass spectra of $[Tyr\text{-}Ala + H]^+$ (m/z 253) after (A) 210-nm and (B) 270-nm photoexcitation.

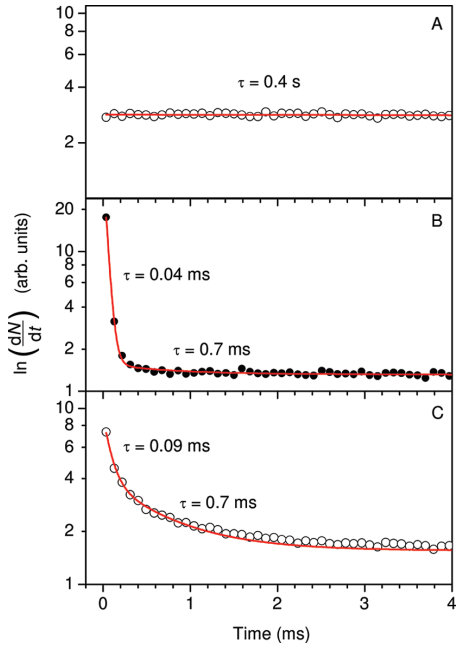

Figure 12. Time spectra of $[Ala\text{-}Tyr + H]^+$(CE) (m/z 517) after (A) no photoexcitation, (B) 220-nm photoexcitation, and (C) 270-nm photoexcitation. The lifetime associated with the exponential corresponding to the background was 0.4 s, which was found by fitting an exponential to the data in (A). The solid curves in (B) and (C) are fits of three exponentials to the data with one of the exponentials in both cases corresponding to the background decay. For (B) it was found that the lifetimes associated with the first two exponentials were 0.04 and 0.7 ms, while for (C) the lifetimes associated with the first two exponentials were 0.09 and 0.7 ms.

excitation within the 220-nm band whereas a^+ ions are formed in highest abundance after excitation within the 270-nm band; the transition between the two channels is quite abrupt at 245 nm. Side chain cleavages are also seen to take place as well as loss of CO and H_2O. Loss of the tyrosine side chain radical to give the fragment ion at m/z 146 has been attributed to dissociation from an excited electronic state of $[Tyr + H]^+$.[48] The distance between phenol and ammonium is assumed to be the same in $[Tyr\text{-}Ala + H]^+$ and $[Tyr + H]^+$, but H loss would again result in ions with too low an internal energy to give delayed formation of neutrals after 270-nm excitation.

To summarize the results for the bare ions, we have found that it is not possible to measure a 270-nm absorption band from delayed dissociation after half a revolution (at least not with the photon fluxes provided by our tunable laser system), which we have taken to be due to (i) the coupling between the $\pi\pi^*$(phenol) and $\pi\sigma^*(NH_3)$ states and subsequent hydrogen loss leaving ions with too low internal energy for further fragmentation and (ii) a too short lifetime of the parent ions after internal conversion back to the electronic ground state. Absorption does indeed happen in this wavelength region, which is evident from our photodissociation mass spectra (and from previous work by others), but we are blind to it in the delayed dissociation experiments. To circumvent this artifact of action spectroscopy, we decided to look at complexes between the dipeptide cations and crown ether. The latter targets the N-terminal ammonium group and raises the $\pi\sigma^*$ state up in energy, and most likely out of the spectral region even at the lowest wavelengths. In any case, the H-loss reaction is blocked. Second, the complex has more degrees of freedom and should as a result have a longer lifetime with respect to statistical dissociation. As we will show, the lifetime is also increased since the mobile proton mechanism that accounts for the facile breakage of peptide bonds[54,55] is no longer operative, which implies that the activation energy for dissociation is higher for the complex than for the bare ion itself.

Crown Ether Complexes. Sample time spectra for $[Ala\text{-}Tyr + H]^+$(CE) after no photoexcitation, 220-nm photoexcitation, and 270-nm photoexcitation are shown in Figure 12. Clearly, delayed dissociation (sampling neutrals formed between 46 and 77 μs after photoexcitation in the first instance, and then after successive rotations in the ring) is now also measured at the high wavelength, which is in support of our earlier interpretation for the absence of the peak in the bare ion spectra. Indeed, it was found that the time constants for the two decay processes increased as a function of wavelength, as expected for statistical dissociation processes. The spectra for $[Tyr\text{-}Ala + H]^+$(CE) (data not shown) were found to be similar to those for $[Ala\text{-}Tyr + H]^+$(CE). Based on the lifetime spectra and exponential fits to the data points, we have obtained the absorption spectra (Figures 7B and 8B). These display two absorption bands at 220 and 270 nm in the case of $[Ala\text{-}Tyr + H]^+$(CE) and at 226 and 272 nm in the case of $[Tyr\text{-}Ala + H]^+$(CE), with the second absorption band appearing to be larger than the first one for $[Tyr\text{-}Ala + H]^+$(CE). In fact, the ratio between the maxima of the 220 and 270 nm bands in both cases is smaller than that observed from the solution-phase spectra (Figures 7B and 8B). It should be mentioned though that the lifetimes after excitation at the low wavelengths are short and measured based on just two points which introduces some uncertainty when we calculate back to time zero to obtain the total number of photoexcited ions. Also fast dissociation from excited states may be more prominent at 220-nm excitation than at 270 nm, which results in some decay not being sampled at the lower wavelength. In previous work, Joly et al.[34,35] recorded the spectra of the doubly

TABLE 1: Absorption Spectra Band Maxima

	in vacuo	in aqueous solution
	λ_{max} (nm)	λ_{max} (nm)
$[Tyr + H]^+$	225	222, 275
$[Ala\text{-}Tyr + H]^+$	220	221, 276
$[Tyr\text{-}Ala + H]^+$	221	222, 275
$[Ala\text{-}Tyr + H]^+(CE)$	220, 270	222, 277
$[Tyr\text{-}Ala + H]^+(CE)$	226, 272	223, 275

negatively charged angiotensin II variant (DRVYVHPF) and DYKDDDDK peptides from photodetachment yields and found maximum absorption between 260 and 300 nm. Their spectra appear more to the red compared to ours, which may be linked to differences in the electric field at the tyrosine chromophore and the folding pattern. The solution-phase spectra of $[Ala\text{-}Tyr + H]^+(CE)$ and $[Tyr\text{-}Ala + H]^+(CE)$ are included in Figures 7 and 8. Our data reveal that solvation of the phenol chromophore by water has little influence. Thus, it is evident that water perturbs the high-energy transition by about 3 nm while the band at 270 nm red shifts by about 5 nm (Table 1). A similar pattern is expected when a tyrosine amino acid residue located in a hydrophobic pocket turns inside out and becomes solvated by water. This information may be useful for protein dynamics experiments that are based on either absorption or resonance Raman spectroscopy.

IX

Photodissociation mass spectra of both $[Ala\text{-}Tyr + H]^+(CE)$ and $[Tyr\text{-}Ala + H]^+(CE)$ after 220-nm photoexcitation are shown in Figure 13, while the spectra obtained after 270-nm photoexcitation are shown in Figure 14. Product ions produced up to 31 μs after photoexcitation were sampled. The spectra are similar for both complexes and reveal that the dominant channel is loss of the tyrosine side chain (m/z 410). It is found that H_2O and CO losses increase in importance with higher

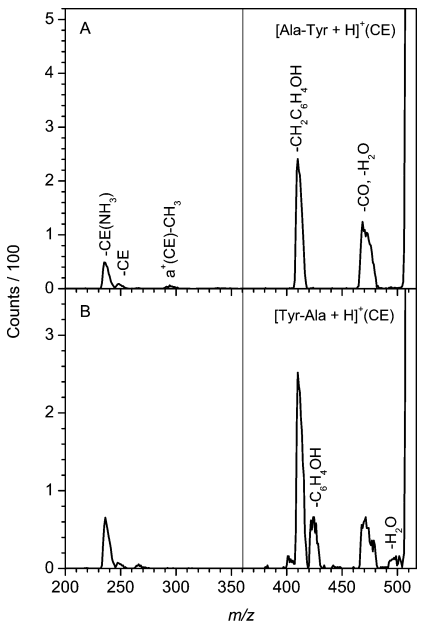

Figure 13. Photodissociation mass spectra of (A) $[Ala\text{-}Tyr + H]^+(CE)$ (m/z 517) and (B) $[Tyr\text{-}Ala + H]^+(CE)$ (m/z 517) after 220-nm photoexcitation. The ions with $m/z < 360$ were dumped on the detector after 1.5 revolutions, while the ions with $m/z > 360$ were dumped on the detector after 9.5 revolutions.

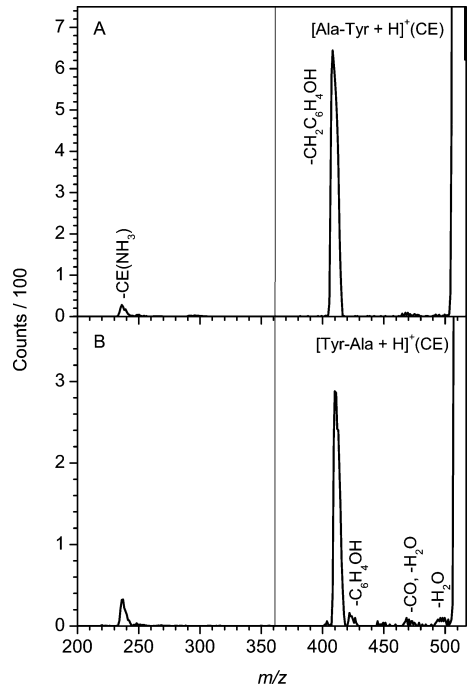

Figure 14. Photodissociation mass spectra of (A) $[Ala\text{-}Tyr + H]^+(CE)$ (m/z 517) and (B) $[Tyr\text{-}Ala + H]^+(CE)$ (m/z 517) after 270-nm photoexcitation. The ions with $m/z < 360$ were dumped on the detector after 1.5 revolutions, while the ions with $m/z > 360$ were dumped on the detector after 9.5 revolutions.

excitation energies. In the lower m/z region, there are peaks that correspond to fragments formed after loss of CE or CE and ammonia, with protonated crown ether also being measured. It is worthwhile to notice that no or very little fragmentation of the peptide backbone is seen to occur. For comparison, y^+ ions were formed in high yields after 270-nm photoexcitation of bare $[Ala\text{-}Tyr + H]^+$ ions. It is generally accepted that after vibrational heating of a peptide cation, the ionizing proton is no longer sequestered at the most basic site—in the case of $[Ala\text{-}Tyr + H]^+$ and $[Tyr\text{-}Ala + H]^+$, this is the N-terminal amino group—but is instead mobile and can explore less basic sites such as the amide nitrogens. Amide protonation weakens the C(O)−N bond and accounts for the formation of y and b fragments. In the complexes, however, crown ether firmly binds the ammonium protons[42] and reduces or prevents internal proton transfer reactions after excitation. Channels other than backbone cleavages, such as side chain losses, are then possible (see Figure 15).

Conclusions

In general, measurement of an action spectrum requires that ionic dissociation takes place within the relevant time window of the instrument. Complications arise when fast nonstatistical processes occur that may be highly wavelength dependent, e.g., hydrogen loss from neutralized ammonium groups. Dehydrogenated ions will have low internal energies, and in some cases the energy will be too low for subsequent dissociation to be recorded in a delayed dissociation experiment. To prevent hydrogen loss, we have introduced a scheme based on crown ether attachment to the ammonium group since this brings the $\pi\sigma^*$ state on ammonium outside the spectral region. The

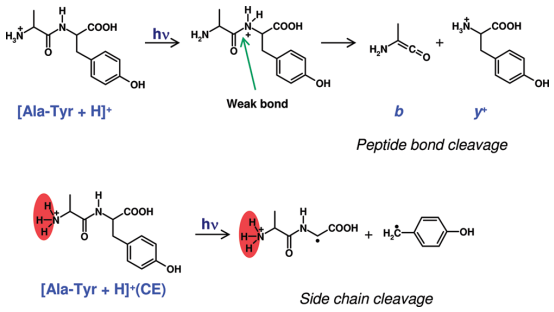

Figure 15. For the dipeptides, the ionizing proton is mobile. Breakage of the weakest bond forms *y* and *b* fragments, which is the dominant channel at high wavelengths in the case of $[Ala\text{-}Tyr + H]^+$. In the complexes, 18-crown-6 ether (indicated in red) prevents internal proton transfer after excitation. Channels other than backbone cleavages, such as side chain losses, are then possible.

photoactive electron instead duly jumps back to the electronic ground state (internal conversion) to give vibrationally hot ions that dissociate statistically. In this way, we succeeded in recording the gas-phase absorption spectra of the dipeptides $[Ala\text{-}Tyr + H]^+(CE)$ and $[Tyr\text{-}Ala + H]^+(CE)$ using an electrostatic ion storage ring. The spectra were obtained from measurements of the time decays as a function of excitation wavelength. The decays were to a good approximation exponential, which allowed us to estimate the initial number of photoexcited ions (relative numbers). In a ring experiment, we do not encounter the complication of kinetic shifts as seen in other instruments that rely on a finite time for sampling the fragments. The gas-phase absorption spectra of the two crown ether peptide complexes are very similar to those obtained in aqueous solution, which indicates that the environment only weakly perturbs the electronic transition energies. Absorption band maxima of all species under study are summarized in Table 1, from which it is evident that the band maxima are nearly the same for protonated Tyr, Ala-Tyr, and Tyr-Ala. This implies that the phenol group is the photoactive group at all wavelengths from 210 to 300 nm. Finally, we have reported photodissociation mass spectra as a function of excitation wavelength both for bare dipeptides and crown ether complexes. The latter are less prone to internal proton transfer after excitation, and as a result side chain cleavages take over from the backbone cleavages observed for the bare ions. Tagging ammonium groups by crown ether serves a dual purpose: it eliminates H loss and sequesters the protons.

Acknowledgment. We gratefully acknowledge support from Villum Kann Rasmussen fonden, Lundbeckfonden (Junior Group Leader Fellowship), Carlsbergfondet (grant 2006-01-0229), FNU (grant 272-06-0427), and Dir. Ib Henriksens Fond.

References and Notes

(1) Brøndsted Nielsen, S.; Lapierre, A.; Andersen, J. U.; Pedersen, U. V.; Tomita, S.; Andersen, L. H. *Phys. Rev. Lett.* **2001**, *87*, 228102.
(2) Andersen, L. H.; Nielsen, I. B.; Kristensen, M. B.; El Ghazaly, M. O. A.; Haacke, S.; Brøndsted Nielsen, M.; Petersen, M. Å. *J. Am. Chem. Soc.* **2005**, *127*, 12347.
(3) Nielsen, I. B.; Lammich, L.; Andersen, L. H. *Phys. Rev. Lett.* **2006**, *96*, 018304.
(4) Lykkegaard, M. K.; Ehlerding, A.; Hvelplund, P.; Kadhane, U.; Kirketerp, M. B. S.; Brøndsted Nielsen, S.; Panja, S.; Wyer, J. A.; Zettergren, H. *J. Am. Chem. Soc.* **2008**, *130*, 11856.
(5) Kirketerp, M.-B. S.; Petersen, M. Å.; Wanko, M.; Leal, L. A. E.; Zettergren, H.; Raymo, F. M.; Rubio, A.; Brøndsted Nielsen, M.; Brøndsted Nielsen, S. *Chem. Phys. Chem.* **2009**, *10*, 1207.
(6) Marques, M. A. L.; Gross, E. K. U. *Annu. Rev. Phys. Chem.* **2004**, *55*, 427.
(7) Olsen, S.; Smith, S. C. *J. Am. Chem. Soc.* **2007**, *129*, 2054.
(8) Patnaik, S. S.; Trohalaki, S.; Naik, R. R.; Stone, M. O.; Pachter, R. *Biopolymers* **2007**, *85*, 253.
(9) Altoe, P.; Stenta, M.; Bottoni, A.; Garavelli, M. *Theor. Chem. Acc.* **2007**, *118*, 219.
(10) Hasegawa, J. Y.; Fujimoto, K.; Swerts, B.; Miyahara, T.; Nakatsuji, H. *J. Comput. Chem.* **2007**, *28*, 2443.
(11) Send, R.; Sundholm, D. *Phys. Chem. Chem. Phys.* **2007**, *9*, 2862.
(12) Wanko, M.; Hoffmann, M.; Frauenheim, T.; Elstner, M. *J. Phys. Chem. B* **2008**, *112*, 11462.
(13) Soderhjelm, P.; Husberg, C.; Strambi, A.; Olivucci, M.; Ryde, U. *J. Chem. Theory Comput.* **2009**, *5*, 649.
(14) Møller, S. P. *Nucl. Instrum. Methods Phys. Res., Sect. A* **1997**, *394*, 281.
(15) Andersen, J. U.; Hvelplund, P.; Brøndsted Nielsen, S.; Tomita, S.; Wahlgreen, H.; Møller, S. P.; Pedersen, U. V.; Forster, J. S.; Jørgensen, T. J. D. *Rev. Sci. Instrum.* **2002**, *73*, 1284.
(16) Støchkel, K.; Kadhane, U.; Andersen, J. U.; Holm, A. I. S.; Hvelplund, P.; Kirketerp, M. B. S.; Larsen, M. K.; Lykkegaard, M. K.; Brøndsted Nielsen, S.; Panja, S.; Zettergren, H. *Rev. Sci. Instrum.* **2008**, *79*, 023107.
(17) Harada, I.; Takeuchi, H. Raman and Ultraviolet Resonance Raman Spectra of Proteins and Related Compounds. In *Spectroscopy of Biological Systems*; Clark, R. J. H., Hester, R. E., Eds.; John Wiley & Sons Ltd.: New York, 1986.
(18) Tabarin, T.; Kulesza, A.; Antoine, R.; Mitric, R.; Broyer, M.; Dugourd, P.; Bonacic-Koutecky, V. *Phys. Rev. Lett.* **2008**, *101*, 213001.
(19) Weinkauf, R.; Schanen, P.; Metsala, A.; Schlag, E. W.; Burgle, M.; Kessler, H. *J. Phys. Chem.* **1996**, *100*, 18567.
(20) Weinkauf, R.; Schlag, E. W.; Martinez, T. J.; Levine, R. D. *J. Phys. Chem. A* **1997**, *101*, 7702.
(21) Hu, Y. J.; Hadas, B.; Davidovitz, M.; Balta, B.; Lifshitz, C. *J. Phys. Chem. A* **2003**, *107*, 6507.
(22) Cui, W.; Hu, Y.; Lifshitz, C. *Eur. Phys. J. D* **2002**, *20*, 565.
(23) Armentrout, P. B. Threshold Collision-Induced Dissociations for the Determination of Accurate Gas-Phase Binding Energies and Reaction Barriers. In *Modern Mass Spectrometry*; Springer-Verlag: Berlin, 2003; Vol. 225; p 233.
(24) Gregoire, G.; Dedonder-Lardeux, C.; Jouvet, C.; Desfrancois, C.; Fayeton, J. A. *Phys. Chem. Chem. Phys.* **2007**, *9*, 78.
(25) Kang, H.; Jouvet, C.; Dedonder-Lardeux, C.; Martrenchard, S.; Gregoire, G.; Desfrancois, C.; Schermann, J. P.; Barat, M.; Fayeton, J. A. *Phys. Chem. Chem. Phys.* **2005**, *7*, 394.
(26) Boyarkin, O. V.; Mercier, S. R.; Kamariotis, A.; Rizzo, T. R. *J. Am. Chem. Soc.* **2006**, *128*, 2816.
(27) Fujihara, A.; Matsumoto, H.; Shibata, Y.; Ishikawa, H.; Fuke, K. *J. Phys. Chem. A* **2008**, *112*, 1457.
(28) Yoon, S. H.; Kim, M. S. *J. Am. Soc. Mass Spectrom.* **2007**, *18*, 1729.
(29) Oh, J. Y.; Moon, J. H.; Kim, M. S. *J. Mass Spectrom.* **2005**, *40*, 899.
(30) Nolting, D.; Schultz, T.; Hertel, I. V.; Weinkauf, R. *Phys. Chem. Chem. Phys.* **2006**, *8*, 5247.
(31) Weinkauf, R.; Schanen, P.; Yang, D.; Sonkara, S.; Schlag, E. W. *J. Phys. Chem.* **1995**, *99*, 11255.
(32) Sobolewski, A. L.; Shemesh, D.; Domcke, W. *J. Phys. Chem. A* **2009**, *113*, 542.
(33) Cohen, R.; Brauer, B.; Nir, E.; Grace, L.; de Vries, M. S. *J. Phys. Chem. A* **2000**, *104*, 6351.
(34) Joly, L.; Antoine, R.; Allouche, A. R.; Broyer, M.; Lemoine, J.; Dugourd, P. *J. Am. Chem. Soc.* **2007**, *129*, 8428.
(35) Joly, L.; Antoine, R.; Broyer, M.; Lemoine, J.; Dugourd, P. *J. Phys. Chem. A* **2008**, *112*, 898.
(36) Kang, H.; Dedonder-Lardeux, C.; Jouvet, C.; Martrenchard, S.; Gregoire, G.; Desfrancois, C.; Schermann, J. P.; Barat, M.; Fayeton, J. A. *Phys. Chem. Chem. Phys.* **2004**, *6*, 2628.
(37) Lepere, V.; Lucas, B.; Barat, M.; Fayeton, J. A.; Picard, V. J.; Jouvet, C.; Carcabal, P.; Nielsen, I.; Dedonder-Lardeux, C.; Gregoire, G.; Fujii, A. *J. Chem. Phys.* **2007**, *127*, 134313.
(38) Andersen, J. U.; Cederquist, H.; Forster, J. S.; Huber, B. A.; Hvelplund, P.; Jensen, J.; Liu, B.; Manil, B.; Maunoury, L.; Brøndsted Nielsen, S.; Pedersen, U. V.; Rangama, J.; Schmidt, H. T.; Tomita, S.; Zettergren, H. *Phys. Chem. Chem. Phys.* **2004**, *6*, 2676.
(39) Holm, A. I. S.; Larsen, M. K.; Panja, S.; Hvelplund, P.; Brøndsted Nielsen, S.; Leib, R. D.; Donald, W. A.; Williams, E. R.; Hao, C. T.; Turecek, F. *Int. J. Mass Spectrom.* **2008**, *276*, 116.
(40) Kadhane, U.; Andersen, J. U.; Ehlerding, A.; Hvelplund, P.; Kirketerp, M. B. S.; Lykkegaard, M. K.; Brøndsted Nielsen, S.; Panja, S.; Wyer, J. A.; Zettergren, H. *J. Chem. Phys.* **2008**, *129*, 184304.
(41) Raevsky, O. A.; Solovev, V. P.; Solotnov, A. F.; Schneider, H. J.; Rudiger, V. *J. Org. Chem.* **1996**, *61*, 8113.

IX

(42) Julian, R. R.; Beauchamp, J. L. *Int. J. Mass Spectrom.* **2001**, *210*, 613.
(43) Wilson, J. J.; Kirkovits, G. J.; Sessler, J. L.; Brodbelt, J. S. *J. Am. Soc. Mass Spectrom.* **2008**, *19*, 257.
(44) Andersen, J. U.; Cederquist, H.; Forster, J. S.; Huber, B. A.; Hvelplund, P.; Jensen, J.; Liu, B.; Manil, B.; Maunoury, L.; Brøndsted Nielsen, S.; Pedersen, U. V.; Schmidt, H. T.; Tomita, S.; Zettergren, H. *Eur. Phys. J. D* **2003**, *25*, 139.
(45) Fayeton, J. A.; et al. Personal communication.
(46) Tabarin, T.; Antoine, R.; Broyer, M.; Dugourd, P. *Rapid Commun. Mass Spectrom.* **2005**, *19*, 2883.
(47) Joly, L.; Antoine, R.; Broyer, M.; Dugourd, P.; Lemoine, J. *J. Mass Spectrom.* **2007**, *42*, 818.
(48) Stearns, J. A.; Mercier, S.; Seaiby, C.; Guidi, M.; Boyarkin, O. V.; Rizzo, T. R. *J. Am. Chem. Soc.* **2007**, *129*, 11814.
(49) Stearns, J. A.; Guidi, M.; Boyarkin, O. V.; Rizzo, T. R. *J. Chem. Phys.* **2007**, *127*, 154322.
(50) Chakraborty, T.; Holm, A. I. S.; Hvelplund, P.; Brøndsted Nielsen, S.; Poully, J. C.; Worm, E. S.; Williams, E. R. *J. Am. Soc. Mass Spectrom.* **2006**, *17*, 1675.
(51) Gabryelski, W.; Li, L. *Rev. Sci. Instrum.* **1999**, *70*, 4192.
(52) Yoon, T. O.; Choi, C. M.; Kim, H. J.; Kim, N. J. *Bull. Korean Chem. Soc.* **2007**, *28*, 619.
(53) Lucas, B.; Barat, M.; Fayeton, J. A.; Perot, M.; Jouvet, C.; Gregoire, G.; Brøndsted Nielsen, S. *J. Chem. Phys.* **2008**, *128*, 164302.
(54) Wysocki, V. H.; Tsaprailis, G.; Smith, L. L.; Breci, L. A. *J. Mass Spectrom.* **2000**, *35*, 1399.
(55) Wysocki, V. H.; Resing, K. A.; Zhang, Q. F.; Cheng, G. L. *Methods* **2005**, *35*, 211.

JP904053D

THE JOURNAL OF PHYSICAL CHEMISTRY A

ARTICLE

pubs.acs.org/JPCA

Role of Nearby Charges on the Electronic Structure of π-Conjugated Molecules: Symmetric versus Asymmetric Charge Distributions in Oligo(*p*-phenyleneethynylene)

Maj-Britt Suhr Kirketerp,[*,†] Torben Ryhding,[‡] Kristian Støchkel,[†] Mogens Brøndsted Nielsen,[*,‡] and Steen Brøndsted Nielsen[†]

[†]Department of Physics and Astronomy, Aarhus University, Ny Munkegade, DK-8000 Aarhus C, Denmark

[‡]Department of Chemistry, University of Copenhagen, Universitetsparken 5, DK-2100 Copenhagen Ø, Denmark

ABSTRACT: Oligo(*p*-phenyleneethynylene)s (OPEs) are conjugated oligomers of great interest within materials science and molecular electronics on account of their highly applicable electronic and optical properties. Here we use gas-phase action spectroscopy to elucidate how the intrinsic electronic properties of these chromophores are affected by nearby charges. An OPE3 chromophore with two nearby ammonium groups was synthesized. This molecule and a related OPE3 with only one amine protonation site were transferred to the gas phase by electrospray ionization and subjected to action spectroscopy. Ions were bunched in a 14-pole ion trap, accelerated to 50-keV kinetic energies, mass-to-charge selected by a magnet, and photoexcited in a crossed-beam configuration. Fragment ions were finally mass-analyzed by an electrostatic analyzer. The setup enables photodissociation mass spectrometry and action spectroscopy on the microsecond time scale. The gas-phase absorption of the mono- and dication was measured and compared to that of neutral chromophores in solution. Similar absorption was found for neutral chromophores (in solution) and the dication (in gas phase or solution), whereas the monocation absorbs at lower energies in the gas phase. Simple electrostatic considerations lead to an energy difference like the one found from the experiment. The work presented here addresses how the electronic properties of a π-conjugated system are affected by nearby charges, a question of fundamental interest in, for example, molecular electronics.

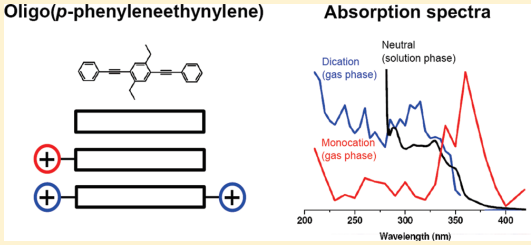

INTRODUCTION

Oligo(*p*-phenyleneethynylene)s (OPEs) and similar conjugated oligomers are widely used within materials science and, among others, they have potential as wires in molecular electronics.[1] It is possible to tune the optical properties by a change of the length or addition of substituents to the chromophore. Despite extensive work, the intrinsic electronic properties of the molecules are not yet fully understood.

Earlier studies of OPEs revealed that a nearby positive charge affected the electronic properties of the chromophore.[2] The nearby charge was obtained by attachment of a CH_2C-H_2NH_2 group to the chromophore (Figure 1). The group does not influence the conjugated entity, but it enables protonation and thereby provides a nearby charge. The energy gap between the highest occupied molecular orbital (HOMO) and the lowest unoccupied molecular orbital (LUMO) of the monocation (**1**) in gas phase was found to be smaller than that of the neutral chromophore (**0**) in solution,[3] in contrast to the expected hypsochromic solvent shift. Hence the dominant effect must stem from the nearby charge. Here we follow this line and present synthesis and gas-phase absorption of the chromophore with two symmetrically placed nearby charges (**2**) with the aim to further explore the effect of nearby charges on a conjugated system.

The earlier reported gas-phase experiment of **1** was carried out at the electrostatic ion storage ring in Aarhus (ELISA),[4,5] where the number of neutrals formed after photoexcitation was measured as a function of wavelength. The experiment only sampled neutrals formed by delayed fragmentation, from tens of microseconds onward. Due to a shorter fragmentation time for the dication (**2**), the storage ring was not applicable here. Instead an instrumental setup was built that facilitates gas-phase photodissociation mass spectroscopy and action spectroscopy on the time scale of a few microseconds. This setup was used to record the action spectrum of the symmetric OPE dication in vacuo.

SYNTHESIS

The symmetrical OPE3 **2** was prepared according to Scheme 1. First the amine **3** was protected with *t*-butyloxycarbonyl (Boc), which provided compound **4**. A palladium-catalyzed Sonogashira cross-coupling reaction[6] with triisopropylsilylacetylene furnished compound **5**, by use of the catalyst system developed by Hundertmark et al.[7] Desilylation by tetrabutylammonium fluoride provided the terminal alkyne that was then subjected to a 2-fold

Received: November 22, 2010
Published: February 3, 2011

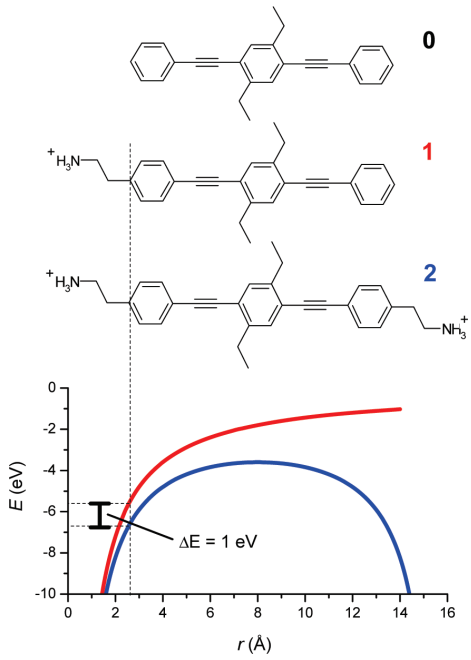

Figure 1. Oligo(*p*-phenyleneethynelene) chromophore as a neutral chromophore (**0**), as a cation (**1**) with one protonation site, and as a dication (**2**) with two protonation sites. The lower part shows the potential of an electron for **1** and **2** being asymmetric and symmetric, respectively.

Sonogashira reaction with the known diiodide **6**. Hereby the symmetrical OPE3 **7** was obtained. Finally, the Boc groups were removed by treating **7** with phenol and trimethylsilyl chloride in dichloromethane, which caused the hydrochloride salt **2**·2Cl$^-$ to precipitate. Precipitation was completed by the addition of pentane, and the product was washed thoroughly with toluene.

INSTRUMENTAL SETUP

The setup for action spectroscopy was constructed from a tandem accelerator mass spectrometer that has previously been used for collision and electron capture induced dissociation experiments.[5,8] The instrument is equipped with an electrospray ion source. A 14-pole trap was implemented to allow for pulsed experiments, and a 20-Hz pulsed tunable EKSPLA laser was used for photodissociation; see Figure 2. Ions formed by electrospray ionization were accumulated in the trap and thermally equilibrated by collisions with a room-temperature helium buffer gas therein. This ion source setup is successfully used in the storage ring experiment. The ions were accelerated as a bunch to 50-keV kinetic energies per charge, and a bending magnet was used to select the appropriate ions. Subsequently the ions were irradiated by a nanosecond laser pulse perpendicular to the ion beam, that is, a crossed-beam configuration. Ions that existed after photoexcitation, that is, daughter and parent ions, were selected according to their kinetic-energy-to-charge ratio by an electrostatic analyzer (ESA) and guided to a channeltron detector. The flight times from the interaction region to the ESA are 3.8 and 2.8 μs for **1** and **2**, respectively, and thus we sampled daughter ions formed within this time. The repetition rate of the experiment was 20 Hz.

Scheme 1

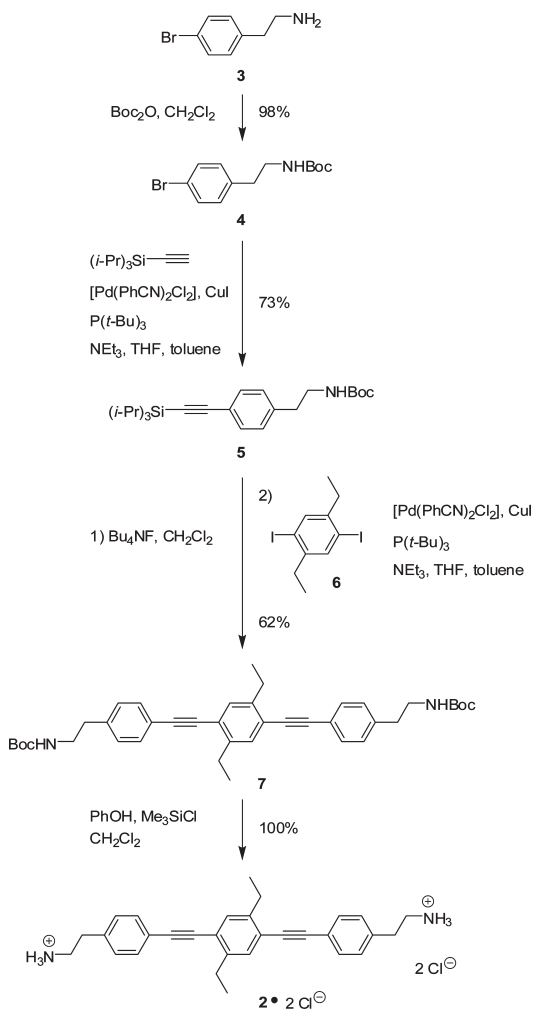

The laser is a Nd:YAG laser where the third harmonic (355 nm) pumps an optical parametric oscillator (OPO). The visible output from this OPO was frequency-doubled in a crystal providing UV light. Typical pulse energies are 0.2−4 mJ (UV region), 1.8 mJ (visible region), and 0.3−1.5 mJ (IR region). For electrospray the molecules were dissolved in water/methanol (1:1) with acetic acid (10% vol).

RESULTS

First we measured the number of daughter ions with a particular *m/z*- ratio that hit the detector as a function of time. Figure 3 shows the spectrum of the daughter ions formed from loss of two ammonia [$M^{2+} - 2NH_3$] from the parent dication after photoexcitation with 300-nm laser light. The time spectrum contains a constant background level and a laser-induced peak.

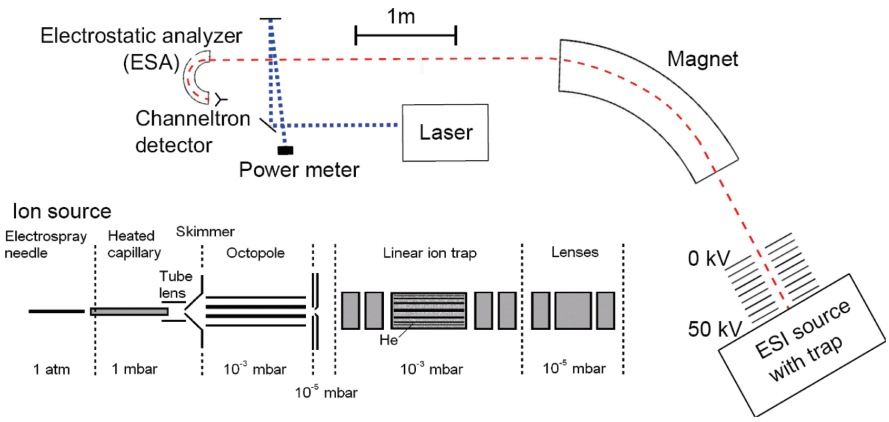

Figure 2. Setup used for photodissociation mass spectroscopy and action spectroscopy on gas-phase molecular ions on the microsecond time scale. A tandem mass spectrometer is combined with an ESI ion source (see details in the text), a trap, and a tunable laser system.

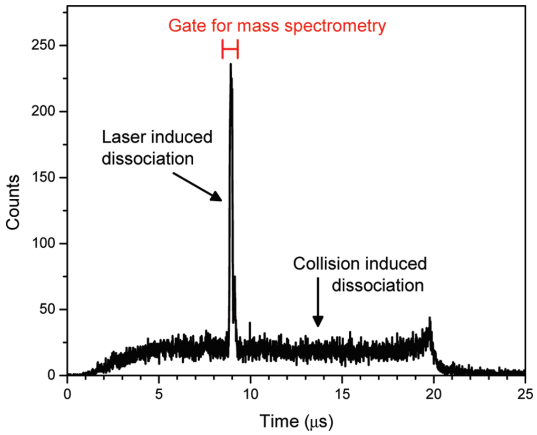

Figure 3. Time spectrum of the m/z 194 fragment ions of **2** hitting the detector as a function of time. The ion bunch is 25 μs long. Collision-induced dissociation results in a constant background level, and laser-induced dissociation occurs as a 310-nm laser pulse is fired. The timing gate used for mass spectrometry is shown.

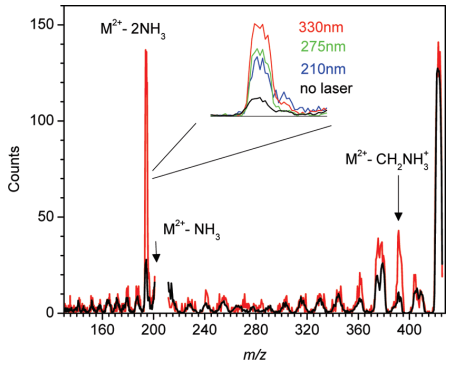

Figure 4. Mass spectrum of **2** without laser (black line) and with 310-nm laser light (red line). Photodissociation is found for three fragments (m/z 194, 203.5, and 394). Note that the m/z 203.5 fragment is not discernible in the full spectrum but is found with a narrow scan around this mass region. (Inset) Wavelength dependency of the m/z 194 fragment.

The width of the ion bunch was 25 μs, and the laser was fired in the first half of the pulse. The background level was a result of collision-induced dissociation (CID) as the ions collide with residual gas in the beamline, where the pressure is on the order of 10^{-6} mbar. The level serves as a measure of the ion beam intensity. Photoexcitation led to an increase in the daughter ion formation, which appears as the sharp "laser peak" in the spectrum. The number of counts in the peak is proportional to the number of photoexcited ions that dissociate into this particular fragment, that is, the photofragment yield.

To obtain a photodissociation mass spectrum, a timing gate of 400 ns was set around the laser-induced peak, as illustrated in Figure 3. The voltage on the ESA was then scanned to measure the photofragment yield as a function of mass/charge. The gate helps to increase the signal-to-noise ratio of the measurement, since only the CID contribution within the timing of the gate is counted. Figure 4 displays the fragments formed by CID (black curve) and photoinduced dissociation (PID) (red curve) at 300 nm for **2**. A photoinduced signal is found for three fragments (m/z 194, 203.5, and 394), corresponding to loss of two NH_3, one NH_3, and $CH_2NH_3^+$, respectively. The inset shows how the photo yield depends on the wavelength for the $M^{2+} - 2NH_3$ fragment. The photodissociation mass spectrum reveals the photoinduced fragments to be monitored for action spectroscopy.

Absorption cross sections, relative rather than absolute numbers, are obtained from the time spectra as the photo yield divided by the ion beam intensity (CID background) and the number of photons in the laser pulse. The dissociation is a result of single photon absorption as the photofragment yield increases linearly with the energy of the laser pulse; see Figure 5. The action spectra for the three laser-induced fragments of **2** are presented in Figure 6. Absorption initiates at 360 nm and increases with decreasing wavelength. From the time spectra it is evident that the m/z 194 fragment has the highest photo yield.

Only a single photoinduced fragment, $M^+ - NH_3$, was found for **1**, and the corresponding action spectrum is given in Figure 7,

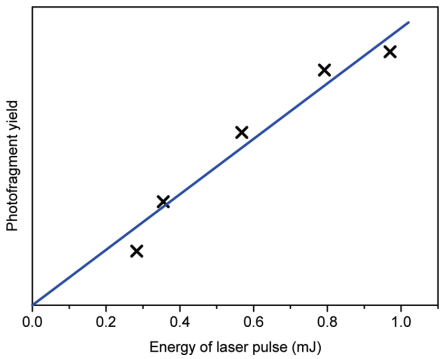

Figure 5. Photo yield of the m/z 194 fragment from **2** as a function of pulse energy at 310 nm. The dissociation is due to single photon absorption as the yield increases linearly with laser energy.

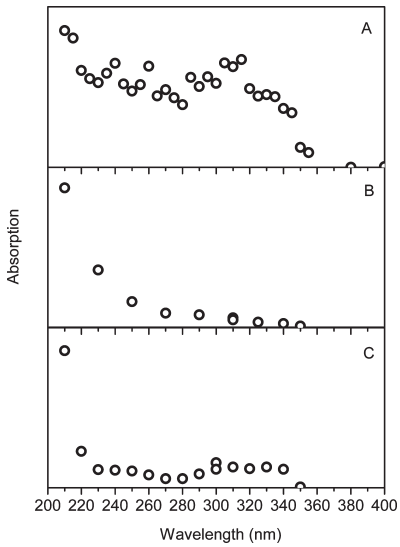

Figure 6. Action spectrum of **2** for the three photosensitive fragment ions: (A) m/z 194, (B) m/z 203.5, and (C) m/z 394. Absorption initiates at 360 nm and increases with decreasing wavelength.

panel B. Panel A shows the previous spectrum from the storage ring experiment. Notice the similarity of the two spectra despite the difference in the experimental method; one samples all neutrals formed from 40 μs and so on, and the other a single daughter ion formed right after excitation and up to 3.8 μs. In both spectra, the absorption initiates at 390 nm with a band maximum at about 360 nm.

Figure 8 displays the absorption of the corresponding neutral amine of **1** (unprotonated) in toluene and the chloride salt of **2** in acetonitrile. For both compounds the absorption starts from 360 nm and extends below 300 nm as a broad band with some fine structure. For the neutral amine of **1**, longest-wavelength absorption peaks/shoulders are found at 348 and 329 nm and for compound **2**·2Cl$^-$ at 349

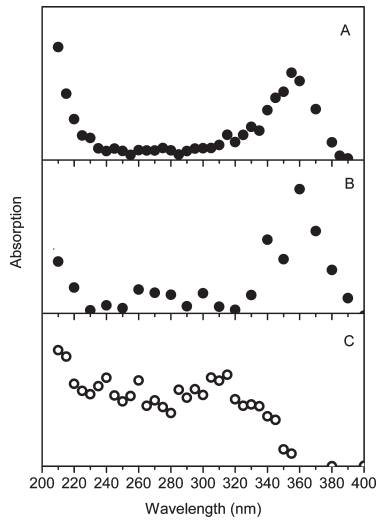

Figure 7. Action spectra of **1** measured (A) at the storage ring and (B) at the new instrumental setup. The two spectra show absorption from 390 nm and band maxima at 360 nm. (C) Reprint of the m/z 194 action spectrum of **2** (Figure 6 A) for easy comparison. It is seen that the absorption of **1** is 30 nm to the red of that of **2**.

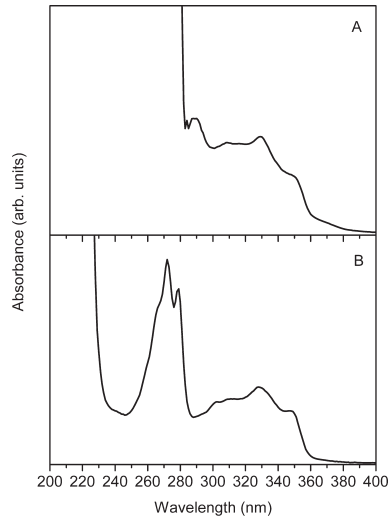

Figure 8. Absorption spectra of (A) the neutral amine of **1** in toluene and (B) the salt **2**·2Cl$^-$ in acetonitrile.

and 329 nm. Addition of trifluoroacetic acid to the neutral amine solution of **1**, causing protonation, did not alter the absorption maxima, but the intensities increased somewhat. The similar absorption behavior of the compounds studied in solution resembles that of related, neutral OPE3s, such as **0**,[3] All in all, solvent and ion-pairing effects seem to screen for any effect exerted by the positive charges in the cations **1** and **2**.

DISCUSSION

We now combine the above results to obtain knowledge on the effect of nearby charges. The similar absorption found for the three neutral chromophores in solution indicates that the CH_2C-H_2NH_2 groups alone do not affect the longest-wavelength absorption. Thus the change in the absorption of the ions in the gas phase must be an effect of the nearby charges. For the dication, an absorption profile similar to the one for the neutral chromophores is found, whereas the absorption of the monocation initiates further to the red by approximately 30 nm.

As one nearby charge is added to the chromophore, an asymmetric potential like the one shown in Figure 1 arises, with subsequent decrease in the HOMO−LUMO gap. Upon excitation the electron moves closer to the single positive charge in **1**, and consequently the excitation energy decreases. For comparison, Jouvet and co-workers[10] recently showed that the absorption of protonated naphthalene is to the red of that of neutral naphthalene by 1.53 eV. The addition of yet another charge results in a symmetric potential, Figure 1, and an increase in the HOMO−LUMO gap. As the electron moves closer to one positive charge, it moves away from the other, and thus the energy gained from the Coulomb interaction is less. From simple electrostatic considerations the difference in the potentials for **1** and **2**, at the carbon closest to the nearby charge in **1**, is found to be 1 eV (maximum shift), in nice agreement with the experimental results. Symmetric charge distributions (**0** and **2**) result in similar absorption profiles (cf. solution spectrum of **0** and gas-phase spectrum of **2**), whereas the asymmetric charge distribution in **1** results in a red-shifted gas-phase absorption spectrum. Hence the effect of nearby charges on the chromophores is merely determined by the charge distribution.

CONCLUSION

The effect of a nearby charge on a conjugated system has been studied by action spectroscopy experiments. A new oligo(*p*-phenyleneethynylene) with two ammonium groups was prepared by palladium-catalyzed reactions. The gas phase action spectrum of this dicationic compound was recorded and compared to an OPE3 with only one ammonium group (monocation). We find that the asymmetric charge distribution of the monocation results in a decrease in the HOMO−LUMO energy gap compared to the dication. Simple electrostatic consideration provides a similar energy shift. Thus, from gas-phase studies on isolated molecules, it transpires that nearby positive charges clearly affect the electronic absorption of π-conjugated molecular ions. This effect is not revealed from solution studies, as the solvent and counterions effectively cancel out any influence exerted by the ammonium group. These results may be of relevance to charge transfer through conducting molecular wires.

EXPERIMENTAL SECTION

General Procedures. All catalytic couplings were performed in degassed solvents and under Ar. Dry solvents were provided by an Innovative Technology Puresolv apparatus or dried over 4 Å molecular sieves. Silica gel (0.040−0.063 mm) was used for flash chromatography. When carbamates were purified by flash chromatography, the silica was neutralized by use of triethylamine followed by several flushes with the eluent. Thin-layer chromatography (TLC) was performed on silica gel-coated aluminum foils (alumina foil 60 F_{254}). NMR spectra were obtained on Varian 300 or 500 MHz instruments at room temperature. Melting points were obtained by use of a melting table microscope. Microwave synthesis was performed in suitable vials fitted with septa.

***tert*-Butyl 4-Bromophenethylcarbamate (4).** Compound **3** (100 mg, 0.50 mmol) was dissolved in CH_2Cl_2 (20 mL) and treated with $(Boc)_2O$ (120 mg, 0.55 mmol). The mixture was left to stir for 3 h, after which it was washed with aqueous NH_4Cl (saturated, 20 mL), $NaHCO_3$ (saturated, 20 mL), and water (20 mL). The organic phase was dried with $MgSO_4$ and the solvent was removed in vacuo. The solid residue was crystallized from cyclohexane to afford the product **4** (0.148 g, 98%) as an off-white solid, mp 61−63 °C. ^{1}H NMR (300 MHz, $CDCl_3$): δ = 1.42 [s, 9H, $C(CH_3)_3$], 2.75 (t, J = 6.8 Hz, 2H, CH_2), 3.34 (t, J = 6.8 Hz, 2H, CH_2), 4.55 (br s, 1H, NH), 7.06 (d, J = 8.5 Hz, 2H, Ar), 7.42 (d, J = 8.5 Hz, 2H, Ar). ^{13}C NMR (75 MHz, $CDCl_3$): δ = 27.7, 28.6, 35.9, 41.8, 120.5, 130.8, 131.9, 138.2, 156.0. MS (FAB^+): m/z = 300.1 (MH^+). Calcd for $C_{13}H_{18}BrNO_2$: C 52.01, H 6.04. Found: C 52.13, H 6.31.

***tert*-Butyl 4-[(Triisopropylsilyl)ethynyl]phenethylcarbamate (5).** $[Pd(PhCN)_2Cl_2]$ (25 mg, 0.065 mmol) and CuI (6 mg, 0.03 mmol) were dissolved in tetrahydrofuran (THF, 1 mL) and toluene (1 mL), and then $(t\text{-Bu})_3P$ (0.10 mL, 1 M in toluene) was added to the catalyst, resulting in a black mixture. The bromide **4** (200 mg, 0.66 mmol) was transferred to a microwave vial and flushed with Ar for a couple of minutes, and then triisopropylsilylacetylene (1 mL, 3.8 mmol) was added. The preformed catalyst mixture was transferred to this mixture via syringe, followed by Et_3N (2 mL). The mixture was heated in a microwave reactor at 45 °C for 15 min. The resulting mixture was diluted with CH_2Cl_2 (20 mL) and washed with aqueous NH_4Cl (saturated, 20 mL). The organic phase was dried with $MgSO_4$ and the solvent was removed in vacuo. Purification by flash chromatography (SiO_2, CH_2Cl_2/cyclohexane 1:1) gave the product **5** (195 mg, 73%) as a slightly yellow oil. ^{1}H NMR (300 MHz, $CDCl_3$): δ = 1.12 (s, 21H, *i*-Pr), 1.43 [s, 9H, $(CH_3)_3$], 2.78 (t, J = 6.8 Hz, 2H, CH_2), 3.36 (t, J = 6.8 Hz, 2H, CH_2), 4.46 (br s, 1H, NH), 7.12 (d, J = 8.2 Hz, 2H, Ar), 7.42 (d, J = 8.2 Hz, 2H, Ar). ^{13}C NMR (75 MHz, $CDCl_3$): δ = 11.4, 19.2, 28.6, 34.6, 40.5, 78.7, 98.6, 102.4, 120.1, 129.7, 133.7, 138.7, 156.7. HR-MS (ESP^+) m/z = 402.2844 (MH^+); calcd for $C_{24}H_{39}NO_2Si$ m/z = 402.2828.

***tert*-Butyl 2,2′-[4,4′-(2,5-Diethyl-1,4-phenylene)bis(ethyne-2,1-diyl)bis(4,1-phenylene)]bis(ethane-2,1-diyl) Dicarbamate (7).** Compound **5** (250 mg, 0.62 mmol) was dissolved in CH_2Cl_2 (10 mL), and Bu_4NF (1 M in THF, 1 mL, 1 mmol) was added. The desilylation was complete within 1 h according to TLC inspection. The solution was diluted with diethyl ether (25 mL) and washed with water (25 mL). The organic solvent was removed at reduced pressure and the terminal alkyne product was carried on to the next step without further purification. $[Pd(PhCN)_2Cl_2]$ (25 mg, 0.065 mmol) and CuI (6 mg, 0.03 mmol) were dissolved in THF (1 mL) and toluene (1 mL), and then $(t\text{-Bu})_3P$ (0.10 mL, 1 M in toluene) was added to the catalyst, resulting in a black mixture. The diiodide **6** (100 mg, 0.24 mmol) was transferred to a microwave vial and flushed with Ar for a couple of minutes, whereupon the terminal alkyne was added. The preformed catalyst mixture was added by syringe, followed by Et_3N (1 mL), and the mixture was heated in a microwave reactor at 45 °C for 15 min. The resulting mixture was diluted with CH_2Cl_2 (20 mL) and washed with aqueous NH_4Cl (saturated, 20 mL). The organic phase was dried with $MgSO_4$, and

the solvent was removed in vacuo. Purification by flash column chromatography (SiO_2, CH_2Cl_2) afforded the product **7** (102 mg, 62%) as an off-white solid. ^{1}H NMR (300 MHz, $CDCl_3$): δ = 1.30 (t, J = 7.6 Hz, 6H, CH_3), 1.44 [s, 18H, $(CH_3)_3$], 2.83 (m, 8H, CH_2), 3.38 (br m, 4H, CH_2), 4.54 (br s, 2H, NH), 7.19 (d, J = 8.2 Hz, 4H, Ar), 7.37 (s, 2H, Ar), 7.47 (d, J = 8.2 Hz, 4H, Ar). ^{13}C NMR (75 MHz, $CDCl_3$): δ = 14.9, 27.4, 28.6, 36.4, 41.8, 78.9, 88.3, 94.1, 121.8, 122.7, 129.1, 131.7, 131.9, 139.7, 143.6, 156.0. HR-MS (ESP^+) m/z = 643.3533 ($M + Na^+$); calcd for $C_{40}H_{48}N_2O_4Na$ m/z = 643.3512.

2,2′-[4,4′-(2,5-Diethyl-1,4-phenylene)bis(ethyne-2,1-diyl)bis(1,4-phenylene)]diethylammoniumchloride (2·2Cl$^-$). The Boc-protected amine **7** (96 mg, 0.15 mmol) was dissolved in CH_2Cl_2 (1.0 mL), and then phenol (90 mg, 1 mmol) and chlorotrimethylsilane (0.15 mL, 1.2 mmol) were added. After 40 min, TLC showed complete Boc deprotection, and the HCl salt of the amine started to precipitate. Pentane (2 mL) was added to enforce complete precipitation, and the precipitate was collected and washed twice with toluene to afford the product **2**·2Cl$^-$ (64 mg, 100%) as an off-white solid, mp 260 °C (decomp). ^{1}H NMR (500 MHz, DMSO-d_6): δ = 1.17 (t, J = 7.5 Hz, 6H, CH_3), 2.78 (q, J = 7.5 Hz, 4H, CH_2), 2.91 (t, J = 7.6 Hz, 4H, CH_2), 3.06 (br t, 4H, CH_2), 7.33 (d, J = 8.2 Hz, 4H, Ar), 7.43 (s, 2H, Ar), 7.51 (d, J = 8.2 Hz, 4H, Ar), 8.02 (br, 6H, NH_3^+). Not soluble enough for ^{13}C NMR. HR-MS (ESP^+) m/z = 211.1334 ($[M - 2Cl]^{2+}$); calcd for doubly charged $C_{30}H_{34}N_2$ m/z = 211.1355.

X

AUTHOR INFORMATION

Corresponding Author

*E-mail msk@phys.au.dk (M.-B.S.K.), mbn@kiku.dk (M.B.N.).

ACKNOWLEDGMENT

We are grateful to the Lundbeck Foundation for funding this work.

REFERENCES

(1) (a) Donhauser, Z. J.; Mantooth, B. A.; Kelly, K. F.; Bumm, L. A.; Monnell, J. D.; Stapleton, J. J.; Price, D. W.; Rawlett, A. M.; Allara, D. L.; Tour, J. M.; Weiss, P. S. *Science* **2001**, *292*, 2303. (b) Sørensen, J. K.; Vestergaard, M.; Kadziola, A.; Kilså, K.; Brøndsted Nielsen, M. *Org. Lett.* **2006**, *8*, 1173. (c) Risko, C.; Zangmeister, C. D.; Yao, Y.; Marks, T. J.; Tour, J. M.; Ratner, M. A.; van Zee, R. D. *J. Phys. Chem. C* **2008**, *112*, 13215.

(2) Ryhding, T.; Kirketerp, M.-B. S.; Kadhane, U.; Lykkegaard, M. K.; Panja, S.; Brøndsted Nielsen, S.; Brøndsted Nielsen, M. *Tetrahedron* **2008**, *64*, 11475.

(3) Ding, C. H.; Babu, G.; Orita, A.; Hirate, T.; Otera, J. *Synlett* **2007**, 2559.

(4) (a) Møller, S. P. *Nucl. Instrum. Methods A* **1997**, *394*, 281. (b) Andersen, J. U.; Hvelplund, P.; Brøndsted Nielsen, S.; Tomita, S.; Wahlgreen, H.; Møller, S. P.; Pedersen, U. V.; Forster, J. S.; Jørgensen, T. J. D. *Rev. Sci. Instrum.* **2002**, *73*, 1284. (c) Andersen, L. H.; Heber, O.; Zajfman, D. *J. Phys. B: At. Mol. Opt.* **2004**, *37*, R57.

(5) Brøndsted Nielsen, S.; Andersen, J. U.; Hvelplund, P.; Liu, B.; Tomita, S. *J. Phys. B: At. Mol. Opt.* **2004**, *37*, R25.

(6) Sonogashira, K.; Tohda, Y.; Hagihara, N. *Tetrahedron Lett.* **1975**, 4467.

(7) Hundertmark, T.; Littke, A. F.; Buchwald, S. L.; Fu, G. C. *Org. Lett.* **2000**, *2*, 1729.

(8) Larsson, M. O.; Hvelplund, P.; Larsen, M. C.; Shen, H.; Cederquist, H.; Schmidt, H. T. *Int. J. Mass. Spectrom.* **1998**, *177*, 51. Boltalina, O. V.; Hvelplund, P.; Jørgensen, T. J. D.; Larsen, M. C.; Larsson, M. O.; Sharoitchenko, D. A. *Phys. Rev. A* **2000**, 6202.

(9) (a) Drefahl, G.; Plotner, G. *Chem. Ber.* **1958**, *91*, 1280. (b) Nakatsuji, S.; Matsuda, K.; Uesugi, Y.; Nakashima, K.; Akiyama, S.; Fabian, W. *J. Chem. Soc., Perkin Trans. 1* **1992**, 755. (c) Samori, S.; Tojo, S.; Fujitsuka, M.; Ryhding, T.; Fix, A. G.; Armstrong, B. M.; Haley, M. M.; Majima, T. *J. Org. Chem.* **2009**, *74*, 3776.

(10) Alata, I.; Omidyan, R.; Broquier, M.; Dedonder, C.; Dopfer, O.; Jouvet, C. *Phys. Chem. Chem. Phys.* **2010**, *12*, 14456.

International Journal of Mass Spectrometry 297 (2010) 63–66

Contents lists available at ScienceDirect

International Journal of Mass Spectrometry

journal homepage: www.elsevier.com/locate/ijms

Absorption spectrum of isolated tris(2,2′-bipyridine)ruthenium(II) dications *in vacuo*

Maj-Britt Suhr Kirketerp, Steen Brøndsted Nielsen*

Department of Physics and Astronomy, Aarhus University, Ny Munkegade 120, DK-8000 Aarhus C, Denmark

ARTICLE INFO

Article history:
Received 28 February 2010
Received in revised form 18 May 2010
Accepted 18 May 2010
Available online 12 June 2010

Keywords:
Action spectroscopy
Storage ring experiment
$Ru(bipy)_3^{2+}$
Metal to ligand charge transfer

ABSTRACT

Here we report the gas-phase action spectrum of tris(2,2′-bypyridine)ruthenium(II) dications, $Ru(bipy)_3^{2+}$, recorded over a broad wavelength region from 210 nm to 650 nm. Ions formed by electrospray ionization were thermalized in collisions with helium buffer gas at room temperature in a 22-pole ion trap. A bunch of ions was then accelerated to keV-kinetic energies and injected into an electrostatic ion storage ring in which they circulated with a revolution time of 69 microseconds. After several milliseconds to allow for the decay of metastable ions, the ions were photoexcited and their decay monitored in time. Dissociation was found to occur on the microsecond time scale. Based on the time spectra, the initial number of photoexcited ions was estimated at each wavelength (relative and not absolute numbers). This approach circumvents the problem of kinetic shifts often encountered when dissociation is sampled within a finite time interval in the case of finite length time-of-flight instruments. The obtained absorption spectrum is found to be similar to the solution phase spectrum (acetonitrile solvent) but with a blueshift of the lowest energy metal-to-ligand charge transfer transition. This finding indicates a localized electronic transition in solution involving only one of the bipyridine ligands. There are small differences in the relative intensities of the bands between the gas-phase and solution-phase spectra. Finally, our gas-phase spectrum serves as a reference to benchmark theoretical calculations of excited states.

XI

1. Introduction

Tris(2,2′-bipyridine)ruthenium(II), $Ru(bipy)_3^{2+}$, has become a text-book case for coordination chemistry. It is one of the most extensively studied and widely used transition metal complexes due to its interesting photophysical and photochemical properties [1–3]. The ground state of the complex is a singlet, and the highest occupied molecular orbitals are predominantly localized on the metal whereas the lowest unoccupied molecular orbitals are on the ligands. Electronic transitions can be categorized as metal-centered (dd), ligand-centered ($\pi\pi^*$), metal-to-ligand (ML) and ligand-to-metal (LM) charge transfer (CT). The transition energies depend on the metal and ligand orbitals and the coupling between them, and they may be perturbed by a chemical environment such as a solvent. Owing to its stability, high extinction coefficients and long-lived excited states, $Ru(bipy)_3^{2+}$ is suitable as a light-harvesting antenna, applicable in dye-sensitized solar cells and in artificial photosynthesis [4–7].

While the complex that belongs to the D_3 point group has zero dipole moment in its electronic ground state, it may have a permanent dipole moment in an excited state if the excitation is localized, that is, if the photoactive electron is localized on a single ligand rather than delocalized over all three. The molecular symmetry is then reduced from D_3 to C_2, *cf.* $[Ru(III)(bipy)^-(bipy)_2]^{2+}$. Experiments in different solvents have been performed to elucidate the character of the transitions, and it was found that the lowest energy band was slightly sensitive to solvent which implies a non-zero dipole moment in the excited state [8–10]. Raman experiments point in the same direction [11,12] whereas evidence has been found in solid matrices for the photoexcited electron to be delocalized among the ligands [13,14]. Femtosecond time-resolved absorption anisotropy measurements revealed time dependence in nitrile solutions attributed to initial delocalization followed by charge localization [15].

Information on the nature of the excited state can also be obtained from a comparison between the absorption spectrum of the bare ion isolated in vacuum and that of the ion in bulk solution. The difference is expectedly larger than that between different solvents. An obstacle, however, is that the binding energy of the bidentate bipyridine ligand is high, and it is therefore difficult to identify photofragmentation within the limited sampling time interval of for example time-of-flight instruments. Previous work by Posey and co-workers [16–19] was focused on microsolvated $Fe(bipy)_3^{2+}$ and $Fe(terpy)_2^{2+}$ (terpy = 2,2′,2″-terpyridyl) ions

* Corresponding author.
E-mail address: sbn@phys.au.dk (S.B. Nielsen).

1387-3806/$ – see front matter © 2010 Elsevier B.V. All rights reserved.
doi:10.1016/j.ijms.2010.05.019

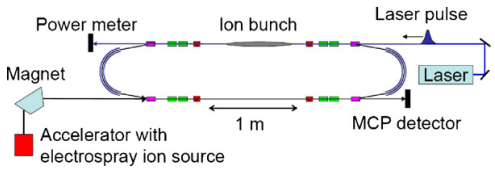

Fig. 1. Schematic layout of the electrostatic ion storage ring ELISA.

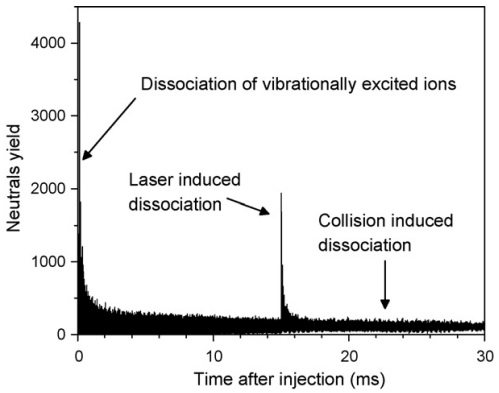

Fig. 2. Time spectrum of $Ru(bipy)_3^{2+}$. At early times, decay of vibrationally excited ions dominate over decay due to collisions with residual gas in the ring. Photoexcitation leads to an increased yield of neutrals.

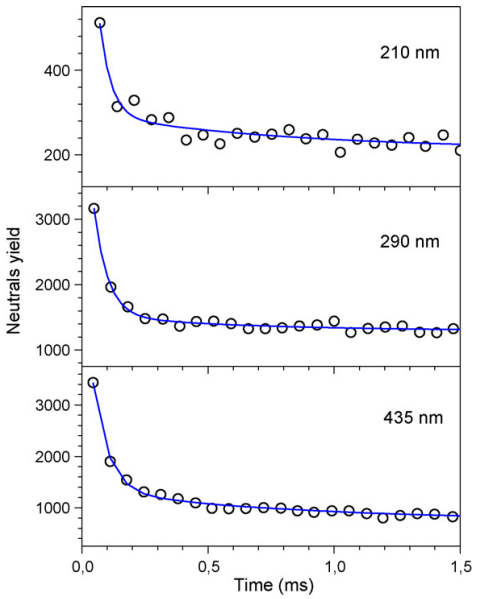

Fig. 3. Yield of neutrals as a function of time after photo-excitation. The sum of three exponentials was fit to the data. Time constants of about 50 μs and 500 μs were found for dissociation of photoexcited ions while dissociation due to collisions with residual gas in the ring occurred with a time constant of 100 ms.

for which solvent molecules readily evaporate after photoexcitation.

The problem of observing dissociation in action spectroscopy experiments is largely overcome in storage ring experiments or ion traps where fragmentation is monitored over a long time scale, in rings often from tens of microseconds to tens of milliseconds [20,21]. In the present work we have probed the influence of solvent on the energy of electronic transitions of the coordination complex $Ru(bipy)_3^{2+}$ from measurements on bare ions using the electrostatic ion storage ring in Aarhus (ELISA). The yield of photofragments was monitored from 210 nm to 650 nm.

2. Experimental

Experiments were carried out at the electrostatic ion storage ring in Aarhus (ELISA) (see Fig. 1) [22,23]. $[Ru(bipy)_3](ClO_4)_2$ was dissolved in MeOH to a concentration of about 10 mM and electrosprayed [24]. In this way $Ru(bipy)_3^{2+}$ ions were produced that were subsequently accumulated in a 22-pole ion trap and thermally equilibrated by collisions with a room temperature helium buffer gas therein. The ions were accelerated as an ion bunch to kinetic energies of 22 keV × q (q = charge state), and a bending magnet was used to select the appropriate ions. Following injection into the ring, the ions were stored for several milliseconds before being irradiated by a nanosecond light pulse from a tuneable, pulsed EKSPLA laser. This allowed for the decay of ions that were collisionally excited during the extraction from the ion trap or during injection into the ring (see Fig. 2). The laser is an Nd:YAG laser where the third harmonic (355 nm) pumps an optical parametric oscillator (OPO). The visible output from this OPO was frequency doubled in a crystal providing UV light with a beam diameter of about 5 mm. The repetition rate of the experiment was 10 Hz. Dissociation was a result of one-photon absorption (*vide infra*). In another experiment on $Fe(bipy)_3^{2+}$, where the ring was used as a mass spectrometer, it was found that a dominant fragmentation channel is loss of bipy, and likewise bipy loss has been observed in collision-induced dissociation experiments on $Ru(bipy)_3^{2+}$ [24,25]. Lifetimes were obtained from measurements of the yield of neutrals hitting the microchannel plate (MCP) detector located at the end of the straight section opposite to the side where photoexcitation was performed (*i.e.*, delayed dissociation experiment). The pressure in the ring was about 10^{-10} mbar.

Solution-phase absorption spectroscopy was carried out using a Thermo Spectronic heλlios α instrument. The $[Ru(bipy)_3](ClO_4)_2$ salt was home-made and dissolved in acetonitrile.

3. Results and discussion

Time spectra taken at three different excitation wavelengths are shown in Fig. 3. Three exponentials are required to satisfactorily describe the decays. Photon absorption leads to dissociation on the microsecond time scale while dissociation due to collisions with residual gas in the ring occurs on the hundred millisecond timescale. The smallest time constant increases with wavelength from 45 μs at 210 nm to 62 μs at 435 nm in accordance with statistical dissociation. The second time constant is about 500 μs for all three wavelengths, and finally the third time constant is 100 ms.

The yield of photofragments increases linearly with the number of photons in the laser pulse (see Fig. 4 for 430-nm excitation), which implies that the dissociation is due to absorption of one photon. The requirement of two time constants to account for the decay due to photon absorption is most likely a consequence of the width of the internal energy distribution; not all ions have exactly the same energy after photoexcitation [26,27]. In principle there would be a time constant associated with each internal energy determined by the activation energy and preexponential factor for the dissociation process but since two are sufficient we decide against using more exponentials. Another interpretation of the long life-

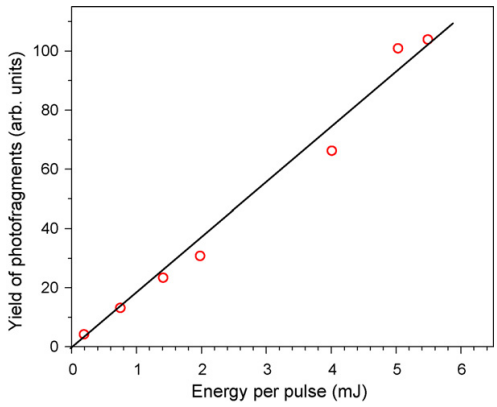

Fig. 4. The yield of photofragments as a function of energy of the laser pulse. The wavelength of the light was 430 nm.

time component is trapping in a long-lived electronically excited state that acts a bottleneck to the dissociation (*vide infra*).

Based on the exponentials, we estimated the initial number of photoexcited ions (relative numbers) at each wavelength. These numbers were divided by the average number of photons in the pulse and corrected for differences in ion beam intensities to provide values for absorption. The signal from collision induced dissociation serves as a measure of the ion beam intensity. A clear advantage of this method is that we correct for variations in dissociation lifetimes after photoexcitation, which is an issue when dissociation is sampled in a too short time interval.

In our experiment, we can only identify absorption if it leads to fragmentation (action spectroscopy), and neutrals have to be formed. Light emission would result in cold ions that do not have enough excess energy for dissociation. To equate the action spectrum with the absorption spectrum, it is therefore an assumption that the luminescence quantum yield is the same for all excitation wavelengths. It is known for $Ru(bipy)_3^{2+}$ that radiationless deactivation to the lowest excited state, ^{3}MLCT, occurs quickly with a quantum yield close to unity [1]. This state does not undergo fast radiationless decay to the ground state, and it is highly luminescent (quantum yield of about 0.4). The radiative lifetime of the excited complex in a rigid alcoholic glass is 13 μs but both the emission lifetime and quantum yield decrease with temperature as thermally activated radiationless deactivation can occur via upper-lying metal-centered excited states (dd) [1]. Since vibrational cooling does not occur for isolated ions *in vacuo* neglecting infrared emission, the excited-state lifetime and luminescence are likely smaller than in solid phase. Still we caution that the luminescence quantum yield may change with excitation wavelength though most likely not very much within a band. Also if dissociation occurs promptly in an electronically excited state or two singly charged ions are formed in a Coulomb explosion process, we are blind to it. High-energy collision experiments (keV energies) that lead to broad internal energy distributions and that often involve electronically excited states, however, reveal that the formation of $[Ru(bipy)_2\text{-}H]^+$ and $bipyH^+$ is a minor process compared to loss of bipy [25].

Decay is first sampled 35 μs after photoexcitation which is longer than the excited-state lifetime of 13 μs, and we assume that most of the ions at this time are in their electronic ground state. The attribution of the second time constant to long-lived triplet-state excited ions is therefore less likely.

The action spectrum is shown in Fig. 5, top panel. The uncertainties in the data points are dominated by fluctuations in laser pulse

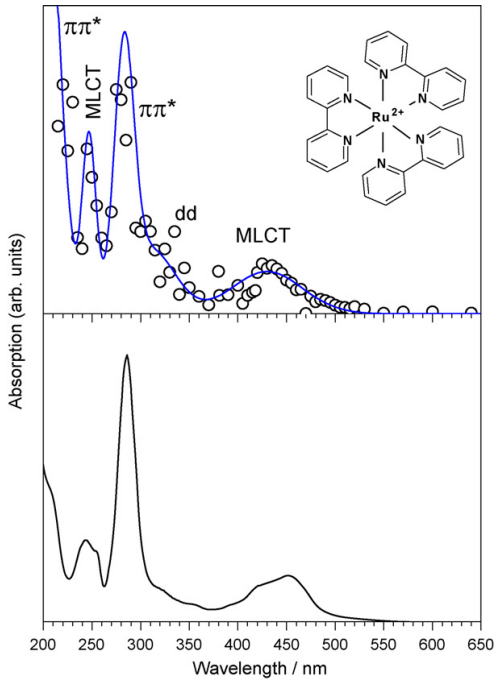

Fig. 5. Absorption spectra of $Ru(bipy)_3^{2+}$ isolated in vacuum (top panel) and in acetonitrile solution (lower panel). Band assignments are taken from [2]. The blue line is drawn to guide the eye. (For interpretation of the references to color in the caption of this figure, the reader is referred to the web version of the article.)

Table 1
Absorption band maxima (in nm) of $Ru(bipy)_3^{2+}$.

Transition	LMCT	dd	ππ*	LMCT	ππ*
In vacuo	430	310	283	247	<210
In acetonitrile solution	452	319	286	243	195

energies and are estimated to be less than 10%. Bands are assigned to MLCT transitions at 430 nm and 247 nm, ligand-centered ππ* transitions at 283 nm and 210 nm, and a metal-centered dd transition at 310 nm, see [2]. For comparison, the solution-phase spectrum taken in acetonitrile is shown in the lower panel of the figure. The band maxima are summarized in Table 1. The band positions are almost identical with the exception of a significant redshift of the 430-nm band to 452 nm upon solvation. This can be explained by charge localization introduced by the solvent which decreases the energy of the charge transfer from the metal to the ligand. The MLCT bands are known to be most sensitive to solvent effects [9]. For comparison, Posey and co-workers [17] measured the red edge of the MLCT band of $Fe(bipy)_3^{2+}$ and found that methanol caused a redshift in the absorption band, which reflects a more favorable interaction between the excited state of $Fe(bipy)_3^{2+}$ and the methanol molecules relative to its ground state. In the case of $Ru(bipy)_3^{2+}$, the ground state is nonpolar whereas the MLCT excited state is highly polar; a value for the excited-state dipole moment of 14.1 ± 6.1 D has been reported by Meyer and co-workers [8]. Our data are consistent with the formulation of the excited state as localized, $Ru(bipy)_2^{3+}(bipy)^-$, and not delocalized having the promoted electron confined to the π* orbital over all three bipy ligands. Interestingly, a redshift was not measured for the 247-nm band, which indicates that in this case the excited state has more delocalized character.

Small differences are seen in the relative intensities of the bands where the high energy band is much larger in the gas phase than in solution. Also the dd transition is more pronounced in the gas phase. These differences could be related to wavelength-dependent luminescence.

Acknowledgement

SBN gratefully acknowledges support from Lundbeckfonden (Junior Group Leader Fellowship).

References

[1] A. Juris, V. Balzani, F. Barigelletti, S. Campagna, P. Belser, A. Vonselewsky, Coordin. Chem. Rev. 84 (1988) 85, references therein.
[2] V. Balzani, G. Bergamini, S. Campagna, F. Puntoriero, Top. Curr. Chem. 280 (2007) 117.
[3] N.H. Damrauer, G. Cerullo, A. Yeh, T.R. Boussie, C.V. Shank, J.K. McCusker, Science 275 (1997) 54.
[4] T.J. Meyer, Acc. Chem. Res. 22 (1989) 163.
[5] J.H. Alstru-Acavedo, M.K. Brennaman, T.J. Meyer, Inorg. Chem. 44 (2005) 6802.
[6] B.D. Koivisto, K.C.D. Robson, C.P. Berlinguette, Inorg. Chem. 48 (2009) 9644.
[7] F. Barigelletti, A. Juris, V. Balxani, P. Belser, A. von Zelewsky, Inorg. Chem. 22 (1983) 3335.
[8] E.M. Kober, B.P. Sullivan, T.J. Meyer, Inorg. Chem. 23 (1984) 2098.
[9] P.Y. Chen, T.J. Meyer, Chem. Rev. 98 (1998) 1439.
[10] H. Riesen, L. Wallace, E. Krausz, Inorg. Chem. 35 (1996) 6908.
[11] P.J. Carroll, L.E. Brus, J. Am. Chem. Soc. 109 (1987) 7613.
[12] P.G. Bradley, N. Kress, B.A. Hornberger, R.F. Dallinger, W.H. Woodruff, J. Am. Chem. Soc. 103 (1981) 7441.
[13] D. Braun, P. Huber, J. Wudy, J. Schmidt, H. Yersin, J. Phys. Chem. 98 (1994) 8044.
[14] H. Yersin, E. Gallhuber, J. Am. Chem. Soc. 106 (1984) 6582.
[15] A.Y. Yeh, C.V. Shank, J.K. McCusker, Science 289 (2000) 935.
[16] T.D. Burns, T.G. Spence, M.A. Mooney, L.A. Posey, Chem. Phys. Lett. 258 (1996) 669.
[17] T.G. Spence, T.D. Burns, G.B. Guckenberger, L.A. Posey, J. Phys. Chem. A 101 (1997) 1081.
[18] T.G. Spence, B.T. Trotter, L.A. Posey, J. Phys. Chem. A 102 (1998) 7779.
[19] T.G. Spence, B.T. Trotter, T.D. Burns, L.A. Posey, J. Phys. Chem. A 102 (1998) 6101.
[20] J.A. Wyer, A. Ehlerding, H. Zettergren, M.-B.S. Kirketerp, S. Brøndsted Nielsen, J. Phys. Chem. A 113 (2009) 9277.
[21] A. Ehlerding, J.A. Wyer, H. Zettergren, M.-B.S. Kirketerp, S. Brøndsted Nielsen, J. Phys. Chem. A 114 (2010) 299.
[22] S.P. Møller, Nucl. Instrum. Meth. A 394 (1997) 281.
[23] J.U. Andersen, P. Hvelplund, S. Brøndsted Nielsen, S. Tomita, H. Wahlgreen, S.P. Møller, U.V. Pedersen, J.S. Forster, T.J.D. Jørgensen, Rev. Sci. Instrum. 73 (2002) 1284.
[24] V. Katta, S.K. Chowdhury, B.T. Chait, J. Am. Chem. Soc. 112 (1990) 5348.
[25] A.B. Nielsen, P. Hvelplund, S. Brøndsted Nielsen, Int. J. Mass Spectrom. 232 (2004) 79.
[26] J.U. Andersen, H. Cederquist, J.S. Forster, B.A. Huber, P. Hvelplund, J. Jensen, B. Liu, B. Manil, L. Maunoury, S. Brøndsted Nielsen, U.V. Pedersen, J. Rangama, H.T. Schmidt, S. Tomita, H. Zettergren, Phys. Chem. Chem. Phys. 6 (2004) 2676.
[27] J.U. Andersen, H. Cederquist, J.S. Forster, B.A. Huber, P. Hvelplund, J. Jensen, B. Liu, B. Manil, L. Maunoury, S. Brøndsted Nielsen, U.V. Pedersen, H.T. Schmidt, S. Tomita, H. Zettergren, Eur. Phys. J. D 25 (2003) 139.

Chemical Physics Letters 502 (2011) 53–56

Contents lists available at ScienceDirect

Chemical Physics Letters

journal homepage: www.elsevier.com/locate/cplett

On the stability of isolated $Pt(SCN)_4^{2-}$ dianions *in vacuo* and action spectroscopy experiments

Christian Nygaard Hansen, Maj-Britt Suhr Kirketerp, Mads Bejder Kristensen, Steen Brøndsted Nielsen *, Kristian Støchkel, Jean Ann Wyer

Department of Physics and Astronomy, Aarhus University, DK-8000 Aarhus C, Denmark

ARTICLE INFO

Article history:
Received 21 October 2010
In final form 6 December 2010
Available online 8 December 2010

ABSTRACT

Tetrathiocyanoplatinate(II), $Pt(SCN)_4^{2-}$, isolated *in vacuo* was subjected to a range of experiments. From storage ring measurements the dianions were found to be stable on the seconds time scale. At another instrumental setup, ions were photoexcited with UV light, and the dominant decay channel was electron detachment. The yield of $Pt(SCN)_4^-$ monoanions as a function of wavelength provided the action spectrum. Maximum absorption occurs at ~240 nm, and the spectrum is similar to the absorption spectrum of $Pt(SCN)_4^{2-}$ in methanol solution, which implies that a solvent perturbs the ground state and the electronically excited state in the same manner.

1. Introduction

Molecular dianions have spurred the interest of experimentalists and theorists for several years due to the fact that these fragile ions exhibit very different physics and chemistry when isolated *in vacuo* compared to when they are in solution phase [1–6]. Familiar dianions like sulfate that exist in solution do not survive for long without a stabilizing water environment [7,8]. In general, decay processes involve either electron autodetachment or Coulomb explosion into two monoanions with a significant release of translational kinetic energy. In both cases an internal Coulomb barrier has to be surmounted, which implies that unstable dianions may still live long enough (>microseconds) for mass spectrometric identification. The time for electron loss is often determined by the tunneling rate through the barrier. Dianions are optimal benchmark systems for quantum chemical calculations since they are systems for which electron correlation is of the utmost importance.

One class of important dianions is inorganic metal ion complexes that are characterized by a positively charged metal center and negatively charged ligands. Significant work has been carried out to understand their fundamental physical properties [9–23] but there is limited spectroscopic information on their electronically excited states. Here we focus on the $Pt(SCN)_4^{2-}$ complex and report results from lifetime measurements in an electrostatic ion storage ring as well as spectroscopy experiments at a single pass beam instrument. The formal oxidation state of the platinum center is +II with a d^8 electron configuration. This dianion displays very different behavior to that of $Cr(SCN)_4^{2-}$ which was previously studied in our laboratory [10]. Our results are compared to those for other four-coordinate platinum complexes, and the role of solvation on the excited state physics is discussed.

XII

2. Experimental

Experiments were carried out at two different instrumental setups; the electrostatic ion storage ring in Aarhus (ELISA) [24,25] and an accelerator mass spectrometer [26,27]. In both cases, ions were produced by electrospray ionization of $K_2Pt(SCN)_4$ dissolved in methanol. These were accumulated in a multipole ion trap and thermalized to room temperature in collisions with helium buffer gas. Ion bunches were accelerated to keV energies (22 and 50 kV acceleration voltages for the ring and single pass experiments, respectively), and ions of interest selected by a bending magnet.

ELISA was used to measure dianion lifetimes. Briefly, ions with a certain mass-to-charge ratio (m/z) were injected into the ring where they were stored based on electrostatic deflectors. The yield of neutral fragments produced in one of the straight sections of the ring was monitored as a function of time with a microchannel plate detector. The pressure in the ring was about 10^{-10} mbar which set an upper limit on the storage time due to collisions with residual gas. The ring was emptied of ions and filled with a new ion bunch every 5 s.

At the other setup, mass-selected ions were photoexcited with laser light in a perpendicular configuration. To produce the necessary UV light, the output of an Nd:YAG laser was first frequency tripled to 355-nm light. This light was then split into infrared and visible light by an optical parametric oscillator. Finally, the visible

* Corresponding author. Fax: +45 8612 0740.
E-mail address: sbn@phys.au.dk (S.B. Nielsen).

0009-2614/$ - see front matter © 2010 Elsevier B.V. All rights reserved.
doi:10.1016/j.cplett.2010.12.025

light was frequency doubled to provide ultraviolet light with a pulse width of about 6 ns. The laser system is from EKSPLA, and the repetition rate of the experiment was 20 Hz. An electrostatic analyzer and a channeltron detector were used to determine the product ions and their abundances. To improve the signal-to-noise ratio of the measurement and to minimize the contribution from residual gas collisions, a time gate was used to record ions produced mainly by photoexcitation.

Solution-phase absorption spectroscopy experiments were carried out using a Thermo Spectronic helios α instrument. $K_2Pt(SCN)_4$ was dissolved in methanol and a spectrum recorded from 200 to 300 nm.

3. Results and discussion

The time spectrum of $Pt(SCN)_4^{2-}$ (m/z 213) is shown in Figure 1 together with that of adenosine 5′-monophosphate (AMP) (m/z 345). AMP is a stable monoanion, and its time spectrum provides a measure for the time constant with respect to destruction from collisions with residual gas in the ring. Both ions display long lifetimes of about 0.6 s, and we therefore conclude that the dianion is stable on the seconds time scale. There is a contribution to the decay from a component that has a shorter lifetime of 0.15 s. This is most likely due to the decay of collisionally excited ions formed during extraction from the ion trap. A similar component is present in the AMP time spectrum but there the time constant is shorter (18 ms).

Storage ring experiments on $Pt(SCN)_6^{2-}$, $Ni(CN)_4^{2-}$, $Pt(CN)_4^{2-}$, $Pt(CN)_6^{2-}$, $Pd(CN)_4^{2-}$, and $Pd(NO_2)_4^{2-}$, all produced by electrospray ionization, showed that these square-planar and octahedral complexes are also stable on the seconds time scale (data not shown). The lifetime of $Ni(CN)_4^{2-}$ (m/z 81) is shortest (0.3 s) which is ascribed to its higher velocity; after 22-kV acceleration its velocity is a factor of two higher than that of AMP. In other words, the distance $Ni(CN)_4^{2-}$ travels in 0.3 s is approximately the same as that which AMP travels in 0.6 s.

Interestingly, the behavior of $Pt(SCN)_4^{2-}$ is very different from that of $Cr(SCN)_4^{2-}$ formed after electron transfer from sodium atoms to $Cr(SCN)_4^-$ monoanions [10]. Attempts to prepare $Cr(SCN)_4^{2-}$ in the ion source and select them by the magnet were unsuccessful. Indeed, $Cr(SCN)_4^{2-}$ was shown to be unstable and Coulomb exploded into $Cr(SCN)_3^-$ and SCN^- on the microsecond time scale with about 3 eV released as translational kinetic energy. In accordance with this, density functional theory calculations indicated that the non-planar dianion with d^4 electron configuration was electronically unstable by 0.1 eV and unstable towards loss of SCN^- by 0.56 eV [12]. The Coulomb barrier for the dissociation process was calculated to be 1.2 eV. In contrast, but in accordance with our lifetime measurements, the closely associated $Ni(CN)_4^{2-}$ dianion (eight d electrons) was predicted to be both electronically and geometrically stable.

Earlier work by Kappes and co-workers [14] on $PtBr_4^{2-}$ and $PtCl_4^{2-}$ revealed that these ions are metastable towards halide loss, and that $PtCl_4^{2-}$ undergoes tunneling electron loss to form $PtCl_4^{2-}$ with a half-life of seconds. It is possible that $Pt(SCN)_4^{2-}$ behaves similar to these two family members but to establish this would require lifetime measurements under better vacuum conditions to prevent ion losses due to collisions with residual gas. On the other hand, photoelectron spectroscopy on $Pt(CN)_4^{2-}$ by Wang and co-workers [16] demonstrated that this ion is electronically stable by 1.69 eV. This high stability was ascribed to the high electron-withdrawing capabilities of the cyano ligands.

Next we present the results from photoexcitation of $Pt(SCN)_4^{2-}$. The ion bunch was irradiated perpendicular to the ion beam trajectory with laser light (250 nm) and the photoproducts subsequently determined. $Pt(SCN)_4^-$ monanions were measured on the detector at different times due to the width of the ion bunch (20 μs), see Figure 2. These ions result from electron detachment in collisions

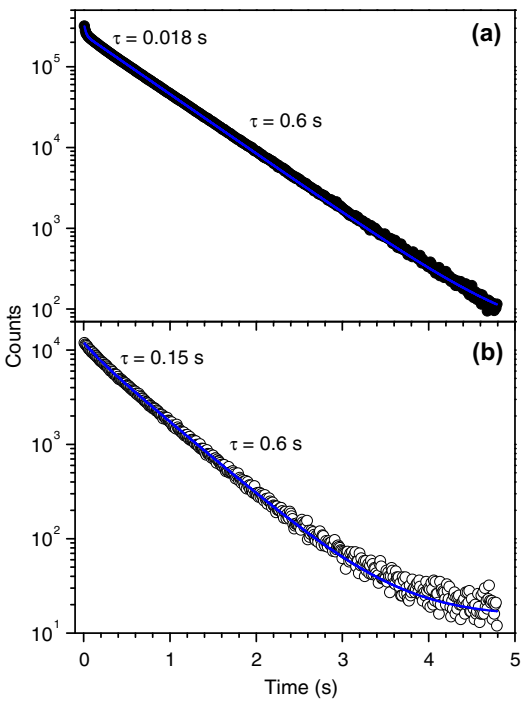

Figure 1. Time spectra of (a) AMP monoanions and (b) $Pt(SCN)_4^{2-}$ dianions measured at the storage ring setup. The yield of neutral products formed on one straight section of the ring was sampled as a function of time; this yield is proportional to the number of ions in the ring. Two exponentials were fit to the count rates (see main text).

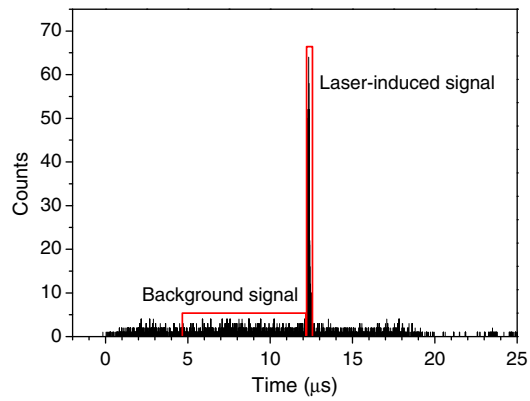

Figure 2. Detection of $Pt(SCN)_4^-$ monoanions formed from $Pt(SCN)_4^{2-}$ dianions at the accelerator mass spectrometer. The broad background is due to residual gas collisions, while the sharp peak is a result of photodetachment after 250-nm photoexcitation. Time zero is defined as the time when the first ions in the bunch reach the detector. For photodissociation mass spectroscopy, a time gate for detection was set around the photoproducts (laser-induced signal). In the action spectroscopy experiments, the photoyield was divided by the background counts which occurred within the depicted time box in order to correct for variations in the ion beam intensity.

with residual gas in the beam line (pressure of 10^{-6} mbar) and from photoexcitation. A strong signal 200-ns broad is evident at the time relating to when the laser light hit the ions.

To obtain a photodissociation mass spectrum, a time gate (width of 350 ns) was set around the photoproduct signal. This ensures that there is little contribution from residual gas collision-induced dissociation products, and that the noise level is kept low. Daughter ion mass spectra from when the laser was on and off are displayed in Figure 3. Photoexcitation at both 215 and 245 nm leads dominantly to electron detachment with minor peaks corresponding to the fragment ions $Pt(SCN)_3^-$, $Pt(CS)_3^-$, and $PtCS_2^-$ seen. These are likely the result of consecutive neutral losses from vibrationally excited $Pt(SCN)_4^-$ since the widths of the peaks are similar to that for $Pt(SCN)_4^-$; a Coulomb explosion process would result in broad peaks as ions scatter in the backward and forward directions [9–11]. Likewise, collisional electron detachment of $Pt(CN)_4^{2-}$ was followed by losses of CN or $(CN)_2$ [9]. We note that $Pt(CN)_4^{2-}$ when vibrationally heated in low-energy collisions Coulomb explodes into $Pt(CN)_3^-$ and CN^- [22]. A scan to lower masses displayed no detectable production of SCN^- or CN^- after photoexcitation. The abundance of $Pt(SCN)_4^-$ relative to that of all photo-ions is to a good approximation the same for the two wavelengths (about 70%), which means that the yield of $Pt(SCN)_4^-$ is directly correlated with the absorption cross section. Finally, it is apparent from Figure 3c that the contribution from residual gas collisions is insignificant.

To obtain an action spectrum, we measured the yield of $Pt(SCN)_4^-$ as a function of laser excitation wavelength from 210 to 300 nm. These yields were corrected for variations in light and ion beam intensities. The latter correction was done based on the signal from residual gas collisions since this signal is proportional to the number of ions in the bunch. Experiments were executed with different laser beam intensities to check for any saturation effects. The results are summarized in Figure 4. It is evident that the data points follow each other, except at the lowest wavelengths where the statistics are poor, and the data below 230 nm should therefore be considered with some caution. Taken together, the spectra indicate that the absorption band maximum is at about 240 nm (5.2 eV).

In methanol solution, $Pt(SCN)_4^{2-}$ absorbs maximally at 242 nm (Figure 4). Hence solvation of the bare ions has basically no effect on the location of the excited state relative to the ground state. Actually, taking into consideration the high uncertainties in the gas phase experiment at low wavelengths where the laser power is low, the overall shapes of the two spectra look almost identical. Furthermore, at low wavelengths direct electron detachment into continuum states not involving a resonance state may occur. This may to some extent account for the, on average, higher-lying gas-phase data points in this region.

While we did not measure any shift in the absorption of this symmetric ion upon solvation, Weber and co-workers [15] found that the absorption band maximum of $PtBr_4^{2-}$ in water and acetonitril compared to the maximum in the photodetachment cross section of $PtBr_4^{2-}$ *in vacuo* was redshifted by 0.7 and 0.55 eV, respectively. These quite large shifts were ascribed to solvent molecules coming close to the metal center and thereby affecting the metal d–d band transitions. It is possible that the larger size of the SCN^- ligands prevents such interactions but a firm understanding calls for quantum mechanical calculations. Furthermore, other work has shown that the metal-to-ligand charge transfer transition of $Ru(bipy)_3^{2+}$ underwent a significant redshift from 430 to 452 nm upon solvation of the complex in acetonitril [28]. There the explanation was based on a localized transition involving only one of the bipyridine (bipy) ligands in solution, which resulted in a permanent dipole moment in the excited state in contrast to the symmetric ground state. Finally, we note that in the case of charge-transfer transitions in π-conjugated anions such as nitrophenolates, solvation by polar molecules causes a significant blueshift due to localization of the negative charge [29,30].

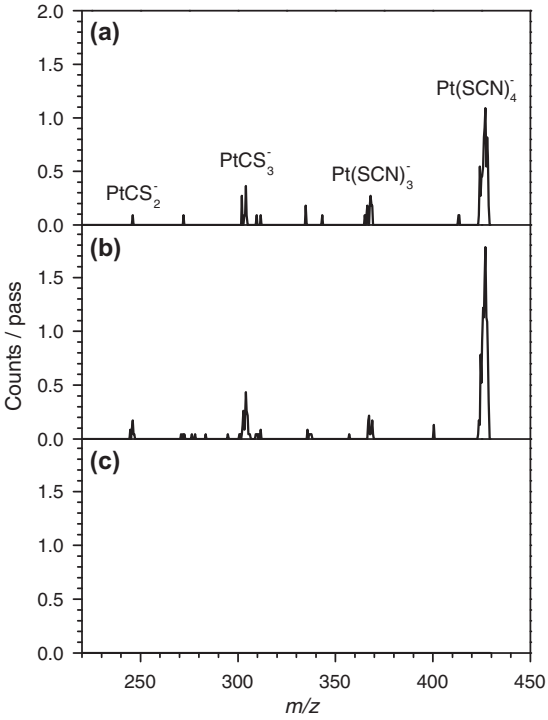

Figure 3. Daughter ion mass spectra of $Pt(SCN)_4^{2-}$ (m/z 213). (a) Laser on (215 nm). (b) Laser on (245 nm). (c) Laser off. The signal intensity of $Pt(SCN)_4^-$ comprises 70% of the total product ion signal at both excitation wavelengths.

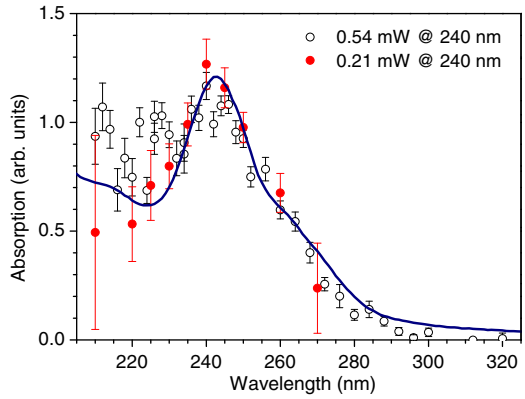

Figure 4. Action spectra for the yield of $Pt(SCN)_4^-$ from $Pt(SCN)_4^{2-}$ as a function of excitation wavelength. Spectra were recorded at two laser powers at each wavelength (powers for 240-nm excitation are indicated). A neutral density filter was implemented in lowering the laser power. Error bars represent one standard deviation. The absorption spectrum of $K_2Pt(SCN)_4$ in a methanol solution is represented by the navy blue curve. (For interpretation of the references in color in this figure legend, the reader is referred to the web version of this article.)

XII

4. Conclusions

In conclusion, the lifetime of $Pt(SCN)_4^{2-}$ dianions in a storage ring was measured to be on the order of half a second, which is the upper time set by collisions with residual gas in the ring. Irradiation of the ions with UV light leads dominantly to electron detachment resulting in $Pt(SCN)_4^-$. There are minor peaks in the daughter ion mass spectrum that correspond to monoanions formed after dissociation. It was found that the highest yield of $Pt(SCN)_4^-$ monoanions was obtained at about 240 nm, which is very close to the maximum absorption of the dianions when they are solvated by methanol (242 nm). This indicates that the electronic structures of the dianions in their ground- and excited-states are not perturbed by a solvent or that the states are shifted by the same amount.

Acknowledgements

S.B. Nielsen gratefully acknowledges support from Lundbeckfonden (Junior Group Leader Fellowship).

References

[1] A.I. Boldyrev, M. Gutowski, J. Simons, Acc. Chem. Res. 29 (1996) 497.
[2] M.K. Scheller, R.N. Compton, L.S. Cederbaum, Science 270 (1995) 1160.
[3] D. Schröder, H. Schwarz, J. Phys. Chem. A 103 (1999) 7385.
[4] A. Dreuw, L.S. Cederbaum, Chem. Rev. 102 (2002) 181.
[5] J. Kalcher, A.F. Sax, Chem. Rev. 94 (1994) 2291.
[6] X.-B. Wang, L.-S. Wang, Annu. Rev. Phys. Chem. 60 (2009) 105.
[7] X.-B. Wang, J.B. Nicholas, L.-S. Wang, J. Chem. Phys. 113 (2000) 10837.
[8] X.-B. Wang, X. Yang, J.B. Nicholas, L.-S. Wang, Science 294 (2001) 1322.
[9] G. Bojesen, P. Hvelplund, T.J.D. Jørgensen, S. Brøndsted Nielsen, J. Chem. Phys. 113 (2000) 6608.
[10] A.B. Nielsen, P. Hvelplund, B. Liu, S. Brøndsted Nielsen, S. Tomita, J. Am. Chem. Soc. 125 (2003) 9592.
[11] K. Drenck, P. Hvelplund, C.J. McKenzie, S. Brøndsted Nielsen, Int. J. Mass Spectrom. 244 (2005) 144.
[12] K. Drenck, F. Jensen, J. Olsen, S. Brøndsted Nielsen, Chem. Phys. 353 (2008) 189.
[13] X.-B. Wang, L.-S. Wang, Phys. Rev. Lett. 83 (1999) 3402.
[14] P. Weis, O. Hampe, S. Gilb, M.M. Kappes, Chem. Phys. Lett. 321 (2000) 426.
[15] D. Löffler, J.M. Weber, M.M. Kappes, J. Chem. Phys. 123 (2005) 224308.
[16] X.-B. Wang, Y.-L. Wang, H.-K. Woo, J. Li, G.-S. Wu, L.-S. Wang, Chem. Phys. 329 (2006) 230.
[17] J. Friedrich, S. Gilb, O.T. Ehrler, A. Behrendt, M.M. Kappes, J. Chem. Phys. 117 (2002) 2635.
[18] C. Rensing, O.T. Ehrler, J.-P. Yang, A.-N. Unterreiner, M.M. Kappes, J. Chem. Phys. 130 (2009) 234306.
[19] J.C. Marcum, J.M. Weber, J. Chem. Phys. 131 (2009) 194309.
[20] X.-B. Wang, L.-S. Wang, J. Chem. Phys. 111 (1999) 4497.
[21] X.-B. Wang, L.-S. Wang, J. Am. Chem. Soc. 122 (2000) 2339.
[22] R.M. Burke, W.E. Boxford, C.E.H. Dessent, J. Chem. Phys. 125 (2006) 021105.
[23] R.M. Burke, W.E. Boxford, C.E.H. Dessent, J. Chem. Phys. 126 (2007) 064308.
[24] S.P. Møller, Nucl. Instrum. Methods Phys. Res. A 394 (1997) 281.
[25] J.U. Andersen et al., Rev. Sci. Instrum. 73 (2002) 1284.
[26] O.V. Boltalina, P. Hvelplund, T.J.D. Jørgensen, M.C. Larsen, M.O. Larsson, D.A. Sharoitchenko, Phys. Rev. A 62 (2000) 023202.
[27] M.O. Larsson, P. Hvelplund, M.C. Larsen, H. Shen, H. Cederquist, H.T. Schmidt, Int. J. Mass Spectrom. Ion Processes 177 (1998) 51.
[28] M.-B.S. Kirketerp, S. Brøndsted Nielsen, Int. J. Mass Spectrom. 297 (2010) 63.
[29] M.-B.S. Kirketerp et al., ChemPhysChem 10 (2009) 1207.
[30] M.-B.S. Kirketerp, M.Å. Petersen, M. Wanko, H. Zettergren, M. Brøndsted Nielsen, S. Brøndsted Nielsen, ChemPhysChem 11 (2010) 2495.

J|A|C|S
COMMUNICATIONS

Published on Web 08/14/2008

A Soret Marker Band for Four-Coordinate Ferric Heme Proteins from Absorption Spectra of Isolated Fe(III)-Heme$^+$ and Fe(III)-Heme$^+$(His) Ions in Vacuo

Morten Køcks Lykkegaard, Anneli Ehlerding, Preben Hvelplund, Umesh Kadhane, Maj-Britt Suhr Kirketerp, Steen Brøndsted Nielsen,* Subhasis Panja, Jean Ann Wyer, and Henning Zettergren

Department of Physics and Astronomy, University of Aarhus, Ny Munkegade, DK-8000 Aarhus C, Denmark

Received May 28, 2008; E-mail: sbn@phys.au.dk

Heme proteins are readily identifiable from their characteristic UV/vis spectra (δ, Soret, Q_0, and Q_1 bands).[1–6] Spectral features depend on the iron oxidation state, peripheral substituents, axial ligands, coordination state, spin state, and nearby amino acid residues. Absorption spectroscopy is essential for comprehending the conformational changes that occur upon ligation or reduction/oxidation of the heme iron, and transient absorption is used extensively to monitor the dynamics of geminate recombination or larger protein conformational changes after, for example, photolysis of an iron-ligand bond.[6,7] Often heme or other biochromophores are located in hydrophobic protein pockets or crevices with minimum access to water. These pockets are in certain cases well simulated by a vacuum.[8] It requires gas-phase experiments to remove the influence of a nearby environment, determined by the protein folding state, from the inherent properties of the heme.

Here we report the absorption spectra in the Soret band region of isolated four-coordinate (4c) Fe(III)-heme$^+$ and five-coordinate (5c) Fe(III)-heme$^+$(His) ions in vacuo from action spectroscopy. Fe(III)-heme$^+$ refers to iron(III) coordinated by the dianion of protoporphyrin IX. We find that the absorption of the 5c complex is similar to that of 5c metmyoglobin variants with hydrophobic binding pockets except for an overall blueshift of about 16 nm. In the case of 4c iron(III), the Soret band is similar to that of 5c iron(III) but much narrower. To our knowledge this is the first unequivocal spectroscopic characterization of 4c ferric heme.

Spectroscopy studies on gaseous heme$^+$ ions are sparse and include the absorption spectrum in the Q-band region of Fe(III)-heme$^+$(DMSO)[9] and a recent vibrational characterization of Fe(III)-heme$^+$(NO) and Fe(III)-heme$^+$(imidazole).[10]

In the present work, Fe(III)-heme$^+$ ions were formed by electrospray of hemin chloride in methanol and CH_2Cl_2 (1:1), and to produce the histidine-coordinated complex, histidine was added to the solution. Ions were thermalized in a 22-pole ion trap with helium buffer gas at room temperature, accelerated as an ion bunch to 22-keV kinetic energies, mass-to-charge (m/z) selected by a magnet, and injected into the electrostatic ion storage ring in Aarhus, ELISA (Figure 1).[8,11] In one experiment, the magnet was set to allow only heme$^+$ ions of m/z 616 to enter the ring and in a second experiment, only heme$^+$(His) ions of m/z 771. This mass selection assured that we had the appropriate ions in the ring. After storage in the ring for 35 ms, the ions were irradiated with light from a pulsed tunable EKSPLA laser at one side of the ring. The width of the laser pulse was about 3.2 ns, and wavelengths were scanned from 330 to 419 nm. Absorption of light leads to vibrationally hot ions, and in separate experiments it was observed that these ions decay primarily by loss of CH_2COOH from heme$^+$ and by loss of His from heme$^+$(His).[12] For absorption spectroscopy, neutrals formed in the side opposite to the photoexcitation region were measured in a microchannel plate detector. Delayed dissociation occurred on a microsecond to millisecond time scale (Figure 2), as has been discussed earlier in the case of protoporhyrin ions.[13] A signal proportional to the absorption cross section was obtained as the yield of neutrals divided by the number of photons in the pulse and normalized to the neutrals yield from residual gas collisions (action spectroscopy). The spectra were the same whether only the first laser peak or the first 10 (see Figure 2) were used, which indicates that the change of dissociation lifetimes with excitation wavelength can be neglected.

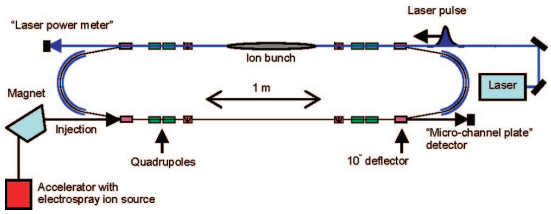

Figure 1. The electrostatic ion storage ring in Aarhus, ELISA, in combination with a laser system. The photofragment yield was obtained as a function of wavelength from the signal of neutrals hitting the detector.

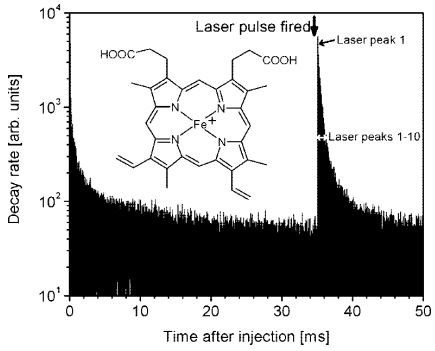

Figure 2. Decay spectrum of Fe(III)-heme$^+$. The high number of neutrals detected immediately after injection is due to metastable ions that have been excited during extraction from the ion trap. After a few milliseconds the signal is dominated by collisional decay in the ring. The pressure was of the order of 10^{-11} mbar. After 35 ms the ions were photoexcited with 390-nm light, which resulted in a large number of neutrals from delayed dissociation. The revolution time of the ions in the ring was 100 μs. The photo yield was obtained from summation over the first 10 laser peaks, indicated by the white double-headed arrow.

In Figure 3 we present the absorption spectra in the Soret band region of Fe(III)-heme$^+$ and Fe(III)-heme$^+$(His). The isolated five-coordinate complex displays a broad absorption band with a maximum at 379 nm, and a pronounced shoulder on the high energy side, which

XIII

10.1021/ja803460c CCC: $40.75

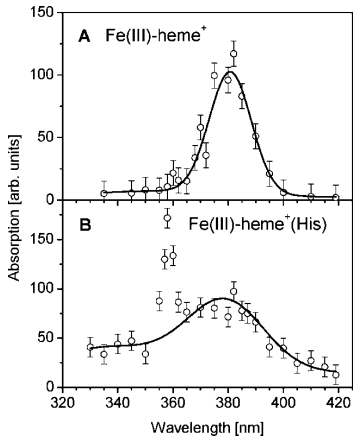

Figure 3. Absorption spectra of four-coordinate Fe(III)-heme$^+$ (A) and five-coordinate Fe(III)-heme$^+$(His) (B) in vacuo.

is likely due to ligand-to-metal charge transfer (LMCT) transitions. The sharp peak at ca. 358 nm is either due to resonant excitation of the ν_4 porphyrin breathing mode[2] or to a different laser beam profile at this wavelength, which has a better overlap with the ion beam. Ignoring this band, the spectrum is similar in shape to that of 5c high-spin Fe(III)-heme in metmyoglobin variants in which the distal histidine is replaced by a nonpolar residue thereby preventing water taking up the available sixth coordinate site.[14] Such protein variants have maximum absorption at about 395 nm, a redshift of 16 nm compared to the isolated complex. According to protein X-ray crystallography, the iron is displaced out of the plane of the porphyrin macrocycle by 0.28 Å to maximize chemical bonding with the histidine.[14a] It should be noted that the propionic acid side chains are ionized in the protein in contrast to the gas-phase species. The spectrum is also similar to that of the adduct between 1,2-dimethyl-imidazole and ferric heme embedded in SDS (sodium dodecyl sulfate) micelles where the maximum is at 400 nm.[15] The environment within the micelle mimics the hydrophobic cavity of heme proteins.

The bare Fe(III)-heme$^+$ absorbs maximally at about 381 nm (Figure 3) like Fe(III)-heme$^+$(His). However, the shoulder toward low wavelengths is absent, and the spectrum appears to be narrower with a full width at half-maximum of 20 nm. This overall change in band shape is linked to the new electronic structure of the heme when the iron occupies the central hole of the porphyrin ring (planar heme). Density functional theory calculations have revealed that the ground-state is a quartet state.[16] For comparison, six-coordinate Fe(III)-heme is either low-spin or high-spin, depending on the axial ligands.[17] Again an indication of a sharp peak at 360 nm is observed. In recent work, Fang et al.[18] synthesized a highly sterically hindered bis-pocket siloxyl Fe(III) porphyrin that is four-coordinate with maximum absorption at 400 nm, red-shifted by 20 nm relative to the gas-phase heme species.

Previous spectroscopic characterization of 4c ferric heme by conventional methods was hampered by the strong affinity of Fe(III) for water and anions. Four-coordinate Fe(III)-heme in Aplysia myoglobin at low pH (<5) was inferred by Giacometti et al.[19] but later abandoned based on resonance Raman experiments.[20] A change in absorption at low pH may be ascribed to both a change in the heme coordination state and its environment due to conformational changes and denaturation. Such problems in the interpretation of absorption spectra are not encountered in gas-phase experiments where ions of interest are selected according to their mass-to-charge ratio by mass spectrometry, and the environment around the heme can be gradually built up in a controlled manner.

Spectroscopic studies on methemalbumin by Kamal and Behere[21] suggest that the heme in this case is devoid of a well-defined heme cavity and that it does not bind to histidine but to a surface residue. The Soret maximum is at 404 nm, and the band is associated with a shoulder to lower wavelengths. A comparison with our absorption spectra indeed supports the assignment of 5c Fe(III)-heme.

In conclusion, our work provides a prediction of the change in absorption of a 5c ferric heme protein upon histidine deligation, namely a sharpening of the band but with a minimal change in the wavelength of maximum absorption. Acid-induced rupture of the iron−histidine bond due to histidine protonation[22] or local heating after multiple photon absorption are possible paths for lowering the coordination state. The spectra also serve as a benchmark for quantum chemistry calculations of excited states.

Acknowledgment. This work was supported by FNU (grant no. 21-04-0514 and no. 272-06-0427), Carlsbergfondet (2006-01-0229), and Lundbeckfonden. S.B.N. would like to thank Profs. T.G. Spiro and J.U. Andersen for enlightening discussions.

References

(1) Eaton, W. A.; Hochstrasser, R. M. *J. Chem. Phys.* **1967**, *46*, 2533.
(2) (a) Spiro, T. G.; Strekas, T. *J. Am. Chem. Soc.* **1974**, *96*, 338. (b) Spiro, T. G.; Burke, J. M. *J. Am. Chem. Soc.* **1976**, *98*, 5482. (c) Spiro, T. G.; Stong, J. D.; Stein, P. *J. Am. Chem. Soc.* **1979**, *101*, 2648.
(3) Edwards, L.; Dolphin, D. H.; Gouterman, M.; Adler, A. D. *J. Mol. Spectrosc.* **1971**, *38*, 16.
(4) Makinen, M. W.; Churg, A. K. Structural and Analytical Aspects of the Electronic Spectra of Hemproteins. In *Iron Porphyrins, Part I*; Lever, A. B. P., Gray, H. B., Eds.; Addison-Wesley Publishing Company, Inc.: Reading, MA, 1983; Chapter 3.
(5) Reynolds, M. F.; Parks, R. B.; Burstyn, J. N.; Shelver, D.; Thorsteinsson, M. V.; Kerby, R. L.; Roberts, G. P.; Vogel, K. M.; Spiro, T. G. *Biochemistry* **2000**, *39*, 388.
(6) Nienhaus, K.; Nienhaus, G. U. *Methods Mol. Biol.* **2005**, *305*, 215.
(7) (a) Petrich, J. W.; Lambry, J. C.; Kuczera, K.; Karplus, M.; Poyart, C.; Martin, J. L. *Biochemistry* **1991**, *30*, 3975. (b) Lambright, D. G.; Balasubramanian, S.; Boxer, S. G. *Chem. Phys.* **1991**, *158*, 249. (c) Konermann, L.; Rosell, F. I.; Mauk, A. G.; Douglas, D. J. *Biochemistry* **1997**, *36*, 6448. (d) Franzen, S.; Boxer, S. G. *J. Biol. Chem.* **1997**, *272*, 9655. (e) Puranik, M.; Nielsen, S. B.; Youn, H.; Bourassa, J. L.; Case, M. A.; Hvitved, A. N.; Tengroth, C.; Balakrishnan, G.; Thorsteinsson, M. V.; Olson, J. S.; Roberts, G. P.; Groves, J. T.; McLendon, G. L.; Spiro, T. G. *J. Biol. Chem.* **2004**, *279*, 21096.
(8) Brøndsted Nielsen, S.; Lapierre, A.; Andersen, J. U.; Pedersen, U. V.; Tomita, S.; Andersen, L. H. *Phys. Rev. Lett.* **2001**, *87*, 228102.
(9) Nonose, S.; Tanaka, H.; Okai, N.; Shibakusa, T.; Fuke, K. *Eur. Phys. J. D.* **2002**, *20*, 619.
(10) Chiavarino, B.; Crestoni, M. E.; Fornarini, S.; Lanucara, F.; Lemaire, J.; Maître, P.; Scuderi, D. *ChemPhysChem.* **2008**, *9*, 826.
(11) (a) Møller, S. P. *Nucl. Instrum. Methods Phys. Res. Sect. A* **1997**, *394*, 281. (b) Andersen, J. U.; Hvelplund, P.; Brøndsted Nielsen, S.; Tomita, S.; Wahlgreen, H.; Møller, S. P.; Pedersen, U. V.; Forster, J. S.; Jørgensen, T. J. D. *Rev. Sci. Instrum.* **2002**, *73*, 1284. (c) Brøndsted Nielsen, S.; Andersen, J. U.; Forster, J. S.; Hvelplund, P.; Liu, B.; Pedersen, U. V.; Tomita, S. *Phys. Rev. Lett.* **2003**, *91*, 048302.
(12) Støchkel, K.; Kadhane, U.; Andersen, J. U.; Holm, A. I. S.; Hvelplund, P.; Kirketerp, M.-B. S.; Larsen, M. K.; Lykkegaard, M. K.; Brøndsted Nielsen, S.; Panja, S.; Zettergren, H. *Rev. Sci. Instrum.* **2008**, *79*, 023107.
(13) Calvo, M. R.; Andersen, J. U.; Forster, J. S.; Hvelplund, P.; Brøndsted Nielsen, S.; Pedersen, U. V.; Rangama, J.; Tomita, S. *J. Chem. Phys.* **2004**, *120*, 5067.
(14) (a) Bogumil, R.; Maurus, R.; Hildebrand, D. P.; Brayer, G. D.; Mauk, A. G. *Biochemistry* **1995**, *34*, 10483. (b) Cao, W.; Christian, J. F.; Champion, P. M.; Rosca, F.; Sage, J. T. *Biochemistry* **2001**, *40*, 5728.
(15) Boffi, A.; Das, T. K.; della Longa, S.; Spagnuolo, C.; Rousseau, D. L. *Biophys. J.* **1999**, *77*, 1143.
(16) (a) Charkin, O. P.; Klimenko, N. M.; Nguyen, P. T.; Charkin, D. O.; Mebel, A. M.; Lin, S. H.; Wang, Y.-S.; Wei, S.-C.; Chang, H.-. *Chem. Phys. Lett.* **2005**, *415*, 362. (b) Siu, C.-K.; Guo, Y.; Hopkinson, A. C.; Siu, K. W. M. *J. Phys. Chem. B* **2006**, *110*, 24207.
(17) Sun, J.; Loehr, T. M.; Wilks, A.; Ortiz de Montellano, P. R. *Biochemistry* **1994**, *33*, 13734.
(18) Fang, M.; Wilson, S. R.; Suslick, K. S. *J. Am. Chem. Soc.* **2008**, *130*, 1134.
(19) (a) Giacometti, G. M.; Ascenzi, P.; Bolognesi, M.; Brunori, M. *J. Mol. Biol.* **1981**, *146*, 363. (b) Giacometti, G. M.; Ascenzi, P.; Brunori, M.; Rigatti, G.; Giacometti, G.; Bolognesi, M. *J. Mol. Biol.* **1981**, *151*, 315.
(20) Rousseau, D. L.; Ching, Y.; Brunori, M.; Giacometti, G. M. *J. Biol. Chem.* **1989**, *264*, 7878.
(21) Kamal, J. K. A.; Behere, D. V. *J. Biol. Inorg. Chem.* **2002**, *7*, 273.
(22) Sage, J. T.; Morikis, D.; Champion, P. M. *Biochemistry* **1991**, *30*, 1227.

JA803460C

Photodissociation of Isolated Ferric Heme and Heme-His Cations in an Electrostatic Ion Storage Ring

Morten Køcks Lykkegaard, Henning Zettergren, Maj-Britt Suhr Kirketerp, Anneli Ehlerding, Jean Ann Wyer, Umesh Kadhane, and Steen Brøndsted Nielsen*

Department of Physics and Astronomy, University of Aarhus, Ny Munkegade, DK-8000 Aarhus C, Denmark

Received: October 31, 2008; Revised Manuscript Received: December 10, 2008

Photodissociation of isolated Fe(III)-heme$^+$ and Fe(III)-heme$^+$(His) ions in the gas phase has been investigated using an electrostatic storage ring. The experiment provides three pieces of information, namely fragmentation channels, dissociation times, and absorption spectra. After photoexcitation with either 390 or 532 nm light, we find that the fragmentation takes place on a microsecond to millisecond time scale, and the channels are CH_2COOH loss (β-cleavage reaction) and histidine loss from Fe(III)-heme$^+$ and Fe(III)-heme$^+$(His), respectively. These channels were also observed by means of collision-induced dissociation. Significant information on the nonradiative processes that occur after photoexcitation was revealed from the decay spectra. At early times (first two to three milliseconds), the decay of the photoexcited ions is well-described by a statistical model based on an Arrhenius-type expression for the rate constant. The activation energy and preexponential factor are 1.9 ± 0.2 eV and 1×10^{17} to 1×10^{21} s^{-1} for heme$^+$ and 1.4 ± 0.2 eV and 1×10^{16} to 1×10^{19} s^{-1} for heme$^+$(His). Decay on a longer time scale was also observed and is ascribed to the population of lower-lying states with higher spin multiplicity because intersystem crossing back to the electronic ground-state is a bottleneck for the dissociation. The measurements give lifetimes for these lower-lying states of about 10 ms after 390 nm excitation and we estimate the probability of spin flip to be 0.3 and 0.8 for heme$^+$ and heme$^+$(His), respectively.

Introduction

Metalloporphyrins are ubiquitous in nature and are responsible for key biological processes such as photosynthesis, oxygen transport and storage, and sensing.[1−3] They have strong absorption bands in the 380−450 nm (Soret band) and 500−600 nm (Q-band) regions due to $\pi-\pi^*$ transitions in the porphyrin ring. The electronic structure is strongly determined by the presence of a metal and its oxidation and spin state, axial ligands, peripheral substituents, and nearby amino acid residues. One class of metalloporphyrins is heme complexes in which iron is situated in the center of a porphyrin ring. These are found in a number of proteins, the most well-known being myoglobin and hemoglobin.

To elucidate the influence of a protein environment, e.g., nearby amino acid side chains, or water on the photophysics of porphyrins and metalloporphyrins, it is important to study isolated species in the gas phase. In addition, such results are necessary to benchmark excited states calculations, typically carried out on small model systems. Neutrals that are easy to evaporate have been studied extensively by spectroscopic methods[2,4] but there is limited experimental work on ions.[5−7] The latter is somewhat difficult because of a low number of absorbing species and the requirement of special instrumentation.

For gas-phase spectroscopy experiments on ions, we have developed a technique that combines an electrostatic storage ring with an electrospray ion (ESI) source and a tunable pulsed laser system. Daughter ion mass spectroscopy has been made possible by the implementation of pulsed power supplies with microsecond response times for all of the ring elements.[8] The ion current is typically 0.1 pA and with a repetition rate of 10 Hz of the experiment, the number of ions per injection is 1×10^5 when all ions are accumulated in a pretrap. This number is too low to cause a measurable change in the number of photons in the laser pulse, and instead we rely on the detection of ionic fragmentation (i.e., action spectroscopy). The setup allows us to obtain three important pieces of information: ion lifetimes, dissociation channels, and absorption spectra. The advantage of using ESI is that the environment around the chromophore, e.g., heme, can gradually be built up by fine-tuning the source conditions or changing the solution used for electrospraying.

In a recent communication, we reported the absorption spectra of isolated Fe(III)-heme$^+$ and Fe(III)-heme$^+$(His) ions (Figure 1) that provide spectroscopic marker bands in the Soret band region for four-coordinate and five-coordinate heme ions.[9] Here, we follow up on this work but now with emphasis on the dissociation kinetics and fragmentation channels that were only briefly discussed in the previous work. High-energy collision-induced dissociation (CID) experiments were performed at an accelerator mass spectrometer for comparison with the photodissociation mass spectra. Finally, quantum chemical modeling was done to aid in the interpretation of the experimental results.

Experimental Section

CID Experiments. Hemin (Fe(III)-protoporphyrin chloride) was dissolved in CH_2Cl_2/methanol (1:1) to produce heme cations by electrospray ionization.[5] To produce heme$^+$(His) ions, we added histidine to the spray solution. Following ionization, the ions were accelerated to 50 keV kinetic energies, and ions with the m/z of interest were selected by a magnet. After collisions with He, the product ions were measured by an electrostatic analyzer that scanned the kinetic energy of the fragment ions. This resulted in mass-analyzed ion kinetic energy (MIKE)

* Corresponding author. E-mail: sbn@phys.au.dk.

10.1021/jp809626v CCC: $40.75
Published on Web 01/30/2009

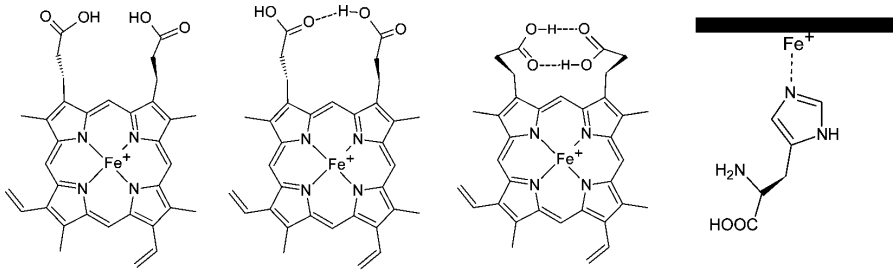

Figure 1. Three structures of Fe(III)-heme$^+$ that differ in the number of hydrogen bonds between the two propionic acid groups (**1**−**3**). The iron atom in Fe(III)-heme$^+$(His) is moved slightly out of the heme plane (black bar) (**4**).

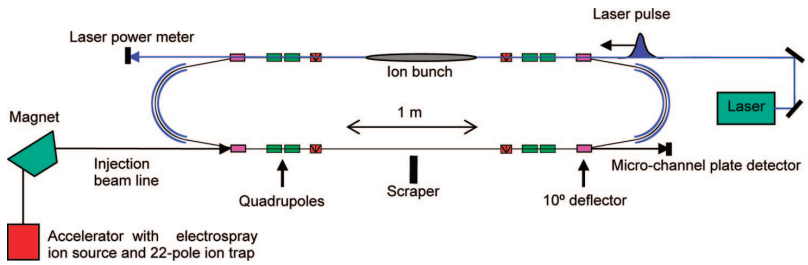

Figure 2. Electrostatic ion storage ring in Aarhus (ELISA) in combination with an ESI source and a laser. The circumference of the ring is 8.3 m. See text for details.

spectra from which the fragment ion masses were identified. More details on the instrumental setup can be found in ref 10.

Storage Ring Experiments. Ions produced by electrospray ionization were accumulated in a 22-pole ion trap in which they were thermally equilibrated with room temperature He gas for 0.1 s. The ion bunch was accelerated to 22 keV, and ions of interest were mass selected before entering ELISA (Figure 2).[8,11] In the ring, the ions have revolution times of ∼100 μs, depending on their mass. After 35 ms of storage time, the bunch was irradiated with light from a pulsed, tunable EKSPLA laser. The laser output is synchronized with the ion trap (10 Hz), and in these experiments we used wavelengths in the 330−532-nm range. Photon absorption led to dissociation into fragment ions and neutral molecules. Neutrals produced on the injection side of the ring were detected with a multichannel plate (MCP) detector. To reach this detector, the ions must survive about half a revolution in the ring (∼50 μs) because ELISA in normal operating mode does not allow fragment ions with lower kinetic energies than that of the parent ion to be stored.

A mass spectrum of the fragment ions was obtained from a quick switch of all ring voltages (within a few microseconds) directly after photoexcitation of the parent ions to store daughter ions with the proper kinetic energy. Daughter ions took about 40 revolutions in the ring before they were dumped on the MCP detector by a fast grounding of the 10° deflector in front of the detector. In other experiments, photoexcited ions were allowed to circulate for ∼100 μs before their fragmentation was monitored. To improve the resolution of the daughter ion mass spectra, a beam scraper on the injection side of the ring was put in to cut off some high energy beam trajectories (see Figure 2).

Computational Details. Calculations were carried out with the GAUSSIAN 03 program package.[12] The geometries of heme$^+$, heme$^+$(His), and smaller fragments were optimized at the B3LYP/6−31G(d) level of theory. Vibrational frequencies were calculated to verify that the stationary points are local minima and not transition states, and frequencies were also used in the calculation of heat capacities for decay modeling. Reaction energies were all corrected for zero-point vibrational energies.

Results and Discussion

First, we consider the results from quantum chemical modeling on heme$^+$ and heme$^+$(His). The electronic ground-state of heme$^+$ was found to be a quartet state in accordance with earlier reports.[13,14] In the case of heme$^+$(His), the quartet electronic state is also lower in energy than doublet and sextet states.

A closer look at the optimized structures reveals that the iron atom in heme$^+$ is located in the plane as opposed to the heme$^+$(His) structure where the iron is displaced a few tenths of an Ångström out of the porphyrin plane to maximize chemical bonding with the histidine. Three different calculated structures of heme$^+$ have been discussed in the literature, and they differ in the number of hydrogen bonds between the two propionic groups, 0, 1, and 2, denoted as structures **1**, **2**, and **3** in Figure 1. We have found that **2** is lower in energy than **1** by 0.3 eV at the B3LYP/6−31G(d) level of theory which is consistent with B3LYP/6−31++G(d,p) calculations by Siu et al.[14] They also found that **3** is lower in energy than **2** by 0.03 eV, but this structure is likely to be entropically disfavored.

The high-energy CID-MIKE spectra of heme$^+$ and heme$^+$(His) after collisions with He are shown in Figure 3. The dominant dissociation channel of heme$^+$ is β-cleavage, which results in loss of one or two CH_2COOH (CMe) groups, each of mass 59. This is in accordance with previous experimental[5,15] and theoretical reports[13] in the literature where β-cleavage is shown to be the lowest energy channel for fragmentation. The other peaks are assigned to loss of one or more side chains of CH_3 (15), $CHCH_2$ (27), COOH (45), CH_2COOH (59) and CH_2CH_2COOH (73) (mass). It is evident from the heme$^+$(His) CID-MIKE spectrum that the dominant dissociation channel is loss of the His ligand of mass 155, which is expected because

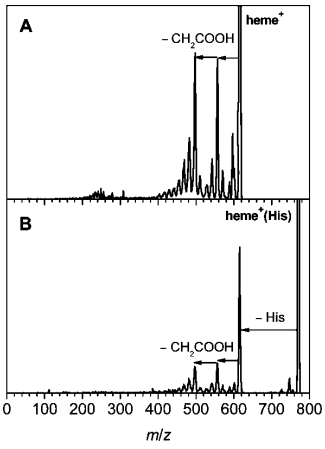

Figure 3. MIKE spectra obtained from collisions between (A) helium and heme$^+$ (*m*/*z* 616) and (B) helium and heme$^+$(His) (*m*/*z* 771).

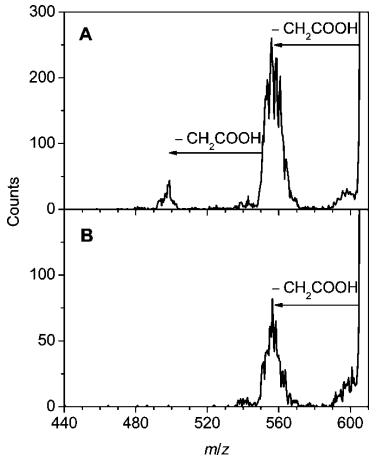

Figure 4. Fragmentation spectra for heme$^+$ acquired (A) at ELISA immediately after photoexcitation with 532 nm light and (B) after storage of the photoexcited ions for one revolution (100 μs).

histidine is bound noncovalently to the iron atom. Earlier multiphoton IR photodissociation experiments on heme$^+$(imidazole) also revealed that imidazole is lost most readily.[7] Significant losses of one or two CMe groups are also seen in the MIKE spectrum. These CID spectra are to be compared with the photodissociation mass spectra taken at ELISA.

Daughter ion mass spectra recorded right after 532-nm photoexcitation of heme$^+$ ions and after a delay of 100 μs are shown in Figure 4. Similar spectra were obtained after 390 nm light absorption (spectra not shown). The resolution is poor ($\Delta m/m \approx 100$) but high enough for identifying the fragment ions from a comparison with the CID spectrum. In the 532 nm spectrum associated with rapid dissociation, 0−20 μs, (cf., Figure 4A), there are two prominent peaks that are due to loss of one or both CMe groups. Two minor peaks are assigned to ions that have lost either H_2O or CH_2CH_2COOH. Delayed dissociation (Figure 4B) also resulted in loss of CMe, H_2O, and CH_2CH_2COOH, whereas a peak due to loss of two CMe groups is absent.

We ascribe the loss of two CMe groups to two-photon absorption because no or few such highly excited ions are

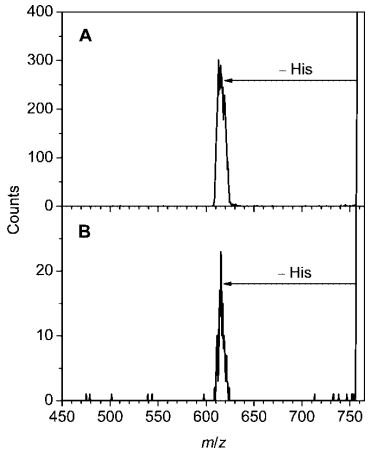

Figure 5. Fragmentation spectra for heme$^+$(His) acquired at ELISA (A) immediately after photoexcitation with 532 nm light and (B) after storage of the photoexcited ions for one revolution (112 μs).

expected to survive the 100 μs delay. This interpretation is in accordance with calculations because one 532 nm photon (2.33 eV) does not possess enough energy to cause two successive β-cleavages. Prior to photon absorption, the ions have an average internal energy of 1.04 eV based on B3LYP/6−31G(d)-calculations of vibrational frequencies and assuming a temperature of 300 K in the ion trap. Hence, after 532 nm photon absorption, the internal energy of the ions is predicted to be 3.37 eV. This is enough for one β-cleavage, calculated to require 2.49 eV (for structure **2**), but not enough for two. Charkin et al.[13] calculated the energies for loss of one and two CMe groups from structure **1** to be 1.80 and 2.41 eV, respectively, and thus the total energy needed to break both bonds must be at least 4.21 eV, which is more than the calculated internal energy of 3.37 eV. At the B3LYP/6−31G(d) level of theory we find the required energy to be 2.20 eV for loss of one CMe from **1**, 0.4 eV more than Charkin et al.

The peak close to the parent ion may be due to either loss of CH_3 or H_2O. However, we calculated that it requires 4.7 eV to lose CH_3, which is in fair agreement with calculations by Charkin et al.,[13b] and therefore this channel is not open upon one-photon absorption. Instead, we find that H_2O loss from propionic acid only requires 1.8 eV, significantly less than the internal energy of 3.37 eV, not considering the barrier to the reaction.

As in the case for heme$^+$, we found similar fragmentation patterns for heme$^+$(His) after both 390 and 532 nm excitation. The only peak observed was due to loss of histidine (Figure 5). We have calculated the dissociation energy for this process to be 1.18 eV. The average energy prior to excitation is 1.36 eV while after 532 nm light absorption, it is 3.69 eV. Dissociation results in ions with too little excess energy to dissociate further on the time scale of the experiment.

Next, we present the results from lifetime experiments in which the yield of neutrals was measured as a function of time after injection of the ions into the ring. Decay spectra are shown for heme$^+$ and heme$^+$(His) in Figure 6. The high yield of neutrals seen immediately after injection is due to metastable ions that were excited during extraction from the ion trap because of collisions with He buffer gas. However, after some milliseconds the decays were dominated by collisions with residual gas in the ring. After 35 ms, the ions were irradiated by 390 nm light, which resulted in an increased yield of neutrals.

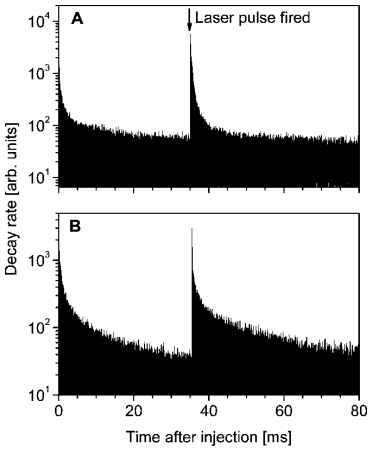

Figure 6. Decay spectra of (A) heme$^+$ and (B) heme$^+$(His). A laser pulse (390 nm photons) was fired after 35 ms.

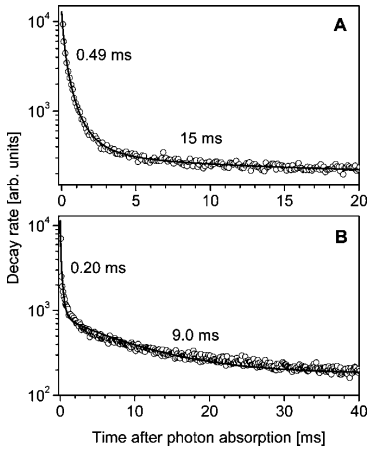

Figure 7. Decay spectra obtained after irradiation of (A) heme$^+$ and (B) heme$^+$(His) with 390 nm light. The spacing of the points is 100 and 112 μs, respectively, which is the revolution time in the ring. The given numbers are the lifetimes.

To describe the observed decays after laser excitation, we use a previously applied model in which the rate constant k is represented by an Arrhenius-like expression[16−18]

$$k(T) = A\exp\left[\frac{-E_a}{k_B(T - E_a/2C)}\right] \quad (1)$$

where T is the microcanonical temperature, C the microcanonical heat capacity, k_B the Boltzmann constant, A the preexponential factor, E_a the activation energy, and $E_a/2C$ is the so-called finite heat-bath correction to the temperature. The average internal energy of the ions before laser excitation was evaluated from an independent harmonic oscillator model with vibrational frequencies obtained from Gaussian calculations. The microcanonical heat capacity C is obtained as the derivative of the microcanonical energy with respect to temperature. The temperature distribution of the ions, $g(T)$, is established in the ion trap and is of the Maxwell−Boltzmann type but is for simplicity approximated by a Gaussian. A final expression for the decay rate of ions in ELISA is then given by

$$I(t) = \int k(T)g(T)\exp[-k(T)t]\,dT \quad (2)$$

The decay of heme$^+$ ions after 390 nm light absorption (Figure 7A) is well-described by eq 2 for the earlier part of the decay, but an additional exponential is required to account for decay at longer times. This analysis gives dissociation lifetimes of 0.49 ± 0.10 ms and 15 ± 5 ms. The first time constant is associated with a preexponential factor A of 1×10^{17} to 1×10^{21} s^{-1} and an Arrhenius activation energy E_a of 1.9 ± 0.2 eV for the β-cleavage reaction. For a simple dissociation reaction, a minimum for the preexponential factor is the transition state constant k_BT/h,[19] where h is Planck's constant. The calculated temperature of heme$^+$ after 390 nm excitation is 648 K and k_BT/h is therefore 1.4×10^{13} s^{-1}. This number is lower than A, which indicates that an increase in entropy is also a driving force for the dissociation reaction.

For heme$^+$(His) (Figure 7B), we have used the same approach and find a preexponential factor of 1×10^{16} to 1×10^{19} s^{-1} and an activation energy of 1.4 ± 0.2 eV for histidine loss, close to the calculated dissociation energy of 1.2 eV. The fit provides two lifetimes of 0.20 ± 0.07 ms and 9 ± 4 ms.

The short lifetime components of sub-milliseconds are the result of internal conversion from the excited state to the electronic ground state with subsequent dissociation of vibrationally excited ions. Here the dissociation itself is the rate-limiting step. The fact that we need an additional exponential with a long lifetime of milliseconds to describe both decays properly is ascribed to a bottleneck for dissociation. Instead of internal conversion directly to the ground state, the ions may undergo intersystem crossing to a lower-lying electronic state with a higher spin. Another spin flip is required to reach the electronic ground state, which is considered to be the rate-limiting step. Thus the ions will eventually relax to the ground-state but with a much smaller rate constant than that for the subsequent dissociation reaction. The second part of the decay is not fully described by an exponential, which is due to the spread in internal energy. It appears here that quite a large fraction of the ions has undergone intersystem crossing, and similar findings were earlier reported for porphyrin ions.[18] We estimate the probability of spin flip after 390 nm excitation from the branching ratio between the two decay channels and found it to be 0.3 ± 0.1 and 0.8 ± 0.1 for heme$^+$ and heme$^+$(His), respectively. The difference is likely due to the withdrawal of the iron atom out of the ring by the histidine ligand thereby affecting the electronic structure of the porphyrin ring. We stress that these values are upper limits for the spin flip probabilities because luminescence has been neglected in the analysis.

To fit the experimental data, our initial guesses for the activation energies were the calculated bond energies of 2.49 eV (for structure **2**) and 1.18 eV (structure **4**). These values should in principle give lower limits for the activation energy. However, an acceptable fit to the various heme$^+$ data based on an E_a of 2.49 eV could not be made. A lower value of 1.9 eV was required to account for the tailing at longer times, which suggests that the ions dissociate from structure **1**.

The time scale for histidine deligation is a lower limit when the Fe(III)-heme$^+$ is located in a protein cavity since heat diffusion to the surroundings will occur. The time constant for vibrational cooling is ∼4 ps in the case of horse heart cytochrome c as reported by Negrerie et al.[20] on the basis of time-resolved spectroscopy measurements. Indeed, the same authors also report that photodissociation of axial ligands does not occur from ferric heme in this protein in full agreement with the hundred microsecond time scale for dissociation

reported here. The ground-state population was recovered within 20 ps, which was explained by immediate return of photoexcited heme into the hot ground state with subsequent vibrational cooling.[20] In other work, electronic relaxations involving excited states of various origins have been inferred.[21−23] If decay on the millisecond time scale in our experiment is correctly interpreted to be due to trapping in a particular long-lived excited state, it implies that a protein microenvironment provides a doorway to the deexcitation pathway or that it quickly quenches excited states. This issue is to be explored in the future by gradually building the natural heme environment.

Conclusions

In summary, we have used an electrostatic storage ring in combination with a laser to obtain information on the fragmentation channels and dissociation lifetimes of photoexcited Fe(III)-heme$^+$ and Fe(III)-heme$^+$(His) cations. For both ions, dissociation takes place on a microsecond to millisecond time scale, and the main channels are ascribed to loss of CH_2COOH and histidine, respectively. To account for the total decay of ions, both statistical decay and decay delayed by the population of states with different electronic spin has to be included. The time resolution of storage ring experiments is well-suited to disentangling the importance of such competing processes.

Acknowledgment. We thank Prof. Jens Ulrik Andersen for fruitful discussions on the decay modeling. S.B.N. gratefully acknowledges support from the Danish Natural Science Research Council (Grant 272-06-0427), Carlsbergfondet (Grant 2006-01-0229), Villum Kann Rasmussen Fonden, Lundbeckfonden, and Dir. Ib Henriksens Fond.

References and Notes

(1) Berg, J. M.; Tymoczko, J. L.; Stryer L. *Biochemistry*, 6th ed.; W. H. Freeman and Company: New York, 2007.

(2) Makinen, M. W.; Churg, A. K. Structural and Analytical Aspects of the Electronic Spectra of Hemeproteins. In *Iron Porphyrins*; Lever, A. B. P., Gray, H. B., Eds.;; Addison-Wesley: Reading, MA, 1983; Part I.

(3) Kalyanasundaram, K. *Photochemistry of Polypyridine and Porphyrin Complexes*; Academic Press: London, 1997.

(4) Edwards, L.; Dolphin, D. H.; Gouterman, M.; Adler, A. D. *J. Mol. Spectrosc.* **1971**, *38*, 16.

(5) (a) Nonose, S.; Tanaka, H.; Okai, N.; Shibakusa, T.; Fuke, K. *Eur. Phys. J. D* **2002**, *20*, 619. (b) Nonose, S.; Iwaoka, S.; Tanaka, H.; Okai, N.; Shibakusa, T.; Fuke, K. *Eur. Phys. J. D* **2003**, *24*, 335. (c) Nonose, S.; Iwaoka, S.; Mori, K.; Shibata, Y.; Fuke, K. *Eur. Phys. J. D* **2005**, *34*, 315.

(6) (a) Goto, M.; Togawa, M.; Jinno, S.; Takao, T.; Matsumoto, J.; Shiromaru, H.; Achiba, Y.; Tanuma, H.; Azuma, T. *Chem. Phys. Lett.* **2008**, *460*, 46. (b) Goto, M.; Yasuda, Y.; Jinno, S.; Takao, T.; Hanada, K.; Tanuma, H.; Azuma, T.; Sugiura, K.-I.; Shiromaru, H.; Achiba, Y. *Eur. Phys. J. D* **2007**, *43*, 65.

(7) Chiavarino, B.; Crestoni, M. E.; Fornarini, S.; Lanucara, F.; Lemaire, J.; Maître, P.; Scuderi, D. *ChemPhysChem* **2008**, *9*, 826.

(8) Støchkel, K.; Kadhane, U.; Andersen, J. U.; Holm, A. I. S.; Hvelplund, P.; Kirketerp, M.-B. S.; Larsen, M. K.; Lykkegaard, M. K.; Brøndsted Nielsen, S.; Panja, S.; Zettergren, H *Rev. Sci. Instrum.* **2008**, *79*, 023107.

(9) Lykkegaard, M. K.; Ehlerding, A.; Hvelplund, P.; Kadhane, U.; Kirketerp, M.-B. S.; Brøndsted Nielsen, S; Panja, S.; Wyer, J. A.; Zettergren, H *J. Am. Chem. Soc.* **2008**, *130*, 11856.

(10) (a) Larsson, M. O.; Hvelplund, P.; Larsen, M. C.; Shen, H.; Cederquist, H.; Schmidt, H. T *Int. J. Mass Spectrom.* **1998**, *51*, 177. (b) Boltalina, O. V.; Hvelplund, P.; Jørgensen, T. J. D.; Larsen, M. C.; Larsson, M. O.; Sharoitchenko, D. A. *Phys. Rev. A* **2000**, *62*, 023202.

(11) (a) Møller, S. P. *Nucl. Instrum. Methods Phys. Res., Sect. A* **1997**, *394*, 281. (b) Andersen, J. U.; Hvelplund, P.; Brøndsted Nielsen, S.; Tomita, S.; Wahlgreen, H.; Møller, S. P.; Pedersen, U. V.; Forster, J. S.; Jørgensen, T. J. D *Rev. Sci. Instrum.* **2002**, *73*, 1284.

(12) Frisch, M. J.; Trucks, G. W.; Schlegel, H. B.; Scuseria, G. E.; Robb, M. A.; Cheeseman, J. R.; Montgomery, J. A.; Vreven, T.; Kudin, K. N.; Burant, J. C.; Millam, J. M.; Iyengar, J.; Tomasi, J.; Barone, V.; Mennucci, B.; Cossi, M.; Scalmani, G.; Rega, N.; Petersson, G. A.; Nakatsuji, H.; Hada, M.; Ehara, M.; Toyota, K.; Fukuda, R.; Hasegawa, J.; Ishida, M.; Nakajima, T.; Honda, Y.; Kitao, O.; Nakai, H.; Klene, M.; Li, X.; Knox, J. E.; Hratchian, H. P.; Cross, J. B.; Adamo, C.; Jaramillo, J.; Gomperts, R.; Strattman, R. E.; Yazyev, O.; Austin, A. J.; Cammi, R.; Pomelli, C.; Ochterski, J. W.; Ayala, P. Y.; Morokuma, K.; Voth, G. A.; Salvador, P.; Dannenberg, J. J.; Zakrzewski, V. G.; Apprich, S.; Daniels, A. D.; Strain, M. C.; Farkas, O.; Malick, D. K.; Rabuck, A. D.; Raghavachari, K.; Foresman, J. B.; Ortiz, J. V.; Cui, Q.; Baboul, A. G.; Clifford, S.; Cioslowski, J.; Stefanov, B. B.; Liu, G.; Liashenko, A.; Piskorz, P.; Komaromi, I.; Martin, R. L.; Fox, D. J.; Keith, T.; Al-Laham, M. A.; Peng, C. Y.; Nanayakkara, A.; Challacombe, M.; Gill, P. M. W.; Johnson, B.; Chen, W.; Wong, M. W.; Gonzalez, C.; Pople, J. A. *Gaussian 03, Revision B.05*; Gaussian, Inc.: Pittsburgh, PA, 2003.

(13) (a) Charkin, O. P.; Klimenko, N. M.; Nguyen, P. T.; Charkin, D. O.; Mebel, A. M.; Lin, S. H.; Wang, Y.-S.; Wei, S.-C.; Chang, H.-C. *Chem. Phys. Lett.* **2005**, *415*, 362. (b) Charkin, O. P.; Klimenko, N. M.; Charkin, D. O.; Chang, H.-C.; Lin, S.-H. *J. Phys. Chem. A* **2007**, *111*, 9207.

(14) Siu, C.-K.; Guo, Y.; Hopkinson, A. C.; Siu, K. W. M. *J. Phys. Chem. B* **2006**, *110*, 24207.

(15) Van Berkel, G. J.; McLuckey, S. A.; Glish, G. L. *Anal. Chem.* **1991**, *63*, 1098.

(16) Andersen, J. U.; Bonderup, E.; Hansen, K. *J. Chem. Phys.* **2001**, *114*, 6518.

(17) (a) Andersen, J. U.; Cederquist, H.; Forster, J. S.; Huber, B. A.; Hvelplund, P.; Jensen, J.; Liu, B.; Manil, B.; Maunoury, L.; Brøndsted Nielsen, S.; Pedersen, U. V.; Schmidt, H. T.; Tomita, S.; Zettergren, H *Eur. Phys. J. D* **2003**, *25*, 139. (b) Andersen, J. U.; Cederquist, H.; Forster, J. S.; Huber, B. A.; Hvelplund, P.; Jensen, J.; Liu, B.; Manil, B.; Maunoury, L.; Brøndsted Nielsen, S.; Pedersen, U. V.; Rangama, J.; Schmidt, H. T.; Tomita, S.; Zettergren, H *Phys. Chem. Chem. Phys.* **2004**, *6*, 2676. (c) Andersen, L. H.; Bluhme, H.; Boyé, S.; Jørgensen, T. J. D.; Krogh, H.; Nielsen, I. B.; Brøndsted Nielsen, S.; Pedersen, U. V.; Svendsen, A *Phys. Chem. Chem. Phys.* **2004**, *6*, 2617.

(18) (a) Calvo, M. R.; Andersen, J. U.; Hvelplund, P.; Brøndsted Nielsen, S.; Pedersen, U. V.; Rangama, J.; Tomita, S.; Forster, J. S *J. Chem. Phys.* **2004**, *120*, 5067. (b) Nielsen, C. B.; Forster, J. S.; Ogilby, P. R.; Brøndsted Nielsen, S. *J. Phys. Chem. A* **2005**, *109*, 3875.

(19) Laskin, J.; Futrell, J. H. *J. Phys. Chem. A* **2003**, *107*, 5836.

(20) Negrerie, M.; Cianetti, S.; Vos, M. H.; Martin, J.-L.; Kruglik, S. G. *J. Phys. Chem. B* **2006**, *110*, 12766.

(21) Petrich, J.; Poyart, C.; Martin, J. L. *Biochemistry* **1988**, *27*, 4049.

(22) Petrich, J. W.; Martin, J. L.; Houde, D.; Poyart, C.; Orszag, A. *Biochemistry* **1987**, *26*, 7914.

(23) Franzen, S.; Kiger, L.; Poyart, C.; Martin, J. L. *Biophys. J.* **2001**, *80*, 2372.

JP809626V

Absorption by DNA single strands of adenine isolated *in vacuo*: The role of multiple chromophores

L. M. Nielsen, S. Ø. Pedersen, M.-B. S. Kirketerp and S. Brøndsted Nielsen*

Department of Physics and Astronomy, Aarhus University, Ny Munkegade, DK-8000 Aarhus C, Denmark

DNA single strands of adenine, isolated as anions *in vacuo* and free of solvent were photodissociated in a storage ring, and absorption as a function of excitation wavelength was recorded. Action spectra are similar for all strands and closely resemble that of the monomer. However, for strands with 3 and 4 bases a small blueshift in the band maximum of about 3 nm is seen compared to the monomer spectrum which is a sign of exciton coupling between two stacked bases. At high photon energies, internal conversion competes with electron detachment even for dianions as revealed from the time spectra.

The damaging effects of solar UV light are reduced by the extraordinary photostability of DNA. This photoprotection is linked to the excited state physics of the bases. For nucleosides and nucleotides that contain a single base, internal conversion (IC) via conical intersections is ultrafast and within a few picoseconds the excess vibrational energy is dissipated to the solvent [1, 2]. The lifetime with respect to dissociation of isolated nucleotides *in vacuo* is long, on the order of microseconds [3], and hence vibrational cooling in solution is rapid enough to prevent dissociation. The photostability of individual DNA bases is considered a key factor for the evolution of life in the prebiotic era when the ozone layer had not yet developed. The situation is, however, much more complicated and less understood in complex DNA where several bases (multiple chromophores) interact through stacking and base pairing. New quantum states arise as linear combinations of single base wavefunctions which are denoted Frenkel excitons and represent coherent excitation of two or more bases. The spatial extent of the exciton and the quantum state dynamics is hotly debated [4-12]. This issue is not only relevant for photoprotection but also for the ability of DNA strands to conduct current since the strength of π-stacks and the presence of delocalized domains determine the efficiency of electron hopping over long distances [13].

The population of exciton states was for many years considered insignificant since the absorption spectra of DNA strands resemble those of single bases with no splitting of the band located at around 260 nm as was predicted by theory for exciton states [14]. Recent nontrivial calculations by Markovitsi and co-workers [7, 15] on model strands indicated, however, that the change in absorption induced by excitation to exciton states is to the blue since upper eigenstates carry high oscillator strengths but that the shift is small. Furthermore, individual strands in aqueous solution experience different microenvironments and therefore have different absorption spectra, which cause an inhomogeneous broadening that makes it even harder to use absorption spectroscopy to identify exciton states. To eliminate this complication, we investigated the

absorption by DNA strands isolated *in vacuo* free of solvent. The work presented here confirms that electronic communication between adenine bases causes only a small blueshift in the absorption.

The DNA strands chosen for study contained two, three and four adenine bases, denoted dA_2, dA_3, and dA_4, and are either singly or doubly negatively charged. The charge is carried by the phosphate groups. We also included the RNA mononucleotide, AMP (adenosine 5'-monophosphate), in our study for comparison. Gas-phase spectroscopy experiments were carried out in the electrostatic ion storage ring in Aarhus (ELISA, Fig. 1) [16, 17]. AMP was purchased from Sigma-Aldrich and dA_2, dA_3, and dA_4 from DNA Technology, Aarhus. Electrospray ionization of nucleotides in methanol solutions was used to produce the ions that were subsequently accumulated in a 22-pole ion trap and thermally equilibrated by collisions with a helium buffer gas therein. The ions were accelerated as an ion bunch to kinetic energies of 22 keV × charge state, and a bending magnet was used to select the appropriate ions according to their mass-to-charge (*m/z*) ratio. Following injection into the ring, the ions were stored for about 35 ms to allow for the decay of metastable ions before being irradiated by a nanosecond light pulse from a tunable EKSPLA laser. This is an Nd:YAG laser where the third harmonic (355 nm) pumps an optical parametric oscillator (OPO). The visible output from this OPO is frequency doubled in a crystal providing UV light. The repetition rate of the experiment was 10 Hz. Dissociation was as a result of either one-photon or two-photon absorption (*vide infra*). Lifetimes were obtained from measurements of the yield of neutrals hitting the microchannel plate (MCP) detector located at the end of the straight section opposite to the side where the photoexcitation was performed, that is, delayed dissociation was sampled. Ion revolution times were 75 μs, 96 μs, 119 μs, 139 μs, and 98 μs for AMP^- (*m/z* 345), dA_2^- (*m/z* 563), dA_3^- (876), dA_4^- (*m/z* 1189), and dA_4^{2-} (*m/z* 594), respectively. The pressure in the ring was about 10^{-10} mbar, which set an upper limit of several seconds on the storage time.

Since the experiments were done at room temperature, multiple conformers are present in the ion beam, and the absorption by all of these was sampled. Based on ion-mobility experiments and molecular modeling calculations, Bowers and co-workers [18] showed that the dA_2 dinucleotide monoanions rapidly interconvert between conformers belonging to two distinct families of conformations at room temperature, an "open" family in which the two bases are separated from each other and one in which the two bases are stacked. It was found that stacking interactions between adenine bases are more common than H-bonding and that the structure opens up with temperature. No structural data exist for the larger strands, but stacking interactions should become more and more important with increasing strand length. Exciton coupling is therefore expected to be strongest for dA_4. For dA_3 and dA_4, the negative charge carrier can be on different phosphate groups which results in different isomers.

The lifetime of photoexcited AMP^- is short; *e.g.* 16 μs after 266-nm excitation [3] and decreasing with shorter wavelengths. Time spectra of dA_n^- (n = 2, 3, 4), and dA_4^{2-} after 250-nm and 210-nm photoexcitation are shown in Figures 2 and 3. These provide information on the number of photons absorbed according to a similar analysis done earlier for protonated adenine strands [19]. The lifetime is shortest at the lowest wavelength for dA_2^- and dA_4^- as expected since more energy is deposited in the ions after photon absorption; in the case of dA_3^- and dA_4^{2-} it is difficult to make a clear conclusion due to poor data quality. It is also evident that at 250 nm the lifetime is longer for dA_2^- than for AMP^-, which is simply due to more degrees of freedom in the dinucleotide than in the mononucleotide. For AMP^- the dissociation is a result of one-photon absorption [3]; hence the longer lifetime of dA_2^- indicates that its dissociation is also due to one-photon absorption. On the other hand, the lifetime is shorter for dA_3^- than for dA_2^-, which is ascribed to the absorption of two photons. The lifetime is longer for dA_4^- than for dA_3^- and roughly the same as that for dA_2^-, and the dissociation of dA_4^- is taken to be due to the absorption of two photons. In summary, we ascribe the

decay of dA_2^- to one-photon absorption and of dA_3^-, dA_4^-, and dA_4^{2-} to two-photon absorption over the whole wavelength region.

In the case of AMP^- the count rates of photo-induced neutrals in the MCP detector measured half a turn after photoexcitation was divided by the background signal from residual gas collisions (proportional to the ion beam intensity) and the number of photons in the laser pulse at each excitation wavelength to provide action spectra (Fig. 4). The dissociation lifetime depends on the excitation wavelength but the dissociation times are too short to make meaningful corrections for this. Instead we explored the role of the actual time of irradiation; this was done by firing the laser pulse at two different times (see Fig. 1). From Fig. 4, it is clearly evident that the spectra depend on the delay between photoexcitation and the measurement of neutrals. If the delay is long, there is a discrimination against short wavelengths since a significant number of the photoexcited ions decay too quickly to make it to the other side of the ring. Hence for AMP^- it is difficult to establish any quantitative measure of the absorption band maximum and the band width. We will in the following instead compare with a previously published spectrum of 2'-deoxyadenosine-5'-monophosphate, $dAMP^-$, measured at a time-of-flight instrument by Weber and co-workers [20].

The lifetimes of photoexcited adenine strands were, on the other hand, long enough to allow for exponential fits to the data to obtain time constants. This allows us to obtain a value for the initial number of photoexcited ions at each excitation wavelength corrected for lifetime variations. The analysis is detailed in [21].

The action spectra of dA_2^-, dA_3^-, and dA_4^- are shown in Fig. 5; all ions have maximum absorption around 250-253 nm and similar band widths (25 – 28 nm). Importantly, the spectra are very similar to that of $dAMP^-$ [20] where the absorption band maximum is at 253 nm. However, it is evident that for dA_3^- and dA_4^- the absorption bands are slightly shifted to the blue; in the latter

case maximum absorption is at 250 nm. The reason for the dip in the centre of the dA_3^- spectrum is unclear. We note that the spectra are the result of absorption by both unstacked and stacked bases.

Calculations by Miyata and Yomosa [14] predicted base-base interactions to give tens of eV shifts in the absorption while recent calculations by Bouvier et al. [15] on $(dA)_{20}$:$(dT)_{20}$ duplexes indicated absorption blueshifts of less than 3 nm in the spectral region with respect to the absorption of the sum of the monomers. These calculations were for isolated systems and can therefore be directly compared to our experimental results where a blueshift of about 3 nm is observed due to base-base interactions, which supports the theoretical calculations by Bouvier et al.

The electronic properties of DNA depend on the presence of a water environment: The absorption spectrum of neutral adenine molecules in the gas phase is displaced toward the blue by about 10 nm compared to that of solvated adenine [22], a shift similar to that observed for the $dAMP^-$ and oligonucleotide anions. The difference in the absorption observed for bare ions and solvated ones is therefore mainly ascribed to interactions between the bases and water molecules and less to shielding of the negative charge by water solvation.

All dA_n^- ions also display an absorption band with a maximum below or close to 210 nm in accordance with solution phase spectra [9]. The actual band position and band width cannot be established in the gas phase experiment since the lower limit of our laser system is 210 nm. The adiabatic electron detachment energies are 5.55 eV, 5.72 eV, and 5.62 eV for dAMP, dA_2^-, and dA_3^- [23] which correspond to wavelengths of 224 nm, 217 nm, and 221 nm. Hence direct photodetachment is a possible process below the respective wavelengths, and the actual absorption is underestimated in our experiment. However, since delayed dissociation is measured for these ions after several microseconds, internal conversion to the electronic ground state can compete with coupling to continuum states.

The spectrum of the dA_4^{2-} dianion was also recorded (Fig. 6). It displays absorption to the blue of the monoanions with a maximum at about 245 nm, which seems to indicate stronger stacking interactions for the dianions. As discussed above the negative charge itself does not influence the absorption much. The actual spectral shape should, however, be taken with some caution: The dominant channel for multiply charged DNA strands is electron photodetachment [24-26], likely as autodetachment from excited states [26]. Also multiply charged DNA anions are often metastable with respect to electron loss [27, 28]. The detachment energy is smaller for the dianions than that for the monoanions, and hence the action spectrum based on measuring photo-neutrals may not represent the actual absorption spectrum. Also dianions may dissociate into two monoanions in a Coulomb explosion, and this process may be wavelength dependent. Still our data clearly show that internal conversion can again compete with electron detachment but it is uncertain how the relative importance of the two depends on excitation wavelength.

To summarize, while the absorption spectra of DNA nucleotides have earlier been published by Weber and co-workers, this is the first report of spectra of multi-base DNA anions. We find that base-stacking interactions cause a blueshift in the absorption but that this is small, in accordance with high level quantum chemical calculations. Our spectra serve as a benchmark for future theoretical modeling of complex multichromophore systems but also provide a basic understanding of the electronic coupling between bases free of solvent which is important in nanotechnology for the generation of nanowires based on DNA strands.

We gratefully acknowledge support from Lundbeckfonden and The Danish Council for Independent Research | Natural Sciences (#10-082088) and thank Prof. J.-M. Weber for making the dAMP spectral data available to us.

* sbn@phys.au.dk

[1] C. E. Crespo-Hernández, B. Cohen, P. M. Hare, and B. Kohler, Chem. Rev. **104**, 1977 (2004).

[2] C. T. Middleton, K. de La Harpe, C. Su, Y. K. Law, C. E. Crespo-Hernández, and B. Kohler, Annu. Rev. Phys. Chem. **60**, 217 (2009).

[3] S. Brøndsted Nielsen, J. U. Andersen, J. S. Forster, P. Hvelplund, B. Liu, U. V. Pedersen, and S. Tomita, Phys. Rev. Lett. **91**, 048302 (2003).

[4] C. E. Crespo-Hernández, B. Cohen, and B. Kohler, Nature **436**, 1141 (2005).

[5] D. Markovitsi, F. Talbot, T. Gustavsson, D. Onidas, E. Lazzarotto, and S. Marguet, Nature **441**, E7 (2006).

[6] I. Buchvarov, Q. Wang, M. Raytchev, A. Trifonov, and T. Fiebig, Proc. Natl. Acad. Sci. USA **104**, 4794 (2007).

[7] D. Markovitsi, T. Gustavsson, and A. Banyasz, Mutat. Res. Rev. **704**, 21 (2010).

[8] A. I. S. Holm, L. M. Nielsen, S. V. Hoffmann, and S. Brøndsted Nielsen, Phys. Chem. Chem. Phys. **12**, 9581 (2010).

[9] U. Kadhane, A. I. S. Holm, S. V. Hoffmann, and S. Brøndsted Nielsen, Phys. Rev. E **77**, 021901 (2008).

[10] I. Vayá, T. Gustavsson, F.-A. Miannay, T. Douki, and D. Markovitsi, J. Am. Chem. Soc. **132**,

11834 (2010).

[11] D. Markovitsi, T. Gustavsson, and I. Vayá, J. Phys. Chem. Lett. **1**, 3271 (2010).

[12] B. Kohler, J. Phys. Chem. Lett. **1**, 2047 (2010).

[13] J. C. Genereux and J. K. Barton, Chem. Rev. **110**, 1642 (2010).

[14] T. Miyata and S. Yomosa, J. Phys. Soc. Jpn. **27**, 727 (1969).

[15] B. Bouvier, J.-P. Dognon, R. Lavery, D. Markovitsi, P. Millié, D. Onidas, and K. Zakrzewska, J. Phys. Chem. B **107**, 13512 (2003).

[16] S. P. Møller, Nucl. Instrum. Meth. Phys. Res. A **394**, 281 (1997).

[17] J. U. Andersen, P. Hvelplund, S. Brøndsted Nielsen, S. Tomita, H. Wahlgreen, S. P. Møller, U. V. Pedersen, J. S. Forster, and T. J. D. Jørgensen, Rev. Sci. Instrum. **73**, 1284 (2002).

[18] J. Gidden and M. T. Bowers, Eur. Phys. J. D **20**, 409 (2002).

[19] B. Liu, P. Hvelplund, S. Brøndsted Nielsen, and S. Tomita, Phys. Rev. A **74**, 052704 (2006).

[20] J. C. Marcum, A. Halevi, and J. M. Weber, Phys. Chem. Chem. Phys. **11**, 1740 (2009).

[21] J. A. Wyer and S. Brøndsted Nielsen, J. Chem. Phys. **133**, 084306 (2010).

[22] L. Li and D. M. Lubman, Anal. Chem. **59**, 2538 (1987).

[23] X. Yang, X.-B. Wang, E. R. Vorpagel, and L.-S. Wang, Proc. Natl. Acad. Sci USA **101**, 17588 (2004).

[24] Z. Q. Guan, N. L. Kelleher, P. B. O'Connor, D. J. Aaserud, D. P. Little, and F. W. McLafferty, Int. J. Mass Spectrom. Ion Processes **158**, 357 (1996).

[25] V. Gabelica, F. Rosu, T. Tabarin, C. Kinet, R. Antoine, M. Broyer, E. De Pauw, and P. Dugourd, J. Am. Chem. Soc. **129**, 4706 (2007).

[26] V. Gabelica, T. Tabarin, R. Antoine, F. Rosu, I. Compagnon, M. Broyer, E. De Pauw, and P. Dugourd, Anal. Chem. **78**, 6564 (2006).

[27] A. S. Danell and J. H. Parks, J. Am. Soc. Mass Spectrom. **14**, 1330 (2003).

[28] J. M. Weber, I. N. Ioffe, K. M. Berndt, D. Löffler, J. Friedrich, O. T. Ehrler, A. S. Danell, J. H. Parks, and M. M. Kappes, J. Am. Chem. Soc. **126**, 8585 (2004).

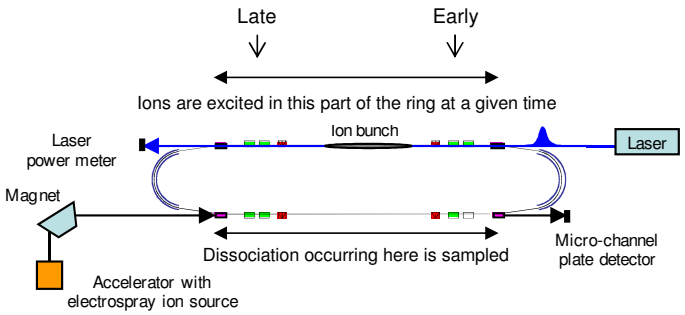

FIG. 1 (color online). The electrostatic ion storage ring in Aarhus (ELISA).

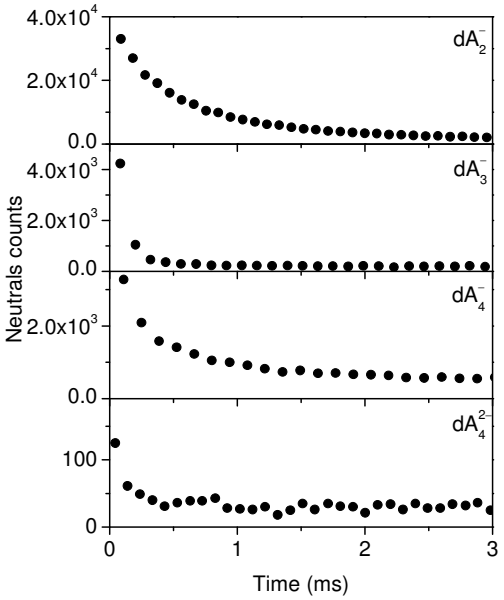

FIG. 2. Time spectra of dA_n^- (n = 2, 3, and 4) and dA_4^{2-} anions after 250-nm photoexcitation.

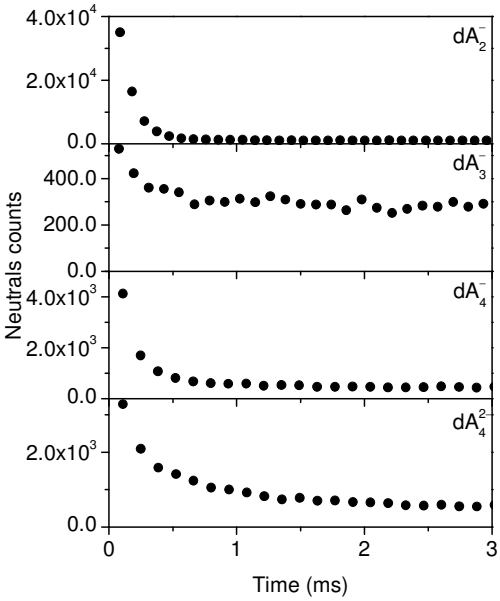

FIG. 3. Time spectra of dA_n^- (n = 2, 3, and 4) and dA_4^{2-} anions after 210-nm photoexcitation.

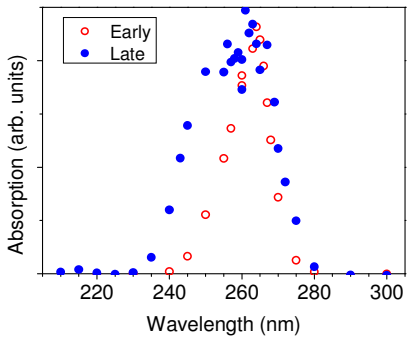

FIG. 4 (color online). Action spectra of AMP anions recorded after two different excitation times in the ring (see Fig. 1). At low wavelengths and early excitation times, the decay is over before the photoexcited ions have made it to the straight section where dissociation is sampled. As a result there is a discrimination against measuring the decay at low wavelengths.

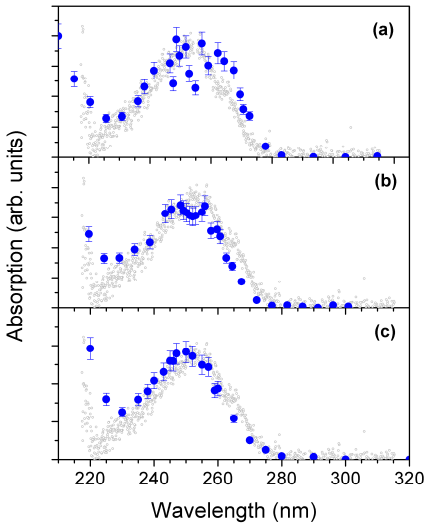

FIG. 5 (color online). Action spectra of dA_n^- anions recorded from the measurements of the yield of neutrals as a function of excitation wavelength. (a) n = 2; (b) n = 3, (c) n = 4. The action spectrum of $dAMP^-$ is shown on each panel (grey points) [20].

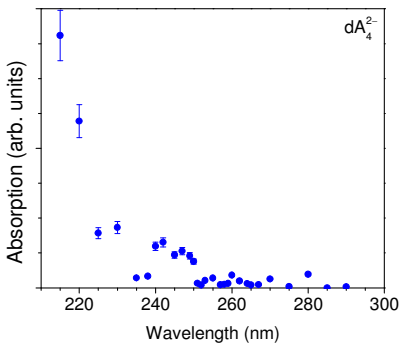

FIG. 6 (color online). Action spectrum of dA_4^{2-} anions recorded from the measurements of the yield of neutrals as a function of excitation wavelength.

Laser Pump-Probe Experiments on Microsecond to Millisecond Timescales at an Electrostatic Ion Storage Ring: Triplet–Triplet Absorption by Protoporphyrin-IX Anions

Kristian Støchkel, Jean Ann Wyer, Maj-Britt Suhr Kirketerp, and Steen Brøndsted Nielsen

Department of Physics and Astronomy, Aarhus University, Aarhus, Denmark

Here we demonstrate that pump-probe experiments can be carried out on microsecond to millisecond timescales using an electrostatic ion storage ring. As a test case, we have chosen protoporhyrin IX anions that have lifetimes with respect to dissociation after photoexcitation on this time scale. Ions were photoexcited on one side of the ring with either 430- or 535-nm light (pump) and then allowed to take a certain number of revolutions before they were photoexcited by a second laser pulse (probe) with wavelengths between 650 and 950 nm. If ions were first excited by the pump, an increased yield of neutral products caused by the absorption of red light was measured in a microchannel plate detector located on the other side of the ring. This implies that it is possible to pick out ions that were photoexcited by the pump pulse and to spectroscopically characterize these ions. We report absorption spectra of 535 nm photoexcited porphyrin anions, with time delays of 0.19 and 0.57 ms between the pump and probe pulses, and find that absorption occurs over a broad region in the red. (J Am Soc Mass Spectrom 2010, 21, 1884–1888) © 2010 Published by Elsevier Inc. on behalf of American Society for Mass Spectrometry

Time-resolved experiments on ions in vacuo have been carried out with great success on the femtosecond to picosecond timescales in recent years. On this timescale, the ions only move slightly between the laser pulses, and the experiment therefore relies on a good overlap between the two laser beams for the probe photons to interact with the same molecules that were excited by the pump photons. These experiments have provided important information on lifetimes of electronically excited states and on de-excitation pathways back to the electronic ground state. Examples include protonated aromatic amino acids, peptides, flavin, DNA nucleobases, C_{60}, and cluster anions [1–9].

To study longer timescale processes, larger time delays between the pump and probe laser beams are needed. Dunbar and coworkers [10–12] have investigated the radiative cooling of ions in an ion cyclotron resonance (ICR) ion trap using time delays between the two laser pulses of 100 ms and up to seconds. On the shorter timescale of microseconds to milliseconds, there is very little work. Using UV light, Joly et al. [13] recently photodetached an electron from a tryptophan-based pentapeptide dianion stored in a quadrupole ion trap. The radical monoanion was shown to be stable for long periods (at least 40 μs) based on photodissociation experiments using a probe laser pulse (visible light) delayed in time.

In the present work, our goal is to address long-lived excited states. For example, photoexcitation of an even-electron species to a singlet state is often followed by intersystem crossing to a lower-lying triplet state. Such a molecule is trapped in its triplet state for a long time since the required spin-flip introduces a bottleneck for returning to the electronic ground state. Porphyrins are known to have high triplet-quantum yields and triplet-state lifetimes of microseconds to milliseconds [14–18]. Hence they are well-suited as test cases for triplet-triplet absorption spectroscopy. Gas-phase time-resolved experiments at these long timescales are possible using ion traps, e.g., quadrupolar and ICR ion traps. Here we show, using protoporphyrin IX (pp) anions (Figure 1), how the implementation of two pulsed lasers at an electrostatic ion storage ring also allows for such experiments. A benefit of the ring technique is that only ions with the same mass-to-charge ratio are stored at any time.

Experimental

Experiments were performed at the electrostatic ion storage ring in Aarhus (ELISA) (see Figure 2) [19–21]. Electrospray ionization was used to produce ions,

Address reprint requests to Drs. K. Støchkel or S. Brøndsted Nielsen, Department of Physics and Astronomy, Aarhus University, Ny Munkegade, DK-8000 Aarhus, Denmark. E-mail: krst@phys.au.dk or sbn@phys.au.dk

1044-0305/10/$32.00
doi:10.1016/j.jasms.2010.07.004

Published online July 16, 2010
Received April 20, 2010
Revised June 30, 2010
Accepted July 9, 2010

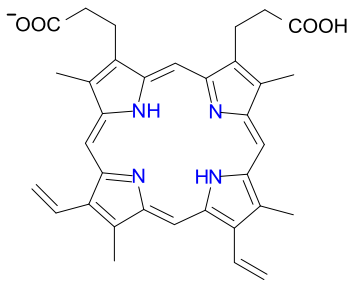

Figure 1. Structure of protoporphyrin IX (pp) anions.

which were subsequently accumulated in a 22-pole ion trap and thermally equilibrated by collisions with a helium buffer gas therein (Figure 2). The ions were accelerated as an ion bunch to kinetic energies of 22 keV, and a bending magnet was used to select the appropriate ions. Following injection into the ring, the ions were stored for about 35 ms to ensure the decay of highly vibrationally excited ions before being irradiated by a nanosecond light pulse from a tunable laser (Spectra Physics). This is an Nd:YAG laser where the third harmonic (355 nm) pumps an optical parametric oscillator (OPO), which subsequently has a visible output. The excitation wavelength for the experiment was chosen to be either 430 or 535 nm. The photoexcited ions were allowed to take a certain number of revolutions before they were excited in the same region as before by a second laser pulse from a tunable laser (EKSPLA). This is also an Nd:YAG laser in combination with an OPO. The wavelength was scanned between 650 and 950 nm. Note that at 709 nm the beam-exit window of the laser changes. For the 430-nm pump experiment, a dichroic mirror that reflects blue light (pump) and transmits red light (probe) was used to align the beams. For the 535-nm pump experiment, the dichroic mirror does not reflect. Instead, the mirror was removed and a nearly parallel path was introduced for the probe beam relative to the pump beam using two different mirrors. The repetition rate of the experiment was 10 Hz. Lifetimes with respect to dissociation were obtained from measurements of the yield of neutrals at each cycle hitting the microchannel plate (MCP) detector located at the end of the straight section opposite the straight side where photoexcitation was performed (i.e., delayed dissociation).

The pressure in the ring was of the order of 10^{-10} mbar, which set an upper limit of 1–2 s on the storage time. The protoporhyrin IX compound was purchased from Sigma-Aldrich (St. Louis, MO, USA) and dissolved in methanol.

Results and Discussion

A time spectrum of pp anions is shown in Figure 3. The high count rate after injection is due to the decay of vibrationally excited ions that were formed during the transmission from the 22-pole ion trap to the ring. After

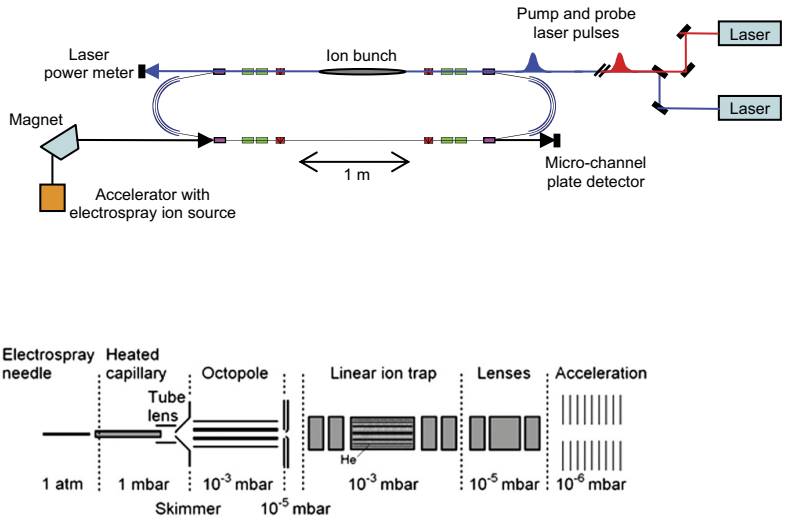

Figure 2. Two-laser experiment at the electrostatic ion storage ring in Aarhus (ELISA). Ions are stored in the ring for a certain number of revolutions before they are photoexcited by the first laser pulse (pump). A second laser pulse (probe) delayed in time relative to the first is then used to monitor photoexcited ions from an increased yield of neutrals in the MCP detector. Note that the delay times chosen correspond to three or more revolutions of the ions in the ring; in other words ions move in space between the two pulses. The ion source including the 22-pole ion trap is also shown. See text for more details.

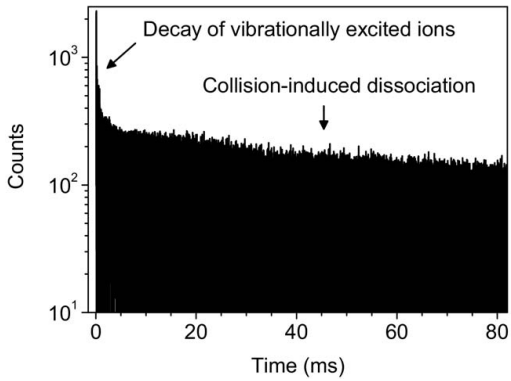

Figure 3. Time spectrum of pp anions.

about 5 ms, the decay rate is nearly constant and is ascribed to collisions with residual gas in the ring. The time constant for storage of the ions in the ring is 200 ms according to a long time measurement (Figure S1, which can be found in the electronic version of this article).

After about 35 ms, the ions were irradiated by light (430 nm) that lies within the Soret absorption band region ($S_0 \rightarrow S_2$ transition). This gave rise to an increased yield of neutrals as can be seen in the delayed dissociation measurement (see Figure 4a). Hence, the ions absorb light at this wavelength. There is a fast decay process with a time constant of 67 ± 30 μs, assigned to statistical dissociation after internal conversion to the electronic ground state, and a slower decay process with a time constant of 0.87 ± 0.30 ms (Figure 4a). The slow one is likely due to the trapping of ions in an excited-triplet state that acts as a bottleneck for dissociation as has been discussed in detail earlier [22, 23]. Briefly, intersystem crossing back to the electronic ground state is slow and occurs approximately with the time constant of 0.87 ms. A power-dependence measurement reveals that the long-lifetime component is due to one-photon absorption. The short-lifetime component is dominated by one-photon absorption, with the contribution from two-photon absorption estimated to be less than 10%. Finally, we note that the dominant dissociation channel is loss of CO_2 as was earlier reported [22], and that the photon energy is not high enough for photodetachment to occur since the electron binding energy of the anion is at least 3.4 eV (electron binding energy of $CH_3CH_2COO^-$).

To spectroscopically characterize the slowly decaying photoexited ions, we fired a second laser pulse after the ions had taken seven cycles in the ring (revolution time is 95.2 μs). At this time most of the vibrationally excited ions had decayed (cf., fast decay process). Triplet-state excited protoporphyrins in solution have been reported to absorb above 550 nm [15, 18]. We therefore chose a probe wavelength of 684 nm to be far away from the strong absorption of the ground-state ions themselves. An increased count rate due to absorption of the probe laser light is clearly visible (Figure 4b). While when the experiment was repeated with the pump laser switched off, no increase in the yield of neutrals was observed (Figure 4c). Possibly, the ions absorb at this wavelength but the photon flux was too low for two-photon absorption to occur (about 1.5 mJ per pulse, laser beam size diameter of about 2 mm). Hence, absorption of 684-nm light is only sufficient to cause dissociation from already photoexcited ions. A similar finding was obtained by pumping with 535-nm light in the Q-band absorption region ($S_0 \rightarrow S_1$ transition).

The results from pump-probe experiments taken with different time delays are shown in Figure 5. There it can be seen that the laser-induced probe signal shifts in time in accordance with the pump-probe delay. Not surprisingly, it is evident that the absorption of the probe light decreased as the time delay increased due to fewer and fewer photoexcited ions.

Next we decided to measure the action spectrum of the 535-nm photoexcited ions. This experiment is com-

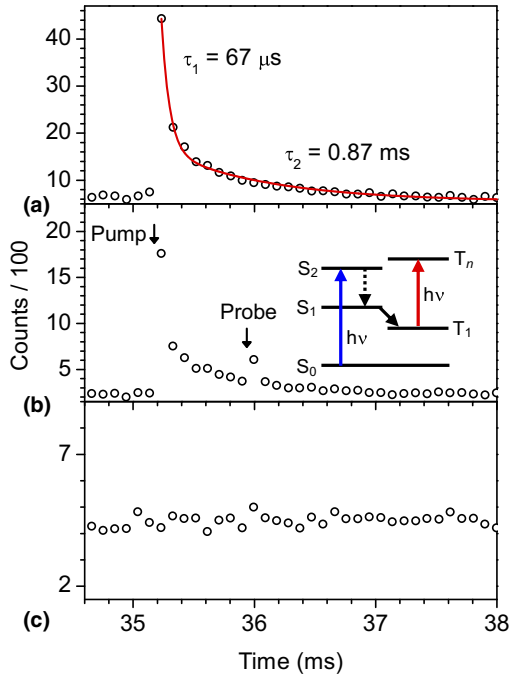

Figure 4. (**a**) Time spectrum of pp anions that were photoexcited after 35.19 ms by 430-nm light (pump). (**b**) Same as (**a**) but a probe laser pulse (684 nm) was fired 0.67 ms after the pump laser pulse. A simplified Jablonski diagram is shown to illustrate the photophysical processes: after excitation to the S2 state, internal conversion occurs to S1 followed by intersystem crossing to the T1 triplet state. Ions in this state absorb red light. (**c**) Time spectrum of pp anions that were photoexcited by the probe laser (684 nm) at 35.86 ms. No prior pump pulse was used and, consequently, no absorption was seen after firing the probe laser.

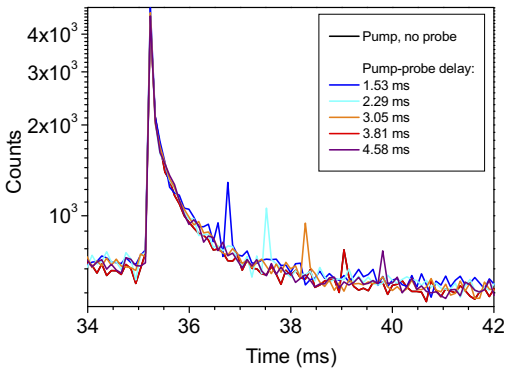

Figure 5. Time spectra of pp anions that were photoexcited after 35.19 ms by 535-nm light. In each spectrum the probe laser pulse (660 nm) was fired after different delay times. The laser-induced probe signal shifts in accordance with the pump-probe delay.

plicated by the fact that fluctuations in the two laser beam intensities need to be corrected. However, this is simplified as variations in the pump laser power were less than 5%. Therefore, in the analysis the power of the pump laser was taken to be constant for all measurements. A correction for variations in ion beam intensity is also needed and was done based on the yield of neutrals before photoexcitation. This yield is the result of collisions between ions and residual gas and is therefore directly proportional to the number of ions in the ring. The increased yield of neutrals due to the probe laser represents the absorption by the photoexcited ions (i.e., action spectroscopy). After correcting for ion beam fluctuations, the yield at each wavelength was subsequently divided by the number of photons in the probe laser beam. The number of photons in the probe laser beam was obtained from an established correlation between wavelength and laser output power and is estimated to be associated with an uncertainty of 10%. We estimate that the overall uncertainty in the yield of photoneutrals is about 20%. This high uncertainty makes it difficult to find the actual positions of band maxima. Nevertheless, action spectra were acquired for the case where the time delay between the pump and probe laser beams was 0.19 ms and that where it was 0.57 ms (Figure 6). In both spectra, it can be seen that absorption is strong at 650 nm and that it decreases as the wavelength increases, with little or no absorption seen above 800 nm. Furthermore, the band appears sharper after the longer delay time (0.57 ms) than after the shorter one (0.19 ms), which may be due to a colder population at longer delay times. It would have been useful to go to lower probe wavelengths but this is complicated due to absorption by these anions in their ground state.

The absorption observed here is within the expected absorption region for porphyrins excited to triplet states [15, 18]. In benzene solution, Chantrell et al. [18] found a very small band centered around 700 nm for protoporhyrin-IX dimethyl ester. A redshift from gas phase to solution phase is commonly seen for $\pi\pi^*$ transitions since the polarizability of a molecule increases with its level of excitation, which favors solute-solvent interactions. It should be stressed that absorption by vibrationally hot pp anions may also contribute to some of the absorption seen in this region. However, no increase in the yield of neutrals was observed in a separate experiment where irradiation by 685-nm light was carried out right after the injection of ions into the ring (data not shown). Here, the count rate of neutrals is already particularly high (first 5 ms, see Figure 3) due to the decay of vibrationally excited ions. These ions are present in the bunch since some collisions with residual gas occur during transfer from the 22-pole ion trap to the ring. From the absence of an increase in neutrals after light irradiation, we conclude that "hot" band absorption is not significant and, therefore, the photoexcited signal due to the probe laser pulse in the pump-probe experiment arises from absorption by triplet-state ions.

In conclusion, we have demonstrated that pump-probe experiments on the microsecond to millisecond timescale are indeed possible using an electrostatic ion

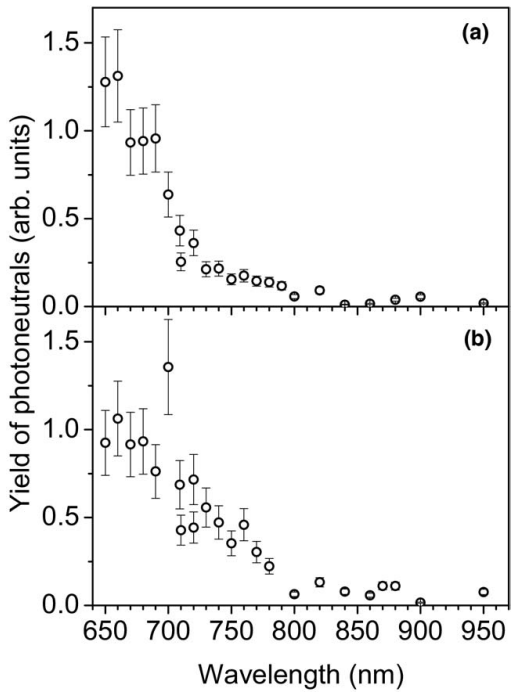

Figure 6. Action spectra obtained as the yield of photoneutrals due to the probe laser pulse as a function of probe wavelength. The pump laser was set to produce light at 535 nm. Time delays between the pump and probe were 0.57 ms (**a**) and 0.19 ms (**b**).

storage ring in combination with two lasers. The time resolution of the experiment is the ion revolution time. Finally, we note that ion trap experiments have an advantage over the current setup due to better overlap between the two laser beams and the ion cloud.

Acknowledgments

The authors acknowledge generous support from Lundbeckfonden, Villum Kann Rasmussen Fonden, and Dir. Ib Henriksens Fond.

Appendix A Supplementary Material

Supplementary material associated with this article may be found in the online version at doi:10.1016/j.jasms.2010.07.004.

References

1. Kang, H.; Jouvet, C.; Dedonder-Lardeux, C.; Martrenchard, S.; Grégoire, G.; Desfrancois, C.; Schermann, J. P.; Barat, M.; Fayeton, J. A. Ultrafast Deactivation Mechanisms of Protonated Aromatic Amino Acids Following UV Excitation. *Phys. Chem. Chem. Phys.* **2005,** *7,* 394–398.
2. Grégoire, G.; Kang, H.; Dedonder-Lardeux, C.; Desfrancois, C.; Onidas, D.; Lepere, V.; Fayeton, J. A. Statistical vs. Non-Statistical Deactivation Pathways in the UV Photo-Fragmentation of Protonated Tryptophan-Leucine Dipeptide. *Phys. Chem., Chem. Phys.* **2006,** *8,* 122–128.
3. Nolting, D.; Schultz, T.; Hertel, I. V.; Weinkauf, R. Excited State Dynamics and Fragmentation Channels of the Protonated Dipeptide H_2N-Leu-Trp-COOH. *Phys. Chem., Chem. Phys.* **2006,** *8,* 5247–5254.
4. Guyon, L.; Tabarin, T.; Thuillier, B.; Antoine, R.; Broyer, M.; Boutou, V.; Wolf, J.-P.; Dugourd, P. Femtosecond Pump-Probe Experiments on Trapped Flavin: Optical Control of Dissociation. *J. Chem. Phys.* **2008,** *128,* 075103.
5. Nolting, D.; Weinkauf, R.; Hertel, I. V.; Schultz, T. Excited-State Relaxation of Protonated Adenine. *Chem. Phys. Chem.* **2007,** *8,* 751–755.
6. Ehrler, O. T.; Yang, J. P.; Hättig, C.; Unterreiner, A. N.; Hippler, H.; Kappes, M. M. Femtosecond Pump/Probe Photoelectron Spectroscopy of Isolated C_{60} Negative Ions. *J. Chem. Phys.* **2006,** *125,* 074312.
7. Gerhardt, P.; Niemitz, M.; Kim, Y. D.; Ganteför, G. Fast Electron Dynamics in Small Aluminum Clusters: Non-Magic Behavior of a Magic Cluster. *Chem. Phys. Lett.* **2003,** *382,* 454–459.
8. Niemietz, M.; Gerhardt, P.; Ganteför, G.; Kim, Y. D. Relaxation Dynamics of the Au_3^- and Au_6^- Cluster Anions. *Chem. Phys. Lett.* **2003,** *380,* 99–104.
9. Kim, Y. D.; Niemietz, M.; Gerhardt, P.; von Gynz-Rekowski, F.; Ganteför, G. Relaxation Dynamics of Magic Clusters. *Phys. Rev. B* **2004,** *70,* 035421.
10. Dunbar, R. C.; Chen, J.-H. Two-Pulse Photodissociation Measurement of Infrared Fluorescence Relaxation in Bromobenzene Ion. *J. Phys. Chem.* **1984,** *88,* 1401–1404.
11. Asamato, B.; Dunbar, R. C. Observation of the Infrared Relaxation of Iodobenzene Ions Using Two-Light-Pulse Photodissociation. *J. Phys. Chem.* **1987,** *91,* 2804–2807.
12. Faulk, J. D.; Dunbar, R. C. Ion Cyclotron Resonance Ion Trap Measurements of Energy Relaxation in Gas-Phase Ions: Three Techniques Compared for Thiophenol Ion. *J. Phys. Chem.* **1989,** *93,* 7785–7789.
13. Joly, L.; Antoine, R.; Allouche, A.-R.; Dugourd, P. Formation and Spectroscopy of a Tryptophan Radical Containing Peptide in the Gas Phase. *J. Am. Chem. Soc.* **2008,** *130,* 13832–13833.
14. Sinclair, R. S.; Tait, D.; Truscott, T. G. Triplet States of Protoporphyrin IX and Protoporphyrin IX Dimethyl Ester. *J. C. S. Faraday. I* **1980,** *76,* 417–425.
15. Bonnett, R.; Charalambides, A. A.; Land, E. J.; Sinclair, R. S.; Tait, D.; Truscott, T. G. Triplet States of Porphyrin Esters *J. C. S. Faraday. I* **1980,** *76,* 852–859.
16. Lafferty, J.; Truscott, T. G. Triplet State of Protoporphyrin IX. *J. C. S. Chem. Commun.* **1978,** 51–52.
17. Charlesworth, P.; Truscott, T. G.; Kessel, D.; Medforth, C. J.; Smith, K. M. Photophysical Studies of Substituted Porphyrins. *J. Chem. Soc. Faraday Trans.* **1994,** *90,* 1073–1076.
18. Chantrell, S. J.; McAuliffe, C. A.; Munn, R. W.; Pratt, A. C.; Land, E. J. Excited States of Protoporphyrin IX Dimethyl Ester: Reaction on the Triplet with Carotenoids. *J. Chem. Soc. Faraday Trans.* **1977,** *73,* 858–865.
19. Møller, S. P. ELISA, an electrostatic storage ring for atomic physics. *Nucl. Instrum. Methods A* **1997,** *394,* 281–286.
20. Andersen, J. U.; Hvelplund, P.; Brøndsted Nielsen, S.; Tomita, S.; Wahlgreen, H.; Møller, S. P.; Pedersen, U. V.; Forster, J. S.; Jørgensen, T. J. D. The Combination of an Electrospray Ion Source and an Electrostatic Storage Ring for Lifetime and Spectroscopy Experiments on Biomolecules. *Rev. Sci. Instrum.* **2002,** *73,* 1284–1287.
21. Støchkel, K.; Kadhane, U.; Andersen, J. U.; Holm, A. I. S.; Hvelplund, P.; Kirketerp, M.-B. S.; Larsen, M. K.; Lykkegaard, M. K.; Brøndsted Nielsen, S.; Panja, S.; Zettergren, H. A New Technique for Time-Resolved Daughter Ion Mass Spectrometry on the Microsecond to Millisecond Time Scale Using an Electrostatic Ion Storage Ring. *Rev. Sci. Instrum.* **2008,** *79,* 023107.
22. Calvo, M. R.; Andersen, J. U.; Hvelplund, P.; Brøndsted Nielsen, S.; Pedersen, U. V.; Rangama, J.; Tomita, S. Photophysics of Protoporphyrin Ions In Vacuo: Triplet-State Lifetimes and Quantum Yields. *J. Chem. Phys.* **2004,** *120,* 5067–5072.
23. Nielsen, C. B.; Forster, J. S.; Ogilby, P. R.; Brøndsted Nielsen, S. Delayed Dissociation of Photoexcited Porphyrin Cations in a Storage Ring: Determination of Triplet Quantum Yields. *J. Phys. Chem. A* **2005,** *109,* 3875–3879.

A new technique for time-resolved daughter ion mass spectrometry on the microsecond to millisecond time scale using an electrostatic ion storage ring

Kristian Støchkel,[1] Umesh Kadhane,[2] Jens Ulrik Andersen,[2] Anne I. S. Holm,[2] Preben Hvelplund,[2] Maj-Britt Suhr Kirketerp,[2] Mikkel Koefoed Larsen,[2] Morten Køcks Lykkegaard,[2] Steen Brøndsted Nielsen,[2] Subhasis Panja,[2] and Henning Zettergren[2]
[1]*Institute for Storage Ring Facilities, University of Aarhus, Ny Munkegade, DK-8000 Aarhus C, Denmark*
[2]*Department of Physics and Astronomy, University of Aarhus, Ny Munkegade, DK-8000 Aarhus C, Denmark*

(Received 12 November 2007; accepted 29 January 2008; published online 28 February 2008)

A new method for time-resolved daughter ion mass spectrometry is presented, based on the electrostatic ion storage ring in Aarhus, ELISA. Ions with high internal energy, e.g., as a result of photoexcitation, dissociate and the yield of neutrals is monitored as a function of time. This gives information on lifetimes in the microsecond to millisecond time range but no information on the fragment masses. To determine the dissociation channels, we have introduced pulsed supplies with switching times of a few microseconds. This allows rapid switching from storage of parent ions to storage of daughter ions, which are dumped into a detector after a number of revolutions in the ring. A fragment mass spectrum is obtained by monitoring the daughter ion signal as a function of the ring voltages. This technique allows identification of the dissociation channels and determination of the time dependent competition between these channels. © *2008 American Institute of Physics.*
[DOI: 10.1063/1.2884121]

I. INTRODUCTION

Electrostatic storage rings have been used successfully during the past decade in the study of the physics of atomic and molecular ions *in vacuo*. Experiments include measurements of geometrical cross sections of ions, lifetimes after photoexcitation to obtain Arrhenius dissociation parameters,[1] absorption spectra (based on action spectroscopy),[2] triplet quantum yields after photoexcitation,[3] rates for electron autodetachment,[4] rates for radiative cooling,[5] dissociative recombination,[6] and electron detachment cross sections of anions and resonant states of multiply charged anions.[7] There are currently three operating instruments, ELISA in Aarhus (Fig. 1),[8] a ring at KEK, Tsukuba,[9] and the TMU E-ring in Tokyo.[10] Three other rings are under construction, DESIREE in Stockholm,[11] CSR in Heidelberg,[12] and FIRE in Frankfurt.[13] Being entirely electrostatic, such rings can store ions of fixed charge and energy with arbitrary mass. They are therefore particularly useful for the study of heavy systems such as clusters, fullerenes, and biomolecules. An ion bunch accelerated to keV energies enters the ring through a differentially pumped beam line. Once injected, the ions circulate in the ring with revolution times of about 10–100 μs until they change their energy/charge ratio. Neutrals formed are not affected by the electric fields and are measured by a detector located at the end of one of the straight sections (discussed later). However, the kinetic energy of a neutral is not large enough to be measured in an energy-sensitive detector as used for MeV beam energies. In a typical experiment, stored ions are excited by a laser pulse in the ring and the yield of neutral fragments from delayed dissociation is then detected turn by turn. Direct or fast processes happening within a few microseconds are only registered as a depletion of the stored beam.

When a parent ion dissociates into two fragments, the fragments share the kinetic energy of the parent ion between them, the kinetic energy of each fragment being proportional to its mass. Since only ions with the proper kinetic energy can be stored in the ring for a fixed setting of the various ring voltages, daughter ions are lost in the first deflector they have to pass. Thus, one major limitation in our previous work has been that we did not know the masses of the fragment ions produced in the ring after say photoexcitation. Thus, we could not identify the reaction channels and whether or not they changed with time. Such information is clearly useful in the analysis and interpretation of results.

In this work, we present a new technique to overcome this limitation, based on the implementation of pulsed power supplies with microsecond switching times. The idea is that a fast scaling of all voltages of the electric elements in the ring allows for storage of a particular fragment ion. After several revolutions, the fragment ions are dumped in the detector to measure their abundance (Fig. 2). Hence, a linear scan of the ring element voltages provides a mass spectrum of the fragment ions formed after, for example, photoexcitation of the original ions. The energy resolution of such a measurement depends on the fragment storage time. Dumping after half a revolution results in an energy acceptance of about 1%.

Hence, an electrostatic storage ring can operate as a mass spectrometer with no change in its basic construction. More importantly, the competition between dissociation channels of photoexcited ions can be determined as a function of time (two qualitative schemes shown in Fig. 3 as

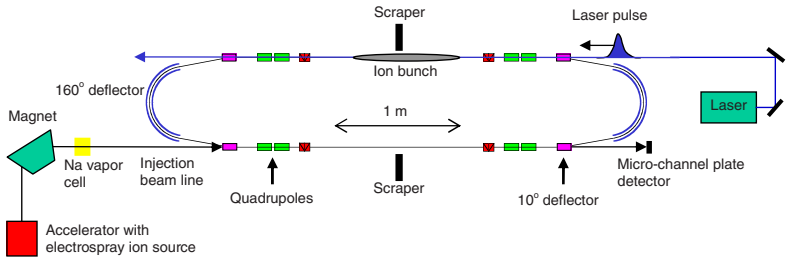

FIG. 1. (Color online) The electrostatic ion storage ring in Aarhus, ELISA, in combination with a laser. Vertical deflectors in the ring are not shown. See text for details.

example); the time scale can be as short as tens of microseconds and extend up to seconds (maximum storage time set by collision-induced dissociation with residual gas in the ring). We emphasize that time-resolved daughter ion mass spectrometry on the microsecond time scale is not easily performed with other mass spectrometers, such as fourier transform ion cyclotron resonance (FT-ICR) instruments that typically cover time scales of tens of milliseconds. The success of such an upgrade of ELISA is demonstrated here with a few examples, together with a description of the characteristics of the new power supplies.

II. PRINCIPLES OF THE ELECTROSTATIC ION STORAGE RING IN AARHUS, ELISA

The instrumental setup in Aarhus is shown in Fig. 1.[8] Ions are typically formed by electrospray ionization and accumulated in a multipole ion trap in which they are thermally equilibrated with a helium buffer gas for 0.1 s. The ion bunch is accelerated through a kilovolt electrostatic potential, and ions of interest are selected by a magnet and injected into ELISA through a differentially pumped beam line. As seen in Fig. 1, the ring consists of two 160° cylindrical deflectors with a 10° parallel-plate deflector and an electrostatic quadrupole doublet on each side of the deflectors. The circumference of the ring is 8.3 m, and the ions are typically accelerated to 22 keV before injection, which results in revolution times in the range of 10–100 μs, depending on the mass. Once injected, the ions circulate in the ring until the value of their energy/charge ratio changes by decay or in a reaction. Neutral products are not affected by the electric fields and will be measured by a detector located at the end of the straight section (see Fig. 1). The probability of collision-induced dissociation in the ring is low because of the low pressure (a few times 10^{-11} mbar), which results in storage times of seconds. Therefore, to obtain a larger decay rate and as a result more ionic fragments for mass analysis, we have excited ions either by photoabsorption in the ring or by electron capture in the injection beam line.

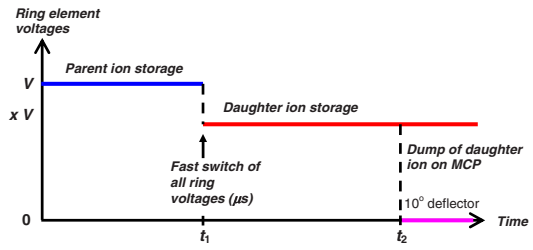

FIG. 2. (Color online) Scheme for daughter ion mass spectrometry in ELISA. Parent ions are stored until time t_1 at which all ring voltages are quickly scaled by x (within a few microseconds) to store a certain daughter ion with the proper kinetic energy. At time t_2, daughter ions are dumped in the MCP detector by setting the 10° deflector to 0 V.

III. RESULTS AND DISCUSSION

The principle of the new operation of ELISA is exemplified with the results of two test studies. The molecular ions were chosen on the basis of knowledge of their fragmentation obtained from other studies.

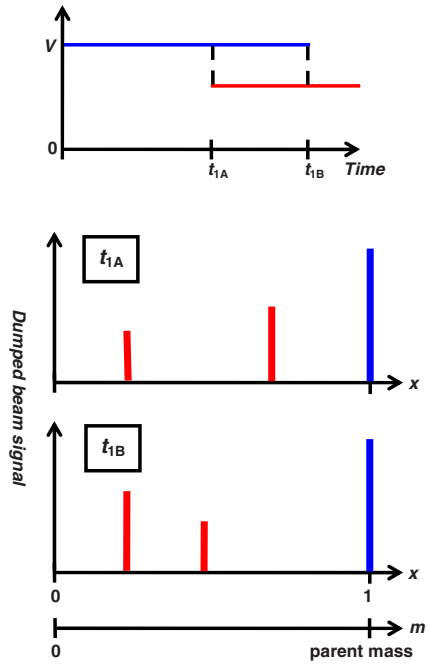

FIG. 3. (Color online) Time-resolved daughter ion mass spectrometry: the fragmentation spectrum of the excited parent ions is recorded at two different times, t_{1A} and t_{1B}.

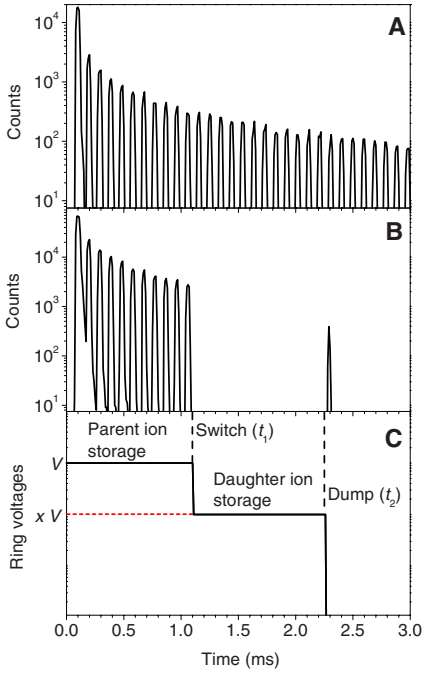

FIG. 4. (Color online) (A) Time spectrum of neutrals counts for stored $Ru(bipy)_3^+$ in ELISA. (B) At time t_1=1.10 ms, ring voltages are switched to store the daughter ion $Ru(bipy)_2^+$. At time t_2=2.25 ms, these ions are dumped onto the MCP detector. (C) Ring voltages as a function of time.

A. Fragmentation of metastable $Ru(bipy)_3^+$ formed after electron capture by $Ru(bipy)_3^{2+}$

A bunch of $Ru(bipy)_3^{2+}$ (bipy=2,2′-bipyridine) dications was accelerated through an 11 kV electrostatic potential. After mass selection by the magnet, the ions were collided with sodium atoms in a collision cell, inducing either dissociation or electron transfer. The ring voltages were set to store singly charged ions, $Ru(bipy)_3^+$, formed after electron capture (energy per charge=22 keV). The decay spectrum of metastable $Ru(bipy)_3^+$ is shown in Fig. 4(a) [signal in microchannel plate (MCP) detector as a function of time]. Such monocations are known to undergo dissociation with loss of bipyridine as the main channel.[14]

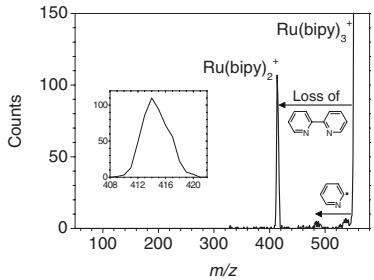

FIG. 5. Daughter ion mass spectrum of $Ru(bipy)_3^+$ obtained at ELISA. Inset showing the resolution of about 100 ($m/\Delta m$=413/4).

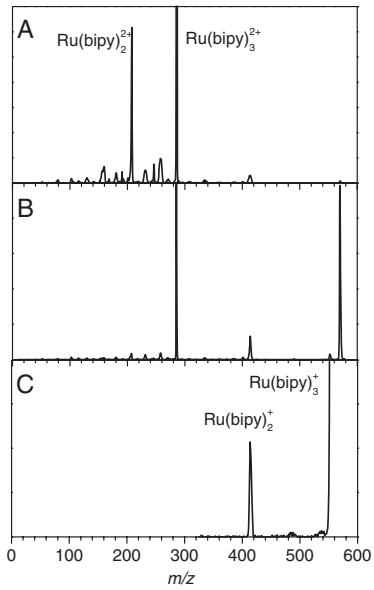

FIG. 6. Fragmentation spectra obtained from collisions between $Ru(bipy)_3^{2+}$ and (A) He and (B) Na, taken at an accelerator mass spectrometer. (C) Fragmentation spectrum of metastable $Ru(bipy)_3^+$ obtained at ELISA.

In another experiment, we stored the $Ru(bipy)_3^+$ ions in the ring for a few revolutions (revolution time of 96 μs). The ring voltages were then switched to store the daughter ion $Ru(bipy)_2^+$ (t_1=1.10 ms), and after 1.15 ms, the daughter ion bunch was dumped into the MCP detector by a fast switch of the 10° deflector in front of the MCP detector to 0 V. The dumped-beam signal is seen at 2.25 ms (t_2) in Fig. 4(b). The corresponding switching logic is plotted in Fig. 4(c). Based on the neutrals counts just before switching and the counts of the dumped ion beam, the storage efficiency of daughter ions is estimated to be at least 40%. There is some loss since the spatial extent of the ion bunch is rather large, two or three meters, which implies that not all daughter ions are in a field-free region when the voltages are switched. This could be improved by shortening the length of the ion bunch to a maximum of 20% of the circumference of ELISA, i.e., by emptying the multipole ion trap more quickly (within 20 μs).

In order to collect a daughter ion mass spectrum, we set a hardware gate on the dumped-beam signal and measured the intensity of the signal as a function of the daughter ion storage voltages as they were scaled from x=5% to 100% of the voltages used to store the parent ion. The mass spectrum is shown in Fig. 5. The most prominent feature is, not surprisingly, loss of bipyridine. There is also a peak which is assigned to an ion that has lost half of the bipyridine ligand.

Fragmentation due to collisional activation in the ring was found to be negligible due to the low pressure ($\sim 3\times 10^{-11}$ mbar); however, if required, the pressure can be increased to increase the collision induced dissociation (CID)

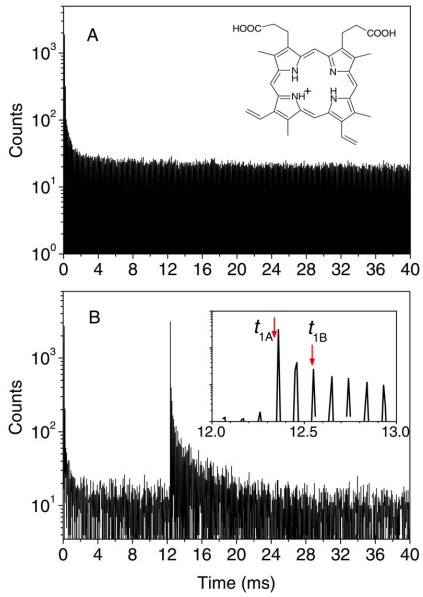

FIG. 7. (Color online) (A) Time spectrum of neutrals counts for stored pp^+ ions. (B) Time spectrum obtained when the ions were excited by a 390 nm laser pulse at a time of 12.36 ms after injection. The arrow marks in inset show the times for switching of the ring voltages.

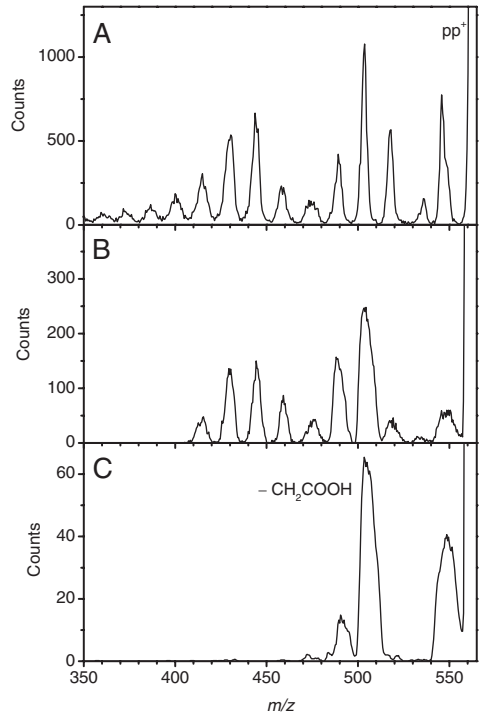

FIG. 8. (A) Fragmentation spectrum obtained from collisions between pp^+ and He, taken at an accelerator mass spectrometer. (B) Fragmentation spectrum acquired at ELISA immediately after photoexcitation. Dissociation within the first 5 μs was sampled. (C) Fragmentation spectrum acquired at ELISA after about 190 μs of storage of the photoexcited ions.

contribution. Such an option is particularly useful for more accurate mass calibration (discussed later).

We reported earlier the fragmentation spectra of $Ru(bipy)_3^{2+}$ obtained after high-energy collisions with either helium or sodium. In the case of He, only CID was observed, whereas in the case of Na both CID and electron-capture induced dissociation (ECID) were seen.[14] The spectra are summarized in Fig. 6 together with the present measurement of $Ru(bipy)_3^+$. In the ELISA experiment, we have resolved the CID contribution from that of ECID since here only fragmentation of the charge-reduced ions was sampled.

B. Photofragmentation of protonated porphyrin

A bunch of protoporphyrin IX cations (pp^+, Fig. 7) was accelerated through a 22 kV electrostatic potential. After mass selection by the magnet, the ions were injected into ELISA and stored. The decay spectrum of pp^+ is shown in Fig. 7(a). The high yield of neutrals immediately after injection is due to metastable ions that have been excited during extraction from the ion trap or during injection into the ring. After a few milliseconds, the signal is dominated by collisional decay in the ring, the lifetime of the ions being about 1 s.

At various times, the ions were irradiated with 390 nm light (photon energy of 3.17 eV) in the side opposite to the injection side (Fig. 1). The light source was a pulsed alexandrite laser that generated 780 nm light which was frequency doubled in a crystal. The laser was triggered by the transistor transistor logic (TTL) pulse generated from the trigger sequence that was used for extracting ions from the trap. This pulse was delayed in order to have a desired temporal overlap of the laser pulse with the stored ions. Enhancement in the decay rate due to photon absorption is clearly seen [Fig. 7(b)].

For daughter ion mass spectrometry, ring voltages were switched to store daughter ions. In one case, the ring voltages were switched immediately after laser excitation to monitor fragment ions produced before the first turn [Fig. 8(b)] and, in another, photoexcited ions circulated twice before the ring voltages were switched [Fig. 8(c)]. The daughter ion mass spectra obtained for these two cases differ significantly with much more fragmentation seen at short times (within about 5 μs) as seen in Fig. 8. The various peaks are assigned to the loss of one or more side chains, CH_3 (15), CH_2CH (27), COOH (45), CH_2COOH (59), and CH_2CH_2COOH (73). Charkin *et al.*[15] have shown that loss of CH_2COOH is the lowest energy dissociation channel, requiring 1.9 ($\pm$0.2) eV, and in our experiment, this channel also dominates for photoexcited ions that dissociate after 190 μs. The signal at this later time is due to one-photon absorption since it increases linearly with the photon flux. We therefore ascribe the larger fragmentation measured within the first few microseconds after laser excitation to be due to two-photon absorption. The lifetime of ions that have absorbed two photons is expected to be short and most, if not

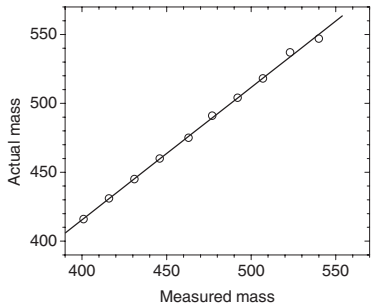

FIG. 9. Actual fragment masses vs measured values at ELISA in the case of pp^+. The calibration is linear with a slope of 0.96 and offset of 31.

all, will dissociate before the first turn in the ring. For comparison, the high-energy CID spectrum of pp^+ ions was recorded at an accelerator mass spectrometer [Fig. 8(a)]. In this case, even more fragmentation was seen but otherwise the spectra are quite similar. Collisions with residual gas in the ring should result in a spectrum similar to Fig. 8(a).

C. Calibration and mass resolution

The mass resolution of the ELISA daughter ion experiment is poor, about 100 $(m/\Delta m)$ (see inset, Fig. 5). The reason is that the energy acceptance of the ring is high together with a high sensitivity of the MCP detector (a large detection area). Best resolution was obtained by insertion of beam scrapers on each side of the ring to reduce the phase space (Fig. 1). All data reported here were taken under these conditions.

Calibration of the daughter ion m/z scale requires that some fragments can be identified; otherwise a CID spectrum has to be acquired and carefully compared with that obtained by a more conventional mass spectrometer. For pp^+ ions, there are many prominent peaks present that can be clearly identified (Fig. 8). The calibration curve in this case is found to be linear and given by $m/z=0.96m/z_{\text{measured}}+31$ (Fig. 9).

IV. FUTURE DIRECTIONS

We have developed a new technique to measure the fragmentation of ions in a storage ring using pulsed power supplies, which opens up for a whole new set of experiments. In the future, we plan to address differences in statistical and nonstatistical fragmentations following photoexcitation, the latter process being close to prompt.[16] Another important issue is the photodissociation of molecular ions and determination of Arrhenius parameters in the high-temperature regime.[1] It would be interesting to measure the fragments and compare with those formed in blackbody infrared radiative dissociation experiments, where dissociation of ions with low internal energy is monitored in the cell of a FT-ICR instrument.[17] In addition, changes in the fragmentation channels as a function of time can be identified. Finally, the setup allows the study of the photophysics of daughter ions, e.g., their absorption spectra can be measured.

ACKNOWLEDGMENTS

This work was supported by the Danish Natural Science Research Council (Grant Nos. 21-04-0514 and 272-06-0427), and Carlsbergfondet (Grant No. 2006-01-0229).

APPENDIX: CHARACTERISTICS OF NEW POWER SUPPLIES FOR ELISA

We have implemented the daughter ion technique by the addition of an extra voltage supply for each plate in the deflectors and fast switches for the supplies. The voltages for the 10° and 160° deflectors are of the order of kilovolts while for the quadrupole a few hundred volts are needed. The switches are of the push/pull type. The voltages for the vertical deflectors are bipolar (between −400 and +400 V) and are switched using fast high voltage amplifiers.

The 10° injection deflector requires three levels for operation: parent ion voltage, daughter ion voltage, and 0 V when the parent ions are injected. Likewise, the 10° dump deflector requires three levels: again parent and daughter ion voltages and 0 V when daughter ions are dumped. However, three-level switches cannot be switched quickly for all transitions between the three levels. For the injection deflector, we have fast switching from 0 V (injection) to parent ion storage and for daughter ion storage. The dump deflector has fast switching from parent ion storage to daughter ion storage to 0 V (dump). The fast switching times are faster than 1 μs, whereas the slow switches can take up to 5 ms. The switch has a limit for the daughter ion voltage that cannot be lower than 5% of the parent ion voltage.

All switches were designed and built at the University of Aarhus and have been integrated into the control system. All voltages are scaled by a common scaling parameter (x), and the switching time is given by an external common trigger.

[1] J. U. Andersen, H. Cederquist, J. S. Forster, B. A. Huber, P. Hvelplund, J. Jensen, B. Liu, B. Manil, L. Manoury, S. Brøndsted Nielsen, U. V. Pedersen, J. Rangama, H. T. Schmidt, S. Tomita, and H. Zettergren, Phys. Chem. Chem. Phys. **6**, 2676 (2004); L. H. Andersen, H. Bluhme, S. Boyé, T. J. D. Jørgensen, H. Krogh, I. B. Nielsen, S. Brøndsted Nielsen, and A. Svendsen, *ibid.* **6**, 2617 (2004).

[2] S. Brøndsted Nielsen, A. Lapierre, J. U. Andersen, U. V. Pedersen, S. Tomita, and L. H. Andersen, Phys. Rev. Lett. **87**, 228102 (2001); S. Boyé, I. B. Nielsen, S. Brøndsted Nielsen, H. Krogh, A. Lapierre, H. B. Pedersen, S. U. Pedersen, U. V. Pedersen, and L. H. Andersen, J. Chem. Phys. **119**, 338 (2003); S. Tomita, J. U. Andersen, O. Echt, K. Hansen, P. Hvelplund, B. Liu, S. Brøndsted Nielsen, U. V. Pedersen, and J. Rangama, Phys. Rev. Lett. **94**, 053002 (2005); I. B. Nielsen, M. A. Petersen, L. Lammich, M. Brøndsted Nielsen, and L. H. Andersen, J. Phys. Chem. A **110**, 12592 (2006).

[3] M. R. Calvo, J. U. Andersen, J. S. Forster, P. Hvelplund, S. Brøndsted Nielsen, U. V. Pedersen, J. Rangama, and S. Tomita, J. Chem. Phys. **120**, 5067 (2004); C. B. Nielsen, J. S. Forster, P. R. Ogilby, and S. Brøndsted Nielsen, J. Phys. Chem. A **109**, 3875 (2005).

[4] U. V. Pedersen, M. Hyde, S. P. Møller, and T. Andersen, Phys. Rev. A **64**, 012503 (2001); S. Tomita, J. U. Andersen, H. Cederquist, B. Concina, B. Huber, P. Hvelplund, J. Jensen, B. Liu, B. Manil, L. Maunoury, S. Brøndsted Nielsen, J. Rangama, H. T. Schmidt, and H. Zettergren, J. Chem. Phys. **124**, 024310 (2006); S. Panja, U. Kadhane, J. U. Andersen, A. I. S. Holm, P. Hvelplund, M.-B. S. Kirketerp, S. Brøndsted Nielsen, K. Støchkel, R. N. Compton, J. S. Forster, K. Kilså, and M. Brøndsted Nielsen, J. Chem. Phys. **127**, 124301 (2007); M. Goto, Y. Yasuda, S. Jinno, T. Takao, K. Hanada, H. Tanuma, T. Azuma, K.-I. Sugiura, H. Shiromaru, and Y. Achiba, Eur. Phys. J. D **43**, 65 (2007).

[5] J. U. Andersen, H. Cederquist, J. S. Forster, B. Huber, P. Hvelplund, J. Jensen, B. Liu, L. Maunoury, B. Manil, S. Brøndsted Nielsen, U. V.

Pedersen, H. T. Schmidt, S. Tomita, and H. Zettergren, Eur. Phys. J. D **25**, 139 (2003).
[6] T. Tanabe, K. Noda, M. Saito, S. Lee, Y. Ito, and H. Takagi, Phys. Rev. Lett. **90**, 193201 (2003); T. Tanabe, E. B. Starikov, K. Noda, and M. Saito, Chem. Phys. Lett. **430**, 380 (2006).
[7] T. Tanabe, K. Noda, M. Saito, E. B. Starikov, and M. Tateno, Phys. Rev. Lett. **93**, 043201 (2004); M. A. O. El Ghazaly, A. Svendsen, H. Bluhme, A. B. Nielsen, S. Brøndsted Nielsen, and L. H. Andersen, *ibid.* **93**, 203201 (2004); A. Svendsen, H. Bluhme, M. A. O. El-Ghazaly, K. Seiersen, S. Brøndsted Nielsen, and L. H. Andersen, *ibid.* **94**, 223401 (2005).
[8] S. P. Møller, Nucl. Instrum. Methods Phys. Res. A **394**, 281 (1997); J. U. Andersen, J. S. Forster, P. Hvelplund, T. J. D. Jørgensen, S. P. Møller, S. Brøndsted Nielsen, U. V. Pedersen, S. Tomita, and H. Wahlgreen, Rev. Sci. Instrum. **73**, 1284 (2002).
[9] T. Tanabe, K. Chida, K. Noda, and I. Watanabe, Nucl. Instrum. Methods Phys. Res. A **482**, 595 (2002); T. Tanabe and K. Noda, *ibid.* **496**, 233 (2003).
[10] S. Jinno, T. Takao, Y. Omata, A. Satou, H. Tanuma, T. Azuma, H. Shiromaru, K. Okuno, N. Kobayashi, and I. Watanabe, Nucl. Instrum. Methods Phys. Res. A **532**, 477 (2004); S. Jinno, T. Takao, K. Hanada, M. Goto, K. Okuno, H. Tanuma, T. Azuma, and H. Shiromaru, *ibid.* **572**, 568 (2007).
[11] H. Danared, L. Liljeby, G. Andler, L. Bagge, M. Blom, A. Källberg, S. Leontein, P. Löfgren, A. Paál, K.-G. Rensfelt, A. Simonsson, H. T. Schmidt, H. Cederquist, M. Larsson, S. Rosén, and K. Schmidt, AIP Conf. Proc. **821**, 465 (2006).
[12] D. Zajfman, A. Wolf, D. Schwalm, D. A. Orlov, M. Grieser, R. von Hahn, C. P. Welsch, J. R. Crespo Lopez-Urrutia, C. D. Schröter, X. Urbain, and J. Ullrich, J. Phys.: Conf. Ser. **4**, 296 (2005).
[13] C. P. Welsch, J. Ullrich, C. Glässner, A. Schempp, R. Dörner, and H. Schmidt-Böcking, Nucl. Instrum. Methods Phys. Res. A **527**, 284 (2004).
[14] A. B. Nielsen, P. Hvelplund, and S. Brøndsted Nielsen, Int. J. Mass. Spectrom. **232**, 79 (2004).
[15] O. P. Charkin, N. M. Klimenko, P. T. Nguyen, D. O. Charkin, A. M. Mebel, S. H. Lin, Y.-S. Wang, S.-C. Wei, and H.-C. Chang, Chem. Phys. Lett. **415**, 362 (2005); O. P. Charkin, N. M. Klimenko, D. O. Charkin, H.-C. Chang, and S.-H. Lin, J. Phys. Chem. A **111**, 9207 (2007).
[16] S. Brøndsted Nielsen, J. U. Andersen, J. S. Forster, P. Hvelplund, B. Liu, U. V. Pedersen, and S. Tomita, Phys. Rev. Lett. **91**, 048302 (2003); E. S. Worm, I. H. Andersen, J. U. Andersen, A. I. S. Holm, P. Hvelplund, U. Kadhane, S. Brøndsted Nielsen, J.-C. Poully, and K. Støchkel, Phys. Rev. A **75**, 042709 (2007).
[17] D. Thölmann, D. S. Tonner, and B. McMahon, J. Phys. Chem. **98**, 2002 (1994); P. D. Schnier, W. D. Price, R. A. Jockusch, and E. R. Williams, J. Am. Chem. Soc. **118**, 7178 (1996); W. D. Price, P. D. Schnier, R. A. Jockusch, E. F. Strittmatter, and E. R. Williams, J. Am. Chem. Soc. **118**, 10640 (1996); R. C. Dunbar and T. B. McMahon, Science **279**, 194 (1998).

Dianions of 7,7,8,8-tetracyano-*p*-quinodimethane and perfluorinated tetracyanoquinodimethane: Information on excited states from lifetime measurements in an electrostatic storage ring and optical absorption spectroscopy

Subhasis Panja, Umesh Kadhane, Jens Ulrik Andersen, Anne I. S. Holm, Preben Hvelplund, Maj-Britt Suhr Kirketerp, Steen Brøndsted Nielsen,[a] and Kristian Støchkel
Department of Physics and Astronomy, University of Aarhus, DK-8000 Aarhus C, Denmark

Robert N. Compton
Department of Physics, The University of Tennessee, Knoxville, Tennessee 37996 and Department of Chemistry, The University of Tennessee, Knoxville, Tennessee 37996, USA

James S. Forster
Département de Physique, Université de Montréal, Montréal, Québec H3C3J7, Canada

Kristine Kilså and Mogens Brøndsted Nielsen
Department of Chemistry, University of Copenhagen, Universitetsparken 5, DK-2100 Copenhagen Ø, Denmark

(Received 2 July 2007; accepted 20 July 2007; published online 24 September 2007)

We have developed an experimental technique that allows us to study the physics of short lived molecular dianions in the gas phase. It is based on the formation of monoanions via electrospray ionization, acceleration of these ions to keV energies, and subsequent electron capture in a sodium vapor cell. The dianions are stored in an electrostatic ion storage ring in which they circulate with revolution times on the order of 100 μs. This enables lifetime studies in a time regime covering five orders of magnitude, $10^{-5}-1$ s. We have produced dianions of 7,7,8,8-tetracyano-*p*-quinodimethane and 2,3,5,6-tetrafluoro-7,7,8,8-tetracyano-*p*-quinodimethane (TCNQ-F_4) and measured their lifetimes with respect to electron autodetachment. Our data indicate that most of the dianions were initially formed in electronically excited states in the electron transfer process. Two levels of excitation were identified by spectroscopy on the dianion of TCNQ-F_4, and the absorption spectrum was compared with spectra obtained from spectroelectrochemistry of TCNQ-F_4 in acetonitrile solution. © *2007 American Institute of Physics*. [DOI: 10.1063/1.2771177]

I. INTRODUCTION

In recent years there has been a growing interest in the physics and chemistry of molecular dianions in the gas phase with numerous reports on their formation and behavior.[1–4] Due to the Coulomb repulsion between the two excess electrons, dianions are often electronically unstable and the binding energy of the second electron depends strongly on the molecular size.[5] The second electron is confined within the Coulomb barrier, which is a result of a short range attraction and the long range Coulomb repulsion, a situation quite similar to that of an α particle inside a metastable nucleus.[6] The dianion may therefore have a long lifetime due to low rates of tunneling through the Coulomb barrier. Dianions are examples of molecular systems in which electron correlation is of major importance, and a fundamental understanding of their physics may pave the way for improvement of quantum chemistry models.

Because of the fragility of dianions, their formation is an experimental challenge. We have developed a technique in which monoanions with high translational energy (keV) collide with alkali-metal atoms in a vapor and pick up electrons to become dianions.[7–14] In this way we produced dianions of 7,7,8,8-tetracyano-*p*-quinodimethane (TCNQ) and 2,3,5,6-tetrafluoro-7,7,8,8-tetracyano-*p*-quinodimethane (TCNQ-F_4) (Fig. 1),[9] which are electron acceptors that have been widely employed for the construction of electrically conductive organic charge-transfer salts.[15] The precursor radical anions were produced with a large yield from electrospray ionization due to the high electron affinities of the neutral mol-

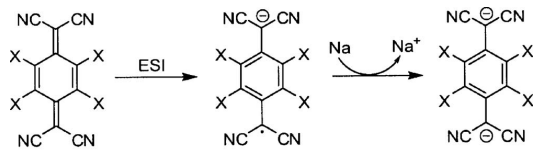

FIG. 1. Sodium-promoted generation of TCNQ and TCNQ-F_4 dianions: Monoanions of TCNQ and TCNQ-F_4 were produced by electrospray ionization and converted to dianions in collisions with Na.

[a]Electronic mail: sbn@phys.au.dk

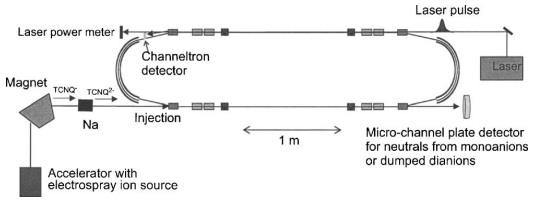

FIG. 2. Schematic layout of the electrostatic storage ring ELISA.

ecules (3.4±0.2 eV of TCNQ).[16–18] The possibility of symmetric cleavage of the radical anions to produce fragment ions of similar mass-to-charge ratio as the dianions was ruled out from selection of the natural ^{13}C isotope at one mass higher.[9] In our previous experiments we did not obtain information about the lifetimes of the dianions with respect to electron autodetachment or about their stabilities, nor did the experiments reveal information on the electronic states being populated in the electron transfer process. To address these questions, we have in this work studied the decay of $TCNQ^{2-}$ and TCNQ-F_4^{2-} dianions in the Electrostatic Ion Storage ring in Aarhus, ELISA and recorded the gas phase absorption spectrum of TCNQ-F_4^{2-}. This work parallels earlier ELISA studies of the dianions of C_{60} and C_{70}.[12] In addition, we have used TCNQ-F_4 in a spectroelectrochemical study in order to obtain absorption maxima in solution.

II. EXPERIMENT

A. Gas phase measurements

The TCNQ and TCNQ-F_4 anions were produced by electrospray ionization of the molecules dissolved in acetonitrile. The solutions were pumped through a needle held at a voltage of −3 kV with a flow rate of 3 μl/min. The nanodroplets were passed through a heated capillary (150 °C) to remove the remaining solvent molecules. The resulting bare ions were stored for typically 0.1 s and thermalized at room temperature in a multipole ion trap filled with a He gas maintained at about 1 mbar with an adjustable gas inlet. Ion bunches ejected from the trap were accelerated to 22 keV, and ions of interest were mass selected with a bending magnet. The ions then passed through a Na vapor cell, in which doubly charged anions $TCNQ^{2-}$ and TCNQ-F_4^{2-} were produced by electron capture from Na. All ions (singly and doubly charged anions) were injected into the electrostatic ion storage ring ELISA,[19,20] which is illustrated in Fig. 2. The ring parameters were first set to store monoanions and later to store dianions.

We first measured lifetimes of monoanions by counting the neutrals hitting the microchannel plate (MCP) detector placed at the end of the first straight section (injection side, cf. Fig. 2). These lifetimes are determined by collisions with the residual gas in the ring which has a pressure of a few times 10^{-11} mbar.

Two methods of observation were used to study the decay of dianions: one determines directly the decay rate, the other the decrease of the number of stored ions. In the first, decay of metastable dianions by electron autodetachment was measured by detection of singly charged anions with a channeltron placed very close to the stored beam after a 10° deflector on the opposite side to injection in the ring (see Fig. 2). The revolution periods for $TCNQ^{2-}$ and TCNQ-F_4^{2-} are 57.8 and 66.1 μs, respectively. The injection rate was normally 10 Hz but was decreased for the observation of long decay times. In the second method, the beam was dumped into the MCP detector at different times after the injection. The dumped beam counts were normalized to the sum of channeltron counts over the first 100 μs.

Absorption spectra of TCNQ-F_4^{2-} dianions were obtained from laser absorption at two different storage times in the ring (0.5 and 1.6 ms). The ions were irradiated with light on the "back side" of the ring (Fig. 2). The laser was an optical parametric oscillator, pumped by the third harmonic radiation from a Nd-doped yttrium aluminum garnet laser. The measurements were made with an unfocused laser beam about 1 cm in diameter and with a pulse energy of 0.15–0.30 mJ and pulse width of 10 ns (full width at half maximum). The pulse repetition rate of the laser was 10 Hz so that each ion bunch was irradiated with only one laser pulse. Monoanions formed upon photodetachment were again measured with the channeltron detector.

B. Solution phase measurements

Cyclic voltammetry was measured in acetonitrile (MeCN, Labscan, HPLC grade, dried over molecular sieves) solutions containing 0.1*M* Bu_4NPF_6 (from Aldrich, used as received) as supporting electrolyte, using a CHI630B potentiostat (CH Instruments, TX). Pt electrodes were used as both working and counterelectrodes, while the reference was Ag/Ag^+ in the same solvent. All potentials are reported relative to ferrocene (Fc^+/Fc, 0.31 V versus standard calomel electrode[21]) measured in the same setup.

The apparatus was also used for the spectroelectrochemical experiments in a 1 mm absorption cuvette (Quartz, Hellma), except that the counterelectrode was separated from the solution by a glass frit, and the working electrode exchanged for a Pt grid (mesh 400). Absorption spectra of the neutral, radical anion, and dianionic species were recorded on a Cary 50 (Varian Inc.) with a potential that was set to be approximately 0.2 V more reductive than the peak potentials found from cyclic voltammetry.

III. RESULTS AND DISCUSSION

A. Lifetimes in the storage ring

The decay spectrum of $TCNQ^{\bullet-}$ monoanions is shown in Fig. 3. The signal in the MCP detector results from neutrals formed by collisions with residual gas in the ring and is well described by exponential decay with lifetime of 1 s. A similar lifetime was obtained for TCNQ-$F_4^{\bullet-}$ indicating a similar collision cross section.

As mentioned above, lifetimes of $TCNQ^{2-}$ dianions were measured in two different ways, either by looking at the decay rate $n \propto -dN/dt$, where N is the number of stored dianions and t is the time after they were formed, or by measuring the number N of stored ions. The results are shown in Fig. 4, and three exponentials were required to describe all of

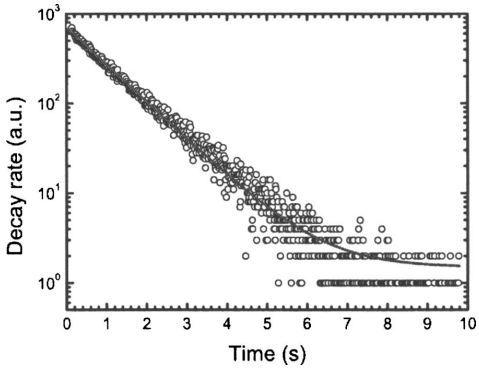

FIG. 3. Time spectrum of neutral counts for stored $TCNQ^{\bullet-}$ ions in ELISA.

the data satisfactorily. The expressions used for the fits to the channeltron data and MCP data are given below as Eqs. (1) and (2), respectively,

$$n(t) \propto -\mathrm{d}N/\mathrm{d}t = A_1 k_1 \exp(-k_1 t) + A_2 k_2 \exp(-k_2 t) + A_3 k_3 \exp(-k_3 t), \quad (1)$$

$$N(t) = A_1 \exp(-k_1 t) + A_2 \exp(-k_2 t) + A_3 \exp(-k_3 t), \quad (2)$$

where A_i and k_i $(i=1,2,3)$ are the three preexponential factors and rate constants. The time constants $\tau_i = 1/k_i$ and the relative contribution of each exponential f_i $(=A_i/[A_1+A_2+A_3])$ are summarized in Table I. In the fits to the two data sets the same time constants and relative contributions were used. The component with a long lifetime of 0.72 s is attributed to collisional electron detachment due to the residual gas and comprises about 1% of the total decay. The majority of ions (95%) decayed with a lifetime of 0.2 ms and about 4% with a lifetime of 1.0 ms.

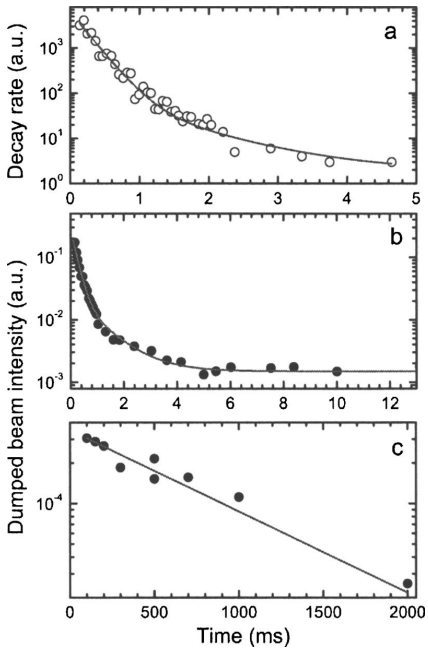

FIG. 4. (a) Electron emission from $TCNQ^{2-}$ in the storage ring, detected as a signal from $TCNQ^{\bullet-}$ in a channeltron placed after the 10° electrostatic deflector. [(b) and (c)] Time dependence of the number of $TCNQ^{2-}$ dianions stored in the ring, measured by dumping the beam onto a microchannel plate detector with a varying delay after the injection.

TABLE I. Dianion lifetimes. The number in parenthesis is the fraction that the component comprises of the total decay.

	τ_1 (ms)	τ_2 (ms)	τ_3 (s)
$TCNQ^{2-}$	0.2 (0.95)	1.0 (0.04)	0.72 (0.01)
$TCNQ\text{-}F_4^{2-}$	0.7 (0.30)	15.0 (0.67)	1.1 (0.03)

The TCNQ dianion has been predicted to be electronically bound by about 0.1 eV,[9] and it is therefore surprising that most of the dianions decayed quickly [with a significantly shorter lifetime than the upper limit (1 s) determined by collisions]. This indicates that in the electron transfer process, two different electronically excited states are populated to account for the two short lifetimes (Fig. 5). Internal conversion results in dianions with high internal energy that decay by thermionic emission of the excess electron. We note that in earlier mass-analyzed kinetic energy measurements there was no measurable broadening of peaks corresponding to monoanionic fragments[9] as has been observed for other dianions formed in this way,[8,13] and we therefore assume that the decay channel is dominantly electron loss and not Coulomb explosion into two singly charged ions. Also, calculations indicate that Coulomb explosion channels are endothermic by at least 1 eV.[9]

Similar experiments were performed for $TCNQ\text{-}F_4^{2-}$, and decay spectra are shown in Fig. 6. Three time constants are again needed to account for the total decay, and the data were fitted with the constraint that τ_i and f_i should be the same for both data sets (channeltron data and MCP data). The values obtained from the fits are given in Table I. The long-lifetime component ($\tau = 1.1$ s) due to collisional electron detachment is larger than that for $TCNQ^{2-}$ but is still only a minor part of

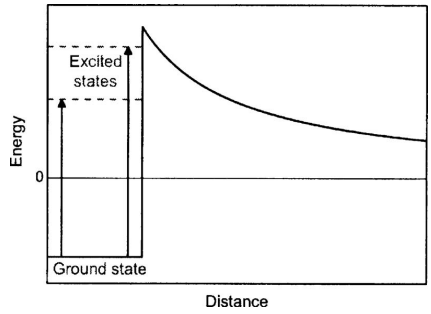

FIG. 5. Potential energy of dianion as a function of the distance between the monoanion and the electron. The potential energy is zero at infinite distance. The electronic ground state is a bound state, whereas the two excited states are unbound. Electron transfer from sodium occurs to either the electronic ground state or to an electronically excited state. The two electronically excited states can also be reached by photon absorption of the dianion in its electronic ground state.

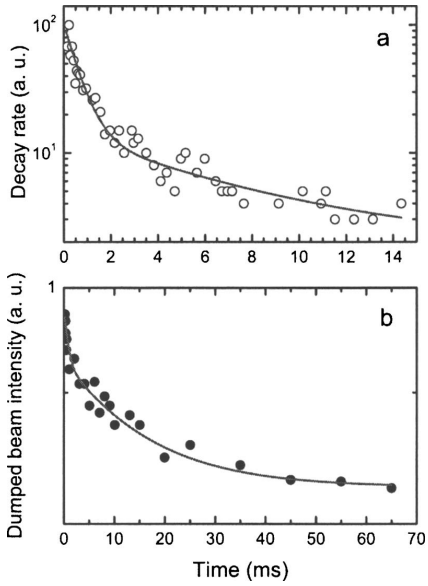

FIG. 6. (a) Electron emission from TCNQ-F_4^{2-} in the storage ring, detected as a signal from TCNQ-$F_4^{\bullet-}$ in a channeltron placed after the 10° electrostatic deflector. (b) Time dependence of the number of TCNQ-F_4^{2-} dianions stored in the ring, measured by dumping the beam onto a microchannel plate detector with a varying delay after the injection.

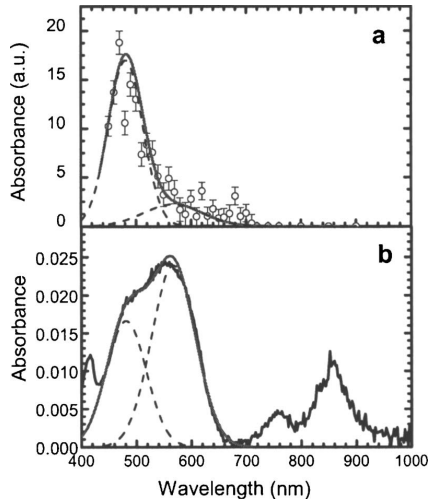

FIG. 7. Gas phase (a) and solution phase (b) absorption spectra of TCNQ-F_4^{2-}. The data between 400 and 700 nm can be described by the sum of two Gaussians.

the total decay (3%). The two shorter lifetimes, 0.7 and 15 ms, are longer than those for $TCNQ^{2-}$. Furthermore, the fraction of the second component of TCNQ-F_4^{2-} (67%) is significantly larger than that for $TCNQ^{2-}$ (4%).

The electron binding energy of the TCNQ-F_4 dianion in its electronic ground state is estimated to be close to 1 eV,[14] but the fact that only a minor number of the ions are electronically stable implies that also for this ion excited states are populated in the electron transfer process. Owing to the electron-withdrawing properties of fluorine, the four C–F bonds are polarized and both the ground state and the excited states are lower in energy relative to the nonfluorinated species. However, the Coulomb barrier is also reduced, and the lifetimes for electron autodetachment for $TCNQ^{2-}$ and TCNQ-F_4^{2-} are therefore quite similar.

The inference of electronically excited states is in agreement with the observation of bound excited states of TCNQ and TCNQ-F_4 radical monoanions.[22–25] Thus, Brinkman *et al.*[22,23] reported electronically excited states of $TCNQ^{-\bullet}$ from electron photodetachment studies and these states were theoretically characterized by Zakrzewski *et al.*[24] Sobczyk *et al.* investigated TCNQ-$F_4^{\bullet}$ theoretically and also found bound excited states for this ion.

B. Absorption spectroscopy

The absorption spectrum in the wavelength region of 450–900 nm of TCNQ-F_4^{2-} after a storage time of 0.5 ms in the ring is shown in Fig. 7(a). A band with maximum at about 481 nm is observed. The band has a small shoulder extending up to about 700 nm indicative of a second electronic transition with lower oscillator strength. Two Gaussians with maxima at 481 and 567 nm (solution phase maximum, *vide infra*) describe the data quite well; the corresponding transition energies are 2.53 and 2.19 eV. It is possible that these two excited states are the initial states being populated in the electron transfer process. It implies that the Coulomb barrier is more than 2.6 eV above the ground state energy. This is reasonable since the distance between the two $C(CN)_2$ groups is about 6 Å and the Coulomb repulsion energy between two electrons separated by this distance is 2.4 eV. We notice that no monoanions produced from photoexcited dianions could be measured after one revolution. A spectrum taken after a longer storage time (1.6 ms) was similar to the 0.5 ms spectrum, but the data quality was worse because of fewer ions in the ring.

We also carried out solution phase experiments to elucidate the role of a solvent on the electronic properties of the dianion. Cyclic voltammetry showed reversible reductions for TCNQ-F_4 at half-wave potentials of −0.10 and −0.65 V vs Fc^+/Fc in MeCN, while the poorer acceptor TCNQ is reduced at −0.20 and −0.76 V vs Fc^+/Fc under the same conditions. Thus, the reductions of TCNQ-F_4 are anodically shifted by the same amount (+0.10 V) relative to those of TCNQ, as previously observed.[26] We performed spectroelectrochemistry on TCNQ-F_4 [Figs. 7(b) and 8], and absorption data for the neutral, radical anion, and dianion species are collected in Table II together with the values found previously for TCNQ.[27,28] The absorption of TCNQ-F_4^{2-} at 335 nm is very close to that of $TCNQ^{2-}$ (334 nm), but in addition TCNQ-F_4^{2-} displays broad absorption bands at approximately 481 and 567 nm (maxima from Gaussian fits). The original spectrum for the neutral TCNQ-F_4 was generated after reoxidation at +0.43 V vs Fc^+/Fc.

Broad absorption in the 450–700 nm region of TCNQ-F_4^{2-} is observed both in the gas phase and in solution.

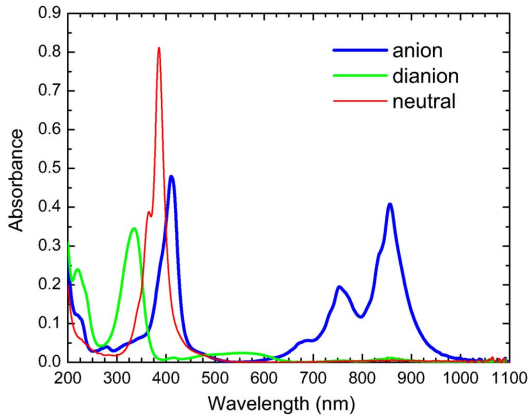

FIG. 8. (Color online) Spectroelectrochemistry of TCNQ-F_4 (0.1 mM) in MeCN containing Bu_4NPF_6 (0.1*M*) as supporting electrolyte. Blue: Anion after electrolysis at −0.10 V vs Fc^+/Fc; Green: Dianion after electrolysis at −0.65 V vs Fc^+/Fc; Red: Neutral species obtained after final electrolysis at +0.43 V vs Fc^+/Fc. Cell path length: 1 mm.

This finding confirms that the solution-state absorption is an intrinsic absorption of the dianion and not the result of aggregation (e.g., dimer formation). Secondly, we note that the electronic transition with maximum at 477 nm in the gas phase is unperturbed by solvation of TCNQ-F_4^{2-} in acetonitrile. For comparison, in the case of TCNQ radical anions, the absorption spectrum of the anion in the gas phase was also found to be very similar to that of the anion in solution phase.[22] However, for TCNQ-F_4^{2-} the oscillator strength of the band at 567 nm is much larger in solution than in gas phase [Fig. 7(b)]. This observation seems to indicate that the two bands should be assigned to separate electronic transitions rather than vibrational fine structure. Finally, the solution spectrum reveals absorption between 700 and 1000 nm, which is most likely due to monoanions in the solution not being reduced to dianions since in the gas phase no absorption occurred in this region. Likewise, the small absorption at 420 nm in solution is due to monoanion absorption.

IV. CONCLUSIONS

Monoanions of 7,7,8,8-tetracyano-*p*-quinodimethane (TCNQ) and 2,3,5,6-tetrafluoro-7,7,8,8-tetracyano-*p*-quinodimethane (TCNQ-F_4), produced by electrospray ionization, were converted into dianions in collisions in a sodium vapor. After injection into an electrostatic ion storage ring, most of the dianions decayed by electron emission on a significantly shorter time scale (microseconds to milliseconds) than for collision-induced dissociation in the ring (seconds). Since the electron binding energies of the dianions in their electronic ground state are close to 0 and 1 eV for $TCNQ^{2-}$ and TCNQ-F_4^{2-}, respectively, the electron is transferred into an electronically excited state of the dianion with positive energy during the femtosecond interaction time of the formation of the dianion. Two short lifetimes (determined by the probability for tunneling through the Coulomb barrier) were measured, indicating that two excited states are formed. In agreement with this, spectroscopy on TCNQ-F_4^{2-} revealed two absorption bands between 450 and 700 nm that were also measured for dianions in acetonitrile solution. Uptake of an electron by the radical monoanion into one of these two electronically excited states followed by internal conversion leads to vibrationally excited dianions that subsequently decay by electron emission with two characteristic lifetimes. The decay of dianions is interpreted as thermally assisted tunneling, either via excited electronic states or with transfer of energy to the electron from vibrational hot bands.

TABLE II. Absorption maxima of TCNQ-F_4 and its reduced species ($10^{-4}M$) in 0.1*M* Bu_4NPF_6/MeCN in comparison to those obtained previously for TCNQ.

	λ_{max} (nm)		λ_{max} (nm)
TCNQ-F_4	386	TCNQ	398[c]
TCNQ-$F_4^{\bullet-}$	410, 754/856[a]	$TCNQ^{\bullet-}$	441, 690, 762[c]
TCNQ-F_4^{2-}	335, 481/567[b]	$TCNQ^{2-}$	334[c]

[a]Electrolysis at −0.10 V vs Fc^+/Fc.
[b]Electrolysis at −0.65 V vs Fc^+/Fc.
[c]References 27 and 28. These literature experiments were performed with a detector range from 300 to 850 nm.

ACKNOWLEDGMENTS

Three of the authors (S.B.N. and M.B.N./K.K.) gratefully acknowledge support from the Danish Natural Science Research Council (Grant Nos. 21-04-0514 and 2111-04-0018).

[1] X.-B. Wang and L. S. Wang, Phys. Rev. Lett. **83**, 3402 (1999).
[2] A. Dreuw and L. S. Cederbaum, Chem. Rev. (Washington, D.C.) **102**, 181 (2002).
[3] M. K. Scheller, R. N. Compton, and L. S. Cederbaum, Science **270**, 1160 (1995).
[4] J. Kalcher and A. F. Sax, Chem. Rev. (Washington, D.C.) **94**, 2291 (1994).
[5] L. S. Wang, C.-F. Ding, X.-B. Wang, and J. B. Nicholas, Phys. Rev. Lett. **81**, 2667 (1998).
[6] W. H. Green, Jr., S. M. Gorun, G. Fizgerald, P. W. Fowler, A. Ceulemans, and B. C. Titeca, J. Phys. Chem. **100**, 14892 (1996).
[7] O. V. Boltalina, P. Hvelplund, M. C. Larsen, and M. O. Larson, Phys. Rev. Lett. **80**, 5101 (1998).
[8] A. B. Nielsen, P. Hvelplund, B. Liu, S. Brøndsted Nielsen, and S. Tomita, J. Am. Chem. Soc. **125**, 9592 (2003).
[9] S. Brøndsted Nielsen and M. Brøndsted Nielsen, J. Chem. Phys. **119**, 1069 (2003).
[10] B. Liu, P. Hvelplund, S. Brøndsted Nielsen, and S. Tomita, Phys. Rev. Lett. **92**, 168301 (2004).
[11] B. Liu, P. Hvelplund, S. Brøndsted Nielsen, and S. Tomita, J. Chem. Phys. **121**, 4175 (2004).
[12] S. Tomita, J. U. Andersen, H. Cederquist *et al.*, J. Chem. Phys. **124**, 024310 (2006).
[13] K. Drenck, P. Hvelplund, C. J. McKenzie, and S. Brøndsted Nielsen, Int. J. Mass. Spectrom. **244**, 144 (2005).
[14] S. Yu. Ovchinnikov, J. Macek, A. A. Tuinman, J. D. Steill, R. N. Compton, P. Hvelplund, A. I. S. Holm, S. Brøndsted Nielsen, and M. Brøndsted Nielsen, Phys. Rev. A **73**, 064704 (2006).
[15] R. C. Wheland and J. L. Gillson, J. Am. Chem. Soc. **98**, 3916 (1976).
[16] C. Jin, R. E. Haufler, R. L. Hettich, R. N. Compton, A. A. Puretzky, A. V. Dem'yanenko, and A. A. Tuinman, Science **68**, 263 (1994).
[17] B. Milián, R. Pou-Amérigo, R. Viruela, and E. Ortí, Chem. Phys. Lett. **148**, 391 (2004).
[18] J. Simons, P. Skurski, and R. Barrios, J. Am. Chem. Soc. **112**, 11893 (2000).
[19] S. P. Møller, Nucl. Instrum. Methods Phys. Res. A **394**, 281 (1994).

[20] J. U. Andersen, J. S. Forster, P. Hvelplund, T. J. D. Jørgensen, S. P. Møller, S. Brøndsted Nielsen, U. V. Pedersen, S. Tomita, and H. Wahlgreen, Rev. Sci. Instrum. **73**, 1284 (2002).
[21] A. J. Bard and L. R. Faulkner, *Electrochemical Methods: Fundamentals and Applications*, 2nd ed. (Wiley, New York, 2001).
[22] E. A. Brinkman, E. Günther, and J. I. Brauman, J. Chem. Phys. **95**, 6185 (1991).
[23] E. A. Brinkman, E. Günther, O. Schafer, and J. I. Brauman, J. Chem. Phys. **100**, 1840 (1994).
[24] V. G. Zakrzewski, O. Dolgounitcheva, and J. V. Ortiz, J. Chem. Phys. **105**, 5872 (1996).
[25] M. Sobczyk, P. Skurski, and J. Simons, J. Phys. Chem. A **107**, 7084 (2003).
[26] N. Ueda, B. Natsume, K. Yanagiuchi, Y. Sakata, T. Enoki, G. Saito, H. Inokuchi, and S. Misumi, Bull. Chem. Soc. Jpn. **56**, 775 (1983).
[27] V. Bellec, M. G. De Backer, E. Levillain, F. C. Sauvage, B. Sombret, and C. Wartelle, Electrochem. Commun. **3**, 483 (2001).
[28] E. Levillain (private communication).

Electron-Capture–Induced Dissociation of Protoporphyrin IX Ions

Virgile Bernigaud,[a] Kasper Drenck,[b] Bernd A. Huber,[a] Preben Hvelplund,[b] Tristan Jabot,[b] Umesh Kadhane,[b] Maj-Britt Suhr Kirketerp,[b] Bo Liu,[c] Morten Køcks Lykkegaard,[b] Bruno Manil,[a] and Steen Brøndsted Nielsen[b]

[a] Centre de Recherche sur les Ions, les Matériaux et la Photonique, Caen Cedex 5, France
[b] Department of Physics and Astronomy, University of Aarhus, Aarhus C, Denmark
[c] Institute of Photo-biophysics, School of Physics and Electronics, Henan University, Kaifeng, China

Electron-capture induced dissociation of protoporphyrin cations and anions has been studied. The cations captured two electrons in two successive collisions and were converted to the corresponding even-electron anions. About one fifth of the ions lost a hydrogen atom to become radical anions but otherwise very little fragmentation was observed. The anions captured an electron to become dianions. No hydrogen loss occurred, and the only fragmentation channel observed was loss of CO_2H, to give a doubly charged carbanion. Our results indicate that protoporphyrin ions are very efficient in accommodating one or even two electrons in the lowest unoccupied molecular orbital of the porphyrin macrocycle, and that electron capture induces only limited dissociation. (J Am Soc Mass Spectrom 2008, 19, 809–813) © 2008 American Society for Mass Spectrometry

Electron-induced fragmentation of biomolecular ions has become a field of surpassing interest after the pioneering work done by McLafferty and Zubarev ten years ago. Most work has focused on peptides and proteins [1–15], oligonucleotides [16], and recently oligosaccharides [17] and lipids [18]. To study the fragmentation channels, three experimental techniques are commonly used in combination with mass spectrometry: (1) electron capture dissociation (ECD), where ions interact with low-energy electrons in an ion trap [1–7]; (2) electron-transfer dissociation (ETD), where the electron donor is an anion [8–12]; and (3) electron-capture induced dissociation (ECID), where ions of high kinetic energy (keV) capture an electron from a gas target—typically sodium or cesium with low ionization energies [13–15]. In contrast to ECD and ETD, ECID works well both for cations and for anions, as has been demonstrated in several papers [13–15, 19, 20], and even singly charged cations can serve as subjects for investigation [21, 22].

To our knowledge there are no reports in the literature on electron capture by isolated porphyrin ions despite the fact that these ions are ubiquitous in nature and play many important roles in biochemistry. In this work, we have therefore studied ECID of protoporphyrin IX (PP) ions (Scheme **1**) that can be produced both as positive and negative ions with electrospray ionization (ESI). Coordination of iron to PP gives heme, which is found in the interior of hemoglobin and myoglobin proteins where it acts as a binding center for dioxygen. In our experiments, ions are accelerated to high energies and collided with cesium vapor. The collision interaction time is a few femtoseconds, and it is therefore reasonable to assume a nearly vertical electron-transfer process. Fragmentation is monitored on a timescale of a few microseconds, which is the flight time from the collision cell to the analyzer.

Experimental

The experimental setup has been described in detail elsewhere [23, 24]. Ions were produced by ESI. Protoporphyrin IX was dissolved in dichloromethane/methanol (1:1) to produce cations and in methanol to produce anions. The ions were accelerated to 50-keV translational energy, and ions with the *m/z* of interest were selected by a magnet. After collisions with cesium vapor, the product ions were analyzed by an electrostatic analyzer that scanned the kinetic energy of the ions. The spectra are denoted mass-analyzed ion kinetic energy (MIKE) spectra. Experiments were also performed with helium or neon as collision gas to measure collision-induced dissociation (CID) processes.

Computational Details

Calculations were performed with the GAUSSIAN 98 program package [25]. The $[PP–H]^-$ anion was geometry

Contribution to the special focus issue "ECD and Related Approaches to Ion Activation," dedicated to Roman Zubarev.

Address reprint requests to Steen Brøndsted Nielsen, University of Aarhus, Department of Physics and Astronomy, Ny Munkegade, DK-8000 Aarhus C, Denmark, e-mail: sbn@phys.au.dk; or to Bo Liu, Institute of Photo-biophysics, School of Physics and Electronics, Henan University, Kaifeng, China, e-mail: boliu@henu.edu.cn.

1044-0305/08/$32.00
doi:10.1016/j.jasms.2008.01.002

Published online January 25, 2008
Received December 10, 2007
Revised January 14, 2008
Accepted January 14, 2008

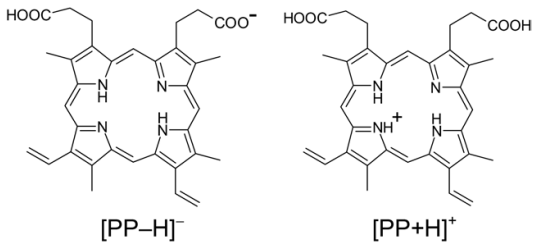

Scheme 1

optimized at the PM3 level, and the lowest unoccupied molecular orbital (LUMO) was calculated at the B3LYP/6-31++G(*d*) level of theory. Energies of the monoanion and the dianion in the same geometry as the monoanion were calculated to determine the vertical electron affinity, and the calculation also provided the singly occupied molecular orbital (SOMO) of the dianion.

Results and Discussion

First we consider the fragmentation of positive ions. The MIKE spectrum obtained for the collisions between $[PP+H]^+$ cations (*m/z* 563) and helium is shown in Figure 1A and resembles previously published fragmentation spectra of similar porphyrin ions [26]. The dominant dissociation channel is loss of CH_2COOH, which is the lowest-energy channel according to work by Charkin et al. [27, 28]. The other peaks are assigned to the loss of one or more side chains: CH_3 (15), CH_2CH (27), COOH (45), CH_2COOH (59), CH_2CH_2COOH (73) (mass). A peak in the center of the spectrum is assigned to the doubly charged $[PP+H]^{2+}$ ion formed after electron detachment, likely due to collisions with residual dioxygen in the beam line [29]. The charge-reversal spectrum, $^+CR^-$, obtained from collisions with cesium (Figure 1B) reveals that the dominant ion is $[PP+H]^-$ (*m/z* 563) formed by capture of two electrons. A narrow scan with higher resolution in the region of the peak shows that the peak has a tail toward lower mass (Figure 2B). We assign this lower mass ion to an ion (*m/z* 562) that has lost one hydrogen atom. A fit of the composite peak to two Gaussians with maxima at 563 and 562 provides an estimate of the ratio of the *m/z*-562 peak to the *m/z*-563 peak of 1/5. To confirm the H loss channel, we used CH_3OD instead of CH_3OH for electrospray to produce deuterated $[PP+H]^+$ ions. The maximum number of exchangeable protons is five ($3 \times NH + 2 \times COOH$). The $[PP+H]^+$–d_4 ion (*m/z* 567) was selected by the magnet for collisions with cesium (the beam contained some contamination by the isobaric ^{13}C-$[PP+H]^+$–d_3), and the spectrum of the product anions in the region of the parent mass is shown in Figure 2C. Signal due to D loss is evident at *m/z* 565, and H loss is also seen. The fragment ions at lower mass (Figure 1B) may be due to electron capture to the parent ion but they may also arise from electron capture to CID fragments, that is, to neutral fragments that are formed together with the positive fragments shown in Figure 1A. The formation of a positive fragment ion that captures two electrons in two consecutive collisions is less likely since it requires a total of three collisions. Still the negatively charged fragments contribute less than 10% of the total signal from negative ions.

In another experiment, $[PP–H]^-$ anions (*m/z* 561) were collided with helium. The dominant CID channel was loss of CO_2 (Figure 3A) but other side-chain losses were also seen, such as loss of CH_3 or CH_2. This spectrum is to be compared with the ECID spectrum to identify new processes. Thus, when the ions collided with cesium, two new peaks appeared (Figure 3B) that are tentatively assigned to the $[PP–H]^{2-}$ dianion (*m/z* 280.5) and the dianion that has lost CO_2H (*m/z* 258). Since the parent ion is nearly symmetric, it is in theory also possible that it would break apart to give a fragment ion with half the *m/z* of that of the parent ion. The high stability of the macrocycle, however, renders such a process rather unlikely. To exclude it with certainty, we selected the parent ion that contained one ^{13}C (*m/z* 562) and found that the peak moved up with 0.5 to *m/z* of 281 as expected for a dianion (Figure 5). Symmetric breakages should give equal abundance of fragment ions at *m/z* 280 and

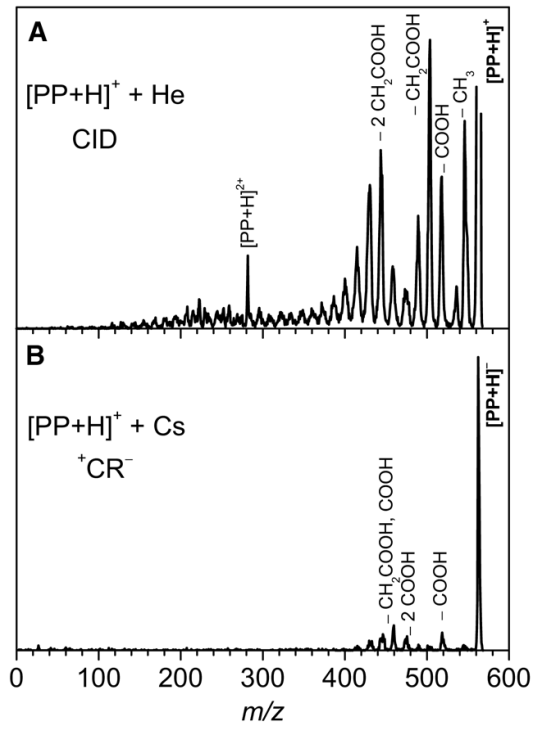

Figure 1. MIKE spectra obtained after collisions between $[PP+H]^+$ and helium (**A**) and cesium (**B**). In the former case, positive ions were measured and in the latter negative ions.

m/z 281 and can be excluded. According to the calibration, the dianion is intact (Figure 4), but it is hard to conclude with certainty because of the width of the peak (1.5 Thomson). However, it is easy to check whether hydrogens on heteroatoms are lost since these can again be exchanged with deuterium by electrospraying from CH_3OD instead of CH_3OH.

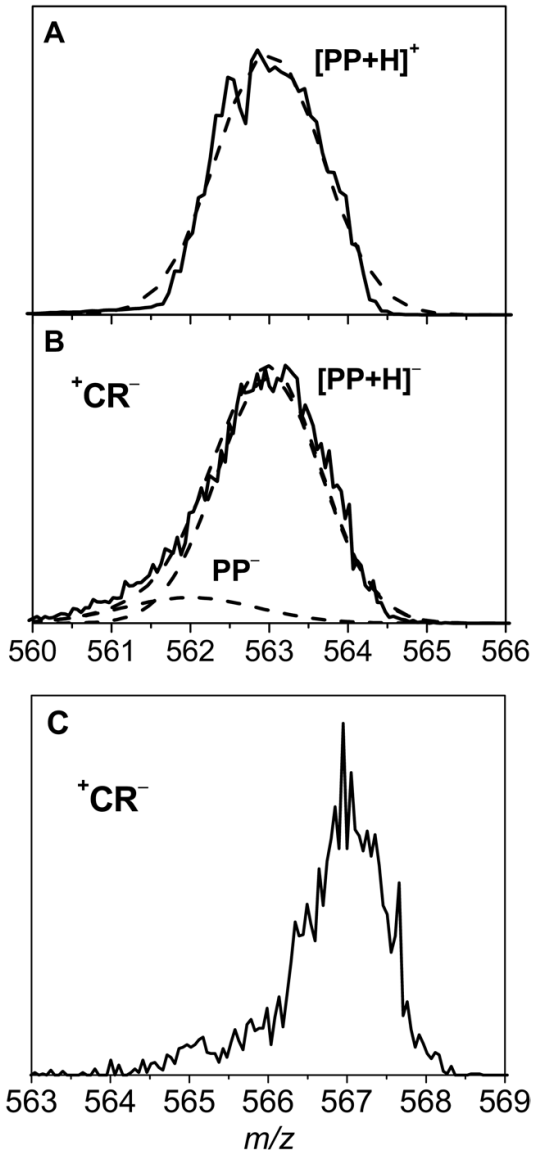

Figure 2. Narrow scans in the region of the parent ion, $[PP+H]^+$ (**A**) and the $[PP+H]^-$ ion formed after two collisions with cesium (**B**). The peaks are described by Gaussians. (**C**) Narrow scan in the region of the $[PP+H]^-$–d_4 ion formed after two collisions between $[PP+H]^+$–d_4 and cesium. Four of five exchangeable protons are replaced with deuterons in the parent ion.

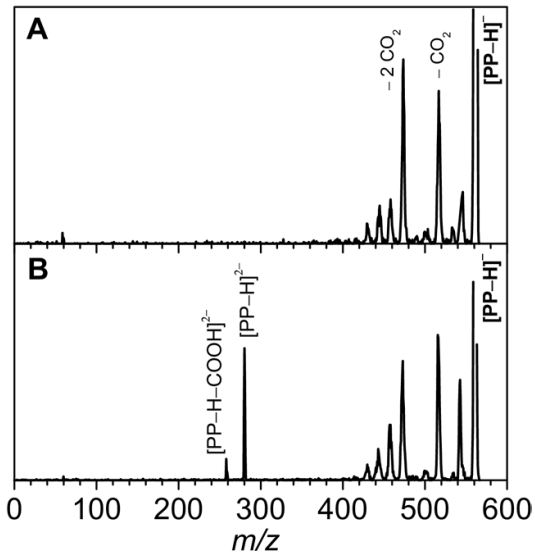

Figure 3. MIKE spectra obtained after collisions between $[PP–H]^-$ and neon (**A**) and cesium (**B**). Negative ions are measured.

We therefore selected ions that had exchanged one, two, and three hydrogens with deuteriums (maximum number is three, 2 × N*H* + COO*H*) and recorded narrow scans in the region around the dianion (Figure 5). It is evident that the peak does not move, that is, it always appears at half the value of the analyzer voltage to transmit the parent ion, and hence we conclude that hydrogen from a heteroatom is not lost. It is stressed that this is an opposite finding to that of nucleotide anions that after electron capture lost a hydrogen atom from one of the base nitrogens [30]. We do not have the compound deute-

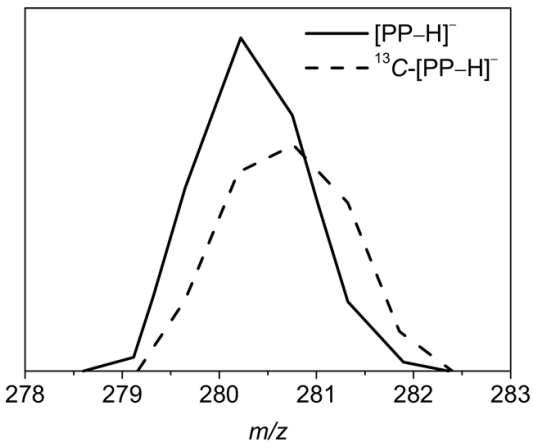

Figure 4. Spectra in the region of the dianion when either $[PP–H]^-$ (*m/z* 561) or ^{13}C-$[PP–H]^-$ (*m/z* 562) that contains one ^{13}C were selected as parent ions.

rium labeled at the carbons for a similar experiment and therefore rely on calculations. These indicate that the LUMO (lowest unoccupied molecular orbital) is a π^* orbital located on the porphyrin macrocycle, but it is not antibonding between carbon and hydrogen (Figure 6); the orbital is similar to the SOMO of the dianion. Finally, we calculated the energies of different C—H and N—H bonds of the porphyrin and found that it requires more than 3.5 eV to cleave an N—H bond and at least 0.8 eV more to cleave a C—H bond. Taken together, we find it safe to conclude that no hydrogen loss occurred after electron capture to the $[PP–H]^-$ anion, which is in accordance with the observation of the intact $[PP+H]^-$ anion from double electron capture to the $[PP+H]^+$ cation in the previous experiment. The dianionic fragment likely results from electron capture by the carboxylic acid group instead of the porphyrin ring followed by loss of COOH to give a carbanion. This competing channel occurs with a probability of about 20%.

We have calculated the electron affinity of the neutral porphyrin macrocycle to be 2.0 eV at the B3LYP/6-31G++(d,p)//6-31G+(d,p) level of theory, which is in accordance with work by others [31]. However, the Coulomb repulsion between the two excess charges likely renders the dianion unbound. The vertical electron affinity of the anion was calculated to be −0.7 eV. Since this value is negative, a strong basis set dependence is expected, and the value should be taken with some caution. Also, possibly the adiabatic electron binding energy of the dianion is positive. If the dianion is unstable to electron autodetachment to the continuum, the electron is still trapped because of the repulsive Coulomb barrier, a phenomenon discussed in great detail in earlier studies [32, 33]. One of the excess charges is on the carboxylate group, and the other is delocalized over the porphyrin macrocycle. For comparison, Goto et al. [34] have recently shown that photoexcited porphyrin anions in a storage ring have a long lifetime with respect to electron autodetachment (microseconds to milliseconds), even when the photon energy is larger than the electron binding energy of the anion, that is, super-excited porphyrin anions were formed. It is therefore reasonable to assume the dianions to be rather long-lived even if electronically unbound.

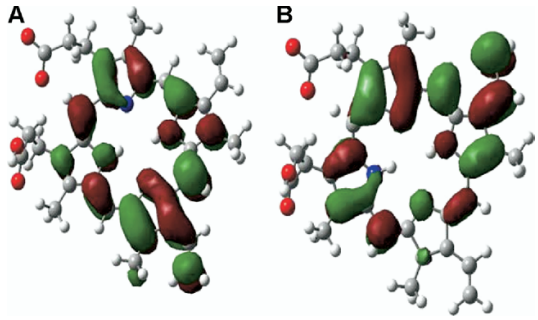

Figure 6. (**A**) The LUMO of the $[PP–H]^-$ anion. (**B**) The SOMO of the $[PP–H]^{2-}$ dianion.

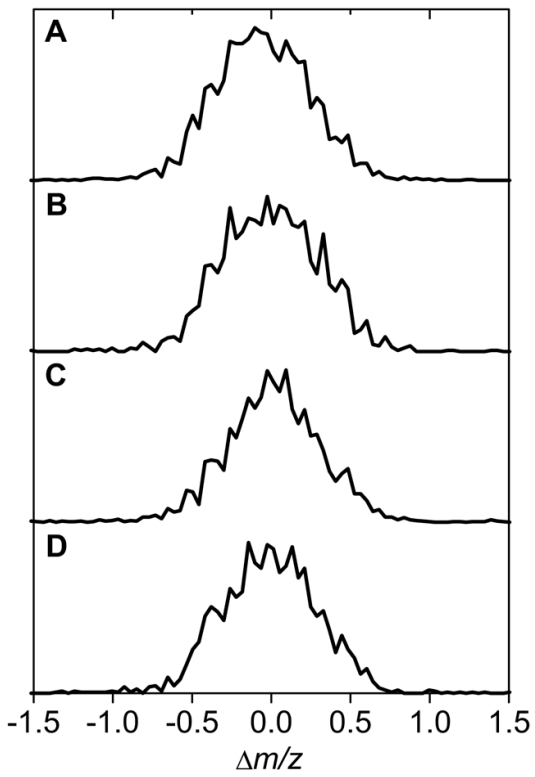

Figure 5. Spectra in the region of the dianion for different degrees of deuterium in the parent ion. The m/z of the intact dianion formed after electron capture corresponds to 0 on the axis. The parent ion is (**A**) $[PP–H]^-$, (**B**) $[PP–H]^-d_1$, (**C**) $[PP–H]^-d_2$, and (**D**) $[PP–H]^-d_3$.

Conclusions

Electron capture by protoporphyrin IX ions leads to limited fragmentation only. In the case of double electron capture by cations hydrogen loss is observed, whereas in the case of single electron capture by anions, the only dissociation process corresponds to the loss of CO_2H.

Acknowledgments

This experiment has been performed at ELISA, part of the distributed LEIF infrastructure. The support received by the European Project ITS LEIF (RII3/026015) is gratefully acknowledged. This work was also supported by Danish Natural Science Research Council Grants 21-04-0514 and 272-06-0427 and Carlsbergfondet Grant 2006-01-0229. Finally, we appreciate many good, fruitful, and highly entertaining discussions with Roman Zubarev over the years and look forward to many more!

References

1. Zubarev, R. A.; Kelleher, N. L.; McLafferty, F. W. Electron Capture Dissociation of Multiply Charged Protein Cations. A Nonergodic Process. *J. Am. Chem. Soc.* **1998,** *120,* 3265–3266.
2. Zubarev, R. A. Reactions of Polypeptide Ions with Electrons in the Gas Phase. *Mass Spectrom. Rev.* **2003,** *22,* 57–77.
3. Ge, Y.; Lawhorn, B. G.; El-Naggar, M.; Strauss, E.; Park, J. H.; Begley, T. P.; McLafferty, F. W. Top Down Characterization of Larger Proteins (45 kDa) by Electron Capture Dissociation Mass Spectrometry. *J. Am. Chem. Soc.* **2002,** *124,* 672–678.
4. Sze, S. K.; Ge, Y.; Oh, H.; McLafferty, F. W. Top-Down Mass Spectrometry of a 29-kDa Protein for Characterization of Any Posttranslational Modification to Within One Residue. *Proc. Natl. Acad. Sci. U.S.A.* **2002,** *99,* 1774–1779.
5. Chamot-Rooke, J.; van der Rest, G.; Dalleu, A.; Bay, S.; Lemoine, J. The Combination of Electron Capture Dissociation and Fixed Charge Derivatization Increases Sequence Coverage for O-Glycosylated and O-Phosphorylated Peptides. *J. Am. Soc. Mass Spectrom.* **2007,** *18,* 1405–1413.
6. Sweet, S. M. M.; Cooper, H. J. Electron Capture Dissociation in the Analysis of Protein Phosphorylation. *Expert Rev. Proteomics* **2007,** *4,* 149–159.
7. Tsybin, Y. O.; Haselmann, K. F.; Emmett, M. R.; Hendrickson, C. L.; Marshall, A. G. Charge Location Directs Electron Capture Dissociation of Peptide Dications. *J. Am. Soc. Mass Spectrom.* **2006,** *17,* 1704–1711.
8. Syka, J. E. P.; Coon, J. J.; Schroeder, M. J.; Shabanowitz, J.; Hunt, D. F. Peptide and Protein Sequence Analysis by Electron Transfer Dissociation Mass Spectrometry. *Proc. Natl. Acad. Sci. U.S.A.* **2004,** *101,* 9528–9533.
9. Coon, J. J.; Syka, J. E. P.; Schwartz, J. C.; Shabanowitz, J.; Hunt, D. F. Anion Dependence in the Partitioning between Proton and Electron Transfer in Ion/Ion Reactions. *Int. J. Mass Spectrom.* **2004,** *236,* 33–42.
10. Pitteri, S. J.; Chrisman, P. A.; Hogan, J. M.; McLuckey, S. A. Electron Transfer Ion/Ion Reactions in a Three-Dimensional Quadrupole Ion Trap: Reactions of Doubly and Triply Protonated Peptides with $SO_2^{\cdot-}$. *Anal. Chem.* **2005,** *77,* 1831–1839.
11. Gunawardena, H. P.; He, M.; Chrisman, P. A.; Pitteri, S. J.; Hogan, J. M.; Hodges, B. D.; McLuckey, S. A. Electron Transfer versus Proton Transfer in Gas-Phase Ion/Ion Reactions of Polyprotonated Peptides. *J. Am. Chem. Soc.* **2005,** *127,* 12627–12639.
12. Srikanth, R.; Wilson, J.; Bridgewater, J. D.; Numbers, J. R.; Lim, J.; Olbris, M. R.; Kettani, A.; Vachet, R. W. Improved Sequencing of Oxidized Cysteine and Methionine Containing Peptides Using Electron Transfer Dissociation. *J. Am. Chem. Soc. Mass Spectrom.* **2007,** *18,* 1499–1506.
13. Hvelplund, P.; Liu, B.; Brøndsted Nielsen, S.; Tomita, S. Electron Capture Induced Dissociation of Peptide Dications. *Int. J. Mass Spectrom.* **2003,** *225,* 83–87.
14. Chakraborty, T.; Holm, A. I. S.; Hvelplund, P.; Brøndsted Nielsen, S.; Poully, J.-C.; Worm, E. S.; Williams, E. R. On the Survival of Peptide Cations after Electron Capture: Role of Internal Hydrogen Bonding and Microsolvation. *J. Am. Soc. Mass Spectrom.* **2006,** *17,* 1675–1680.
15. Holm, A. I. S.; Hvelplund, P.; Kadhane, U.; Larsen, M. K.; Liu, B.; Brøndsted Nielsen, S.; Panja, S.; Pedersen, J. M.; Skrydstrup, T.; Støchkel, K.; Williams, E. R.; Worm, E. S. On the Mechanism of Electron-Capture-Induced Dissociation of Peptide Dications from N-15-Labeling and Crown-Ether Complexation. *J. Phys. Chem. A* **2007,** *111,* 9641–9643.
16. Schultz, K. N.; Hakansson, K. Rapid Electron Capture Dissociation of Mass-Selectively Accumulated Oligodeoxynucleotide Dications. *Int. J. Mass Spectrom.* **2004,** *234,* 123–130.
17. Adamson, J. T.; Hakansson, K. Electron Capture Dissociation of Oligosaccharides Ionized with Alkali, Alkaline Earth, and Transition metals. *Anal. Chem.* **2007,** *79,* 2901–2910.
18. Liang, X.; Liu, J.; LeBlanc, Y.; Covey, T.; Ptak, A. C.; Brenna, J. T.; McLuckey, S. A. Electron Transfer Dissociation of Doubly Sodiated Glycerophosphocholine Lipids. *J. Am. Soc. Mass Spectrom.* **2007,** *18,* 1783–1788.
19. Nielsen, A. B.; Hvelplund, P.; Liu, B.; Brøndsted Nielsen, S.; Tomita, S. Coulomb Explosion upon Electron Attachment to a Four-Coordinate Monoanionic Metal Complex. *J. Am. Chem. Soc.* **2003,** *125,* 9592–9593.
20. Drenck, K.; Hvelplund, P.; McKenzie, C. J.; Brøndsted Nielsen, S. Identification of the Short-lived $Au(N_3)_4^{2-}$ Dianion from its Coulomb Explosion Products. *Int. J. Mass Spectrom.* **2005,** *244,* 144–147.
21. Hvelplund, P.; Liu, B.; Brøndsted Nielsen, S.; Panja, S.; Poully, J.-C.; Støchkel, K. Electron Capture Induced Dissociation of Peptide Ions: Identification of Neutral Fragments from Secondary Collisions with Cesium Vapour. *Int. J. Mass Spectrom.* **2007,** *263,* 66–70.
22. Hayakawa, S.; Hashimoto, M.; Matsubara, H.; Turecek, F. Dissecting the Proline Effect: Dissociations of Proline Radicals Formed by Electron Transfer to Protonated Pro-Gly and Gly-Pro Dipeptides in the Gas Phase. *J. Am. Chem. Soc.* **2007,** *129,* 7936–7949.
23. Boltalina, O. V.; Hvelplund, P.; Jørgensen, T. J. D.; Larsen, M. C.; Larsson, M. O.; Sharoitchenko, D. A. Electron Capture by Fluorinated Fullerene Anions in Collisions with Xe Atoms. *Phys. Rev. A* **2000,** *62,* 023202.
24. Larsson, M. O.; Hvelplund, P.; Larsen, M. C.; Shen, H.; Cederquist, H.; Schmidt, H. T. Electron Capture and Energy Loss in ~100 keV Collisions of Atomic and Molecular Ions on C_{60}. *Int. J. Mass Spectrom.* **1998,** *177,* 51–62.
25. GAUSSIAN 98, Revision A9, Trucks, G. W., Schlegel, H. B., Scuseria, G. E., Robb, M. A., Cheeseman, J. R., Zakrzewski, V. G., Montgomery, J. A., Stratmann, R. E., Burant, J. C., Dapprich, S., Millam, J. M., Daniels, A. D., Kudin, K. N., Strain, M. C., Farkas, O., Tomasi, J., Barone, V., Cossi, M., Cammi, R., Mennucci, B., Pomelli, C., Adamo, C., Clifford, S., Ochterski, J., Petersson, G. A., Ayala, P. Y., Cui, Q., Morokuma, K., Malick, D. K., Rabuck, A. D., Raghavachari, K., Foresman, J. B., Cioslowski, J., Ortiz, J. V., Stefanov, B. B., Liu, G., Liashenko, A., Piskorz, P., Komaromi, I., Gomperts, R., Martin, R. L., Fox, D. J., Keith, T., Al-Laham, M. A., Peng, C. Y., Nanayakkara, A., Gonzalez, C., Challacombe, M., Gill, P. M. W., Johnson, B. G., Chen, W., Wong, M.W., Andres, J. L., Head-Gordon, M., Replogle, E. S., Pople, J. A. Gaussian, Inc., Pittsburgh, PA; 1998.
26. Nonose, S.; Tanaka, H.; Okai, N.; Shibakusa, T.; Fuke, K. Photo-Induced Reactions of $Hemin^+(DMSO)_n$ Clusters (n = 0–3) Produced with Electrospray Ionization. *Eur. Phys. J. D Atomic Mol. Opt. Plasma Physics* **2002,** *20,* 619–626.
27. Charkin, O. P.; Klimenko, N. M.; Nguyen, P. T.; Charkin, D. O.; Mebel, A. M.; Lin, S. H.; Wang, Y.-S.; Wei, S.-C.; Chang, H.-C. Fragmentation of Heme and Hemin(+) with Sequential Loss of Carboxymethyl Groups: A DFT and Mass-Spectrometry Study. *Chem. Phys. Lett.* **2005,** *415,* 362–369.
28. Charkin, O. P.; Klimenko, N. M.; Charkin, D. O.; Chang, H.-C.; Lin, S.-H. Theoretical DFT Study of Fragmentation and Association of Heme and Hemin. *J. Phys. Chem. A* **2007,** *111,* 9207–9217.
29. Hvelplund, P.; Brøndsted Nielsen, S.; Andersen, J. U.; Sørensen, M.; Jørgensen, T. J. D. Electron Loss from Multiply Protonated Lysozyme Ions in High Energy Collisions with Molecular Oxygen. *J. Am. Soc. Mass Spectrom.* **2001,** *12,* 889–893.
30. Liu, B.; Hvelplund, P.; Brøndsted Nielsen, S.; Tomita, S. Hydrogen Loss from Nucleobase Nitrogens upon Electron Attachment to Isolated DNA and RNA Nucleotide Anions. *J. Chem. Phys.* **2004,** *121,* 4175–4179.
31. Tao, M.; Zhou, X.; Jing, M.; Liu, D.; Xing, J. Fluorescence and Electrochemical Properties of Naphthylporphyrins and Porphyrin-Anthraquinone Dyads. *Dyes Pigments* **2007,** *75,* 408–412.
32. Wang, X.-B.; Wang, L.-S. Observation of Negative Electron-Binding Energy in a Molecule. *Nature* **1999,** *400,* 245–248.
33. Wang, X.-B.; Ding, C. F.; Wang, L.-S. Electron Tunneling through the Repulsive Coulomb Barrier in Photodetachment of Multiply Charged Anions. *Chem. Phys. Lett.* **1999,** *307,* 391–396.
34. Goto, M.; Yasuda, Y.; Jinno, S.; Takao, T.; Hanada, K.; Tanuma, H.; Azuma, T.; Sugiura, K.-I.; Shiromaru, H.; Achiba, Y. Electron Detachment of Super-Excited Porphyrin Anions in an Electrostatic Ion Storage Ring. *Eur. Phys. J. D Atomic Mol. Opt. Plasma Physics* **2007,** *43,* 65–68.

Unimolecular Dissociation of Anthracene and Acridine Cations - the C_2H_2 Loss and HCN Loss Channels

H. A. B. Johansson[a], H. Zettergren[a], A. I. S. Holm[a], N. Haag[a], S. Brøndsted Nielsen[b], J. A. Wyer[b], M.-B. S. Kirketerp[b], K. Støchkel[b], P. Hvelplund[b], H. T. Schmidt[a], and H. Cederquist[a]

[a]*Department of Physics, Stockholms University, SE-106 91, Stockholm, Sweden*
[b]*Department of Physics and Astronomy, Aarhus University, DK-8000 Århus C, Denmark*

Abstract

The loss of C_2H_2 is a low activation energy dissociation channel for anthracene ($C_{14}H_{10}$) and acridine ($C_{13}H_9N$) cations. For the latter ion another prominent fragmentation pathway is the loss of HCN. We have studied these two dissociation channels by collision induced dissociation experiments of 50 keV anthracene cations and protonated acridine, both produced by electrospray ionization, in collisions with a neutral xenon target. In addition, we have carried out density functional theory calculations on possible reaction pathways for the loss of C_2H_2 and HCN. The mass spectra display features of multi step processes, and for protonated acridine the dominant first step process is the loss of a hydrogen from the N site, which then leads to C_2H_2/HCN loss from the acridine cation. With our calculations we have identified three pathways for the loss of C_2H_2 from the acridine cation, with three different cationic products: 2-ethynylnaphthalene, biphenylene, and acenaphthylene. The third product is the one with the overall lowest dissociation energy barrier. For the acridine cation our calculated pathway for the loss of C_2H_2 leads to the 3-ethynylquinoline cation, and the loss of HCN leads to the biphenylene cation. Isomerization plays an important role in the formation of the non-ethynyl containing products. All calculated fragmentation pathways should be accessible in the present experiment due to substantial energy deposition in the collisions.

Keywords: Electrospray, anthracene, acridine, acetylene, isomerization, fragmentation

1. Introduction

Polycyclic aromatic hydrocarbons (PAHs) are a class of organic molecules based on two or more fused aromatic rings, with hexagonal rings as a typical dominant constituent. They are found and formed in a wide variety of environments. On Earth, their sources may be both natural and anthropogenic. These include, but are not limited to, incomplete combustion of organic matter [1], oil spills and seeps [2], volcano emissions [3], and biological activity [4]. Sedimentary records show a general good agreement between PAH concentration and the combustion efficiency of industrialization related energy consumption [1]. PAHs are in fact considered to be one of the most widespread organic pollutants [4] and have attracted a lot of attention due to several isomers having toxic, carcinogenic, and mutagenic properties [5].

In extraterrestrial environments, PAHs are believed to be an important component in interstellar dust and gas, and as such responsible for the infrared emission features that dominate the spectra of many galactic and extragalactic sources [6]. PAHs that contain one or more nitrogen atoms, so called polycyclic aromatic nitrogen heterocycles (PANHs), has as of yet not been positively identified in space [7]. They have however been proposed as a possible explanation for the 6.2 μm interstellar emission feature, which is slightly blueshifted from what is observed in laboratory PAH experiments [8], a trend that seems more prominent for protonated PANHs [9]. The existence of PANHs in space has also been inferred by their detection in meteorites [10–12], and they may be present in the haze surrounding Saturn's largest moon Titan [13, 14].

Anthracene, $C_{14}H_{10}$, and acridine, $C_{13}H_9N$, are two representatives of the groups PAHs and PANHs respectively (Fig. 1 presents all the molecules discussed in the introduction). Both molecules consist of three planar aromatic rings, but differ in that a C-H in the central anthracene ring has been replaced by an N to form acridine. The dissociation behavior of anthracene has been studied experimentally through photodissociation[15–17] and collision induced dissociation (CID) [18, 19], and theoretically primarily through density functional theory (DFT) calculations [20, 21]. These studies have shown the lowest unimolecular dissociation channels for the anthracene radical cation, $C_{14}H_{10}^{\bullet+}$, to be the loss of an $H^\bullet$ atom, 2H/H_2, or an acetylene molecule, C_2H_2. Ling and Lifshitz measured the activation energy for these three channels to be 4.38 eV, 4.55 eV and 4.50 eV respectively [17].

The most stable isomer for anthracene$^{\bullet+}$ following acetylene loss is acenaphthylene$^{\bullet+}$ (cf. figure 1). However, experiments have shown that biphenylene$^{\bullet+}$ may be a more plausible product [17, 20], although there is no direct pathway between these two isomers. Biphenylene$^{\bullet+}$ is also the most likely product following acetylene loss from the $C_{14}H_{10}^{\bullet+}$ isomer phenanthrene$^{\bullet+}$, but in this case a direct pathway exists through C_2H_2 elimination from the central ring. The latter led Ling and coworkers to the conclusion that isomerization between the two $C_{14}H_{10}^{\bullet+}$ iso-

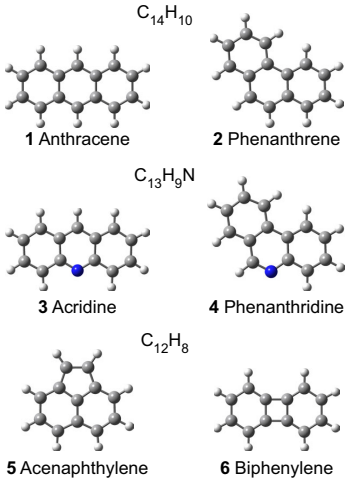

Figure 1: Molecules discussed in the introduction.

mers and direct acetylene loss from anthracene$^{\bullet+}$ are competing processes [17], but no explicit potential energy surface for the two processes was presented. They could also not completely rule out the formation of acenaphthylene$^{\bullet+}$.

For acridine the situation is quite the opposite compared to anthracene in that few references regarding its dissociation behavior can be found in the literature. A comprehensive study was however made by Acheson et al. [22] who obtained a scheme for acridine fragmentation following electron impact excitation. They found that acridine radical cation may decay by emitting an H$^{\bullet}$ atom, 2H/H_2 or a C_2H_2 molecule, just as anthracene does, but with the additional possibility of expelling a hydrogen cyanide molecule, HCN. In order to elucidate the processes involved in the expulsion of HCN Acheson et al. deuterated the central carbon atom in acridine but were unable to detect that deuterium as part of the HCN loss [22].

In this work we study the fragmentation behavior of the anthracene radical cation and protonated acridine, $[C_{13}H_9N + H]^+$, in ion collisions experiments with neutral targets at keV energies. Furthermore, the potential energy surfaces of the C_2H_2 loss channel for anthracene$^{\bullet+}$, and the C_2H_2 and HCN loss channels for acridine$^{\bullet+}$, as well as their isomerization barriers, has been explored with the use of DFT calculations. By means of these calculations we are able to present possible mechanisms for the C_2H_2 and HCN losses.

2. Experimental

The details of the experimental setup has been described elsewhere [23, 24]. In brief, an electrospray ion source was used to produce gas phase ions of anthracene$^{\bullet+}$ and protonated acridine from two separate solutions. The anthracene solution was prepared by dissolving anthracene (≥ 99 % purity, from Fluka) to a 2 ppm concentration in water/methanol (1:1) with 0.1 mmol/L silver nitrate following a procedure outlined by Maziarz et al. [25]. This method makes use of electrochemical effects inherent to the electrospray ion source and allows for the production of anthracene radical cations through an oxidation-reduction reaction with the Ag(I) salt. It is an effective way to produce gas phase ions from non-polar molecules, such as anthracene, that lack a natural site for proton attachment, which is the conventional way of ion production with an electrospray ion source. Acridine, on the other hand, has an excellent site for proton attachment, i.e. the nitrogen atom. Its high electronegativity allows nitrogen to keep its lone pair electrons from delocalizing in the aromatic system and thus be available to bond with ionized atomic hydrogen. Therefore acridine (97 % purity, from Sigma-Aldrich) was dissolved in a methanol solution with 5 % acetic acid acting as a proton donor to create protonated acridine ions.

Both solutions were electrosprayed and accelerated to 50 keV energy, mass-to-charge selected with a bending magnet and passed through a collision cell containing Xe target gas. Fragmentation products were separated with respect to their mass to charge ratios by mens of a hemispherical electrostatic energy analyzer and recorded with a channeltron detector.

3. Computational Details

All calculations were carried out with the use of the GAUSSIAN 09 program package [26] and its implementation of the B3LYP [27, 28] functional to solve for the exchange correlation energy in the Kohn-Sham [29] orbitals approach to density functional theory [30]. This functional has been proven to provide accurate descriptions of the electronic properties in PAHs while maintaining a low computational cost [31].

Geometries were initially optimized with the 6-31G(d) basis set and frequency calculations were carried out to ensure local minima and transition state structures. The geometries were then reoptimized with the larger 6-311G++(2d,p) basis set, including frequency calculations. Quoted energies are relative energies obtained with the use of the larger basis set. Zero point energy corrections, scaled with the factor 0.9877 [32], have also been taken into account. The relative energies with the larger basis set differ from the ones with the smaller basis set by typically less than 0.1 eV, and at most with 0.4 eV. Intrinsic reaction coordinate calculations were carried out at the 6-31G(d) level to confirm connections between transition states and their associated local minima. All energies are quoted in electronvolt (eV).

4. Results and Discussion

Figure 2, shows the complete collision induced dissociation spectra for protonated acridine, $[C_{13}H_9N+H]^+$ (m/q = 180), and the anthracene radical cation, $C_{14}H_{10}^{\bullet+}$ (m/q = 178), in 50 keV collisions with a Xe target. Insets in the panels also show the molecular structure of each ion. The spectra are dominated by the parent ions, which are located to the far right in the left panels in the figures and are off scale by several orders of magnitude. Daughter ions are grouped by their total numbers, n, of

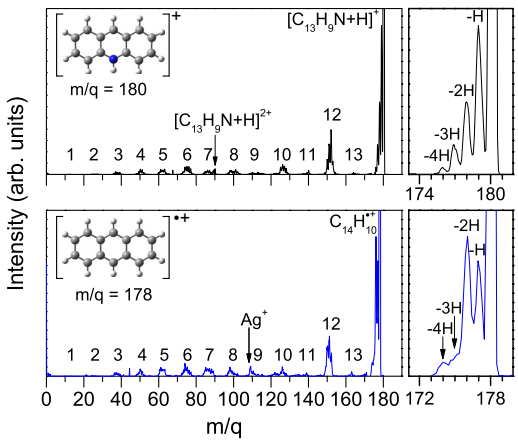

Figure 2: Collision Induced Dissociation mass-to-charge spectra for protonated acridine (top) and the anthracene radical cation (bottom) in collisions with Xe. The parent ion intensities are located furthest to the right and are off scale by several orders of magnitude. The total number, n, of non-hydrogen atoms in each daughter ion group is marked for each group. Also marked is the dication present for the protonated acridine, and the Ag^+ contamination present in the anthracene spectrum. Right panels: Zoom-ins of parent ions with hydrogen loss series.

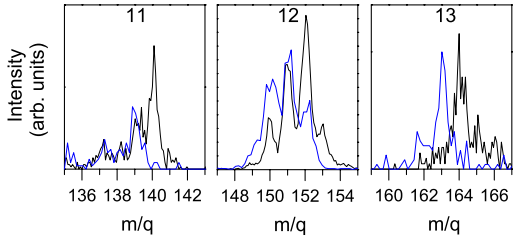

Figure 3: Zoom-ins of daughter ion groups, for n = 11, 12, and 13, where n is the total number of non-hydrogen atoms in the group, in the protonated acridine (black) and anthracene radical cation (blue) spectra from figure 2. The groups are normalized with respect to the total intensity within each group.

non-hydrogen atoms, as indicated in the figure. These groups follow an odd/even pattern, with the even groups having larger intensities than the odd ones, as is typical for thermally activated PAH molecules [33] and fullerenes [34, 35] undergoing multifragmentation processes. This pattern is the most prominent when $n \geq 8$. The fragment groups at $n = 12$ are strong in both spectra and are due to one-step processes. These will be explored in greater detail below. The spectra in figure 2 also show the presence of dications formed from the parent ions. We believe that these peaks are due to collisions with residual oxygen gas in the beamline and not with Xe. In the case of the anthracene cation a peak corresponding to the m/q of singly ionized silver is also seen, and it is a contaminant from the solution used to ionize anthracene. There is a second, unidentified, contamination peak at $m/q = 69$. These contaminants were strongly reduced in intensity through adjustments of the ion source parameters and furthermore they lie outside the mass ranges of interest in this study.

The right panels in figure 2 show zoom-ins of the parent ions and their associated series of hydrogen losses. For $[acridine+H]^+$ the loss of 1H is the dominant fragmentation pathway, while for $anthracene^{\bullet+}$ loss of 2H dominates. The latter could be in the form of two consecutive $H^\bullet$ losses or the loss of an H_2 molecule. Ling et al. performed time-resolved photo-ionization mass spectrometry of pyrene [36] and fluoranthene [37] and reported the two channels to compete, with H_2 molecular loss dominating for photon energies below 19 eV, while consecutive $H^\bullet$ loss becomes more important for higher energies. Dyakov et al. calculated H_2 loss reactions from naphthalene cations and found them to be associated with H atom migrations around the carbon rings with a barrier 60-70 % of the barrier height of H_2 elimination [38]. The dominant 2H loss peak in the $anthracene^{\bullet+}$ spectrum therefore indicates that substantial energy is transferred in the collisions and possibly that significant H atom migration have taken place in the ions prior to dissociation.

The large probability for $[acridine+H]^+$ to loose one $H^\bullet$ atom can be further investigated by comparing the fragmentation pattern of $[acridine+H]^+$ to that of $anthracene^{\bullet+}$. Figure 3 show zoom-ins of the daughter ions groups of $[acridine+H]^+$ and $anthracene^{\bullet+}$ for n = 11, 12, and 13. The mass difference between the two parent ions is 2 amu, but for the three daughter ion groups the mass shift is dominantly 1 amu. In the case of $anthracene^{\bullet+}$ the peaks at m/q = 163, 152, and 139 are attributed to the loss of CH_3, C_2H_2, and C_3H_3 respectively. Lower mass peaks in each group are due to subsequent or preceding $H^\bullet$ or H_2 losses. For the $[acridine+H]^+$ daughter ions the interpretation becomes more ambiguous as the experiment does not allow us to distinguish an m/q of 14 from being N or CH_2. However, the observation that the daughter ions groups in figure 3 are shifted 1 amu with respect to the two parent ions instead of 2 amu, which leads us to the conclusion that the first step in $[acridine+H]^+$ dissociation is strongly dominated by the loss of $H^\bullet$ from the nitrogen site, forming the $acridine^{\bullet+}$ radical cation. This conclusion is supported by our calculations, which show that the most weakly bound hydrogen in $[acridine+H]^+$ is the hydrogen bound to the nitrogen site. Its dissociation energy is 4.07 eV, which is 0.75 eV lower than that for the second weakest bound hydrogen. For comparison, we calculated the smallest C-H dissociation energy in $anthracene^{\bullet+}$ to be 5.28 eV. Further support can be drawn from Acheson et al., whose electron impact induced fragmentation mass spectrum of acridine show the same general features for n = 11, 12, and 13 [22] as our own. They further performed a detailed study of the $n = 12$ group mass region and concluded that $m/q = 153$ is associated with the loss of C_2H_2, while m/q = 152 to 149 are associated with the loss of HCN and subsequent or preceding $H^\bullet$ losses. The similarities between the spectra leads us to believe that our fragment peaks correspond to the same fragmentation channels.

In the next section we will describe the present theoretical

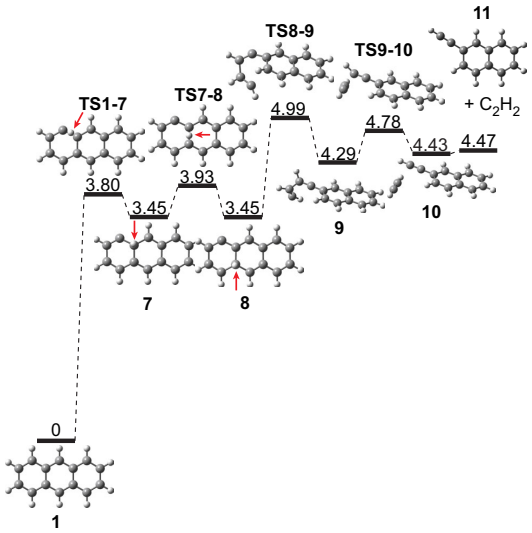

Figure 4: C_2H_2 elimination from an outer ring in the anthracene cation, yielding 2-ethynylnaphthalene$^{\bullet+}$ (**11**).

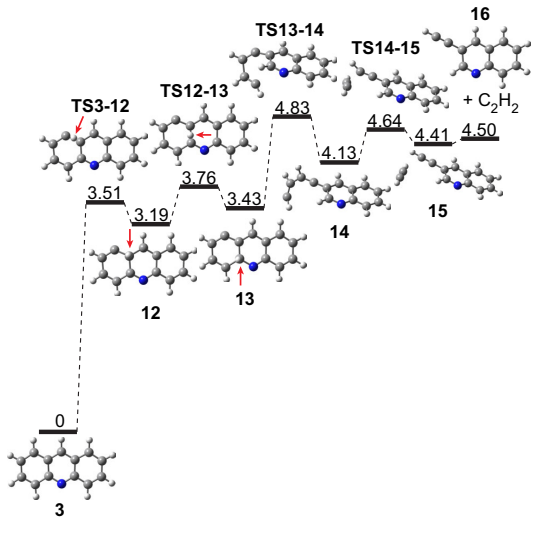

Figure 5: C_2H_2 elimination from an outer ring in the acridine cation, yielding 3-ethynylquinoline (**16**).

calculations, which suggest possible mechanisms for the losses of C_2H_2 from anthracene$^{\bullet+}$ and acridine$^{\bullet+}$, and for the loss of HCN from acridine$^{\bullet+}$.

4.1. C_2H_2 Loss from an Outer Ring

The most obvious locations to remove a C_2H_2 molecule from anthracene$^{\bullet+}$ or acridine$^{\bullet+}$ are from one of the outer rings. Dyakov et al. performed extensive *ab initio* calculations on C_2H_2 loss from the naphthalene radical cation $C_{10}H_8^{\bullet+}$ [38]. They identified three possible pathways for removing C_2H_2, two of which led to benzocyclobutadiene$^{\bullet+}$, which has a four carbon ring. The third led to phenylacetylene$^{\bullet+}$, which has an open ring, and it was this pathway that had the overall lowest barrier in their calculations [38]. Therefore we used the structures corresponding to this third pathway as input parameters to search for similar reaction pathways in anthracene$^{\bullet+}$. The potential energy profile obtained from these calculations is shown in figure 4. The reaction is initiated by a hydrogen from an outer ring shifting two steps to a non-hydrogenated carbon, forming structure **8**. This allows for the outer ring to open up via the transition state (TS) between structures **8** and **9**, **TS8-9**, and bud off a C_2H_2 unit via **TS9-10**, which is removed from the parent molecule through the metastable ion-molecule complex **10**, forming the final product of 2-ethynylnaphthalene$^{\bullet+}$ (**11**). The highest barrier along this reaction pathway is **TS8-9** with 4.99 eV.

A similar pathway exists for removing C_2H_2 from acridine$^{\bullet+}$, as illustrated in figure 5. It also begins with a two-step hydrogen shift to a previous hydrogen free carbon shared by two rings, followed by a break in the outer ring and removal of a C_2H_2 unit. However, a difference exists in that acridine is not symmetric along a plane perpendicular to the plane of the molecule and located along the center of its long axis. A mirrored pathway is thus possible where the hydrogen shifts to the other ring-shared carbon and consequently breaks the bond at a carbon located two steps away from the nitrogen instead of a neighboring one. We found the largest barrier for this alternative pathway to lie 0.12 eV above the largest barrier in figure 5, **TS13-14**. This is not an surprising result considering that the larger electronegativity of nitrogen compared to carbon would exert a larger attraction of the electrons in its vicinity, thereby weakening the double bond character of bonds to its neighboring carbons. We have not computed the alternative pathway for removing C_2H_2 that leads to a cyclobutadiene-like state in the outer ring, as it probably has a larger barrier as in the case of naphthalene [38]. The reaction pathway in figure 5 therefore is the one with the overall lowest barrier, the value of which is 4.83 eV above the ground state of acridine$^{\bullet+}$. Here 3-ethynylquinoline (**16**) is the end product.

4.2. C_2H_2 Loss from Anthracene$^{\bullet+}$ Following Isomerization

Figure 6 shows one possible reaction pathway for eliminating C_2H_2 from anthracene$^{\bullet+}$ via the phenanthrene$^{\bullet+}$ isomer. It is, just as the the previously mentioned pathway for removing C_2H_2 from an outer ring, initiated by a hydrogen shifting two steps to a previously unhydrogenated ring shared carbon. The difference in this case is that the hydrogen originates from one of the center ring's carbons. Structure **18** then allows for the bond to the outer ring at the site of the hydrogenated carbon to be broken, and consequently the outer ring to shift position via **TS18-19**, the spiro structure **19**, and **TS19-2** to form phenanthrene$^{\bullet+}$. The barrier for **TS19-2** is very low, differing from the preceding minimum only at the second decimal. In other words the ring shift proceeds quite easily once it has past

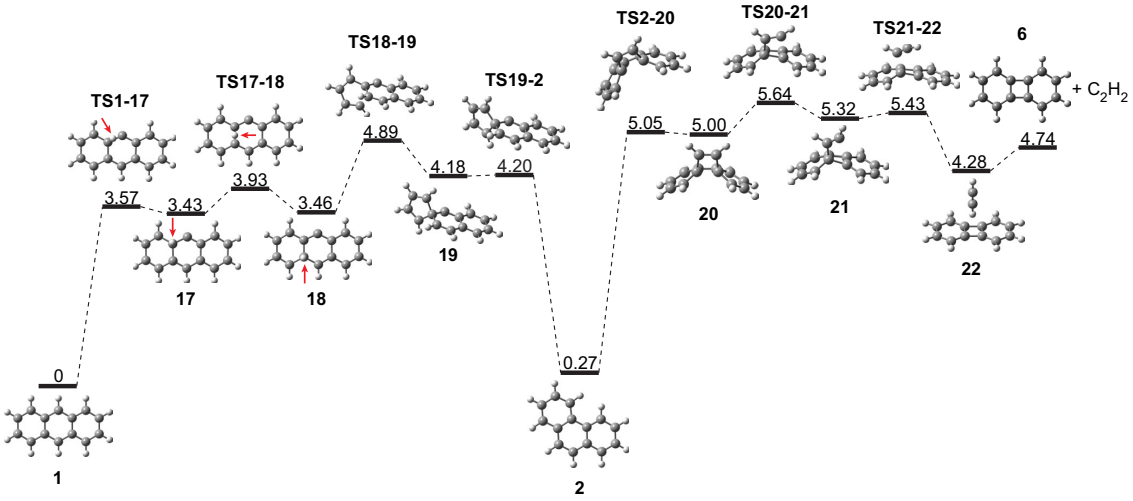

Figure 6: C_2H_2 loss from the anthracene cation (**1**) forms a biphenylene cation (**6**) product via an intermediate phenanthrene cation (**2**) structure.

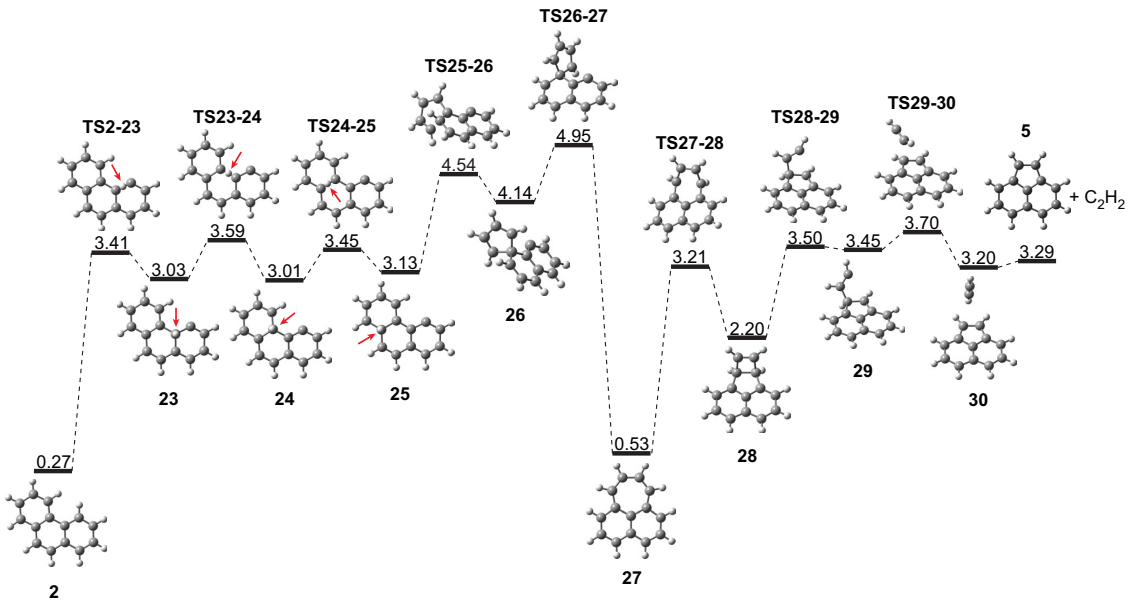

Figure 7: C_2H_2 loss from the phenanthrene cation (**1**). The product is the acenaphthylene cation (**5**), formed via a cyclohepta[de]naphthalene cation (**27**) intermediate structure.

its first barrier **TS18-19**. This mechanism for changing isomer from anthracene$^{\bullet+}$ to phenanthrene$^{\bullet+}$ is similar to the one proposed for the transformation of phenanthrene to anthracene on catalytic surfaces [39].

Phenanthrene$^{\bullet+}$ (**2**) is able to contract and bend to a Dewar-benzene-like state in the central ring (**20**) via transition state **TS2-20**. From here the first C-C bond is broken via **TS20-21** to **21**, and the second C-C bond is broken via **TS21-22**, forming the ion-molecule complex **22**, which is 0.46 eV lower in energy than the final products biphenylene$^{\bullet+}$ (**6**) and C_2H_2.

Instead of releasing C_2H_2 from phenanthrene$^{\bullet+}$ the isomerization process can continue with one additional ring shift to form cyclohepta[de]naphthalene$^{\bullet+}$ (**27**) as is shown in figure 7. This process is also initiated by hydrogen shifts. One hydro-

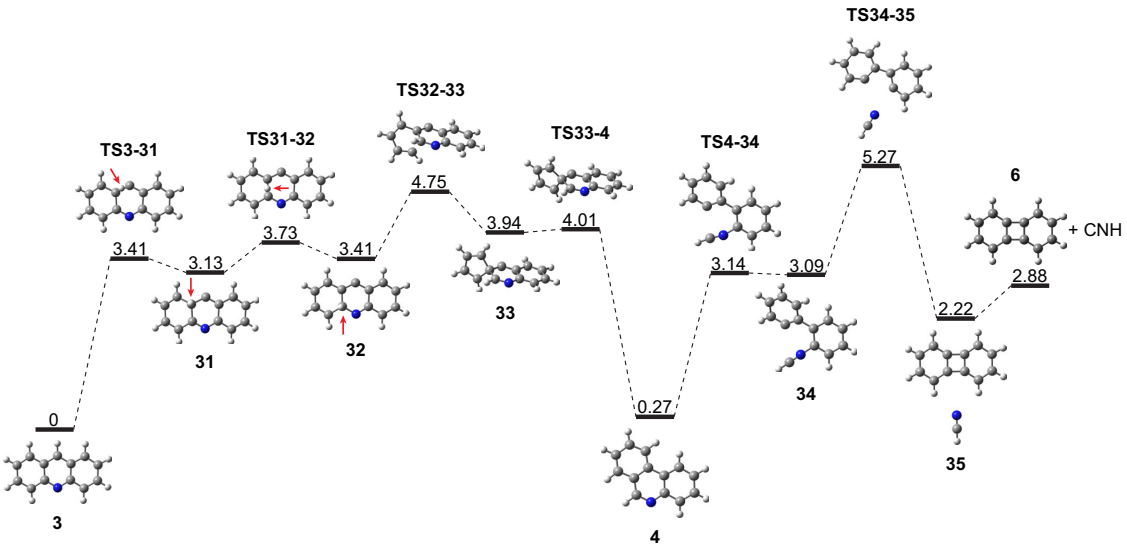

Figure 8: HCN elimination from the acridine cation (**3**) with a biphenylene cation (**6**) product. The reaction proceeds via a phenanthridine cation (**4**) intermediate structure.

gen is shifted from an outer ring carbon to a previously non-hydrogenated carbon shared between the two other rings, forming **25**. The outer ring opens up via **TS25-26**, proceeds to the spiro compound **26**, and forms cyclohepta[de]naphthalene$^{\bullet+}$ (**27**) via **TS26-27**. From here the large 7C ring is able to contract via **TS27-28** to **28**, after which the first C-C bond is broken to form **29** and the second to form the ion-molecule complex **30**, leading to the final products of acenaphthylene$^{\bullet+}$ (**5**) and C_2H_2. The second ring shift to cyclohepta[de]naphthalene$^{\bullet+}$ has a barrier hight of 4.95 eV, which is similar to the first ring shift, and constitutes the largest barrier for this second reaction pathway.

The processes just described show how biphenylene$^{\bullet+}$ and acenaphthylene$^{\bullet+}$ can be formed from an initial anthracene$^{\bullet+}$ during release of C_2H_2 via isomer intermediates. They serve to illustrate that isomerization from anthracene$^{\bullet+}$ to phenanthrene$^{\bullet+}$ and cyclohepta[de]naphthalene$^{\bullet+}$ are competing processes to C_2H_2 elimination. These calculations also indicate that acenaphthylene$^{\bullet+}$ formation has a lower barrier than biphenylene$^{\bullet+}$ formation. It is worth pointing out that due to the complexity if the potential energy surface other reaction pathways leading to the same products may exist as well. The purpose of the ones presented here has been to provide plausible mechanisms without an excessive number of reaction steps.

4.3. HCN Loss from $C_{13}H_9N^{\bullet+}$ Following Isomerization

The strong channel of $C_{13}H_9N^{\bullet+}$ dissociation through elimination of HCN is well known through detailed experimental studies [22], and though our experiment does not allow us to determine the exact elemental composition of the detected fragments, the similarities between our spectrum and that of Acheson et al. [22] leads us to believe that HCN is a prominent dissociation channel in our experiment as well (cf. above). Figure 8 provides a plausible mechanism to remove HCN from $C_{13}H_9N^{\bullet+}$. It resembles the one for removing C_2H_2 from anthracene$^{\bullet+}$ via a phenanthrene$^{\bullet+}$ intermediate and with a biphenylene$^{\bullet+}$ end product as discussed in the previous section. The steps in the change in isomer are in fact the same, except that the energies are shifted to slightly lower values. Once the phenanthridine$^{\bullet+}$ (**4**) isomer has been formed, HCN can be removed from the center ring and the path for doing so is more direct, with one less transition state, compared to the corresponding phenanthrene$^{\bullet+}$ reaction. It is the lack of a hydrogen bonded to the nitrogen that allows for an immediate formation of a straight HCN chain in **34** following **TS4-34**. From here the HCN can detach via **TS34-35** and the ion-molecule complex **35**. The C-N bond is the one that requires the most energy to break with a barrier hight of 5.27 eV.

4.4. Connection to Mass Spectra

A summary of the three different C_2H_2 elimination pathways presented in this study for anthracene$^{\bullet+}$, together with the highest associated isomerization and elimination barrier, is presented in figure 9. It clearly shows that from an energetics point of view acenaphthylene$^{\bullet+}$ is the favored end product. Unfortunately the present experiment does not allows us to determine the energy transferred in the collisions and therefore it is not possible to use the calculated reaction pathways for any quantitative conclusion regarding what isomer is formed. However, the presence of a fragment peak at $m/q = 151$ that is stronger than the one at $m/q = 152$ suggests that the energy transferred in the collisions is sufficient to allow for two step processes, i.e. 1H loss followed by C_2H_2 loss or vice versa. In recent

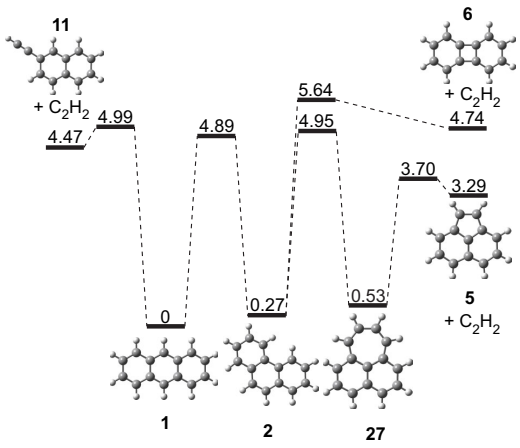

Figure 9: The relative energies of the three $C_{14}H_{10}^{\bullet+}$ isomers and the three products following C_2H_2 loss, together with the highest associated barrier.

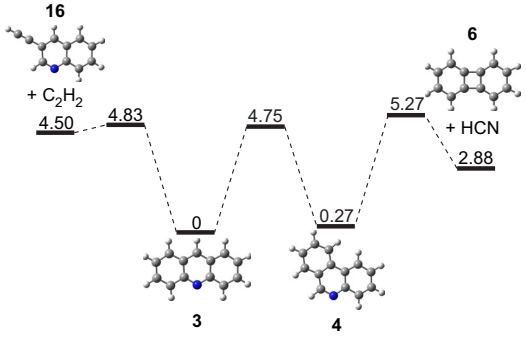

Figure 10: The relative energies of the two $C_{13}H_9N^{\bullet+}$ isomers and the products following C_2H_2 or HCN loss, together with the highest associated barrier.

experiments using 30 keV He^{2+} ions in collisions with neutral anthracene molecules, very similar distributions were measured for the $C_{10}H_6$, $C_{10}H_7$, and $C_{10}H_8$ peaks [40]. These studies also included calculations on the electronic stopping and found it to be 45.8 eV. And even though they determined double electron capture processes to also influence their fragment distribution, it does not seem to affect these three peaks to any large extent considering that Holm et al. obtained a very similar looking distribution with a 22.5 keV He^+ projectile [33]. The 45.8 eV should therefore serve well as a lower limit for the energy transferred in the present experiment. At these energies it is evident that all three fragmentation pathways are accessible and may be present as products in the spectrum.

Figure 10 shows a summary of the calculated C_2H_2 loss and HCN loss pathways for acridine$^{\bullet+}$ together and the highest associated isomerization and elimination barrier. It shows that the loss of C_2H_2 is in close competition to the isomerization to phenanthridine$^{\bullet+}$, and the barrier for HCN loss is only 0.44 eV higher. It is reasonable to assume that similar energies are transferred in the experiment in this case as for anthracene$^{\bullet+}$. Therefore multi step processes should play important roles here as well. Indeed, the observed large probability for the loss of one hydrogen from $[C_{13}H_9N]^+$ (not shown in figure 10) prior to the formation of the $n = 11$, 12 and 13 fragment groups prove that fragmentation in multiple steps do occur. For this reason it seems reasonable that the peak at $m/q = 152$ should not only represent biphenylene$^{\bullet+}$ (HCN loss), but also include contributions from 3-ethynylquinoline$^{\bullet+}$ (C_2H_2 loss) minus H.

5. Summary and Conclusions

We have carried out collision induced dissociation experiments on the anthracene radical cation and protonated acridine in collisions with a Xe gas target. Focus has been on the C_2H_2 and the HCN loss channels for which we have explored the potential energy surface with the use of density functional theory calculations. The loss of C_2H_2 is a prominent fragmentation pathway for anthracene$^{\bullet+}$. With our calculations we have obtained three fragmentation pathways for the loss of C_2H_2 from anthracene$^{\bullet+}$. The first forms 2-ethynylnaphthalene$^{\bullet+}$ through release of C_2H_2 from one of the outer rings. The second forms biphenylene$^{\bullet+}$ via the phenanthrene$^{\bullet+}$ isomer. And the third forms acenaphthylene$^{\bullet+}$ via an additional isomerization to cyclohepta[de]naphthalene$^{\bullet+}$. Of these three pathways the third one has the overall lowest reaction barrier and should therefore dominate near the appearance energy for C_2H_2. All three pathways rely on hydrogen shifts within the rings to enable C-C bonds to be broken. The spectrum of the present experiment however contain elements that indicate that significant energy has been deposited in the collision. Comparison with other work suggests a lower limit 45.8 eV deposited energy. Our spectrum should for this reason include products from all three fragmentation pathways.

For $[\text{acridine+H}]^+$ the fragments observed in the mass spectrum all seem to be stem from processes with at least two steps, where the first step is the loss of a neutral H from the N site. For the resulting acridine$^{\bullet+}$ ion we have presented calculations on pathways for how to loose C_2H_2 and HCN. C_2H_2 can be released directly from an outer ring, while HCN loss requires an isomerization to a phenanthridine $^{\bullet+}$ intermediate structure. The C_2H_2 loss channel has the overall lowest barrier, but as similar energies are deposited as in the case of anthracene$^{\bullet+}$, both fragmentation channels should be well within reach here and should be reflected in the measured spectrum.

Studies of the C_2H_2 loss mechanism, such as the one presented here, are also important for the understanding of the $C_2H_2^+$ loss mechanism, which may determine the ultimate stability limit for multiply charged PAHs [21].

Acknowledgements

The experiments were performed at the ELISA facility, part of the distributed LEIF infrastructure. The support received

by the European Project ITS LEIF (RII3/026015) is gratefully acknowledged. This work is also supported by the Swedish Research Council and the Danish Council for Independent Research/Natural Sciences.

[1] A. L. C. Lima, J. W. Farrington, C. M. Reddy, Combustion-Derived Polycyclic Aromatic Hydrocarbons in the Environment - A Review, Environmental Forensics 6 (2) (2005) 109–131.

[2] J. W. Short, G. V. Irvine, D. H. Mann, J. M. Maselko, J. J. Pella, M. R. Lindeberg, J. R. Payne, W. B. Driskell, S. D. Rice, Slightly weathered exxon valdez oil persists in gulf of alaska beach sediments after 16 years, Environmental Science & Technology 41 (4) (2007) 1245–1250.

[3] L. Culotta, A. Gianguzza, M. R. Mannino, S. Orecchio, Polycyclic aromatic hydrocarbons (pah) in vulcano island (aeolian archipelago) mud utilized for therapeutic purpose, Polycyclic Aromatic Compounds 27 (4) (2007) 281–294.

[4] W. Wilcke, Global patterns of polycyclic aromatic hydrocarbons (pahs) in soil, Geoderma 141 (3-4) (2007) 157–166.

[5] C. Bosetti, P. Boffetta, C. La Vecchia, Occupational exposures to polycyclic aromatic hydrocarbons, and respiratory and urinary tract cancers: a quantitative review to 2005, Annals of Oncology 18 (3) (2007) 431–446.

[6] A. G. G. M. Tielens, Interstellar polycyclic aromatic hydrocarbon molecules, Annual Review of Astronomy and Astrophysics 46 (2008) 289–337.

[7] S. B. Charnley, Y. J. Kuan, H. C. Huang, O. Botta, H. M. Butner, N. Cox, D. Despois, P. Ehrenfreund, Z. Kisiel, Y. Y. Lee, A. J. Markwick, Z. Peeters, S. D. Rodgers, Astronomical searches for nitrogen heterocycles, Space Life Sciences: Astrobiology: Steps Toward Origin of Life and Titan Before Cassini 36 (2) (2005) 137–145.

[8] D. M. Hudgins, C. W. Bauschlicher, L. J. Allamandola, Variations in the peak position of the 6.2 mu m interstellar emission feature: A tracer of n in the interstellar polycyclic aromatic hydrocarbon population, Astrophysical Journal 632 (1) (2005) 316–332.

[9] H. A. Galue, O. Pirali, J. Oomens, Gas-phase infrared spectra of cationized nitrogen-substituted polycyclic aromatic hydrocarbons, Astronomy & Astrophysics 517 (2010) A15. doi:10.1051/0004-6361/201014050.

[10] P. G. Stoks, A. W. Schwartz, Nitrogen-heterocyclic compounds in meteorites - significance and mechanisms of formation, Geochimica Et Cosmochimica Acta 45 (4) (1981) 563–569.

[11] P. G. Stoks, A. W. Schwartz, Basic nitrogen-heterocyclic compounds in the murchison meteorite, Geochimica Et Cosmochimica Acta 46 (3) (1982) 309–315.

[12] O. Botta, J. L. Bada, Extraterrestrial organic compounds in meteorites, Surveys In Geophysics 23 (5) (2002) 411–467.

[13] A. Ricca, C. W. Bauschlicher, E. L. O. Bakes, A computational study of the mechanisms for the incorporation of a nitrogen atom into polycyclic aromatic hydrocarbons in the titan haze, Icarus 154 (2) (2001) 516–521.

[14] H. Imanaka, B. N. Khare, J. E. Elsila, E. L. O. Bakes, C. P. McKay, D. P. Cruikshank, S. Sugita, T. Matsui, R. N. Zare, Laboratory experiments of titan tholin formed in cold plasma at various pressures: implications for nitrogen-containing polycyclic aromatic compounds in titan haze, Icarus 168 (2) (2004) 344–366.

[15] H. W. Jochims, E. R "uhl, H. Baumgärtel, S. Tobita, S. Leach, Size effects on dissociation rates of polycyclic aromatic hydrocarbon cations - laboratory studies and astrophysical implications, Astrophysical Journal 420 (1) (1994) 307–317.

[16] S. P. Ekern, A. G. Marshall, J. Szczepanski, M. Vala, Photodissociation of gas-phase polycylic aromatic hydrocarbon cations, Journal of Physical Chemistry A 102 (20) (1998) 3498–3504.

[17] Y. Ling, C. Lifshitz, Time-dependent mass spectra and breakdown graphs. 21. c14h10 isomers, Journal of Physical Chemistry A 102 (4) (1998) 708–716.

[18] X. M. Wang, H. Becker, A. C. Hopkinson, R. E. March, L. T. Scott, D. K. Bohme, Collision-induced dissociation of 2- and 3-dimensional polycyclic aromatic hydrocarbon cations in a modified ion-trap detector, International Journal Of Mass Spectrometry And Ion Processes 161 (1-3) (1997) 69–76.

[19] R. Arakawa, M. Kobayashi, T. Nishimura, High-energy collision-induced dissociation of small polycyclic aromatic hydrocarbons, Journal Of Mass Spectrometry 35 (2) (2000) 178–182.

[20] Y. Ling, J. M. L. Martin, C. Lifshitz, Energetics of acetylene loss from c14h10 center dot+ cations: A density functional calculation, Journal of Physical Chemistry A 101 (2) (1997) 219–226.

[21] A. I. S. Holm, H. A. B. Johansson, H. Cederquist, H. Zettergren, Dissociation and multiple ionization energies for five polycyclic aromatic hydrocarbon molecules, Journal of Chemical Physics 134 (4) (2011) 044301. doi:10.1063/1.3541252.

[22] R. M. Acheson, R. T. Aplin, R. G. Bolton, Electron-impact-induced fragmentation of acridine, Organic Mass Spectrometry 8 (JAN) (1974) 95–102.

[23] M. O. Larsson, P. Hvelplund, M. C. Larsen, H. Shen, H. Cederquist, H. T. Schmidt, Electron capture and energy loss in similar to 100 kev collisions of atomic and molecular ions on c-60, International Journal of Mass Spectrometry 177 (1) (1998) 51–62.

[24] O. V. Boltalina, P. Hvelplund, T. J. D. Jorgensen, M. C. Larsen, M. O. Larsson, D. A. Sharoitchenko, Electron capture by fluorinated fullerene anions in collisions with Xe atoms, Physical Review A 62 (2) (2000) 023202.

[25] E. Maziarz, G. Baker, T. Wood, Electrospray ionization Fourier transform mass spectrometry of polycyclic aromatic hydrocarbons using silver(I)-mediated ionization, Canadian Journal of Chemistry 83 (11) (2005) 1871–1877. doi:10.1139/V05-195.

[26] M. J. Frisch, G. W. Trucks, H. B. Schlegel, G. E. Scuseria, M. A. Robb, J. R. Cheeseman, G. Scalmani, V. Barone, B. Mennucci, G. A. Petersson, H. Nakatsuji, M. Caricato, X. Li, H. P. Hratchian, A. F. Izmaylov, J. Bloino, G. Zheng, J. L. Sonnenberg, M. Hada, M. Ehara, K. Toyota, R. Fukuda, J. Hasegawa, M. Ishida, T. Nakajima, Y. Honda, O. Kitao, H. Nakai, T. Vreven, J. A. Montgomery, Jr., J. E. Peralta, F. Ogliaro, M. Bearpark, J. J. Heyd, E. Brothers, K. N. Kudin, V. N. Staroverov, R. Kobayashi, J. Normand, K. Raghavachari, A. Rendell, J. C. Burant, S. S. Iyengar, J. Tomasi, M. Cossi, N. Rega, J. M. Millam, M. Klene, J. E. Knox, J. B. Cross, V. Bakken, C. Adamo, J. Jaramillo, R. Gomperts, R. E. Stratmann, O. Yazyev, A. J. Austin, R. Cammi, C. Pomelli, J. W. Ochterski, R. L. Martin, K. Morokuma, V. G. Zakrzewski, G. A. Voth, P. Salvador, J. J. Dannenberg, S. Dapprich, A. D. Daniels, . Farkas, J. B. Foresman, J. V. Ortiz, J. Cioslowski, D. J. Fox, Gaussian 09 Revision A.2, gaussian Inc. Wallingford CT 2009.

[27] A. D. Becke, Density-functional Thermochemistry .3. the Role of Exact Exchange, Journal of Chemical Physics 98 (7) (1993) 5648–5652.

[28] C. T. Lee, W. T. Yang, R. G. Parr, Development of the Colle-salvetti Correlation-energy Formula Into A Functional of the Electron-density, Physical Review B 37 (2) (1988) 785–789.

[29] W. Kohn, L. J. Sham, Self-consistent equations including exchange and correlation effects, Physical Review 140 (4A) (1965) 1133–1138.

[30] P. Hohenberg, W. Kohn, Inhomogeneous electron gas, Physical Review B 136 (3B) (1964) 864–871.

[31] K. B. Wiberg, Properties of some condensed aromatic systems, Journal of Organic Chemistry 62 (17) (1997) 5720–5727.

[32] M. P. Andersson, P. Uvdal, New scale factors for harmonic vibrational frequencies using the b3lyp density functional method with the triple-xi basis set 6-311+g(d,p), Journal of Physical Chemistry A 109 (12) (2005) 2937–2941. doi:10.1021/jp045733a.

[33] A. I. S. Holm, H. Zettergren, H. A. B. Johansson, F. Seitz, S. Rosén, H. T. Schmidt, A. Ławicki, J. Rangama, P. Rousseau, M. Capron, R. Maisonny, L. Adoui, A. Méry, B. Manil, B. A. Huber, H. Cederquist, Ions colliding with cold polycyclic aromatic hydrocarbon clusters, Phys. Rev. Lett. 105 (21) (2010) 213401. doi:10.1103/PhysRevLett.105.213401.

[34] T. Schlatholter, R. Hoekstra, R. Morgenstern, Collisions of oq+ with neutral c-60: Charge transfer and fragmentation, Journal of Physics B-atomic Molecular and Optical Physics 31 (6) (1998) 1321–1331.

[35] H. Cederquist, A. Fardi, K. Haghighat, A. Langereis, H. T. Schmidt, H. Schwartz, J. C. Levin, I. A. Sellin, H. Lebius, B. Huber, M. O. Larsson, P. Hvelplund, Electronic response of c-60 in slow collisions with highly charged ions, Physical Review A 61 (2) (2000) 022712.

[36] Y. Ling, Y. Gotkis, C. Lifshitz, Time-dependent mass-spectra and breakdown graphs .18. pyrene, European Mass Spectrometry 1 (1) (1995) 41–49.

[37] Y. Ling, C. Lifshitz, Time-dependent mass-spectra and breakdown graphs .19. fluoranthene, Journal of Physical Chemistry 99 (28) (1995) 11074–11080.

[38] Y. A. Dyakov, C. K. Ni, S. H. Lin, Y. T. Lee, A. M. Mebel, Ab initio and rrkm study of photodissociation of azulene cation, Physical Chemistry

Chemical Physics 8 (12) (2006) 1404–1415.
[39] C. S. Song, Selective conversion of polycyclic hydrocarbons to specialty chemicals over zeolite catalysts, Cattech 6 (2) (2002) 64–77.
[40] J. Postma, S. Bari, R. Hoekstra, A. G. G. M. Tielens, T. Schlatholter, Ionization and fragmentation of anthracene upon interaction with kev protons and alpha particles, Astrophysical Journal 708 (1) (2010) 435–444.